Optical Properties of Luminescent Solar Concentrators

Adam Peter Green, MPhys

Submitted for the degree of

Doctor of Philosophy (Ph.D)

On completion of research at

The Department of Physics and Astronomy
The University of Sheffield
Sheffield
S3 7RH
England

During

March 2014

Abstract

This thesis on luminescent solar concentrators (LSC) presents work carried out as part of the Electronic and Photonic Molecular Materials (EPMM) group of the department of physics and astronomy at the University of Sheffield. The work is presented in five experimental chapters looking at a range of research aspects from film deposition and measurement instrumentation, to exploring LSC optical properties and device performances by spectral based analytical methods.

A Gauge R & R (GRR) study design is used to assess sources of variance in an absolute fluorescence quantum yield measurement system involving an integration sphere. The GRR statistics yield the total variance split into three proportions; equipment, day-to-day and manufacturing variances. The manufacturing variance, describing sample fabrication, was found to exhibit the smallest contribution to measurement uncertainty. The greatest source of variance was found to be from fluctuations in the laser intensity whose uncertainty is carried into the quantum yield determination due to not knowing the exact laser intensity at the time of measurement.

The solvation phenomenon is explored as a potential way to improve LSC device yields; this occurs due to excitation induced changes to a fluorophore's dipole moment which leads to a response by the surrounding host medium resulting in shifts in fluorophore emission energy. This effect is shown to improve self-absorption efficiency by reducing the overlap of absorption and emission for particular organic fluorophores. This is expected to greatly improve energy yields but current dopant materials are too costly to employ according to the cost evaluations of this thesis.

A spray coating deposition tool is considered for the deposition of thin film coatings for bi-layer LSC devices. A screening study design of experiment is constructed to ascertain the level of control and assess the tool's ability to meet thin film requirements. Despite poor control over the roughness of the thin film layer this property was found to lie close to the acceptable roughness limit in most samples. The biggest issue remains the film thickness achieved by the deposition, which was an order of magnitude too small according to Beer-Lambert absorption models. This spray-coating tool is thus unsuitable for the requirements of a bi-layer LSC.

Concentration quenching is explored in the context of LSC device efficiency. Different fluorophores are seen to exhibited varied quenching decay strengths by looking at quantum yield versus fluorophore concentration. For two fluorophores, 4-(Dicyanomethylene)-2-methyl-6-(4-dimethylaminostyryl)-4H-pyran (DCM) and 2,3,6,7-Tetrahydro-9-methyl-1*H*,5*H*-quinolizino(9,1-*gh*)coumarin (C102), the quenching process is explored further using quantum yield and lifetime

measurements to extract the quenching rate from rate equations. The form of the quenching rate as a function of molecular separation is shown to be of a monomial power law but distinct from the point-like dipole-dipole coupling of Förster resonant energy transfer (FRET). Additional quenching modes including surface-point and surface-surface interactions are considered to explain the power law form.

Spectral analytical models have been constructed to model performance metrics for square-planar LSC devices. In this model the input solar irradiance is considered to be incident normal to the LSC collection face. Device thickness optimisation is explored to ensure maximisation of the absorption efficiency by the fluorophore using Beer-Lambert absorption modelling. The normalised fluorophore emission spectrum is converted to an equivalent irradiant intensity spectrum based on the amount of energy absorbed. Propagation of this energy through the LSC structure is considered in terms of the mean path length of light rays waveguided by total internal reflection and again Beer-Lambert absorption modelling. Self-absorption and host transport losses are included in some detail. Out-coupling of LSC irradiance at the harvesting edges to connected solar cells is then modelled, using c:Si and GaAs power conversion efficiency spectra, and the resultant power output performance can therefore be estimated. Comparison with real devices from literature show that the model works reasonably well compared to these single device configurations and is somewhat conservative in its estimates. Cost efficiency models based on reasonable assumptions conclude the scope of this work showing that current materials fall short of delivering competitive energy solutions by at least factor of 2 in the case of the best dye modelled here.

Acknowledgements

Firstly I give my thanks to my mother, Jane Taylor, and father, Chris Green, for their encouragement which has spurred me on to this achievement.

My sincere thanks to my supervisor, Alastair Buckley, whose guidance and patience were beyond value, ensuring my output of research papers and the eventual completion of this thesis.

A big thanks for all the help, advice and friendship from all of my colleagues, especially to Darren Watters, Andrew Pearson, David Coles, Edward Bovill, Jonathan Griffin, David Lidzey, James Kingsley, Matt Watson, Lisa Hall, Aldous Everard, Giuseppe Colantuono, Jose Mawyin, Britta Kristensen and Yimin Wang.

Also a big thank you to the department's support and technical staff for their help and invaluable work keeping things running smoothly; particularly to Andrew Brook, Steve Collins, Richard Webb, Paul Kerry, Pete Robinson and Chris Vickers.

Much gratitude goes to the team of workshop technicians in the department of physics and astronomy mechanical workshop for the many tasks performed over the years.

Also thanks to the staff of the departmental office and other admin staff for their work organising transactions, flights, maintenance payments to myself and purchases to university suppliers.

Gratitude to BASF for providing the Lumogen F series of fluorophores to the EPMM group which have been a key material set for this thesis.

Thanks also to Cambridge Display Technologies (CDT) for providing two light emitting polymers, F8 and F8BT, to the EPMM group.

If I have left anyone out of this list please accept my apologies and my sincere thanks for your help.

Contents

Glossary of Constants and Notation by Chapter

Physical Constants:

Speed of Light, $\boldsymbol{c}$ = 2.99792458 x 10^{8} ms^{-1}
Planck's Constant, $\boldsymbol{h}$ = 6.62606957 x 10^{-34} m^2kgs^{-1}
Permittivity of Free Space, $\boldsymbol{\varepsilon_0}$ = 8.85418782 x 10^{-12} Fm^{-1}

Chapter 1:

$\boldsymbol{\eta_{PCE}}$ = Solar cell power conversion efficiency

Chapter 2:

$\boldsymbol{C}$ = Concentration ratio; for GSC use C_{GSC}; for LSC use C_{LSC}
$\boldsymbol{L}$ = Irradiant power [Wm^{-2}]; L_1 for incident light; L_2 for output light
θ = Angle [°]; θ_1 for acceptance angle; θ_1 for output angle;
$\boldsymbol{n}$ = Refractive index
$\boldsymbol{\Omega}$ = Solid acceptance angle [Sr]
$\boldsymbol{C_{dye}}$ = Fluorophore concentration [mol]
$\boldsymbol{\eta_{opt}}$ = LSC optical efficiency
$\boldsymbol{\eta_{fr}}$ = Fresnel efficiency
$\boldsymbol{\eta_{trap}}$ = Trapping efficiency
$\boldsymbol{\eta_{TIR}}$ = Total internal reflection efficiency
$\boldsymbol{\eta_{QY}}$ = Fluorescence quantum yield
$\boldsymbol{\eta_{stokes}}$ = Stokes shift efficiency
$\boldsymbol{\eta_{host}}$ = Host light transport efficiency
$\boldsymbol{\eta_{abs}}$ = Efficiency of absorption of solar energy
$\boldsymbol{\eta_{self}}$ = Self-absorption efficiency
$\boldsymbol{R}$ = Reflected fraction; s-polarised light use R_s; p-polarised light use R_p
$\boldsymbol{T}$ = Transmitted fraction
$\boldsymbol{\lambda}$ = Wavelength of light [m]
$\boldsymbol{\nu}$ = Wavenumber of light [cm^{-1}]
$\boldsymbol{I(\lambda)}$ = Intensity spectrum after absorption [$Wm^{-2}nm^{-1}$]
$\boldsymbol{I_0(\lambda)}$ = Initial incident intensity [$Wm^{-2}nm^{-1}$]
$\boldsymbol{l}$ = Mean absorption path length for incident solar light [m]
$\boldsymbol{\alpha_h(\lambda)}$ = Host matrix absorption coefficient [cm^{-1}]
$\boldsymbol{\langle r \rangle}$ = Mean path length of trapped fluorescent irradiance [m]
$\boldsymbol{\langle \alpha \rangle}$ = Mean absorption coefficient [cm^{-1}]
$\boldsymbol{S_0(\lambda)}$ = Absorbed irradiance spectrum [$Wm^{-2}nm^{-1}$]
$\boldsymbol{S_{sun}(\lambda)}$ = AM1.5 solar irradiance spectrum [Wm^{-2}]
$\boldsymbol{S_1(\lambda)}$ = First order fluorescence irradiance spectrum [$Wm^{-2}nm^{-1}$]
$\boldsymbol{S_N(\lambda)}$ = Normalised fluorophore emission spectrum [$Wm^{-2}nm^{-1}$]
$\boldsymbol{J}$ = Absorption-emission overlap integral
$\boldsymbol{\alpha_d(\lambda)}$ = Fluorophore absorption coefficients [cm^{-1}]
$\boldsymbol{\varepsilon_d(\lambda)}$ = Fluorophore extinction coefficients [$M^{-1}cm^{-1}$]
$\boldsymbol{I_{max}}$ = Maximum intensity of fluorophore emission spectrum
$\boldsymbol{p}$ = Integer for the pth order of emission
θ_c = Critical angle in the z-plane for total internal reflection [°]
$\boldsymbol{\phi}$ = Angle in the x-y plane [°]
$\boldsymbol{L}$ = LSC side length [m]
$\boldsymbol{W}$ = LSC thickness [m]
$\boldsymbol{R}$ = Cylindrical LSC radius [m]
$\boldsymbol{C_{opt}}$ = LSC optical concentration
$\boldsymbol{G}$ = Geometric concentration
$\boldsymbol{A_{col}}$ = Solar energy collection area [m^2]
$\boldsymbol{A_{har}}$ = Solar cell harvesting area [m^2]
$\boldsymbol{\Delta E_{stoke}}$ = Stokes' shift in energy [J]

$\Delta\lambda_{stoke}$ = Stokes' shift in wavelength [m]
$\Delta\nu$ = Stokes' shift in wavenumber [cm^{-1}]
k_{fl} = Fluorescence decay rate [s^{-1}]
k_{NR} = Non-radiative decay rate [s^{-1}]
k_{ISC} = Inter-system crossing rate [s^{-1}]
k_Q = Concentration quenching rate [s^{-1}]
τ = Excited state decay lifetime [s]
τ_{fl} = Fluorescence lifetime [s]
τ_{ic} = Internal conversion lifetime [s]
τ_{abs} = Absorption lifetime [s]
τ_p = Phosphorescence lifetime [s]
μ_G = Ground state dipole moment [D]
μ_G = Excited state dipole moment [D]
$\Delta\mu$ = Change in dipole moment [D]
Δf = Orientational polarisability
ε_r = Relative permittivity
a = Onsager radius [m]
$\Delta\nu_o$ = Unperturbed Stokes' shift in wavenumbers [cm^{-1}]
ΔE_o = Unperturbed Stokes' shift in energy [J]
M_w = Molecular weight
ε_{max} = Maximum extinction coefficient [$M^{-1}cm^{-1}$]
η_{PCE} = Solar cell power conversion efficiency
$\eta_{PCE}(\lambda)$ = Solar cell power conversion efficiency spectrum
$\eta_{EQE}(\lambda)$ = Solar cell external quantum efficiency spectrum
$\eta_{ex}(\lambda)$ = Charge extraction efficiency

Chapter 3:

η_{QY} = Fluorescence quantum yield
$I_{L,0}$ = Excitation intensity [counts]
$I_{L,1}$ = Remaining excitation intensity [counts]
I_S = Sample intensity [counts]
I_{abs} = Absorbed intensity [counts]
$L(\lambda)$ = Laser spectrum [counts nm^{-1}]
$S(\lambda)$ = Sample and remaining laser spectrum [counts nm^{-1}]
$C(\lambda)$ = Measured calibration lamp spectrum [counts nm^{-1}]
$R(\lambda)$ = Radiometric calibration lamp spectrum [$\mu Wcm^{-2}nm^{-1}$]
$\phi_{sense}(\lambda)$ = Instrument sensitivity spectrum
$O_{norm}(\lambda)$ = Normalised sample spectrum outside sphere
$S_{norm}(\lambda)$ = Normalised sample spectrum inside sphere
$\phi_{self}(\lambda)$ = Self-absorption correction
$S'(\lambda)$ = Corrected sample and remaining laser spectrum [counts nm^{-1}]
$L'(\lambda)$ = Corrected laser spectrum [counts nm^{-1}]
C_1 = Geometric capacitance [F]
R_1 = Bulk resistance [Ω]
ε_r = Relative permittivity
A = 4.5 x 10^{-6} m^2, Device area
d = Film thickness
$R(\omega)$ = Frequency dependent resistance [Ω]
$X(\omega)$ = Frequency dependent reactance [Ω]
$B(\omega)$ = Frequency dependent susceptance [Ω^{-1}]
$C_p(\omega)$ = Frequency dependent capacitance for parallel RC circuit [F]
$T_0(\lambda)$ = Blank substrate transmission spectrum
$T_1(\lambda)$ = Substrate and sample transmission spectrum
C_{dye} = Fluorophore concentration [mol]
$S_{abs}(\lambda)$ = Absorption spectrum
$\varepsilon(\lambda)$ = Fluorophore extinction coefficients [$M^{-1}cm^{-1}$]
$\langle x \rangle$ = Mean film thickness [m]
$I(\lambda)$ = Intensity spectrum after absorption [$Wm^{-2}nm^{-1}$]
$I_0(\lambda)$ = Initial incident intensity [$Wm^{-2}nm^{-1}$]
t = time
$I(t)$ = Time-resolved intensity after absorption [counts s^{-1}]
I_0 = Initial intensity [counts]
τ = Excited state decay lifetime [s]

Chapter 4:

η_{QY} = Fluorescence quantum yield
n = 3, Number of repeat measurements per sample
o = 3, Number of days of measurement
p = 5, Number of samples
$k = op$ = 15, Number of sub-groups of size n
$\overline{R}_n$ = Average range over the k subgroups
R = Group range over n
R_{URL} = Upper range limit
D_4 = Statistical anti-biasing constant
$\hat{\sigma}_n^2$ = Repeatability variance
$\hat{\sigma}_o^2$ = Reproducibility variance
R_o = Range of o averages
d_2 = Bias correction factor
$\hat{\sigma}_{GRR}^2 = \hat{\sigma}_n^2 + \hat{\sigma}_o^2$ = Total Gauge R & R variance
$\hat{\sigma}_p^2$ = Manufacturing variance
$\hat{\sigma}_t^2 = \hat{\sigma}_{GRR}^2 + \hat{\sigma}_p^2$ = Total variance
$L(\lambda)$ = Laser spectrum [counts nm^{-1}]
$S(\lambda)$ = Sample and remaining laser spectrum [counts nm^{-1}]
$\phi_{sense}(\lambda)$ = Instrument sensitivity spectrum
$\Delta I_{L,0}$ = Excitation laser uncertainty
ΔI_S = Sample emission uncertainty
$\Delta I_{L,1}$ = Remaining laser uncertainty
$\Delta\eta_{QY}$ = Fluorescence quantum yield uncertainty

Chapter 5:

λ = Wavelength of light [m]
v = Wavenumber of light [cm^{-1}]
C_{opt} = LSC optical concentration
η_{opt} = LSC optical efficiency
η_{fr} = Fresnel efficiency
η_{trap} = Trapping efficiency
η_{TIR} = Total internal reflection efficiency
η_{QY} = Fluorescence quantum yield
η_{stokes} = Stokes shift efficiency
η_{host} = Host light transport efficiency
η_{abs} = Efficiency of absorption of solar energy
η_{self} = Self-absorption efficiency
C_{dye} = Fluorophore concentration [g/l] and [wt%]
C_{host} = Host concentration [g/l]
C_{CAA} = Camphoric acid anhydride concentration [wt%]
Δf = Orientational polarisability
ε_r = Relative permittivity
n = Refractive index
ΔE_R = Energy lost to reaction field [J]
ΔE_{stoke} = Stokes' shift in energy [J]
ΔE_o = Unperturbed Stokes' shift in energy [J]
Δv = Stokes' shift in wavenumber [cm^{-1}]
Δv_o = Unperturbed Stokes' shift in wavenumbers [cm^{-1}]
v_{PL} = Peak emission wavenumber [cm^{-1}]
v_{abs} = Peak absorption wavenumber [cm^{-1}]
μ_G = Ground state dipole moment [D]
μ_G = Excited state dipole moment [D]
$\Delta\mu$ = Change in dipole moment [D]
a = Onsager radius [Å]
J = Absorption-emission overlap integral
G = Geometric concentration
p = Integer for the pth order of emission
m = Gradient of lines on Fig. 5.4.4

Chapter 6:

$\langle R_R \rangle$ = Roughness ratio
σ_R = Standard deviation of $\langle R_R \rangle$
R_h = Height Range [m]
$\langle t \rangle$ = Mean film thickness [m]
I_{abs} = Relative absorption intensity
Δw = De-broadening parameter [m]
w = Full width at half maximum [m]
λ = Wavelength of light [m]
$\Delta\lambda_{PL}$ = Change in Stokes' shift [m]
G = Geometric concentration
n = Refractive index
C_{dye} = Fluorophore concentration [wt%]
C_{tot} = Host + fluorophore concentration [g/l]
P_{in} = Spray head pressure [mbar]
T = Temperature [°C]
h = Spray head to substrate distance [mm]

s = Spray head lateral speed [mms^{-1}]
N_{coat} = Number of coats
η_{fr} = Fresnel efficiency
η_{TIR} = Total internal reflection efficiency
η_{abs} = Efficiency of absorption of solar energy
η_{QY} = Fluorescence quantum yield
$\langle \Delta h \rangle$ = Mean height between peaks [m]
$\langle \Delta x \rangle$ = Mean distance between peaks [m]
$S_{abs}(\lambda)$ = Absorption spectrum
NA = Numerical Aperture
D = Derringer-Suich desirability function
d_i = ith individual response desirability function
D_{max} = Maximum desirability
D_{min} = Minimum desirability

Chapter 7:

η_{QY} = Fluorescence quantum yield
τ = Excited state decay lifetime [s]
r = Mean molecular separation
C_{dye} = Fluorophore concentration [g/l] and [M]
C_{host} = Host concentration [g/l]
M_w = Molecular weight
η_{fr} = Fresnel efficiency
η_{trap} = Trapping efficiency
k_{FRET} = Förster resonant energy transfer rate [s^{-1}]
r_0 = Förster radius [m]
τ_0 = Intrinsic decay lifetime of fluorescence state [s]
k_{ET} = Point-surface interaction energy transfer rate [s^{-1}]
r_0 = Radius for point-surface interaction [m]
ρ = Fluorophore density
k_Q = Concentration quenching rate [s^{-1}]
k_{fl} = Fluorescence decay rate [s^{-1}]
k_{NR} = Non-radiative decay rate [s^{-1}]
a = Onsager radius [Å]

Chapter 8:

n = Refractive index
λ = Wavelength of light [m]
ε_r = Relative permittivity
C_{opt} = LSC optical concentration
η_{opt} = LSC optical efficiency
η_{LSC} = LSC power conversion efficiency
η_{fr} = Fresnel efficiency
η_{trap} = Trapping efficiency
η'_{trap} = Corrected trapping efficiency
η_{TIR} = Total internal reflection efficiency
η_{QY} = Fluorescence quantum yield
η_{stokes} = Stokes shift efficiency
η_{host} = Host light transport efficiency
η_{abs} = Efficiency of absorption of solar energy
η_{self} = Self-absorption efficiency
η_{PCE} = Solar cell power conversion efficiency
$\eta_{PCE}(\lambda)$ = Solar cell power conversion efficiency spectrum
$\eta_{EQE}(\lambda)$ = Solar cell external quantum efficiency spectrum
$\eta_{ex}(\lambda)$ = Charge extraction efficiency
$S_{LSC}(\lambda)$ = LSC output irradiance spectrum [Wm^{-2}]
$S_{sun}(\lambda)$ = AM1.5 solar irradiance spectrum [Wm^{-2}]
$S_N(\lambda)$ = Normalised fluorophore emission spectrum [$Wm^{-2}nm^{-1}$]
$S_0(\lambda)$ = Absorbed irradiance spectrum [$Wm^{-2}nm^{-1}$]
$S_p(\lambda)$ = pth order fluorescence irradiance spectrum [$Wm^{-2}nm^{-1}$]
$S_{ECL}(\lambda)$ = Escape cone irradiance spectrum [Wm^{-2}]
$S_{trap}(\lambda)$ = Trapped irradiance spectrum [Wm^{-2}]
p = Integer for the pth order of emission
P_{in} = Power into LSC device from sun [W]
P_{out} = Power out of LSC device [W]

P_N = Relative output power
G = Geometric concentration
L = LSC side length [m]
W = LSC thickness [m]
$\langle r \rangle$ = Mean path length of trapped fluorescent irradiance [m]
l = Mean absorption path length for incident solar light [m]
$\varepsilon(\lambda)$ = Fluorophore extinction coefficients [$M^{-1}cm^{-1}$]
$T(\lambda)$ = Transmitted irradiance
θ_i = Solar irradiance incidence angle [°]
θ_c = Critical angle in the z-plane for total internal reflection [°]
θ_{ECL} = Average angle in z-plane of escape cone light [°]
$\alpha_d(\lambda)$ = Fluorophore absorption coefficients [cm^{-1}]
C_{dye} = Fluorophore concentration [M]
A_{har} = Harvesting area [m^2]
A_{col} = Collection area [m^2]
V_{LSC} = LSC Volume [m^3]
$(£/W)_{conc}$ = LSC cost per unit power delivered [£ W^{-1}]
$(£_{host}/m^3)$ = Cost of host materials per unit concentrator volume [£ m^{-3}]
$(£_{dye}/mol)$ = Cost of dye materials per unit concentration [£ mol^{-1}]
$(£_{PV}/m^2)$ = Cost of solar cells per unit area [£ m^{-2}]
ρ_{PMMA} = Density of PMMA [kg m^{-3}]
J = Absorption-emission overlap integral

List of Figures

List of Tables

Chapter 1

Introduction

Solar energy offers a renewable resource that is both abundant and available across the entire surface of the world. It has potential for a wide range of applications such as large scale power generation, small scale generation for local deployment and building integrated applications. A number of solar energy technologies are currently available which can be broadly grouped into direct and concentrated solar energy systems. Under direct illumination photovoltaic (PV) solar cell modules already offer competitive energy solutions for large and small scale generation systems but lack option for building integrated applications.

Concentrated solar energy systems come in various guises which can be further grouped into geometric solar concentrators (GSC) and luminescent solar concentrators (LSC), as depicted in Fig. 1.1 b) and c), respectively. GSC systems use mirrors or lenses to concentrate solar energy and are used in large and small scale generation applications but currently come at a less competitive cost due to the requirement of solar tracking (heliostatic) and the low manufacturing tolerance of the optical components. In contrast LSC devices use luminescent materials to absorb sunlight and re-emit it into waveguided modes in an optical structure. Waveguided light is concentrated at the edges of the device. They are not suitable to large scale energy generation but have potential for a low cost and attractive solar energy collector, particularly suited for building integrated applications. This thesis explores various aspects of LSC devices to assess performance and look at possible solutions to current technological challenges.

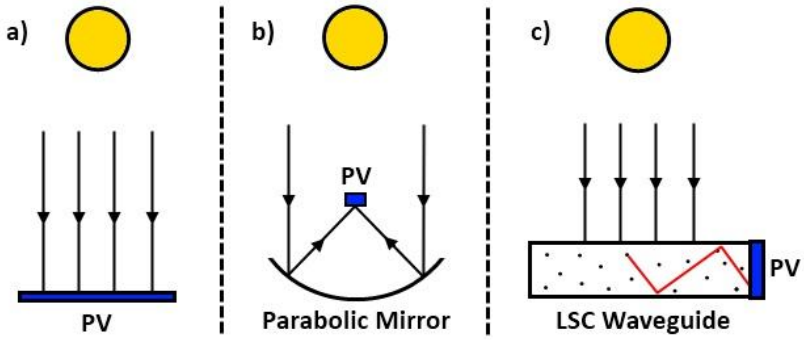

Figure 1.1: Shown here are diagrams illustrating three groups of solar energy systems. In a) a PV module generates power under direct illumination. Shown in b) is a parabolic mirror based GSC system (one of various strategies) with a PV cell/module at the focus; in this case a highly efficient PV would be used. In c) an LSC device is shown illustrating the capture and transport of light to a PV module at the harvesting edges. For an LSC the PV should be spectrally matched to the irradiance of the luminescent material doped into the concentrator.

1.1 World Energy Outlook

According to the International Energy Agency's (IEA) World Energy Outlook 2013 [1], global primary energy demand is expected to increase by around 21% by 2035, reaching 200 trillion kWh yr^{-1}. During this 20 year period fossil fuel production and usage, particularly in natural gas development, is set to rise, though proportionally the share for renewable energy will increase by several percent. The BP Energy Outlook 2035 estimates a 14% global share in renewable energy sources by 2035, up from 5% in 2012 [2]. They also estimate a 41% increase in global energy demand, quite different to IEA predictions.

Currently fossil fuels account for 82% of primary energy use and are heavily subsidised; a total global subsidy of $544 Billion was given in 2012 according to the IEA, which poses a significant obstacle for renewable energy to penetrate the market and gain a larger share. According to a 2012 report from Global Subsidies Initiative (GSI), a group founded by the International Institute for Sustainable Development (IISD), this figure could be as high as $750 Billion but there are large uncertainties due to poor accountancy and/or transparency on these figures [3]. The definition of a fossil fuel subsidy remains vague as much of the funds being spent on the industry do not fall into the category of a normal subsidy, which is generally a state fund to help an industry keep prices low. Large parts of these funds are actually tax exemptions for mining companies, energy producers or consumers, which result in lost national revenue that is equivalent to providing a subsidy. Unfortunately removal of these tax exemptions has some severe knock-on effects with rising petrol prices being a key one as this can lead to economic decline and job losses, often met by bitter protest [4].The GSI report expressed hope for fossil fuel subsidy reform to be a key agenda for the Rio+20 summit of that same year [5] with a target for total global subsidy reform set at 2020. However, despite reaffirmations of commitment to take action on this matter at Rio+20, there is little sign of real progress [4].

With fossil fuel energy share remaining high for decades to come, IEA and Intergovernmental Panel for Climate Change (IPCC) predictions make for gloomy reading with a highly likely increase in global average temperature exceeding the internationally agreed upon maximum of 2°C for dangerous climate change. The IPCC, releasing the Climate Change 2013 report last year [6] and their fifth assessment report this year (March/April 2014), has led calls for a more radical global effort to be made. However, such bold action would require bold leadership, lacking in the political sphere rather than in the scientific one. It would also require bold financing; a Forbes analysis calls for a shift to a 1/3-1/3-1/3 scenario where a third of global energy demand is provided by each of fossil fuels, renewable energy and nuclear. They predict a total cost to achieve this would be around $65 trillion over the next 50 years [7]; the scale of such a global project is unimaginable with current

political leadership. This figure is somewhat higher than the current global public debt burden which is at around $57 trillion and rising.

Many countries are beginning to set ambitious targets on renewable energy, and some already achieve ambitious goals. Denmark approaches the point of generating all of its power by wind alone, as it did at a time of low power consumption in November 2013 [8]. Over December 2013 wind power provided 52% of the country's consumption. However, the situation is more complex because wind capacity is also being imported from Germany, and exported from Denmark to the other Scandinavian countries. Denmark benefits from large wind resources, plus a population of only 5.6 million, and will likely reach 100% renewable energy share by 2050.

Germany has increased its wind and solar capacity considerably but various problems have arisen due to installing renewable capacity without proper planning of grid infrastructure [9]. Grid instabilities due to too much power being delivered at times of low consumption, particularly with large wind farms in East Germany, threaten blackouts and large energy exports to Eastern Europe and Scandinavia have been necessary to control the situation. Since 2013 Germany now produces around 4% of its power from solar energy, making it the largest solar generator in the world at this time, with aims to produce 35% from renewables by 2020 and 100% by 2050 [11]. It faces greater challenge than Denmark in this, however, with a population of 82 million and a much larger fossil fuel share, which is still being subsidised. According to the GSI report Germany spent €7.4 billion on fossil fuel subsidies in 2010 [3].

Spain has spent a lot of capital with aggressive subsidies to introduce renewables widely and has become one of the big producers of wind, hydroelectric and solar energy in Europe. In 2013 20% of the power consumption was delivered from wind power and 3.1% from solar energy marking significant progress in the transition to renewable energy [11]. The result of aggressive subsidisation, high feed-in-tariffs and a complex interplay with lower cost non-renewable sources has left the Spanish power market with a huge financial deficit [12]. This has unfortunately broken confidence in renewable energy in Spain and offers a cautionary tale. However, complexities including the fact that fossil fuels are heavily subsidised should be considered. According to the GSI report Spain spent €2.6 billion on fossil fuel subsidies in 2010 [3].

China has woken up to the consequences of having 90% of its primary energy delivered by coal and has set the target of achieving 15% renewable energy share by 2020 [13], with more to follow in five year plans. In 2012 the renewable share in China was already 9%, largely from hydroelectric and wind power, and plans to install more wind and solar capacity are in motion. By comparison in 2013

the US produced 9% of total power requirements from renewable energy showing a slower uptake in the more mature, fossil fuel dominated energy market of the US [3].

The world's energy mix will continue to change slowly towards renewable energy in a dynamic and sometimes chaotic manner. The success of introduction of renewable energy has been mixed with problems arising from poor planning of infrastructure, intermittent power supply and subsidisation issues. As long as fossil fuel subsidies remain high a true renewable energy revolution to curb dangerous climate change will not be possible.

1.2 The Current State of Photovoltaic Solar Energy

Solar energy currently accounts for less than 1% of the world's primary energy demand and this capacity is mostly comprised of silicon based photovoltaics (PV) with some concentrated solar power plants, particularly in Spain and Australia, and solar thermal installations. Polysilicon feedstock prices have been increasing due to oversupply after the economic crisis in 2008 and, according to GTM Research's Global PV Pricing Outlook 2014, global PV module prices are set to rise by about 9% this year since the PV supply chain stabilised in 2013 [14]. Module prices are forecast to resume the gradual decline of previous years down to around 0.5 $/W for Chinese Tier 1 manufacturers during 2015 and after. As a result competition remains very tight for emerging technologies to penetrate the solar energy market and it seems unlikely that this could happen on a large scale unless a major breakthrough is made. In 2012 China held a 60% share in global PV production whereas the vast majority of demand currently lies in Europe [15].

Photovoltaic technology has come a long way since the first recorded devices of the 1970's with further development of 'classical' photovoltaic technologies and the emergence of many new ones. Classically there are two groups; first are single crystal inorganic semiconductor PV devices, made from Si and GaAs, and second are inorganic thin film PV devices using CdTe, CuInGaSe (CIGS) and amorphous silicon (a:Si). Today many new technologies have emerged including multi-junction inorganic PV, organic semiconductors, multicrystalline silicon (mc:Si), nanomaterials, dye sensitised solar cells (DSSC) and nanocrystals. The best current laboratory and module power conversion efficiencies, η_{PCE}, for a number of PV technologies are given in Table I. η_{PCE} is defined as the ratio of the power out to the power in (see chapter 2.5).

Multi-junction cells have reached efficiencies of up to 44.4% in 2013; this was a triple-junction PV device made by Sharp that utilises concentrator technology to achieve 302 suns [18]. The

thermodynamic limit for a device comprised of an infinite number of junctions under fully concentrated sunlight is 86% [19]. Such devices are technological marvels and have uses in specialised industries, such as for satellites and other space systems requiring high power to weight ratios. For the wider PV market on Earth the issue is one of economics; a low cost per unit power delivered is imperative to make solar energy affordable for the mass market. It is unlikely concentrated photovoltaics (CPV) using multi-junction devices can achieve this requirement, particularly with Chinese c:Si modules looking to reach 0.5 $/W sometime after 2015.

PV Technology	Company	Cell η_{PCE} (%) [16]	Module η_{PCE} (%) [17]
c:Si	UNSW/Gochermann	25.0	22.9
mc:Si	Q-Cells	20.4	18.5
a:Si	LG Electronics	13.4	10.9
CdTe	First Solar	19.6	16.1
CIGS	NREL	20.8	15.7
DSSC	Sharp	11.9	-
Organic	Mitsubishi	11.1	-
GaAs	FhG-ISE	26.4	-
GaAs (Thin Film)	Alta Device	28.8	24.1
2-Junction, III-V	NREL	31.1	-
3-Junction, III-V	Sharp	37.9	-

Table I: For a variety of PV technologies this table shows the NREL best research η_{PCE} [16], with associated companies, and the best module η_{PCE} as of January 2014 [17]. Blank module entries had no relevant information available.

Organic photovoltaic (OPV) technology suffered a major blow in 2012 when Konarka, a major hope for the industry, went into solvency [20]. In the lab OPVs have gone from a few percent power conversion efficiency in 2001 to 11.1% in 2012, curtsey of Mitsubishi who have stated intent to scale up to a roll-to-roll process [21]. The 11.1% device was only of research scale, being a few mm across, and hence scaling losses are certain for larger devices and modules. With power conversion efficiencies still low and device lifetimes of the order of a few years at most, organic PVs have a long way to go to achieve the best possible performances and will likely gain prominence only in niche markets. Development of new materials will continue in the coming years and power conversion efficiencies and device lifetimes will certainly rise.

Some thin film technologies, particularly CdTe, CIGS and a:Si, are beginning to see more widespread usage as large scale power installations (CdTe and CIGS) and transparent PV for power generating windows (a:Si). First Solar Inc. produced the first 1 $/W CdTe module in 2009 but typical panels have power conversion efficiencies of only around 10.6%. Also cadmium is highly toxic and tellurium is a scarce element [22]. Benefits of CdTe include ease of production and increasing module efficiencies to

16% (see Table I). CIGS panels have produced efficiencies of 12 to 16% and costs are expected to fall below 1 $/W by 2014 according to a nanomarkets.net whitepaper [23]. Despite these encouraging developments the PV market has faced some overcapacity and thin film PV market share is expected to suffer as a result. In 2009 thin film PV claimed a 16% share in global PV production but this is expected to drop to around 7% during 2017 [24].

The stage seems set for c:Si and mc:Si technologies to dominate the PV market for decades to come with other technologies taking back seat or niche roles. These niche roles are a motivating focus in this thesis regarding the luminescent solar concentrator technology.

1.3 The Case for Luminescent Solar Concentrators

LSC devices can theoretically achieve the same conversion efficiency as a single junction PVs [25] but suffer from a larger number of loss mechanisms. These losses in the LSC system mean that typical power conversion efficiencies will be lower than standard PV modules under direct solar irradiance. The LSC is therefore unlikely to see a leading role in the global solar energy market.

However, it may be possible to reduce LSC cost significantly enough to make it cost competitive, which is a core research goal for LSC devices. Combined with commonly available materials and ease of processing there is opportunity to develop a useful, low-resource intensity device that could find place in niche markets. Key markets lie in building integrated solar applications where coloured concentrators could create aesthetically pleasing structures whilst generating power for local utility. Many ideas for building integration are in circulation including energy fixtures in bus-stop roofs, paving, awnings, windows and sound barriers [26].

Further non-power generation applications include waveguides for indoor day lighting [27] and thermal energy capture [28, 29]. This latter application utilises one of the most useful properties of the LSC where thermal energy from the sun is separated from the visual wavelengths and dissipated in the bulk of the concentrator. This thermal energy could be utilised with a heat exchange system underneath the concentrator to heat water or indoor spaces.

LSC devices offer some advantage over standard geometric solar concentrators (GSC) using mirrors or lenses. They readily accept diffuse light to large solid angles, as shall be detailed in chapter 2, and as such require no heliostatic tracking systems, which add significant cost. This point is moot for power plant scale solar energy projects since the LSC can hardly replace heliostat arrays. However, the LSC could gain significant share for small scale, terrestrial concentrated solar applications on roof

tops. Additionally LSC devices have been shown to be more efficient at concentrating diffuse light as opposed to direct light by as much as 1.56 times [30]. This is because diffuse spectra are strongly blue shifted and narrower than their direct counterpart and hence absorption becomes more efficient, particularly due to the absence of the long infra-red tail of direct sunlight, which is useless in photovoltaic conversion.

1.4 Thesis Overview

Next, in chapter 2, the relevant theory and background literature on LSC devices are reviewed in some detail. The discussion includes details of host and fluorescent materials (fluorophores), and their properties, geometric considerations, strategies for optimising LSC devices, details of solar cells that might be used in conjunction with LSCs and a brief outline of record LSC devices to date. In chapter 3 the experimental techniques used throughout the thesis are outlined with details of methodology and instrumentation. Chapter 4 is the first experimental chapter detailing results from a Gauge R & R study methodology on absolute measurement of fluorescence quantum yield. The Gauge R & R method exposes sources of variance in the measurement method and sample fabrication to instruct where to focus improvements. Chapter 5 covers an exploration of the solvation phenomenon in the solid state and how this might be used to improve LSC optical efficiency. Chapter 6 exhibits the results of a screening study performed on a spray coating deposition tool. This uses a statistical design of experiment to understand the parameters affecting film quality for spray-deposited LSC thin films. Chapter 7 contains results from a short study on concentration quenching of fluorescence in organic fluorophores, discussing implications for LSC devices. Finally, before the conclusion, chapter 8 details an analytical model using spectral based techniques to explore LSC device performance. In that work LSC losses, optical concentration, power conversion efficiencies and cost efficiencies are estimated for the square-planar geometry with comparison to real devices.

1.5 References

[1] World Energy Outlook 2013, *International Energy Agency* (IEA) (2013), http://www.worldenergyoutlook.org/

[2] Energy Outlook 2035, *British Petroleum Plc.* (BP) (2014), http://www.bp.com/content/dam/bp/pdf/Energy-economics/Energy-Outlook/Energy_Outlook_2035_booklet.pdf

[3] Fossil fuel subsidies and government support in 24 OECD countries, *Global Subsidies Initiative* (GSI) (2012), http://www.iisd.org/gsi/news/report-highlights-fossil-fuel-subsidies-24-oecd-countries

[4] R. Andersen, Business Reporter, *BBC News* (2014), http://www.bbc.co.uk/news/business-27142377

[5] The Future We Want - Outcome Document, Sustainable Development Knowledge Platform, *United Nations* (UN) (2012), http://sustainabledevelopment.un.org/index.php?menu=1298

[6] Climate Change 2013: The Physical Science Basis, *Intergovernmental Panel for Climate Change* (IPCC) (2013), http://www.ipcc.ch/report/ar5/wg1/#.Uvv4_LQa6tM

[7] James Conca, What is Our Energy Future?, *Forbes* (2012), http://www.forbes.com/sites/jamesconca/2012/05/13/what-is-our-energy-future/

[8] Craig Morris, Denmark Surpasses 100 Percent Wind Power, *Energy Transition* (2013), http://energytransition.de/2013/11/denmark-surpasses-100-percent-wind-power/

[9] Richard Fuchs, Wind Energy Surplus Threatens Eastern German Power Grid, *Euro Dialogue* (2011), http://eurodialogue.org/Wind-energy-surplus-threatens-eastern-German-power-grid

[10] Paul Hockenos, Germany's Grid and the Market: 100 Percent Renewable by 2050?, *Renewable Energy World* (2012), http://www.renewableenergyworld.com/rea/blog/post/2012/11/ppriorities-germanys-grid-and-the-market

[11] Peter Moskowitz, Spain becomes first country to rely mostly on wind for energy, *Al Jazeera* (2014), http://america.aljazeera.com/articles/2014/1/16/spain-becomes-firstcountrytorelymostlyonwindforenergy.html

[12] Andrés Cala, Renewable Energy in Spain is Taking a Beating, *New York Times* (2013), http://www.nytimes.com/2013/10/09/business/energy-environment/renewable-energy-in-spain-is-taking-a-beating.html?_r=1&

[13] Josh Bateman, The New Global Leader in Renewable Energy, *Renewable Energy World* (2014), http://www.renewableenergyworld.com/rea/news/article/2014/01/the-new-global-leader-in-renewable-energy

[14] Global PV Pricing Outlook 2014, *Green Tech Media Research* (2013), http://www.greentechmedia.com/research/report/pv-pricing-outlook-2014

[15] Finlay Colville and Steven Han, Solar PV Supply and Demand within Emerging Asian Countries, *Solar Media Ltd.* (2013), http://www.solarbusinessfocus.com/articles/solar-pv-supply-and-demand-within-emerging-asian-countries

[16] Best Research PCE Values, *NREL* (2013), http://www.nrel.gov/ncpv/

[17] M. A. Green, K. Emery, Y. Hishikawa, W. Warta and E. D. Dunlop, Solar Cell Efficiency Tables (version 43), *Prog. Photovolt: Res. Appl.* **22**, 1, 1 - 9 (2014)

[18] Eric Wesoff, Sharp Hits Record 44.4% Efficiency for Triple-Junction Solar Cell, *Green Tech Media* (2013), http://www.greentechmedia.com/articles/read/Sharp-Hits-Record-44.4-Efficiency-For-Triple-Junction-Solar-Cell

[19] J. Nelson, The Physics of Solar Cells, (*Imperial College Press*, London, 2003), Chap. 10, pp. 289 - 301

[20] Ucilia Wang, Organic solar thin film maker Konarka files for bankruptcy, *GIGAOM, Wordpress* (2012), http://gigaom.com/2012/06/01/solar-thin-film-maker-konarka-files-for-bankruptcy/

[21] Tetsuo Nozawa (Nikkei Electronics), Mitsibishi Chemical Claims Efficiency Record for Organic Thin-film PV Cell, *TechOn!* (2012), http://techon.nikkeibp.co.jp/english/NEWS_EN/20120601/221131/

[22] Solar Facts and Advice, *Alchemie Limited Inc.*(2010-2013) http://www.solar-facts-and-advice.com/cadmium-telluride.html

[23] Glen Allen, Renewed Interest in CIGS Creating Real Opportunities in Photovoltaics, *Nanomarkets.net* (2011), http://nanomarkets.net/Downloads/CIGSPaper.pdf

[24] Mark Osborne, NPD Solarbuzz: CIGS suffering in a PV thin-film market decline, *PV Tech* (2013), http://www.pv-tech.org/news/npd_solarbuzz_cigs_suffering_in_a_pv_thin_film_market_in_decline

[25] Tom Markvart, Detailed Balance Method for Ideal Single-Stage Fluorescent Collectors, *J. App. Phys.* **99**, (2006)

[26] Michael G. Debije and Paul P. C. Verbunt, Thirty Years of Luminescent Solar Concentrator Research: Solar Energy for the Built Environment, *Adv. Energy Mater.* **2**, 12 – 35 (2012)

[27] A. A. Earp, G. B. Smith, P. D. Swift and J. Franklin, Maximising the Light Output of a Luminescent Solar Concentrator, *Solar Energy* **76**, 655 667 (2004)

[28] A. Goetzberger and W. Greubel, Solar Energy Conversion with Fluorescent Collectors, *Appl. Phys.* **14**, 123 -139 (1977)

[29] A. Goetzberger, Thermal Energy Conversion with Fluorescent Collector-Concentrators, *Solar Energy* **22**, 5, 435 - 438 (1979)

[30] A. Goetzberger, Fluorescent Solar Energy Collectors: Operating Conditions with Diffuse Light, *Appl. Phys.* **16**, 399 - 404 (1978)

Chapter 2

Theory, Background and Materials

In this chapter luminescent solar concentrator theory and background literature pertinent to the topics of this thesis are discussed. In 2.1 a comparison between luminescent solar concentrators (LSC) and geometric solar concentrators (GSC) is drawn to gain appreciation of the differences in methods of solar energy concentration. In 2.2 LSC devices are then considered in greater detail looking at the optical properties of these structures and developing equations to describe the interaction and waveguiding of light within the LSC. Various LSC structures and configurations are considered in 2.3 with discussion of geometry and methods to reduce loss modes. Section 2.4 begins with relevant theory for organic fluorophores, specifically considering transition rate equations and the solvation mechanism. The rest of 2.4 details organic small molecular fluorophores, light-emitting polymers (LEP) and host materials. The last two sections, 2.5 and 2.6, detail solar cells and the best of LSC devices, respectively.

2.1 Geometric versus Luminescent Solar Energy Concentration

GSC and LSC devices function with different operational principles in the manner they concentrate solar radiation. By definition the concentration ratio, *C*, is given by the ratio of irradiant power (W/m^2) leaving the exit aperture, L_2, to that of the solar power incident on the entrance aperture, L_1, as given by Eq. (2.1.1);

$$C \equiv \frac{L_2}{L_1} \qquad (2.1.1)$$

Note in this thesis the conversion is expressed in terms of energy rather than flux, which is the more typical way of quantifying concentration. This is because integration of a spectrum by energy results in a weighting towards the blue end of said spectrum, yet an LSC does not operate with this bias since the process of energy generation with an LSC is quantum. Therefore flux is the better choice and this was not considered in writing this thesis. This oversight results in the need to consider energy loss in down-conversion, quantified by η_{stokes} introduced in this chapter on page 19, which is not necessary with a flux oriented model.

Eq. (2.1.1) is true for GSC and LSC devices, however the irradiant intensity leaving the exit aperture of these systems differs greatly in its form. GSC devices use mirrors or lenses to achieve concentration and hence the spectrum at the exit aperture will be the same as the solar irradiance spectrum since little or no wavelength dependence in light throughput is present. Lens systems may result in some splitting of wavelength paths within the concentrator and the lens media may absorb some thermal wavelengths, but the rest will all be collected at the exit aperture. A consequence of this is that infrared wavelengths are also directed upon the target absorber, be it a thermal conducting material or a PV. From this point of view GSC devices offer excellent means for solar thermal installations for electrical generation (such as solar power towers) or heating homes and water. The flip side of this is that PV devices under GSC concentration will suffer from excess heating, which is known to reduce efficiency, and therefore will require cooling systems at extra expense.

GSCs come in various forms including parabolic mirrors, flat mirrors, mirror arrays and lens systems. These systems have quite different properties in terms of acceptance angles at the entrance aperture, and in concentration ratios. Mirror based systems absolutely must employ heliostatic tracking to be useful; if the mirror's angle is wrong the light will miss the target and hence acceptance angle is very small. Concentration ratios of mirrors are given by the ratio of mirror area to the area of focus, a much simpler determination than that for lens based GSCs or LSC devices.

For lenses wider angles of acceptance are possible and this depends on the shape of the system and the entrance and exit aperture areas. A treatment for lens systems is reproduced here [1]. For an exit angle of θ_2 = 90° the concentration ratio is given by the sine brightness equation for ideal flux transfer through the system, as in Eq. (2.1.2);

$$C_{GSC} \leq \frac{sin^2\theta_2}{sin^2\theta_1} = \frac{1}{sin^2\theta_1} \quad (2.1.2)$$

Where C_{GSC} is the concentration ratio for GSCs, θ_1 is the entrance or acceptance angle and θ_2 is the exit angle. For concentrators in which the exit aperture is in a medium other than air, such as with immersed lens based systems, this equation is modified using Snell's law such that $\sin\theta_1 = n \sin\theta_1'$ and so becomes;

$$C_{GSC} \leq \frac{sin^2\theta_2}{sin^2\theta_1'} = \frac{n^2 sin^2\theta_2}{sin^2\theta_1} \quad (2.1.3)$$

Most imaging GSC devices display a C_{GSC} value of a factor of 4 lower than what is possible according to Eq. (2.1.3). This is due to θ_2<90° and the fact that maintaining the sun's image impacts on the

ability of the device to concentrate light [2]. With non-imaging concentrators, such as the compound parabolic concentrator, it is possible to approach the limit in Eq. (2.1.3) by overcoming the aforementioned issues.

For minimal seasonal adjustment, with no tracking, a GSC device can be designed to operate with a 2π Sr acceptance angle (thus accepting diffuse light) at what is known as the n^2 limit of concentration giving C_{GSC} = 2.25 for n = 1.5. By reducing the acceptance angle, to the limit of the sun's angular size, this C_{GSC} value can be dramatically increased to many thousands of suns, but cannot concentrate the diffuse component and needs solar tracking. In contrast an LSC device can best the n^2 limit for GSC devices quite comfortably but may never hope to achieve the highest concentration possible with a GSC. This means that by comparison an LSC is particularly suited for diffuse collection conditions, a fact that is elaborated upon through section 2.2 in discussion of LSC loss mechanisms.

Considering the concentration ratio for lens based GSC devices, using Eq. (2.1.3), with the assumption of θ_2 = 90° and n = 1.5, the curve shown in Fig. 2.1.1 is plotted.

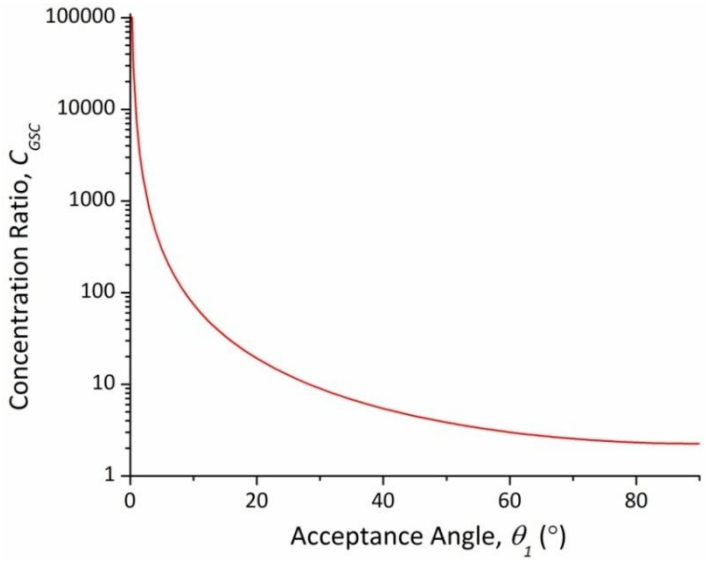

Figure 2.1.1: Concentration ratio for a GSC as a function of acceptance angle.

We see that C_{GSC} only sharply increases below $\theta_1 \approx 20°$, which is the regime where solar tracking will be required. This can be seen from the relation between solid acceptance angle, Ω, and acceptance angle, θ_1, given by $\Omega = 2\pi(1 - \cos\theta_1)$ Sr. A GSC for diffuse collection would need to have a solid acceptance angle near Ω = 2π Sr but for θ_1 = 20° we have Ω = 0.121π Sr. The highest point in Fig. 2.1.1, at the suns angular size of θ_1 = 0.27°, is the maximum possible concentration that could be achieved with a GSC with the given inputs. At $C_{GSC} \approx 100000$, typical practical applications for this would be solar pumped lasers, destruction of hazardous wastes or powerful collimators.

LSC devices involve the coupling of solar irradiance to luminescent irradiance in a steady state photophysical interaction. The irradiance at the output aperture is thus heavily dependent on the spectral sensitivity of the fluorophore used, in absorption and emission. Geometry still plays an important role in LSC devices with regards to the transmission of solar light into the device and the coupling of the fluorophore irradiance to the LSC exit aperture, and hence the attached PV cells. It is the transmission of solar light into the device that defines the ability of an LSC to collect diffuse irradiance and this is governed by reflection at the interface (see Fig. 2.2.3). Determination of LSC concentration ratio, C_{LSC}, is more involved than for the treatment for GSCs here and is dealt with through section 2.2, 2.3 and explored via the spectral analytical models of chapter 8.

LSC devices require no solar tracking because of the large acceptance angle, such tracking would add excess expense for small gains and is therefore not a worthwhile investment. An additional benefit of LSC devices over GSCs is that of thermal energy capture, which is exclusive to the concentrator structure, where it is dissipated, whilst luminescent emission is delivered separately to the PV. This means the PV does not suffer overheating problems, as it might under GSC concentration, and the thermal energy could be extracted by coupling the LSC structure to a heat exchanger.

2.2 Loss Mechanisms in Luminescent Solar Concentrators

To understand how light moves into and propagates through the LSC structure an exploration of the typical geometry and optical properties is necessary. In Fig 2.2.1 a LSC in simplest form is shown; it is a planar rectangle made from some optical quality host material, with refractive index n, and doped with small molecular fluorophores, at some concentration C_{dye}. Fig 2.2.1 shows various processes that have influence over an LSC device's optical efficiency, η_{opt}, which is the fraction of incident light concentrated at the exit aperture.

As shown in Fig. 2.2.1, incident solar radiation (1) impinges on the collecting face of the device and due to Fresnel reflection a small part of that is reflected; about 4% at normal incidence (2). This of course depends on angle of incidence and refractive index, as explored shortly. The remaining 96% enters the device and the fluorescent dopants absorb this (3) and then re-emit it isotropically. Because of Snell's laws of refraction a part of this subsequent emission is able to leave the device without waveguiding (4), so called escape cone loss (ECL), but a larger part, around 75% as detailed later, remains trapped due to total internal reflection (TIR). A large portion of the fluorescent emission is then waveguided directly to the harvesting edge (5), where out-coupling is achieved, but another portion becomes subject to self-absorption of fluorescence, due to the overlap in

absorption and emission spectra of the fluorescent species (6). Finally, because of the imperfect absorption of the solar spectrum, there is a large portion of incident radiation which is transmitted directly through the device without absorption (7).

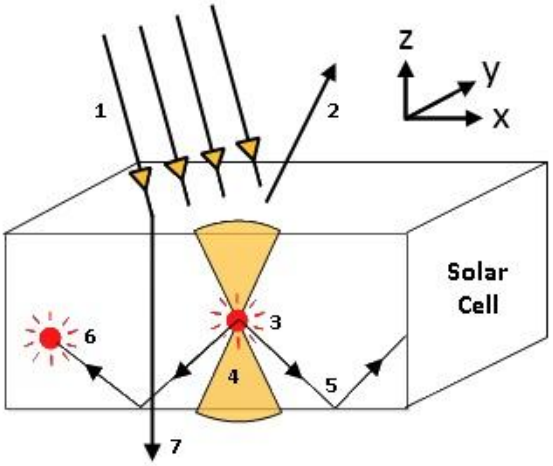

Figure 2.2.1: Here is a schematic diagram of a basic square planar LSC device showing various mechanisms which influence the resultant optical efficiency, η_{opt}. (1) incident light is either reflected (2) or enters the device and is then either absorbed (3) or transmitted out the other side (7). Part of the trapped light is lost to the escape cones (4) whilst the rest is waveguided through the structure until it either reaches the solar cell at the harvesting edges or is self-absorbed (6) by members of the same luminescent species.

Other modes of loss not indicated in Fig 2.2.1 include transport related loss due to matrix scattering, total internal reflection efficiency and a loss due to the quantum yield of the fluorophore. The overall optical efficiency, η_{opt}, is given by the product of all the different loss modes quantified as efficiencies, as in Eq. (2.2.1). Note that η_{opt} is defined here as a power efficiency, which is the convention from older literature [3].

$$\eta_{opt} = \eta_{fr}\eta_{trap}\eta_{TIR}\eta_{QY}\eta_{stokes}\eta_{host}\eta_{abs}\eta_{self} \quad (2.2.1)$$

Where η_{fr} is the Fresnel efficiency due to reflection loss, η_{trap} is the trapping efficiency due to angular onset of TIR, η_{TIR} is the efficiency due to imperfections in the TIR interface, η_{QY} is the quantum yield of the fluorophore, η_{stokes} is the efficiency due to down-conversion of absorbed energy, η_{host} is the efficiency of light transport through the host matrix, η_{abs} is the efficiency of absorption of incident radiation and η_{self} is the efficiency due to self absorption. Each of these shall now be looked at analytically to understand the parameter space they describe.

Fresnel efficiency for LSC devices, η_{fr}, is governed by the Fresnel equations for unpolarised light, where the radiation is made up of equal mixture of *p* (parallel to surface) and *s* (perpendicular to surface) polarisations. The reflection co-efficients, R_S and R_p, for these two polarisations differ and are given by Eqs. (2.2.2) and (2.2.3).

$$R_s = \left| \frac{n_1 \cos\theta_i - n_2 \sqrt{1 - \left(\frac{n_1}{n_2}\sin\theta_i\right)^2}}{n_1 \cos\theta_i + n_2 \sqrt{1 - \left(\frac{n_1}{n_2}\sin\theta_i\right)^2}} \right|^2 \qquad (2.2.2)$$

$$R_p = \left| \frac{n_1 \sqrt{1 - \left(\frac{n_1}{n_2}\sin\theta_i\right)^2} - n_2 \cos\theta_i}{n_1 \sqrt{1 - \left(\frac{n_1}{n_2}\sin\theta_i\right)^2} + n_2 \cos\theta_i} \right|^2 \qquad (2.2.3)$$

Then the unpolarised reflection coefficient is given by $R = (R_s + R_p)/2$ and so the transmitted component, T, is $T = 1 - R$. With this knowledge models can be constructed to look at how different conditions might affect the portion of light that enters the device. Shown in Fig 2.2.2 are models of fractional transmission as a function of the ratio of external to internal refractive indices for different incidence angles.

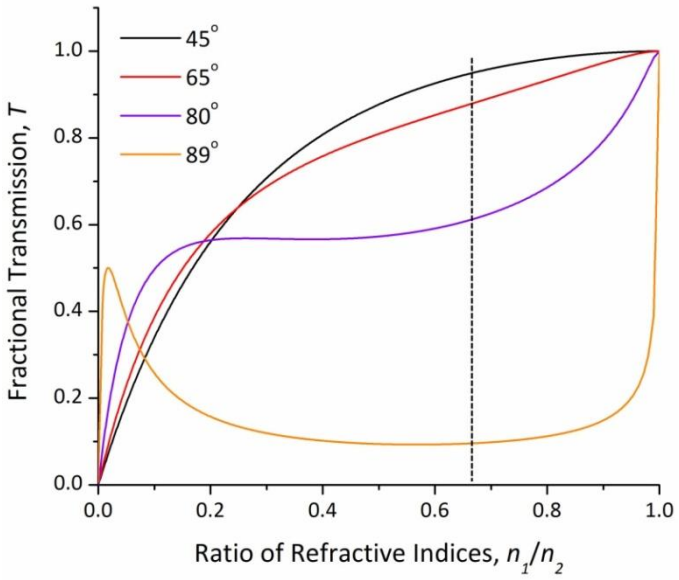

Figure 2.2.2: Fractional transmission against ratio of refractive indices for different angles of incidence. Very little difference is seen between 0° (normal) and 45°, hence the omission of 0° data. The dash line indicates where n_1/n_2 = 0.667, applying to air interfaced with a host of n_2 =1.5.

By using the ratio, n_1/n_2, we construct a generalised parameter space to consider. In a bulk doped LSC device, which consists of a slab of host material doped with fluorophores throughout, the only interface for solar radiation is between the host and air. Thus the range of ratios, n_1/n_2, that can be achieved are defined by the host material's refractive index, n_2. Typical materials have refractive indices in the range $1.3 < n_2 < 1.7$, so there is only a small region of the parameter space that is physically accessible. It is also important to realise that changing refractive index has an impact on other processes such as trapping efficiency and reflection. For bi-layer structures two host materials may be present and additional internal interface reflections may need considering. For out-coupling

of waveguided fluorescence the reflections at the coupling interface, mediated by some coupling material (e.g. silicone grease) to a solar cell, will also need to be considered. Fig 2.2.2 also shows us that the reflected component does not significantly increase at $n_1/n_2 = 0.667$ until the incidence angle is above around 45°. This is best seen by plotting T against θ_i as shown in Fig 2.2.3.

As Fig. 2.2.3 shows when we increase the host material's refractive index there is a small decrease in transmission for normal incidence. For a typical host material good transmission acceptance is expected to around $\theta_i = 65°$, which corresponds to a solid acceptance angle of $\Omega = 1.155\pi$ Sr. Remember a GSC can achieve $\Omega = 2\pi$ Sr for concentration ratios of $C = 2.25$ and $n_2 = 1.5$. This was the n^2 limit of concentration. However, if LSC devices can be shown to achieve much higher C values then the drop in transmission for higher incidence angles may be negated. To argue that LSC devices are better suited to capture diffuse radiation this must be explored along with economic considerations and it is therefore an aim of this thesis to do so (see chapter 8).

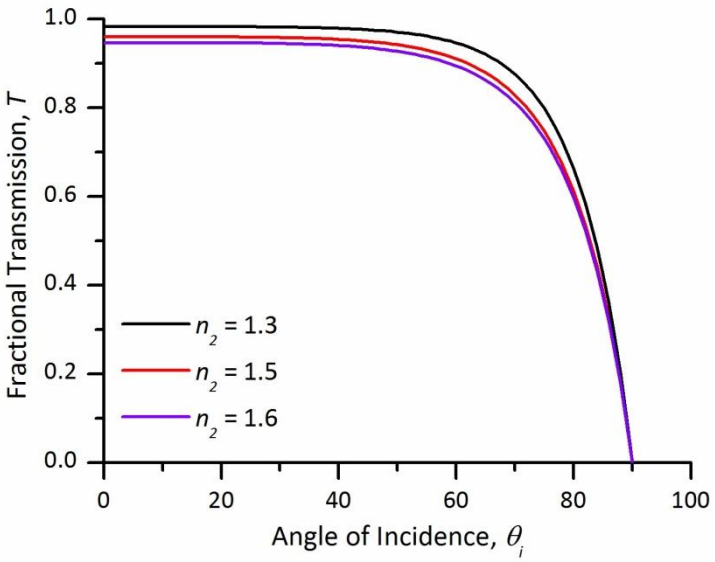

Figure 2.2.3: Fractional transmission against the angle of incidence for air interfaced to various host indices, n_2.

After the radiation has entered the device it either gets absorbed by the fluorophores or transmits straight through. Of the portion that is absorbed some is lost due to the fluorophore's quantum yield but the rest is emitted. This emitted fraction now impinges on the internal interface with air and depending on this angle of incidence of emission, θ_{em}, either undergoes TIR or refracts through the interface and is lost via the ECL. This condition is derived via Snell's law and thus quantified by the trapping efficiency, η_{trap}, given by Eq. (2.2.4) [4].

$$\eta_{trap} = \sqrt{\left(1 - \frac{1}{n_2^2}\right)} \qquad (2.2.4)$$

The derivation for Eq. (2.2.4) assumes isotropic emission, which has been shown to be incorrect due to the distribution of absorption cross-sections for randomly orientated fluorophores [5]. This means that light of a given incidence angle will be preferentially absorbed by fluorophores of a particular orientation, and therefore emission will be skewed in the direction of these fluorophore populations. This effect is not taken into account in this thesis.

From Eq. (2.2.4) it can be seen that as n_2 increases, the trapping efficiency increases, which is converse to the response of η_{fr} with respect to n_2. A plot of η_{fr} and η_{trap} and their combined effect, $\eta_{fr}\eta_{trap}$, against host refractive index gives insight into these loss mechanisms, as shown in Fig 2.2.4.

Angle of incidence affects not just the resultant efficiency after these two processes but also the position of the maximum fractional efficiency achievable. For normal incidence the peak sits exactly at $n_2 = 2$ (purple curve), whereas for 80° incidence the peak is out of the range mapped here (green curve). Again typical materials have refractive indices in the range $1.3 < n_2 < 1.7$, and Fig 2.2.4 indicates that it would be best to work in the upper part of that range. This range of indices equates to a range in combined efficiency at normal incidence of $62.8\% < \eta_{fr}\eta_{trap} < 73.9\%$. Ideally, according to this basic theoretical exploration, a host of $n_2 = 2$ would be selected to maximise the amount of light trapped into waveguide modes at $\eta_{fr}\eta_{trap} = 77.0\%$ for normal incidence.

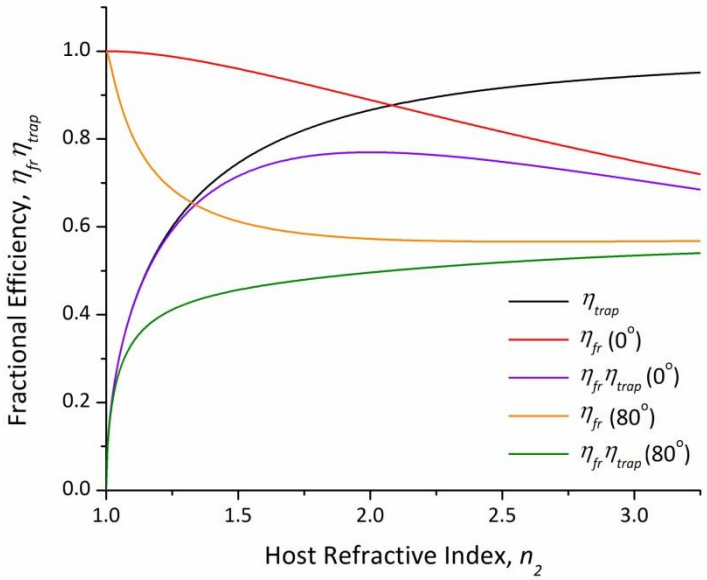

Figure 2.2.4: Efficiency curves for transmission into the device (Red/Yellow curves), trapping of fluorescent radiation (Black curve) and the product of the two (Purple/Green curves). Two incidence angles are compared for Fresnel efficiency, 0° and 80°.

Next to discuss is the TIR efficiency, η_{TIR}, which has been mentioned in literature and is quite difficult to quantify [6]. It is expected to be near unity and higher than that of specular (Al or Ag) and diffuse reflectors (PTFE), making it one of the least problematic of LSC loss modes. Qualitatively TIR losses occur due to imperfections in the internal reflection interface, which include roughness or scattering

due to grain formation or dirt collecting on the outer surface. Other factors include the employment of mirrors; an air gap should always be used as thermally evaporated mirrors will reduce TIR efficiency, because the mirror has a lower reflection efficiency than the host/air interface, and will also lead to further roughening of said interface [7]. Clearly the fabrication process is critical for maximising the TIR efficiency and polishing of the collection face could help reduce this loss mode. The concentrator surface will suffer from the build up of dirt highlighting the need to clean and polish the collection face over time.

The fluorescence quantum yield, η_{QY}, is a key factor which describes the emission efficiency of the fluorophores employed. This encompasses all of the electronic process that affect emission including all radiative and non-radiative recombination pathways. This will be discussed further in section 2.4, but bear in mind here that it has a strong influence over the amount of light being put into waveguided modes. Because of this it also has a strong relationship with the self-absorption loss mode and subsequent orders of emission.

Arguably the Stokes' efficiency, η_{stokes}, doesn't represent a real loss because the loss of energy in down-conversion at the fluorophore is similar to that occurring at the band-gap of a solar cell under direct illumination. Considering that exciton generation is quantum, and so a single photon gives rise to a single exciton, it does not make sense to think of this as a loss. η_{stokes} was quantified in 1981 to have a foreseeable maximum of $\eta_{stokes} = 0.75$ [3], which is the value used throughout this thesis. Ultimately it comes down to the choice between energy (wavelength) or flux in the quantification of irradiance, as discussed at the start of section 2.1, and since this thesis uses energy the value $\eta_{stokes} = 0.75$ must be used. Many researchers include this as a loss mode [3,6,8] because of the choice of energy over flux in their models. However, work in the literature has shown that with the correct choice of solar cell, coupling favourably to the fluorescence radiation field, up to a 20% relative increase in power conversion can be expected [9]. This highlights again that using flux to quantify irradiance is the better choice.

In terms of light transport the host material itself will absorb some energy across the visible spectrum and convert this to heat. Additionally imperfections in the host matrix can cause scattering of light, quantified through the host efficiency, η_{host}, which can be estimated by measuring the optical absorption of undoped sample plates. The number of defects present in the host matrix can be affected by the formation process and the presence of dopants [10] and there is evidence that matrix losses may comprise a major loss mode. This has been shown experimentally by measurement of flux output in the presence and absence of a reflector at the opposite LSC edge to that measured [11]. One would expect a factor of 2 increase in output in this case, which was not

seen. η_{host} has been estimated to have a value between 0.95-0.98 for a PMMA host transporting light in the visible region [12]. Furthermore the properties of the matrix have a significant bearing on the dopant fluorophore in terms of the emission wavelength, quantum yield and lifetime stability (see chapter 7). Given these factors not only is the choice of host material critical, but also how the LSC device is manufactured. This thesis cannot cover the materials science of polymerisation processes in different fabrication and deposition methods, but it is worth taking into account that this engineering is necessary for a high quality LSC. The best polymers to date are made from the materials used for efficient optical fibres such as poly(methyl methacrylate) (PMMA), which has an optical absorption of 3.5×10^{-4} cm^{-1} and n = 1.494 at λ = 550nm [13]. Ideally a host of higher index and similar optical absorption would be chosen. Additional absorption may be present from defects.

To quantify η_{host}, the absorption coefficient, $\alpha_h(\lambda)$, of the host medium must be measured and then the mean path length of waveguide modes determined. $\alpha_h(\lambda)$ is determined through Beer-Lambert law;

$$I(\lambda) = I_0(\lambda)e^{-\alpha_h(\lambda)l} \quad (2.2.5)$$

Where $I(\lambda)$ is the intensity after passing through an absorption path length, l, of a medium of absorption coefficient, $\alpha_h(\lambda)$, with initial incident intensity, $I_0(\lambda)$. For the host matrix the attenuation coefficient $\alpha_h(\lambda)$, with units cm^{-1}, is sufficient but for absorption by fluorophores at some concentration, C_{dye} [M], then we use $\alpha_d(\lambda) = \varepsilon_d(\lambda)C_{dye}$ where $\varepsilon_d(\lambda)$ is the molar absorptivity, or extinction coefficient, with units $M^{-1}cm^{-1}$. Experimentally it is quite challenging to measure $\alpha_h(\lambda)$ for materials like PMMA because it is so low one needs a large thickness to make measurements. This means fabricated plates of material are required instead of thin films made easily in the lab. From Eq. (2.2.5) we can quantify the matrix losses as the ratio of final and initial intensities over the mean path length of waveguide modes traversing a host medium of averaged absorption coefficient $<\alpha>$;

$$\eta_{host} = \frac{I}{I_0} = e^{-<\alpha><r>} \quad (2.2.6)$$

This is an approximation and may be a best estimate since $\alpha_h(\lambda)$ is measured in the absence of dopants. In literature matrix related losses have received some attention; in 1981 the combined effect of η_{TIR} and η_{host} was quantified experimentally as 0.9, with 0.95 expected in the future [11]. As stated above with η_{TIR} expected to be near unity and with $0.95 < \eta_{host} < 0.98$ this is likely to be higher in an optimised device. This will depend on the geometry of the LSC device, and hence path length of light through it, which is an area that requires some thought with a view to optimisation.

Much more can be done using the Beer-Lambert law of Eq. (2.2.5). The absorption efficiency, η_{abs}, is determined by the ratio of the integral of collected irradiance spectrum, $S_0(\lambda)$, to that of the solar irradiance spectrum, $S_{sun}(\lambda)$. By determining $\varepsilon_d(\lambda)$ for a given fluorophore, the absorption of solar energy as a function of depth and dye concentration can be explored. Going further, a multi-dye plate or stack of plates may be considered and it is therefore possible to think about what values for η_{abs} are possible from different LSC device configurations. Additionally if a Förster Resonant Energy Transfer (FRET - see Section 2.4) system of multiple fluorophores were to be employed then Eq. (2.2.5) could be used to model how that system collects incident sunlight. Then, by knowing the quantum efficiencies, FRET efficiencies and the normalised emission spectra, the fluorescence output, $S_1(\lambda)$, of the terminal dye can easily be predicted.

For the simple case of a single fluorophore device of quantum yield η_{QY}, $\varepsilon_d(\lambda)$ is measured experimentally and then $S_0(\lambda)$ is determined via Eq. (2.2.5) with $I_0(\lambda) = S_{sun}(\lambda)$, l as the path length through the LSC and $\alpha_d(\lambda) = \varepsilon_d(\lambda)C_{dye}$ for the fluorophore. Now the first order fluorescence output, $S_1(\lambda)$, is given by equating the quantum yield corrected total absorbed energy to the total emitted energy as in Eq. (2.2.7);

$$\eta_{QY} \int S_0(\lambda) d\lambda = \int S_1(\lambda) d\lambda \qquad (2.2.7)$$

$S_1(\lambda)$ is the goal, which is related to the normalised emission spectrum, $S_N(\lambda)$, from fluorescence spectroscopy on the fluorophore at the required dye concentration, C_{dye}, via some maximum intensity, I_{max}, which we do not know;

$$S_1(\lambda) = I_{max} S_N(\lambda) \qquad (2.2.8)$$

Note that $S_N(\lambda)$ is the fundamental emission spectrum prior to any effect which changes the line-shape, such as self-absorption. Substituting Eq. (2.2.8) into Eq. (2.2.7) allows us to determine I_{max};

$$I_{max} = \frac{\eta_{QY} \int S_0(\lambda) d\lambda}{\int S_N(\lambda) d\lambda} \qquad (2.2.9)$$

This is the scaling factor with which to scale $S_N(\lambda)$ by to achieve a quantum yield corrected equivalent intensity fluorescence output using Eq. (2.2.8). One must also consider the escape cone loss for the true, captured output and so the waveguided irradiance spectrum is given by Eq. (2.2.10);

$$S_1(\lambda) = \frac{\eta_{QY} \eta_{trap} S_N(\lambda) \int S_0(\lambda) d\lambda}{\int S_N(\lambda) d\lambda} \qquad (2.2.10)$$

By knowing the intensity of the fluorescence it is possible to then go on and inform the coupling with the solar cell external quantum efficiency spectrum, $\eta_{EQE}(\lambda,\theta)$, at the harvesting face. $\eta_{EQE}(\lambda,\theta)$ is the ratio of electron hole pairs collected at the interface to the number of incident photons and is a function of both wavelength and incidence angle. Since the angle is typically considered to be normal this is often expressed as just $\eta_{EQE}(\lambda)$.

Eq. (2.2.5) can also be used to describe the change in the fluorescence intensity, as a function of wavelength, with distance through the LSC medium due to the self-absorption process, η_{self}. η_{self} is another parameter that is difficult to measure absolutely and is a function of fluorophore concentration, C_{dye}, and mean fluorescence path length, $\langle r \rangle$. It may have a more complex spatial dependence due to local variations in dye concentration or for bi-layer device structures. Many fluorescent materials exhibit an overlap in their absorption and emission spectra, which means emission in that overlap region may be reabsorbed by other same species dye molecules. This reabsorbed light has a chance of being re-emitted, η_{QY}, and after emission there is a chance of TIR into waveguide modes related to η_{trap}. We also need to consider that this new generation of emission will be subject to matrix and TIR efficiency losses, η_{host} and η_{TIR}. Of course there could be a third generation reabsorption and emission and so on, with each subsequent generation being lower in population than the previous one.

The actual strength of the self-absorption is wavelength dependant but can be estimated in simplest form by the overlap integral, J, as a fraction of the integral of the emission spectrum of a given order, i.e. $\eta_{self} = (1-J)$. Now Eq. (2.2.1) can be expanded to encompass all generations. Note that for higher generations of emission the self-absorption strength, J, is an extra factor;

$$\eta_{opt} = \eta_{fr}\eta_{stokes}\eta_{abs}(1-J)\eta_{trap}^{p}\eta_{TIR}^{p}\eta_{QY}^{p}\eta_{host}^{p}J^{p-1} \quad for\ p = 1,2,3,\ldots \quad (2.2.11)$$

Summation over all generations gives the final optical efficiency;

$$\eta_{opt} = \eta_{fr}\eta_{stokes}\eta_{abs}(1-J)\sum_{p}\eta_{trap}^{p}\eta_{TIR}^{p}\eta_{QY}^{p}\eta_{host}^{p}J^{p-1} \quad for\ p = 1,2,3,\ldots \quad (2.2.12)$$

In practice it can be seen that generations of fluorescence above $p = 3$ have a negligible contribution to the optical efficiency. Contributions for $p = 3$ are typically less than 0.2% of the total and for $p > 3$ this becomes less than 0.01% with exact values depending on the particular fluorophore (i.e. the size of J). However, because this equation does not take into account the mean path length of light in the waveguide it is not valid for particular LSC geometries. Since the overlap integral is a first guess estimator for η_{self} this equation is used only to compare optical efficiencies in a relative manner, as in Chapter 5.

In a more realistic approach it is necessary to use Eq. (2.2.5) in conjunction with the mean path length of fluorescent light, which in turn must be calculated from the geometry analytically or using modelling methods, such as ray tracing or Monte Carlo simulations. Then η_{self} can be determined by one minus the ratio of the self-absorbed intensity to the fluorescence output intensity from Eq. (2.2.10);

$$\eta_{self} = 1 - \left(\frac{\int S_p(\lambda)(1 - e^{-\alpha_d(\lambda)\langle r \rangle})d\lambda}{\int S_p(\lambda)\, d\lambda} \right) \quad p = 1, 2, 3, \ldots \quad (2.2.13)$$

Where <*r*> is the mean path length for waveguide modes and is distinct from *l*, which is the mean path of incident irradiance passing vertically through the device. When using Eq. (2.2.13) it is important to realise that each order of emission, $S_p(\lambda)$, is red-shifted relative to the previous one due to conservation of energy. This is because self-absorption occurs solely in the red-tail of the absorption spectrum and so the subsequent generation of emission cannot occur at energies above this absorption range. As such it is necessary to measure the shift in emission peak due to excitation in the red-tail of absorption to ensure the correct emission spectrum is used for each generation.

To use Eq. (2.2.13) <*r*> must be determined which will vary depending on the geometry; here it is given for a square planar concentrator as determined by R. Sóti *et. al.* (1996) [14].

$$\langle r \rangle = \frac{4\left(\frac{\pi}{2} - \theta_c\right)}{2\pi \cos\theta_c} \frac{\int_0^L \int_0^L \int_{-\phi_1}^{\phi_2} \frac{x}{\cos\phi}\, d\phi dy dx}{L^2} \quad (2.2.14)$$

Where *L* is the length of the sides of the square, θ_c is the critical escape angle in the z-plane and ϕ is the angle in the x-y plane (refer to Fig. 2.2.1). Now η_{self}, instead of (1-*J*), can be used for self-absorption using Eq. (2.2.13) and therefore the optical efficiency can be given by Eq. (2.2.15);

$$\eta_{opt} = \eta_{fr}\eta_{stokes}\eta_{abs}\eta_{self} \sum_p \left(\eta_{trap}^p \eta_{TIR}^p \eta_{QY}^p \eta_{host}^p \left(1 - \eta_{self}\right)^{p-1} \right) \quad for\ p = 1, 2, 3, \ldots \quad (2.2.15)$$

This process of determining the various parameters of the optical efficiency will be utilised extensively in chapter 8 to analytically model LSC devices and estimate their performances.

2.3 Luminescent Solar Concentrator Geometry and Configuration

Eq. (2.2.15) gives us the optical efficiency, describing the various loss mechanisms that light experiences as it moves into the device, couples to fluorescence and is waveguided to the harvesting face. The total optical concentration, C_{opt}, is given by the product of Eq. (2.2.15) with the geometric

concentration, *G*. The geometric concentration is given by the ratio of the areas of the collection face to the harvesting faces as in Eq. (2.3.1);

$$G = \frac{A_{col}}{A_{har}} \quad (2.3.1)$$

So then the optical concentration is given by Eq. (2.3.2);

$$C_{opt} = G\eta_{opt} \quad (2.3.2)$$

In addition to optimising all of the factors that η_{opt} is comprised of it is also necessary to mutually optimise the geometry of the LSC device to maximise *G*. There are two main geometries for LSC devices, square-planar and cylindrical, though triangular designs using mirrors have been suggested for their low mean path lengths and hence lower matrix and self absorption losses [4]. Technically this is a planar arrangement anyway and a number of other planar arrangements, such as hexagonal, have been looked at [14]. In that work the path length is shown to be approximately equal to the square root of the LSC surface area, which increases with the number of sides the LSC has, and hence to minimise self-absorption an equilateral triangle should perform best in terms of optical efficiency. For square-planar devices the geometric concentration, G_{sq}, for a square plate of side lengths *L* and thickness *W* is given by Eq. (2.3.3);

$$G_{sq} = \frac{L^2}{4LW} = \frac{L}{4W} \quad (2.3.3)$$

Similarly the geometric concentration for a cylindrical LSC, G_{cyl}, of length *L* and radius *R* is given by;

$$G_{cyl} = \frac{2RL}{2\pi R^2} = \frac{L}{\pi R} \quad (2.3.4)$$

By relating *R* and *W*, as $R = 2W/\pi$, it has been shown that the relationship between the geometric concentration for a square-planar LSC to that of a cylindrical LSC is as in Eq. (2.3.5) [15];

$$G_{cyl} = 2G_{sq} \quad (2.3.5)$$

Cylindrical LSC geometries can thus potentially achieve double the geometric concentration of a square-planar LSC structure. This benefit is offset by typically longer path lengths and greater Fresnel reflection at the interface. However, the K. R. McIntosh *et. al.* 2007 paper sets the stage for bi-layer LSC device structures as it shows, through geometric arguments, that the cylindrical geometry could outperform square ones by as much as a factor of 1.9 *if* the fluorescence occurs near the surface. In this regime, for a coated cylinder, a more optically dense medium is necessary to maximise absorption (hence a higher fluorophore concentration). Additional small increases in performance

and a reduction of the Fresnel loss, beating that of square-planar geometry, are possible using a multi-cylindrical design, like a corrugated surface. It has been seen in Fig. 2.2.4, for normal incidence, that η_{fr} = 0.96 for a square-planar device of n_2 = 1.5; for a single cylinder this becomes η_{fr} = 0.931 and for a multi-cylindrical LSC we have η_{fr} = 0.973. This shows that a multi-cylindrical LSC structure would reflect less light than a planar geometry LSC at normal incidence. Note also that for diffuse light at smaller angles of incidence K. R. McIntosh *et. al.* 2007 show that cylindrical geometries would outperform the square planar geometry in terms of η_{fr}, lending cylindrical LSC devices to be better for cloudy, northern climes. Therefore a multi-cylindrical design would outperform a planar geometry for both direct and diffuse solar irradiance.

Other potential benefits of the cylindrical approach include ease of affixing a PV cell to the harvesting edge of the device and the higher *G* values meaning smaller PV cells are needed and hence potentially lower cost. One of the main downsides one might expect of the cylindrical approach is due to the larger mean path length through the device, resulting in higher matrix and self-absorption losses. These could be quantified analytically using Eq. (2.2.6) and Eq. (2.2.13) for a deeper comparison of the geometries, which has been done using more advanced Monte Carlo simulation methods [16]. In that work self-absorption is shown to peak for short cylindrical LSC lengths, particularly for coated fibre LSCs where emission close to the surface results in a higher fraction of long, helical paths through the more optically dense outer medium. Despite this the authors show that even after self-absorption peaks the optical concentration continues to rise with increasing cylinder length, unlike with square-planar geometries where self-absorption results in the optical concentration reaching a plateau value. Thus a cylinder can benefit from a longer length, *L*, than a square-planar LSC.

From the above discussion of geometry follows the realisation that bi-layer structures may offer an advantage over conventional bulk-doped designs for the cylindrical geometry. K. R. McIntosh *et. al.* 2007 seems to imply, by omission, that surface emission for square-planar devices offers no benefit over bulk-doping. This was shown rigorously by R. Bose *et. al.* 2007 through experimental devices and ray-tracing models [17].

The configuration of an LSC device includes more aspects than geometric shape. Other factors include the employment of mirrors [11] and wavelength selective filters [18 - 21], multi-stack (tandem) plates [3, 19, 22], multi-dye plates [23], anti-reflection coatings [4], plasmonic enhancements [5, 8, 24], and the use of lenses [25]. These factors are with an aim to maximising η_{fr}, η_{trap}, η_{QY}, η_{abs}, η_{self} and η_{host} and minimising the total cost of the device. Let's go over each of these efficiencies in some detail to see

how different configuration factors can be used to improve the loss mechanisms these efficiencies represent.

The reflection of incident sunlight, governed by η_{fr}, represents a relatively small loss which nonetheless needs optimising. The way to improve this is to use an antireflection coating, such as MgF_2, which works by having a much higher refractive index. Such materials are unsuited to being hosts, but a thin layer on the LSC collection face can have very high transparencies and could provide a relative improvement of transmission efficiency by around 3% [4]. This figure actually depends on the incidence angle, with normal incidence exhibiting the lowest benefits from the coating. Additionally, as seen in the geometry discussion, a multi-cylindrical LSC actually has an advantage in this loss mode over square and single cylindrical designs.

There are two main ways that have been suggested to improve the trapping efficiency, η_{trap}, which represents a major loss of around 25% for $n_2 = 1.5$ according to Eq. (2.2.4). Additionally self-absorption results in further ECL, compounding the problem, particularly for fluorophores with a large overlap integral, J. Since η_{trap} depends only on the refractive index of the host it would seem all that can be done is to change the host matrix, as explored in Fig (2.2.4). However, it is possible to use frequency selective filters to reflect emission wavelengths, but allow incident solar irradiance in the fluorophore absorption regime [11, 18, 19]. These filters are photonic structures and can be made from crystalline materials, such as diamond, ceramics or tantalum oxide, Ta_2O_5, which are formed to have a periodically varying refractive index. This creates stop band regions of disallowed energies which display high reflectivity for photons of those energies and can be tuned to encompass desired ranges. Hence these filters are called wavelength selective mirrors and such structures are known as Distributed Bragg Reflectors (DBR). Other materials include cholesteric coatings, a type of organic liquid crystal that form a helical 3D structure which reflects circularly polarised light aligned with the structure [20]. These have already been shown to reduce the light lost in the escape cone by up to 30% [21]. It has been shown by Monte Carlo ray tracing simulations that the upper limit of efficiency for a LSC is equal to the Shockley-Queisser (SQ) limit for solar cells [18]. It is concluded that to reach the thermodynamic limit of concentration with LSC devices wavelength selective mirrors will be required.

A final possibility to enhance η_{trap} is to align dyes vertically, as opposed to randomly, which will deviate the emission from isotropic to increase photon populations in waveguide modes [26]. A downside to this is a reduction in the absorption cross-section of the dyes relative to normally incident solar irradiance, increasing the required LSC thickness or fluorophore concentration. However, this is for normal incidence; as the sun moves across the sky, and for diffuse light from

clouds, this should not necessarily be a limitation. One would need to optimise the fluorophore alignment angle alongside the absorption efficiency across a day, for local sky conditions, to achieve the best results.

The fluorescence quantum yield, η_{QY}, of fluorophores in an LSC device is required to be near unity, which imposes strict limitations on their properties. Fluorophores must exhibit near unity quantum yield in a solid state host matrix at concentrations that enable maximisation of absorption efficiency, η_{abs}, discussed in detail next. The concentration quenching phenomenon is a major problem in this context (see chapter 7) and careful tuning of both fluorophore concentration and LSC absorption path length are necessary to maximise LSC irradiant output. η_{QY} can be effectively enhanced by plasmonic resonance, which has been shown to increase the absorption and fluorescence transition rates and thus can increase LSC output irradiance [24]. In that work CdSe/ZnS quantum dot fluorophores are coupled to surface plasmons generated on various concentrations of gold nanoparticles, providing up to 53% increase in emission. Work by Zhang *et. al.* (2007) [27] exhibited an enhancement in fluorescence of up to 100% for a perylene based dye deposited on a glass substrate coated with Ag plasmons. As well as enabling enhancement of fluorophore absorption and emission plasmonic resonance has been shown to increase solar cell absorption, and hence quantum efficiency, allowing more energy to be collected in an LSC device [28].

Possibly the biggest issue with LSC devices is in attempting to maximise the amount of solar energy captured, as quantified by η_{abs}. Firstly there is an absorption limit due to the range that can be covered by the spectral sensitivity of the solar cell coupled to the LSC. The absorption spectrum of the fluorophore/s needs to cover the entire range of energies up to the solar cell band edge and the emission spectrum needs to overlap strongly with the absorption band of the cell. The bigger challenge is to design a system to maximise absorption of the possible range of solar energies and there are several proposed ways of doing this.

Firstly the thickness (or radius) of the LSC device is optimised using Eq. (2.2.5), as outlined in the relevant section above. However it is a necessary to add a factor to this thickness optimisation; that being employment of mirrors. It might be wasteful in terms of geometric concentration, and hence solar cell size, to increase the plate thickness too much and so adding an inexpensive mirror or diffuse reflector to the back side of the device can alleviate this [11, 29]. The reflector will give incident light a second pass through the LSC device and hence improve the absorption considerably, whilst allowing optimisation of *G* at the same time. This is explored by spectral models in chapter 8.

The most powerful method suggested so far to optimise η_{abs} is to use multiple fluorophores whose combined absorption approaches the ideal for the collection range. A problem with this approach is that having multiple fluorophores present in one LSC plate can result in lowered efficiencies due to increased number of matrix defects. Reduced quantum yields will also be likely because of introduction of new non-radiative decay modes by neighbouring fluorophores; so-called concentration quenching. However, by having stacks of plates in multi-plate (tandem) LSC designs it is possible to eliminate these extra problems. Upper layers absorb bluer light and lower layers absorb redder light and a solar cell tailored to the emission of the relevant dye is affixed to the harvesting edges of each plate. This can increase the efficiency significantly, but the extra solar cells may again increase total device cost.

Another method is to employ a FRET system of dyes that have finely tuned efficient resonant energy transfer all the way to the terminal dye, which then fluoresces the collected energy. This process is distinct from optical coupling as the energy transfer is non-radiative. For most fluorophores this will not be efficient enough unless they are embedded in an emissive host, such as AlQ_3 [30], which is responsible for capturing most of the solar energy. Unfortunately AlQ_3 requires thermal evaporation, which is a big negative because it will significantly increase the cost of the device. However, an efficient FRET based device involving three BODIPY dyes has been reported achieving 45-170% of the LSC output of their single dye variants [31]. Another possible option is using a light emitting polymer (LEP) as a host for small molecular fluorophores with energy transfer occurring from the host LEP to the small molecule. This was done in OLED device research using the LEP F8BT doped with red small molecular fluorophore DCJTB [32]; both materials are discussed in section 2.4. This would only be useful for bi-layer structures with an undoped waveguide core and an active fluorescent coating. Of course some form of encapsulation coating would be necessary to protect the delicate LEP layer from abrasion and other forms of mechanical wear. For a system of non-polymeric, non-host fluorophores randomly distributed across an inert host it appears inconceivable that they could be brought into close enough contact, particularly as more species of fluorophore are added.

Next to discuss is self-absorption, η_{self}, which is a function of two main influencing factors; the strength of the absorption-emission overlap of the fluorophore and the mean path length through the device. Reducing the overlap strength is non-trivial; one must choose fluorophores that have a weaker overlap, which is greatly limited by the availability of suitable fluorescent materials. The materials studied in this thesis are overviewed through section 2.4. In a FRET system, since energy is transferred non-radiatively, the only overlap integral that matters in terms of reabsorption is that of the terminal dye in the series. This represents a benefit over the tandem design where each plate

has a distinct fluorophore with its own overlap integral to reduce efficiency by. Another method that may prove useful, particularly in tandem designs, is to use the solvation mechanism to increase the dyes Stokes' Shift, ΔE_{stokes}. This only works for polar fluorophores whose dipole moment changes upon excitation to the S_1 state and is facilitated by increasing the relative permittivity, ε_r, of the host medium. This mechanism is explored in greater detail in section 2.4 and chapter 6. The other way to increase η_{self} is by reduction of the mean path length by various means including choice of geometry, optimisation of G and aligning dyes to emit into shorter waveguide modes [26].

The light transport efficiency of the host, η_{host}, is governed by the type of host material, fabrication methods (defects), the presence of unreacted monomer or additives, the fluorophore concentration and type, and the path length of light. Typical polymeric host materials exhibit strong absorption at around 750 nm, due to vibrational modes of C-H bonds, resulting in luminescence quenching due to non-radiative energy transfer of the vibrational energy [33]. This could be improved by substitution of hydrogen for deuterium or fluorine atoms to reduce bond vibration [34]. An alternative would be to use a specialist glass, which reportedly could deliver better transport properties and higher refractive indexes but has the downside of being heavy and more expensive [35].

Host fabrication method is also a critical issue; polymerisation from precursor and monomer components is of low cost but can result in unreacted monomers disrupting the matrix [6]. Another issue is the lack of control over the molecular weight, M_W, and regioregularity of the polymerised host. The conditions of the polymerisation such as temperature, solvent and time all affect the resultant matrix and its properties thus requiring careful tuning of the polymerisation process to achieve the optimal matrix. Another approach is casting from solution with pre-polymerised and purified host materials, which is of low cost and simple but may result in the presence of unwanted solvent residue. Again formation processes are critical including drying time, solvent, temperature and so on. A main benefit of this approach is control of the molecular weight of the host material, which may be crucial for matrix stability over device lifetime. Stability is used here as a general term, being the resistance of the matrix to environmental damage such as from thermal stresses, photodegradation and interactions with oxygen. Most monomers, such as MMA or styrene, are liquids so need to have some level of polymerisation to be solid at room temperature. Further, in the literature it has been shown for PMMA that fracture energy, y, is proportional to the square of molecular weight ($y \propto M_W^2$), up to a critical value of M_W at which y is constant [36]. A strong PMMA structure should therefore have a high M_W, but there are other factors that may need consideration such as M_W impacts on η_{QY}, as briefly explored in chapter 7. Another approach altogether employs sol-gel methods for glass forming, which are widely used and could result in improved LSC yields [37].

Such a large range of potential solutions to the innate complexity of trying to optimise LSC devices as a whole presents a mammoth challenge for technology developers. The developments necessary for LSCs to reach a commercial application, with an optical efficiency of $\eta_{opt} > 10\%$, can be broken down into six main criteria:

1. Broad absorption range
2. Minimum overlap of absorption and emission spectra
3. High quantum yield, η_{QY}, (modern organic dyes and rare earth materials have $\eta_{QY} > 90\%$)
4. Low matrix attenuation
5. Lifetime in excess of ten years (Si-cells have 20 year lifetimes)
6. Competitive device cost (< 1 $/W)

Because of the sheer number of loss modes and their possible solutions, optimisation by empirical methods is an incredibly complex and daunting task. Therefore it is good idea to take a modelling approach to inform the optimisation process and reduce the vast number of permutations that need exploring [3, 38-40]. Thermodynamics provides the maximum limits possible. Equations governing geometrical optics, as discussed earlier, are used to compare different geometries and to understand the importance of the optical properties of the host. Monte Carlo and ray tracing methods are typically employed to explore the movement of light and how introduction of configuration factors, such as PBS filters, can influence this. Such work is critically informative to the experimental research process.

2.4 Semiconductor Physics for LSC Devices and Materials

Various fluorophore materials are under consideration for LSC devices including organic dyes [41, 42], inorganic nanocrystals [43-45] and rare earth materials [46-48]. The underlying physical processes that govern these materials are essentially the same, involving the quantum mechanics of transitions, albeit with varying degrees of complication. In this thesis organic dye systems are the focus and the following discussion relates to these in particular.

LSC devices rely on photoexcitation of the fluorophores and therefore typically involve allowed, asymmetric quantum mechanical transitions, giving rise to photoluminescence (PL). There are some major deviations from this for particular materials, so called phosphors, which exhibit strong spin-orbit coupling resulting in high intersystem crossing rates and hence the triplet emission form of PL.

Such materials are typically organometallic compounds with a metal atom, such as Iridium or Europium, as a core structure.

In photon absorption an electron in the ground state is promoted to a higher energy state of the fluorophore. The absorption process allows for any ground state (S_0) electron to be excited to a higher energy level, so long as the photon has the energy to do so. Because of vibrational modes coupling with the principal quantum states, each energy level is actually a manifold of states resulting in observed broadening of the spectrum. These coupled vibronic states are often called vibronic satellites. This can be seen by considering a configuration diagram, which represents the potentials of each energy level and the associated coupled vibronic structure, as shown in Fig 2.4.1.

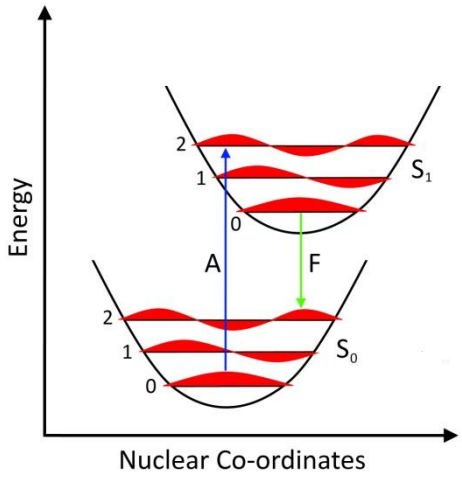

Figure 2.4.1: Configuration diagram showing transitions between the S_0 and S_1 excited states. Each transition mode has a particular probability of occurrence depending on the wavefunction overlap in vertical transitions. Note the different energies of absorption (A) and fluorescence (F) due to energy lost to nuclear vibrations in excited state relaxation. This explains the Stokes' shift, ΔE_{stokes}.

The nature of these vibronic states arises from oscillations in the nucleus and is described by the Franck-Condon Principle [49], which also gives an explanation for ΔE_{stokes}. The nucleus responds very slowly relative to the absorption process, which takes roughly a femtosecond, and is therefore essentially static. However, the excited state exists for around a nanosecond during which time the nucleus starts to oscillate like a spring due to the new electronic configuration putting the nucleus in a non-equilibrium position. The nucleus can oscillate many thousands of times in the lifetime of the excited state over which most if not all of this vibrational energy is transferred to the surrounding medium as heat, a process called Internal Conversion (IC). Then fluorescence takes place from the lowest vibrational state of the electronic manifold of the S_1 excited state.

The Frank-Condon Principle is best exhibited though the absorption and emission spectrum of a simple organic fluorophore, such as perylene, since such molecules have strong vibrational coupling. More complex and flexible organic molecules tend to have absorption and emission dominated by a

particular transition between states, which are numbered 0, 1, 2 and so on to represent the vibronic satellites of each principle quantum state, as in Fig 2.4.1. The absorption and emission spectra of Perylene are shown in Fig 2.4.2 to illustrate this.

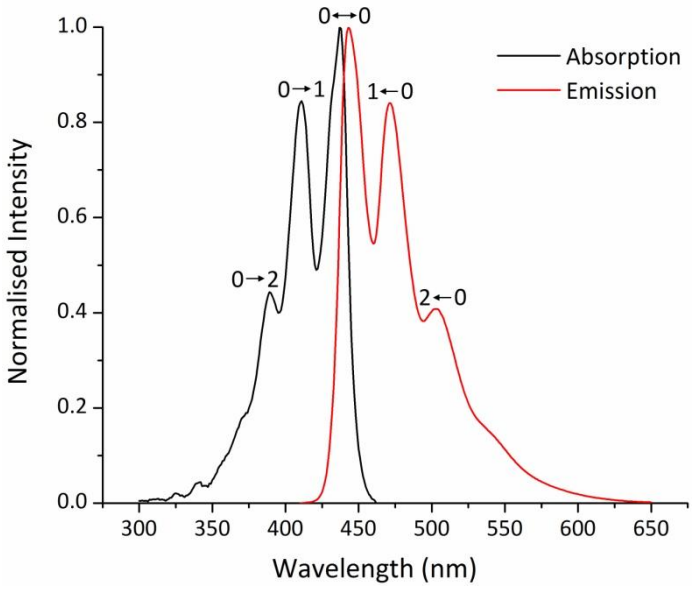

Figure 2.4.2: Absorption and emission of perylene in PMMA at C_{dye} = 2.97x10^{-3} M. Franck-condon factors are labelled next to each associated transition peak.

For perylene each transition is well defined and the spectra are a close mirror image of each other with a small ΔE_{stokes} likely due to interaction between the fluorophore and host material. The relative intensity of the transitions are given theoretically by the quantum mechanical Franck-Condon factors associated with them, for 0-0, 0-1 and so on. Each transition, unlike the sharp, narrow ones of atomic transitions, is broadened thus merging all the separate transitions into a wider spectrum. This inhomogeneous broadening is so called due to the variation in local electronic interactions with the host medium and other dye molecules [50]. This is a relevant effect for all fluorophore types and actually is a benefit in terms of the absorption spectrum since a broad absorption will result in better collection of solar irradiance. A broad emission spectrum is not ideal however and it is difficult to quantify the true impact of the inhomogeneous broadening effect on LSC performance.

The probability of a given transition occurring can be determined by the ratio of the transition rate to the sum of all transition rates. Decay rates, the inverse of state lifetimes ($k = 1/\tau$), are useful in visualising the processes of emission and are often displayed qualitatively with a Jablonski diagram as shown in Fig 2.4.3.

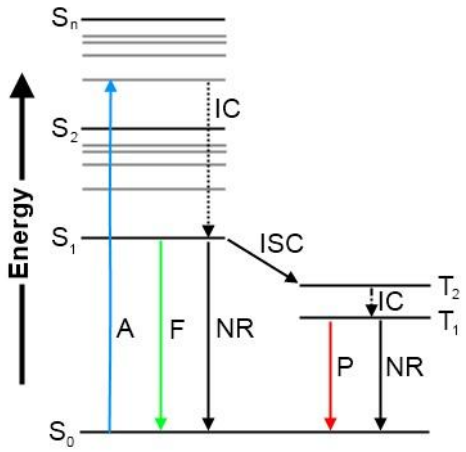

Figure 2.4.3: A Jablonski diagram showing a schematic of a fluorophore's energy levels with various processes that may occur in a typical case. S_0 is the ground singlet electronic state, S_1 is the first singlet excited state and so on to the nth singlet excited state, S_n. T_1 and T_2 are triplet electronic states. The arrows represent energies for absorption (A), fluorescence (F), non-radiative decay (NR), internal conversion (IC), intersystem crossing (ISC) and phosphorescence (P).

From Fig 2.4.3 various processes are shown. Absorption (A) happens with lifetimes of $\tau_{abs} \approx 10^{-15}$ s followed by internal conversion (IC) which has lifetimes of $\tau_{IC} \approx 10^{-12}$ s. Three things may generally happen to the excited state now; fluorescence (F) may occur with typical lifetimes of $\tau_{fl} \approx 10^{-9}$ s, intersystem crossing (ISC) may happen at a rate depending on the LS coupling strength and finally various non-radiative decay routes (NR) may be present with associated lifetimes. If ISC occurs the singlet state transfers to a triplet where further IC may occur and finally phosphorescence (P) which has typical lifetimes of $\tau_P \approx 10^{-6}$ s, or further non-radiative decay.

Understanding the emission process in terms of rate equations leads to a definition of the quantum yield of fluorescence. From Fig 2.4.3 it can be seen that three processes compete for the decay of the S_1 singlet excited state, which are fluorescence, non-radiative decay and intersystem crossing. Therefore the quantum yield can be given by;

$$\eta_{QY} = \frac{k_{fl}}{k_{fl} + k_{ISC} + k_{NR}} \qquad (2.4.1)$$

Where k_{fl} is the radiative decay rate, including transitions to any available vibronic satellites in the ground state, k_{ISC} is the intersystem crossing rate and k_{NR} is the non-radiative decay rate and includes various quenching modes that may be present. In practice when one measures fluorescent lifetimes by single photon counting one actually measures the inverse of the sum of all rates, the denominator in Eq. (2.4.1). Even cooling your sample in a cryostat, with liquid N or He, does not guarantee the elimination of all non-radiative decay modes and so direct measurement of k_{fl} is incredibly difficult. Therefore separate measurement of η_{QY} is typically employed, thus allowing k_{fl} to be found.

To maximise fluorescence η_{QY}, fluorophores for LSC devices are therefore to be chosen on the condition of negligible k_{ISC} and k_{NR}. Non-radiative decay may take the form of intrinsic non-radiative pathways in the molecule, such as conformational changes, or as a result of external influences. In the solid state dynamic or collisional quenching is negligible but concentration quenching may become an issue. The exact mechanism of concentration quenching is unclear in many cases though dipole-dipole deactivation interactions have been observed in the case of the Iridium based phosphor complexes in OLED host materials [51]. Other forms of quenching include excimer formation, as seen for perylene and perylene orange doped into PMMA [52], and due to the presence of quenching agents [53]. This process is explored experimentally in chapter 7. Designing materials that do not suffer strong concentration quenching is clearly an important goal, particularly for surface coated LSC devices where higher concentrations in a thin surface layer are necessary. Possibilities include the development of dendrimers [54] or novel organic fluorophores exhibiting high yields in the pure, solid state [55].

Having a small overlap integral between absorption and emission spectra is another property that an ideal dye would possess to optimise LSC optical efficiency, by maximising η_{self} in this case. Self-absorption, as described earlier in Section 2.2, can result in significant loss of trapped luminescence. This is a function of C_{dye} and mean path length, $\langle r \rangle$, and is typically limited by the LSC dimensions, the PV configuration and the choice of dye. However, for certain fluorophores the solvation mechanism can be employed to decrease the overlap integral, J. Solvation occurs for polar dyes, whose dipole moment changes upon excitation, embedded in a strongly polarisable host, i.e. one with a high dielectric constant. The process can be understood by considering a Jablonski diagram as in Figure 2.4.4.

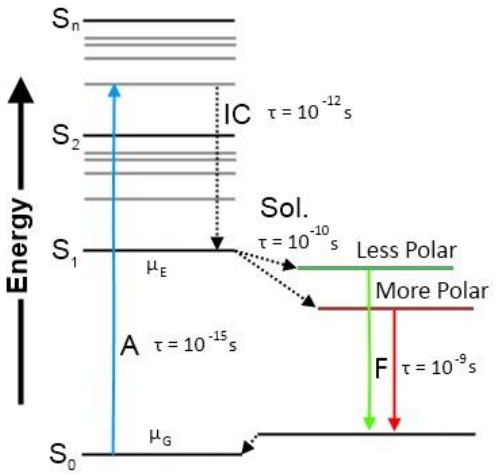

Figure 2.4.4: Jablonski diagram showing the influence of solvation (Sol.) on the new excited state. Other labels are as in Fig. 2.4.3 with transition timescales included. More polar solvents result in a greater redshift in the emission spectrum.

As Fig. 2.4.4 shows solvation occurs approximately ten times as fast as the fluorescence process. When the fluorophore's ground state dipole moment μ_G changes upon excitation to μ_E the surrounding medium responds by physically and electronically reorganising itself around the new dipole. This process creates a reaction field which in turn relaxes the excitation prior to emission. The host medium's ability to do this, the so-called orientational polarisability, Δf, is a function of its refractive index, n, and the relative permittivity, ε_r. By maximising Δf the relaxation can be increased and therefore gains made in reducing J. Solvation is described by the classical Lippert-Mataga (LM) equation [56] and whilst having first been discovered in liquids it has been studied in solids since at least the late 1990's [57, 58]. The LM equation is given by Eq. (2.4.2).

$$\nu_F - \nu_A = \frac{2}{hc}\left(\frac{\varepsilon_r - 1}{2\varepsilon_r + 1} - \frac{n^2 - 1}{2n^2 + 1}\right)\frac{(\mu_E - \mu_G)^2}{a^3} + \Delta\nu_0 \ [cm^{-1}] \qquad (2.4.2)$$

Where ν_F and ν_A are the energy (wavenumbers) of fluorescence and absorption, respectively, the energy difference $\Delta\nu = \nu_F - \nu_A$ is the Stokes' shift, a is the fluorophore Onsager cavity radius and $\Delta\nu_o$ is a constant equal to the unperturbed Stokes' shift. The large bracketed term with the optical constants is Δf, the orientational polarisability. This equation allows us to predict the energy shift due to solvation as long as we know the optical constants of the host and the dipole moments and Onsager radius of the fluorophore. LM theory can break down, particularly in the liquid state, as a result of the formation of new states that change the fluorophore's electronic configuration. Such states include exciplex formation, hydrogen bonding, charge transfer complexes and other environmental effects. A detailed investigation involving Eq. (2.4.2) is undertaken in chapter 5.

Having looked briefly at the basic physics governing emission processes what follows is a detailed review of different fluorophores and their properties. This thesis is concerned largely with small molecular singlet emitting fluorophores but a few additional materials, a metal complex and three LEPs, were also explored at various points.

2.4.1 Organic Small Molecular Fluorophores

Materials in this category include organic materials such as rhodamines, perylenes, dicyanomethylenes, coumarins and anthracenes, to name a few chemical families. It also includes organometallic complexes made up of conjugated units attached to Iridium, Europium and other heavy metals. Two definitions have come in here; that of organic chemistry and that of conjugation in organic molecules. Organic chemistry covers all that pertaining to carbon based compounds and

the significant complexity and richness carbon provides because of its energetic requirement to form four bonds.

Conjugation is a phenomenon observed for a large sub-group of organic chemistry. This phenomenon plays the central role in giving organic semiconductors their electronic properties and in the properties of absorptive and emissive materials. Conjugation is when alternating double and single bonds along carbon chains give rise to the delocalisation of p-orbitals (pi bonding orbitals) across the conjugation length of the molecule. This delocalisation results in conduction properties, charge redistribution and new energy level structure in the molecule. Natural pigments such as beta-carotene, curcuminoids, porphyrins, pthalocyanines and chlorophyll (a and b) are prime examples of conjugated organic molecules which absorb strongly in the visible region. Despite this absorption these molecules tend to display weak or negligible singlet or triplet emission, and are thus not suitable for LSC devices, with a few key exceptions for particular porphyrins and pthalocyanines [5].

Since the first conception of the LSC organic fluorophores have been reviewed extensively for applications. The current state-of-the-art materials are perylene based fluorophores, the perylenebisimides, which includes many of a series made by BASF under the trade name Lumogen™. Another class, which has been historically interesting though has been largely given up on, is the laser dye 4-(Dicyanomethylene)-2-methyl-6-(4-dimethylaminostyryl)-4H-pyran (DCM) and its derivatives such as DCM2, DCJTB, DCQTB and so on. As laser dyes [59] and OLED dopants [58] this class of materials has found success, however, for the high yield requirements of LSC devices they are not efficient enough and suffer severe photobleaching effects. This last point is one of benefits of the perylenebisimide compounds as they are designed for their photostability, with Lumogen F Red 305 (perylene red, PR) shown to lose efficiency to just above 80% over the course of a year [60].

All organic small molecular fluorophores exhibit some level of overlap in absorption and emission, from the strong overlap of Rhodamine 6G (R6G) to the relatively weak overlap of DCM. Heavy metal phosphors, such ADS067RE in Fig. 2.4.15, exhibit small to negligible overlaps resulting in minimised self-absorption. However, they are relatively expensive compared to purely organic dyes due to the more expensive materials needed for their production. Additionally, absorption coefficients are lower than that of organic fluorescent dyes and so require higher concentrations, which can be adversely affected by concentration quenching effects. Also greater LSC device thicknesses will result in reduced geometric concentration according to Eq. (2.3.3).

What follows now is a case by case exhibition of the spectra for organic fluorophores that have been explored here for their potential in LSC devices. optical measurements have been performed

including determination of extinction coefficient spectra, normalised emission spectra and fluorescence quantum yields. All measurements are done using PMMA as a host material at concentrations ranging from 0.1 %wt to 1 wt% depending on fluorophore absorption and quantum yield. Film thicknesses are typically of the order of several microns from spin coating, necessary to achieve optimal signal in these measurements. In Table II is a summary of the key properties of each emitter. The full optical spectroscopy methodology is described in chapter 3.3, including determination of absorption coefficients from a transmission spectrum. Quantum yields are measured as described in chapter 3.1.

Dye	M_w	ε_{max} ($M^{-1}cm^{-1}$)	$\Sigma(\varepsilon(\lambda))$	λ_{abs} (nm)	λ_{em} (nm)	$\Delta\lambda$ (nm)	η_{QY} (±0.02)
ADS067RE	711.87	5058	5.26E+05	349	610	261	0.11
C102	255.32	25641	1.42E+06	381	430	49	0.46
DCJTB	453.63	75021	1.13E+07	506	598	92	0.44
DCM	303.37	32766	4.14E+06	462	548	86	0.31
DCM2	355.44	44351	6.43E+06	503	583	80	0.44
DANS	268.31	28371	3.31E+06	434	574	140	0.33
PO	710.873	61479	4.63E+06	491	537	46	0.68
PR	963.956	58646	6.00E+06	574	612	38	0.60
Perylene	252.32	31900	1.47E+06	437	443	6	0.86
Ph660	290.32	34426	3.77E+06	516	594	78	0.15
Pyridine 1	378.85	40265	6.40E+06	479	619	140	0.13
Pyridine 2	526	60790	9.13E+06	501	619	118	0.20
R6G	479.02	91392	5.17E+06	536	558	22	0.76

Table II: Small molecular organic fluorophore properties at C_{dye} = 0.1 wt% in PMMA.

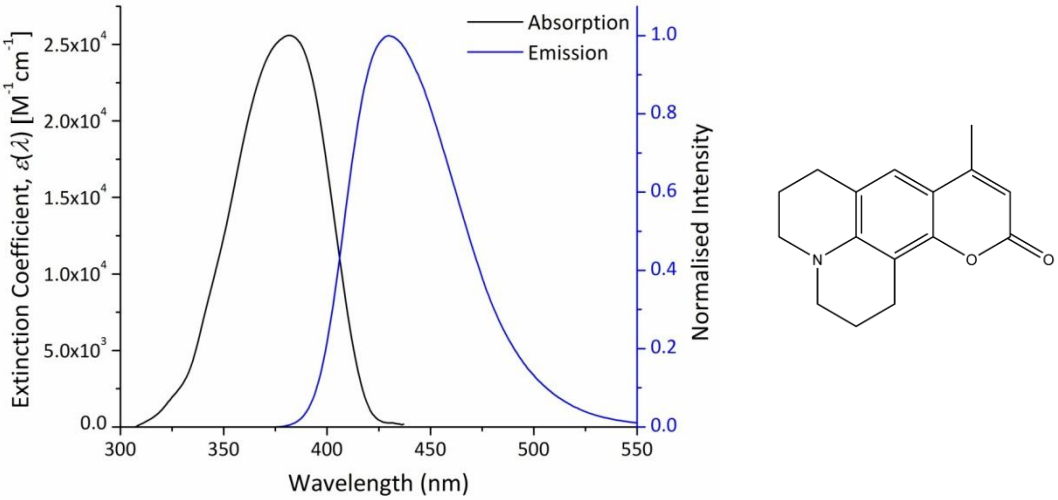

Figure 2.4.5: The chemical structure and spectra for blue emitting laser dye Coumarin 102 (C102); 2,3,6,7-Tetrahydro-9-methyl-1*H*,5*H*-quinolizino(9,1-*gh*)coumarin.

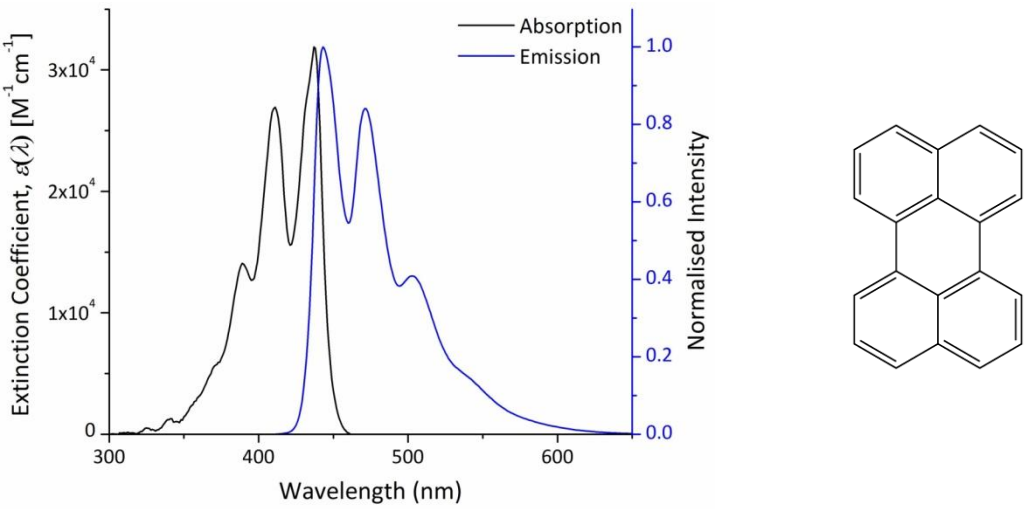

Figure 2.4.6: The chemical structure and spectra for blue-green emitting perylene

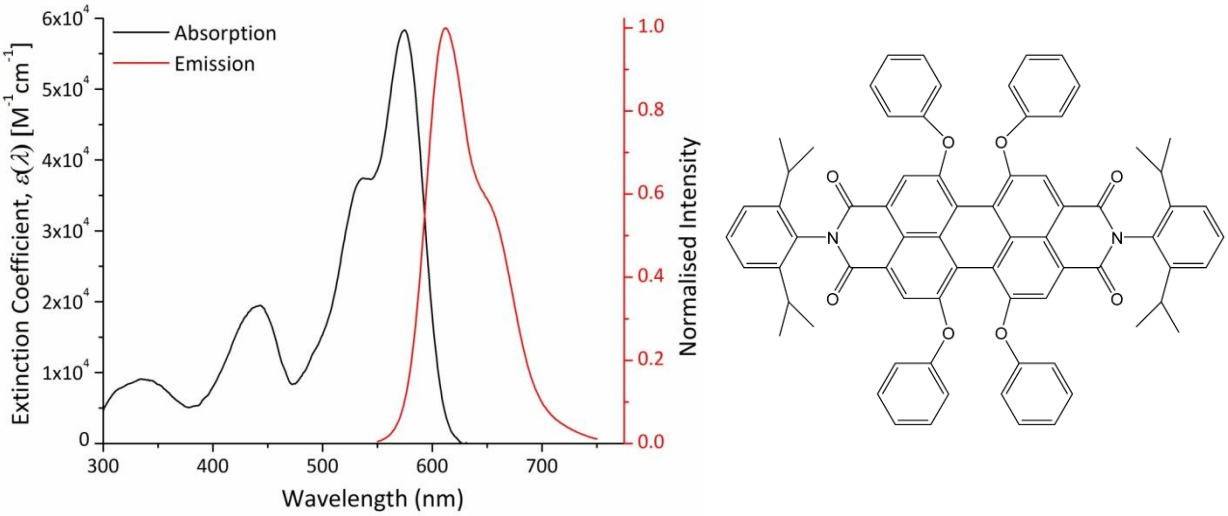

Figure 2.4.7: The chemical structure and spectra for perylene red (PR), also known as Lumogen F Red 305.

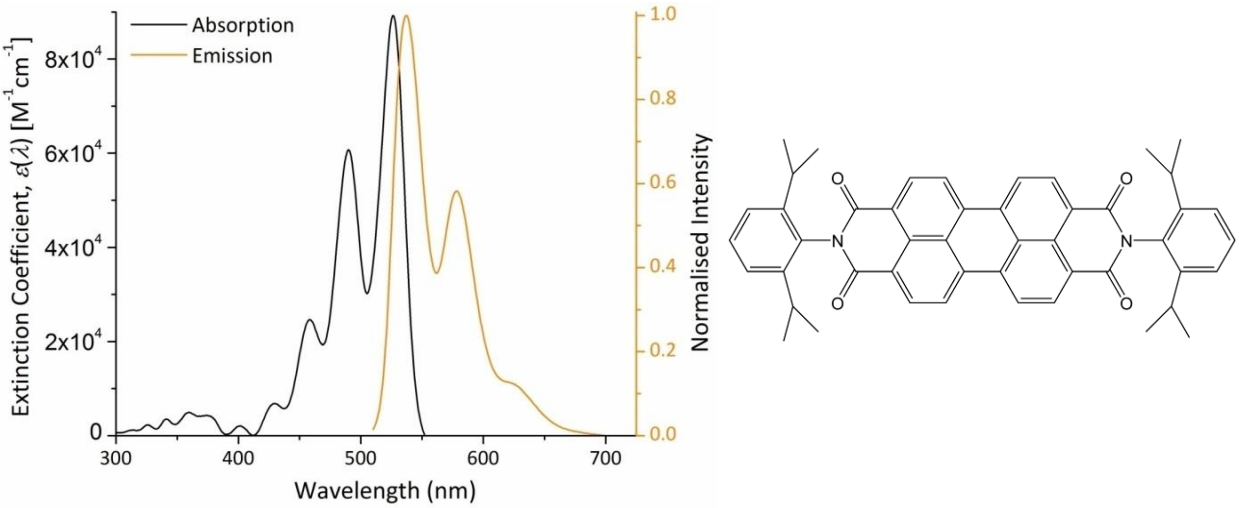

Figure 2.4.8: The chemical structure and spectra for perylene orange (PO), also known as Lumogen F Orange 240.

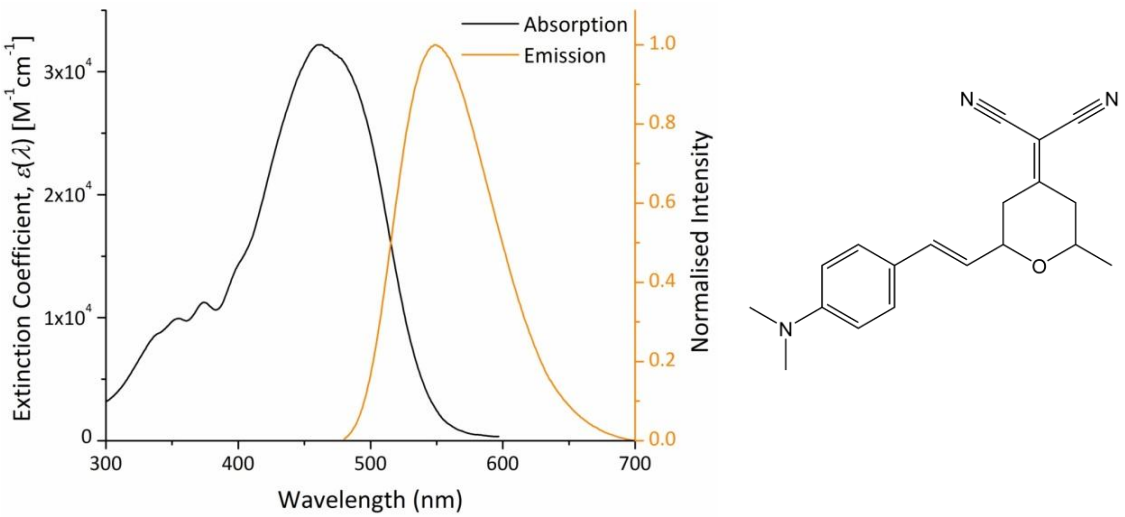

Figure 2.4.9: The chemical structure and spectra for yellow-orange laser dye DCM; 4-(Dicyanomethylene)-2-methyl-6-(4-dimethylaminostyryl)-4H-pyran

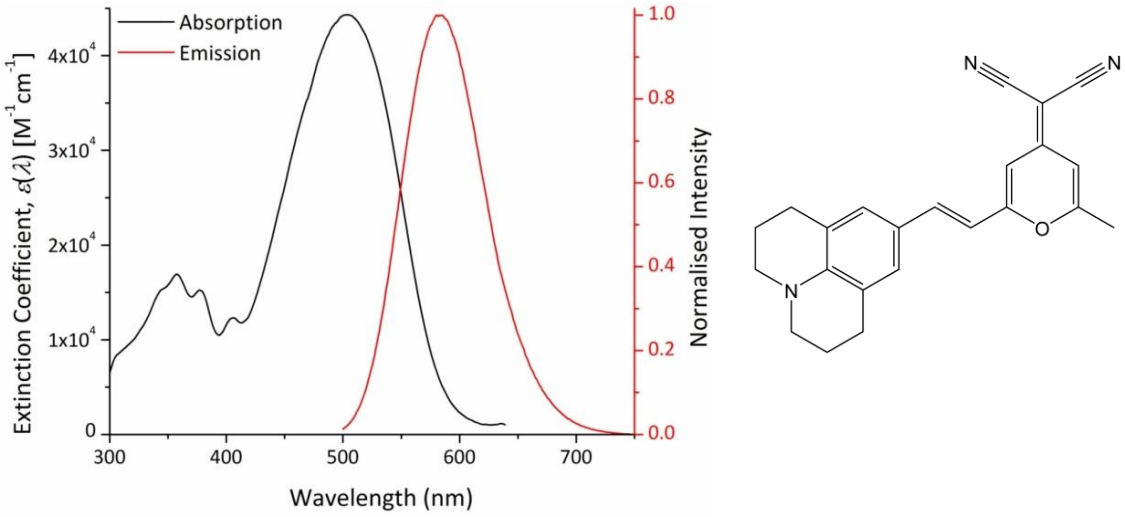

Figure 2.4.10: The chemical structure and spectra for red emitting laser dye DCM2; [2-methyl-6-[2-[(2,3,6,7-tetrahydro-1H,5H-benzo[ij]quinolizin-9-yl)ethenyl]-4H-pyran-4-ylidene]propanedinitrile.

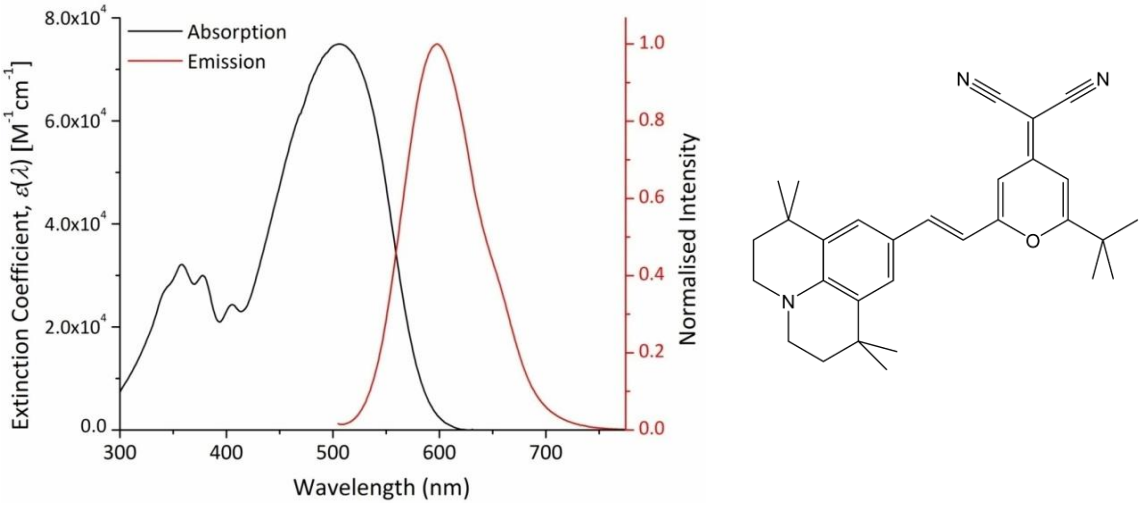

Figure 2.4.11: The chemical structure and spectra of red emitting laser dye DCJTB; 4-(Dicyanomethylene)-2-tert-butyl-6-(1,1,7,7-tetramethyljulolidin-4-yl-vinyl)-4H-pyran.

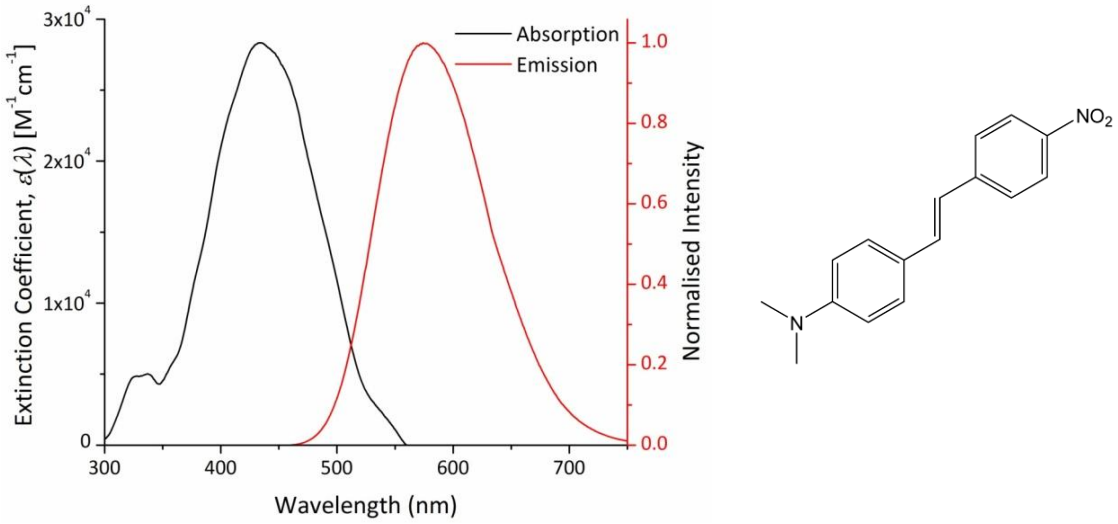

Figure 2.4.12: The chemical structure and spectra of red emitting fluorophore DANS; 4-Dimethylamino-4'-nitrostilbene.

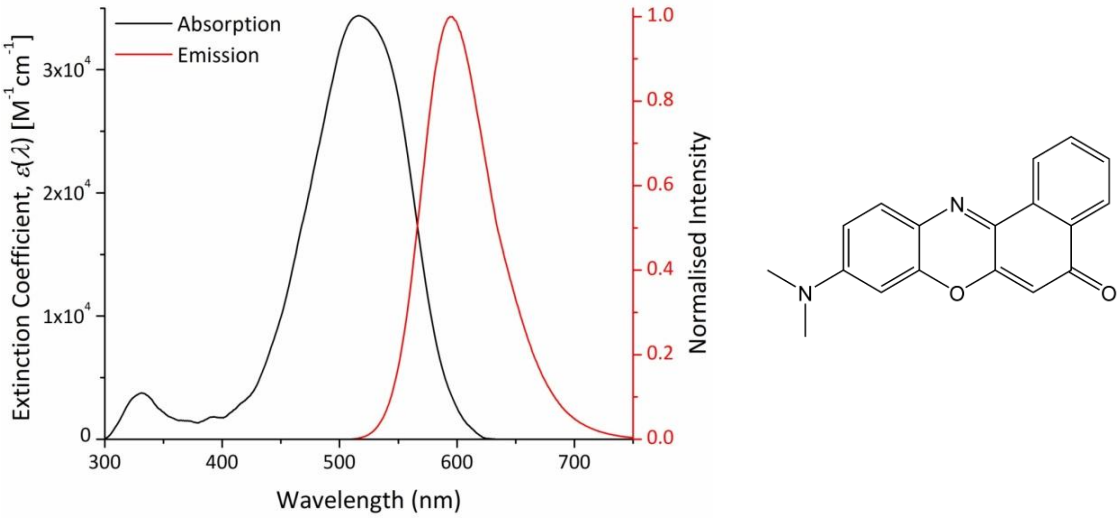

Figure 2.4.13: The chemical structure and spectra of red emitting fluorophore Phenoxazine 660 (Ph660); 9-(Dimethylamino)-5H-benzo[a]phenoxazin-5-one.

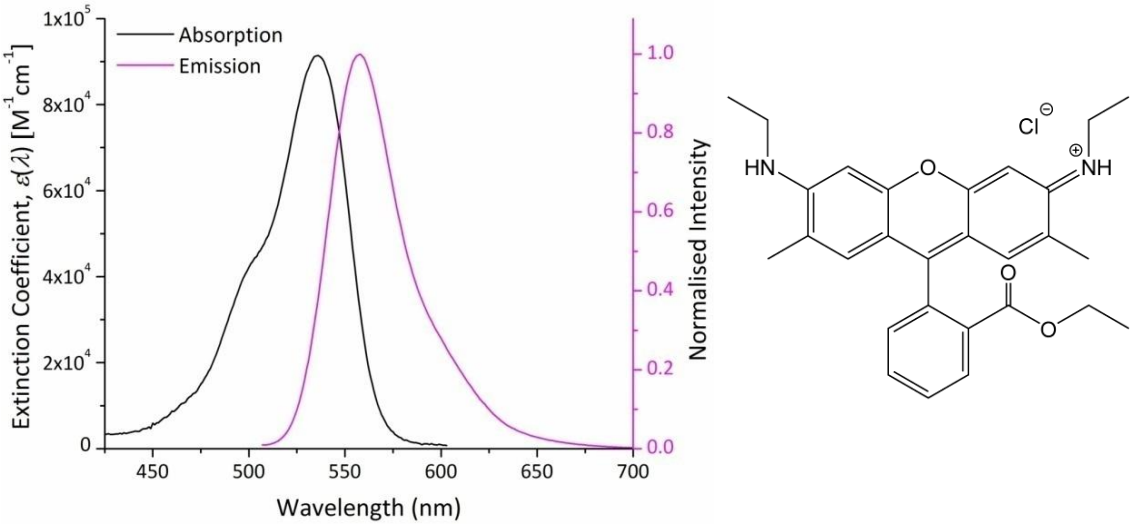

Figure 2.4.14: The chemical structure and spectra of laser dye salt Rhodamine 6G (R6G).

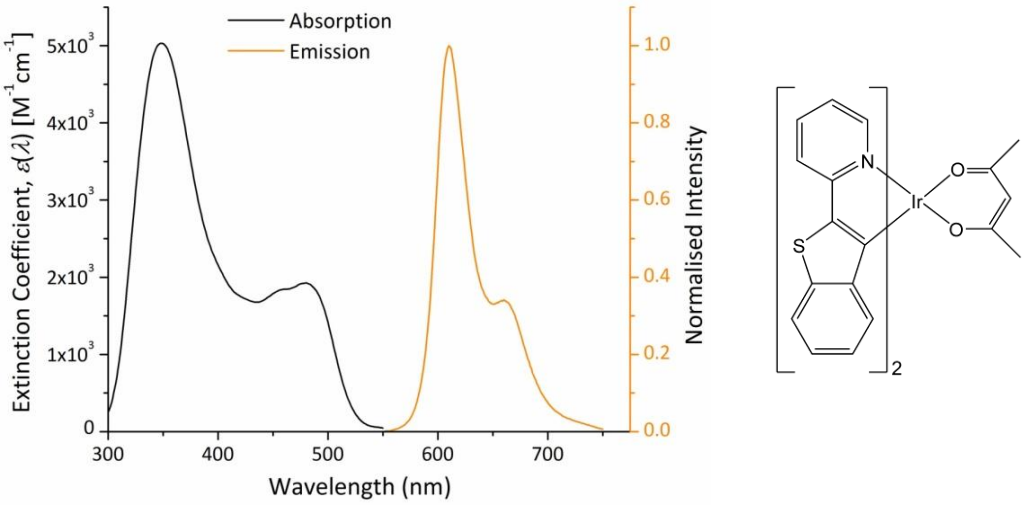

Figure 2.4.15: The chemical structure and spectra of heavy metal complex ADS067RE; Iridium (III) bis(2-(2'-benzo-thienyl)pyridinatoN,$C^{3'}$)(acetyl-acetonate).

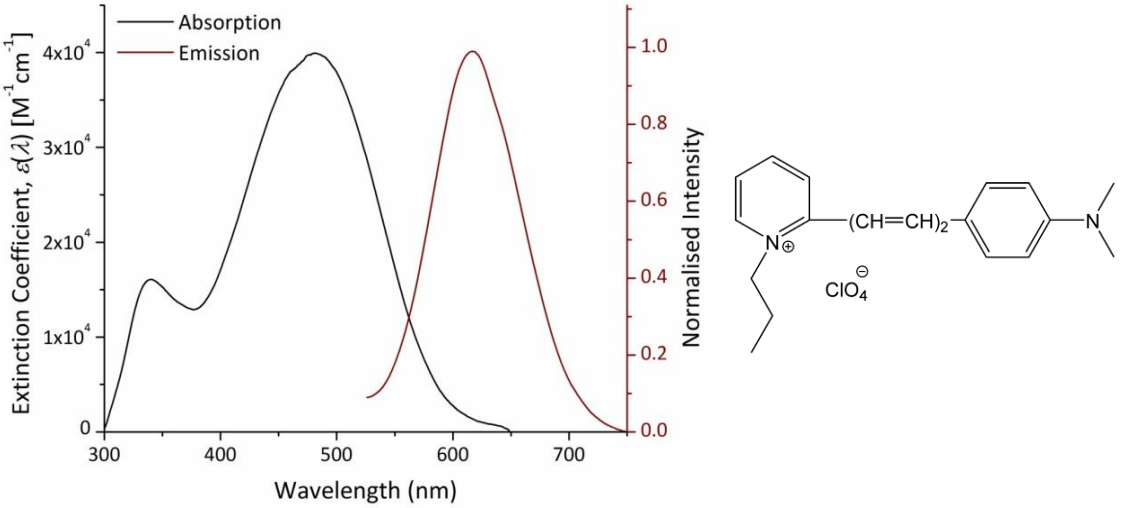

Figure 2.4.16: The chemical structure and spectra of deep red emitting laser dye salt Pyridine 1; [2-[4-[4-(dimethylamino)phenyl]-1,3-butadienyl]-1-ethylpyridinium monoperchlorate.

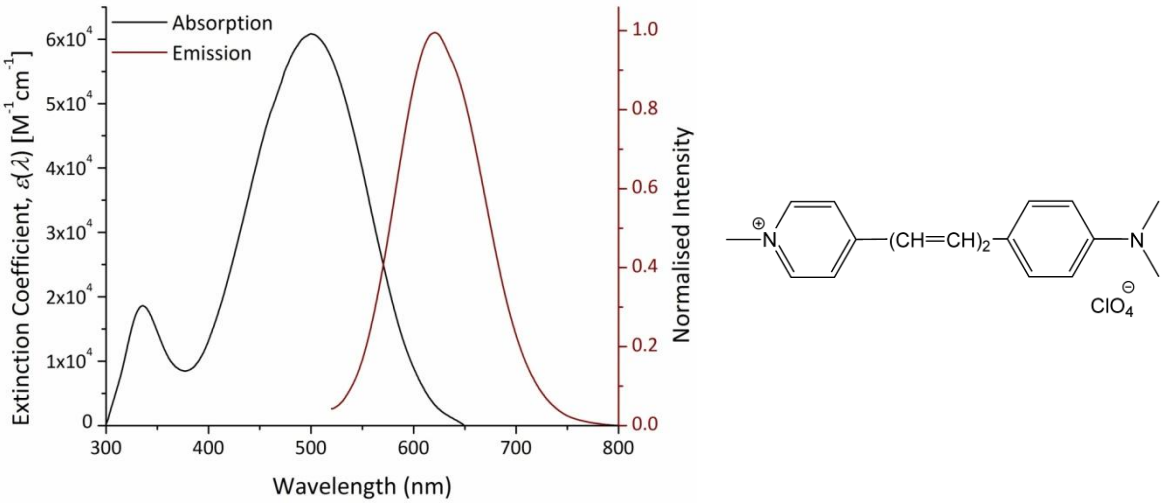

Figure 2.4.17: The chemical structure and spectra of deep red laser dye salt Pyridine 2; 4-[4-[4-(dimethylamino)phenyl]-1,3-butadienyl]-1-ethyl-pyridinium perchlorate.

2.4.2 Light Emitting Polymers (LEP)

Three light emitting polymers have been looked at in this work for different purposes. These polymers are blue emitting poly(9,9-dioctylfluorene) (F8), green emitting poly(9,9-dioctylfluorene-alt-benzothiadiazole) (F8BT) and red-emitting poly[{9,9-dihexyl-2,7-bis(1-cyanovinylene) fluorenylene}-alt-co-{2,5-bis(N,N'-diphenylamino)-1,4-phenylene}] (ADS111RE). F8 is used in chapter 4 as part of the Gauge R & R study on absolute measurement of quantum yield.

F8BT and ADS111RE were both considered for LEP based bi-layer LSC devices where the coating is an LEP layer, possibly doped with some small molecular fluorophore. The LEP could act as an energy transfer host, such as the F8BT:DCJTB system for efficient OLEDs mentioned in section 2.3 [32]. In that research F8BT was seen to stabilise the DCJTB excited state and thus enhance fluorescence efficiency. In other research F8BT optical properties are measured giving a refractive index in the order of n = 1.6 across the visible spectrum [61]. For such a bi-layer device a suitable core material with higher refractive index would be needed, such as flint glass which has n = 1.62, but this would add to a LSCs expense. In Figs. 2.4.18, 2.4.19 and 2.4.20 are normalised absorption and emission spectra for F8, F8BT and ADS111RE, respectively, with their chemical structures.

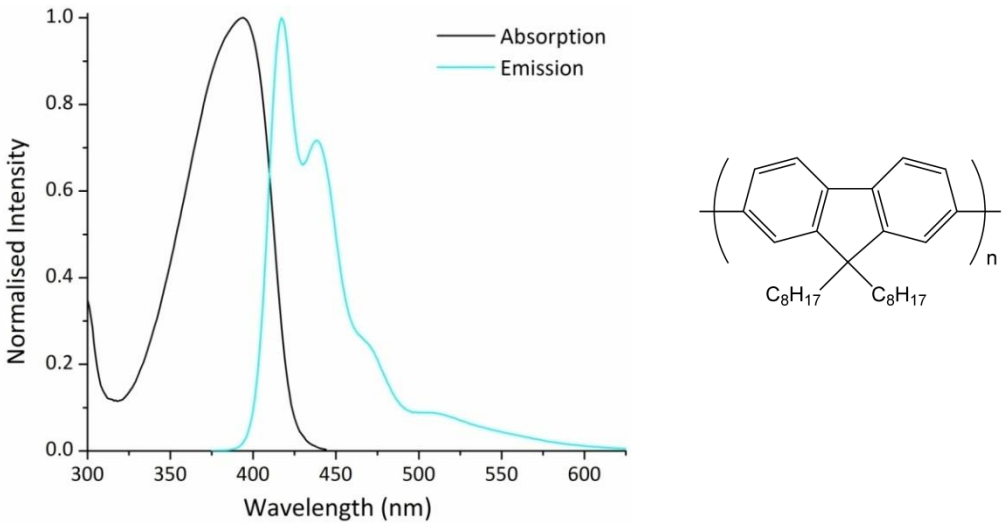

Figure 2.4.18: Normalised absorption and emission spectra for F8; poly(9,9-dioctylfluorene)

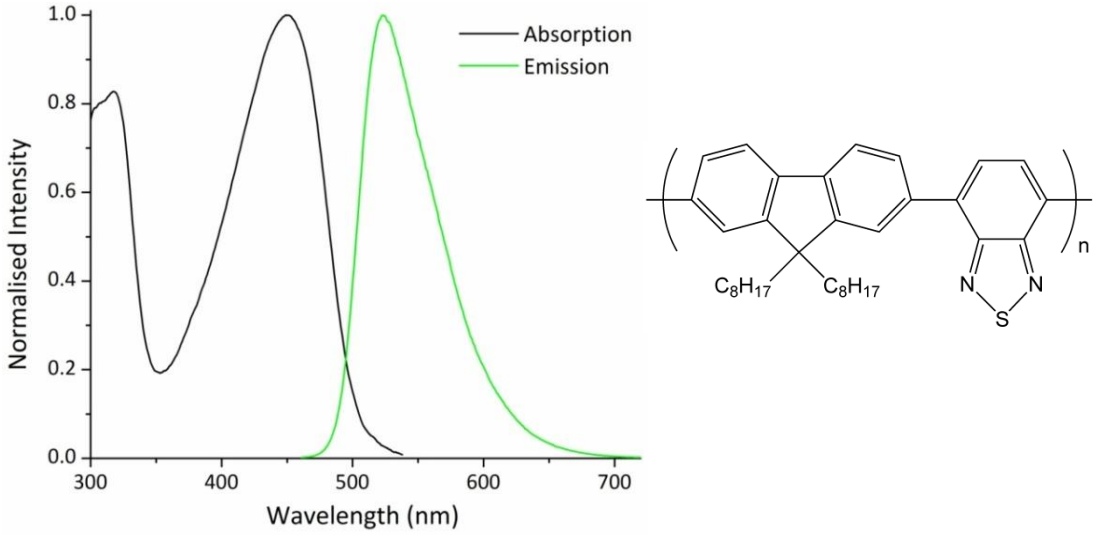

Figure 2.4.19: Normalised absorption and emission spectra for F8BT; poly(9,9-dioctylfluorene- alt-benzothiadiazole)

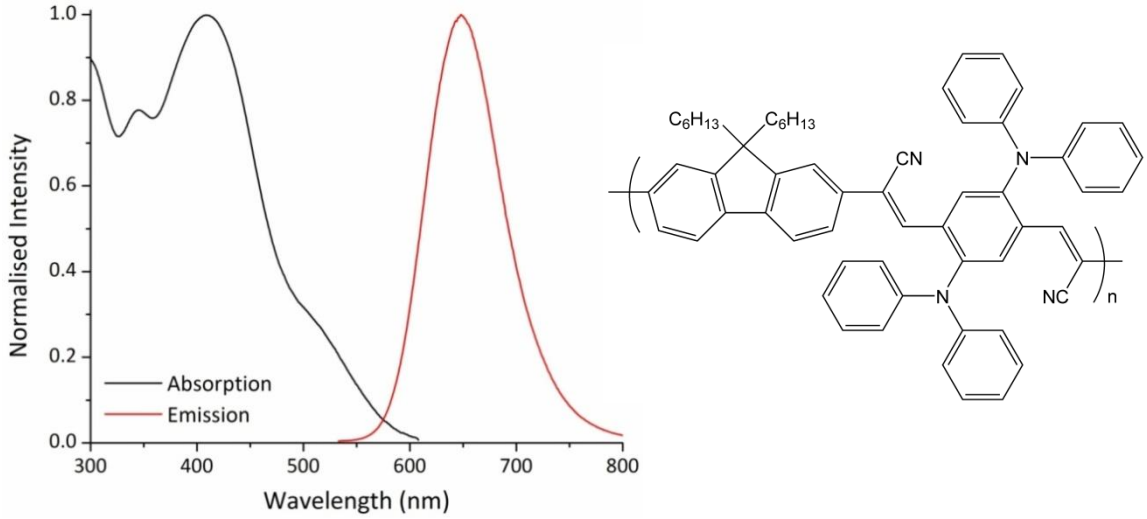

Figure 2.4.20: Normalised absorption and emission spectra for ADS111RE; Poly[{9,9-dihexyl-2,7-bis(1-cyanovinylene)fluorenylene}-alt-co-{2,5-bis(N,N'-diphenylamino)-1,4-phenylene}]

The spectral properties and quantum yield for these LEPs are summarised in Table III. As can be seen quantum yields are too low for use in a LSC, although high stokes' shifts and small overlaps are offered by F8BT and ADS111RE. $F8_x$:$F8BT_{1-x}$ blends have been shown to achieve $\eta_{QY} = 0.7$ for x = 0.95 due to dipole-dipole coupling from F8 to F8BT [62]. Such methods using blends of LEPs could in principle allow wide spectral coverage and efficient emission in the red.

Dye	λ_{abs} (nm)	λ_{em} (nm)	$\Delta\lambda$ (nm)	η_{QY} (±0.02)
F8	394	417	23	0.45
F8BT	462	523	61	0.43
ADS111RE	408	648	240	0.11

Table III: Light emitting polymer properties.

2.4.3 Matrix/Host Materials

A number of polymeric host materials have been explored in this thesis though, as with literature, the dominant host material has been poly(methyl methacrylate) (PMMA). This host has suitable and well understood optical properties, and ease of processibility, making it an obvious choice for LSC structures. Historically in LSC literature PMMA was the first host matrix material considered and to date essentially all of the record LSC power conversion efficiencies have been made by devices using this material.

As has been seen throughout sections 2.2 and 2.3 the properties of the host material must meet a range of criteria to minimise losses and maximise the optical concentration. A high refractive index, towards $n_2 = 2$, is ideal to maximise the amount of light trapped inside the device after reflection loss and ECL. Available polymer host materials exhibit indices in the range $1.3 < n_2 < 1.6$ so there is room for improvement from polymer science. Polystyrene (PS) is the highest shown here with n = 1.596. Specialist glasses can achieve higher refractive indices [35]; for example flint glass has $1.5 < n < 2$. Additionally glass is robust though it may add extra mass to a LSC device. Solar grade glass has n = 1.47 according to one source [63] but with different fabrications methods will undoubtedly vary. It is typically manufactured by either cast or float, costs in the region of £24 m^{-2} and £64 m^{-2}, depending on the fabrication route [64], and is a significant percentage of the cost of a PV panel. However, this is of a similar order of cost to that of LSC structures fabricated with polymer host materials, as is shown for PMMA in chapter 8.

The host material must provide a suitable environment for guest fluorophores. This must be inert, so that the host does not act as a fluorescence quenching agent, and also offer low attenuation across the visible spectrum. PMMA offers some of the best performance in this area with an absorption coefficient of $\alpha_h = 3.4 \times 10^{-4}$ cm^{-1} at 550 nm [65]. This differs somewhat from polymer to polymer, for example polycarbonate (PC) shows the greatest attenuation here at around 10^{-3} cm^{-1} at 550 nm [66]. A relatively new host material in LSC literature is poly(lactic acid) (PLA) which reportedly shows similar attenuation to PMMA (measured by transmittance) and an oligothiophene fluorophore exhibited greater quantum yield in PLA than PMMA [67]. PLA also offers a renewable, eco-friendly alternative to petrochemical plastics.

A range of polymers for optical applications are summarised in Table IV with quantum yields measured for the fluorophore DCM at $C_{dye} = 0.1$ wt%.

Polymer	n	$\eta_{fr}\eta_{trap}$	α_h(cm^{-1})	η_{QY} ± 0.02 (DCM)
PMMA	1.494	0.714	3.4x10^{-4}	0.31
PC	1.589	0.737	10^{-3}	0.32
PS	1.596	0.738	4 x10^{-4}	0.16
PLA	1.450	0.700	3.5x10^{-4}	0.31
PVDF-HFP	1.407	0.683	-	0.40
Topas 513	1.533	0.724	4 x10^{-4}	0.14
Zeonex 480R	1.525	0.722	3x10^{-4}	0.10

Table IV: Data for several hosts; the refractive index, n, the product of reflection and trapping efficiencies, $\eta_{fr}\eta_{trap}$, the absorption coefficient, α_h, at 550 nm and the fluorescent quantum yield, η_{QY}, for DCM at C_{dye} = 0.1 wt%.

2.5 Solar Cells for LSC Devices

A basic understanding of photovoltaic devices is requisite for this thesis, specifically to be used in chapter 8 where spectral methods are used to determined LSC power output. No LSC devices with solar cells attached were tested under AM1.5 by their IV characteristics, so discussion of such theory is not included. Here the power conversion properties of solar cells are introduced in terms of spectral considerations. The power conversion characteristics of a solar cell are characterised in two ways; power conversion efficiency of the solar cell, η_{PCE}, and the external quantum efficiency, $\eta_{EQE}(\lambda)$.

The power conversion efficiency, η_{PCE}, is generally measured under the AM1.5 solar irradiance spectrum and is given by the ratio of power in to power out. The power out is unknown but the power in comes from the solar irradiance, $S_{sun}(\lambda)$, for direct irradiance on to a cell of area A_{har}. Thus η_{PCE} may be written as in Eq. (2.5.1);

$$\eta_{PCE} = \frac{P_{out}}{A_{har} \int S_{sun}(\lambda) d\lambda} \qquad (2.5.1)$$

A_{har} is used deliberately since this is the area of solar cell used around a LSC according to the definition used here, as in Eq. (2.3.1). Table V shows the η_{PCE} for a selection of the latest in solar cell technologies that may be applicable LSC devices. These devices are a multicrystalline silicon (mc:Si) device by Q-Cells [69], a crystalline silicon (c:Si) device by Panasonic [71], a copper-indium-gallium-selenide (CIGS) device by NREL [71], an organic semiconductor device by Mitsubishi [70] and a gallium arsenide (GaAs) device by Alta [70]. A row is included for a simple scaling of 0.6 to represent the power conversion efficiency of the cells in a modular configuration.

	mc:Si	CIGS	Organic	c:Si	GaAs
η_{PCE}	0.195	0.233	0.10	0.256	0.283
$0.6\eta_{PCE}$	0.117	0.140	0.06	0.154	0.170

Table V: η_{PCE} values for a range of solar cells; multicrystalline silicon (mc:Si), copper-indium-gallium-selenide (CIGS), organic semiconductor, crystalline silicon (c:Si) and gallium arsenide (GaAs). The scaled values assumed for modular cell configurations are shown in the row for $0.6\eta_{PCE}$.

For a LSC the solar irradiance spectrum in Eq. (2.5.1) is replaced with the LSC output irradiance, $S_{LSC}(\lambda)$, arriving at the mounted solar cells. Because η_{PCE} depends on the light intensity incident on the solar cell it is difficult to relate literature measurements of solar cells to their performance as part of a LSC. Ideally one would measure η_{PCE} for each cell, with a range of different optical concentrations, C_{opt}, so that the efficiency-concentration dependence could be determined. Such work has been done for particular solar cells under different intensities of the solar spectrum. For instance characterisations of GaAs [72] and c:Si [73] cells show similar behaviour, with an increase in efficiency with increased light concentration. This continues until a threshold is reached where overheating and current saturation issues arise, typically in the hundreds of suns. In Fig. 2.5.1 a plot of efficiency dependence on concentration is reproduced here to illustrate this point [72].

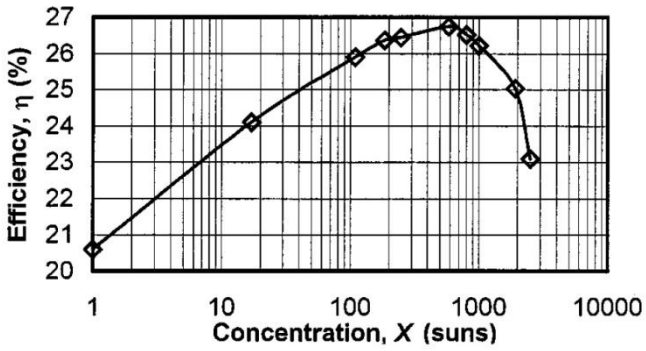

Figure 2.5.1:[72] Power conversion efficiency, in this paper denoted η, as a function of the intensity of incident light in units of the AM1.5 solar intensity.

Figure 2.5.1 implies that below one sun there is a sharp continuing decrease in efficiency. For low light intensities the efficiency decrease is due to a change in the balance of resistances in the solar cell, with an increasing proportion being lost to the shunt resistance [74]. However, a typical LSC will operate in the 1 to 10 sun regime and so the η_{PCE} of this GaAs cell in an LSC device would be expected to somewhere between 20.6% to 23.5%.

The spectral response of the cell characterised by the external quantum efficiency spectrum, $\eta_{EQE}(\lambda)$. This is equivalent to the spectral responsivity (A/W), but without units, and is a measure of the fraction of charge carriers collected at the electrode interface as a function of wavelength. In Fig. 2.5.2 are the $\eta_{EQE}(\lambda)$ spectra of the solar cells in Table V, digitised from graphical data [69-71].

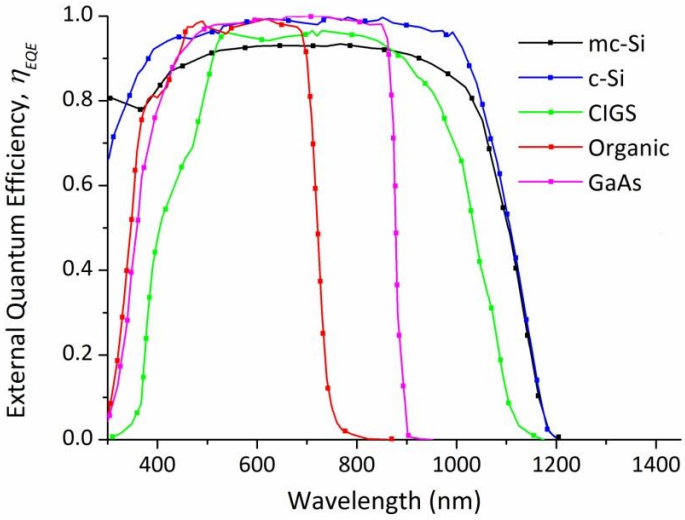

Figure 2.5.2: EQE spectra for the solar cells detailed in Table V.

The $\eta_{EQE}(\lambda)$ spectrum takes into account recombination, reflection and transmission losses but it does not describe the charge extraction process at the electrode, where loss occurs due to the energy barrier. For the spectral modelling in chapter 8 we want to know the power conversion efficiency as a function of wavelength and to determine this the charge extraction efficiency, $\eta_{ex}(\lambda)$, must be determined. Since the spectral responsivity and averaged η_{PCE} are known for the AM1.5 irradiance spectrum it is possible to determine $\eta_{ex}(\lambda)$ by spectral methods. The power conversion efficiency is the ratio of power out to power in, as stated already, but the power out can now be written in terms of the input irradiance, $S_{sun}(\lambda)$, the losses in charge collection to the interface, $\eta_{EQE}(\lambda)$, and our unknown charge extraction efficiency. $\eta_{ex}(\lambda)$ is thus given by Eq. (2.5.2);

$$\eta_{ex}(\lambda) = \frac{\eta_{PCE} \int S_{sun}(\lambda)\, d\lambda}{\int S_{sun}(\lambda)\eta_{EQE}(\lambda)\, d\lambda} \qquad (2.5.2)$$

Now the power out in Eq. (2.5.1) can be rewritten as a product of the cell area, input irradiance, $\eta_{EQE}(\lambda)$ and $\eta_{ex}(\lambda)$. From Eq. (2.5.2) it can be realised that the power conversion efficiency spectrum, $\eta_{PCE}(\lambda)$, is the product of $\eta_{EQE}(\lambda)$ and $\eta_{ex}(\lambda)$, as in Eq. (2.5.3);

$$\eta_{PCE}(\lambda) = \eta_{ex}(\lambda)\eta_{EQE}(\lambda) = \frac{\eta_{PCE}\eta_{EQE}(\lambda) \int S_{sun}(\lambda)\, d\lambda}{\int S_{sun}(\lambda)\eta_{EQE}(\lambda)\, d\lambda} \qquad (2.5.3)$$

From the $\eta_{EQE}(\lambda)$ data presented in Fig. 2.5.2, the known average η_{PCE} values scaled by 0.6 for module configurations presented in Table V and the solar irradiance spectrum at AM1.5, the $\eta_{PCE}(\lambda)$ spectra for AM1.5 irradiance have been determined as shown in Fig. 2.5.3.

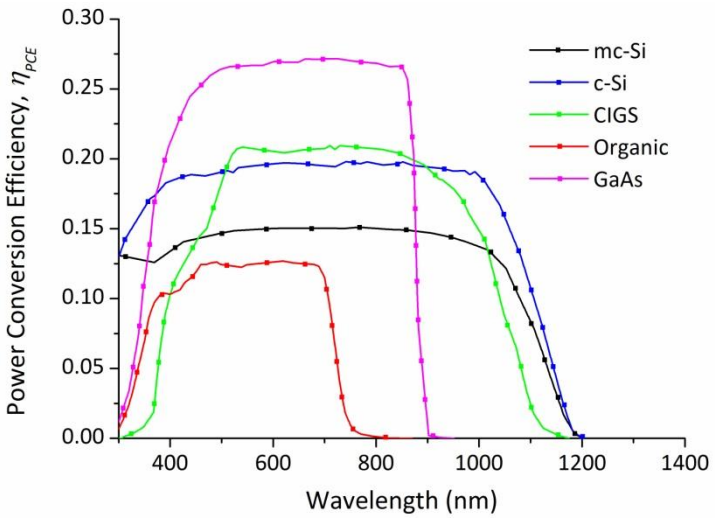

Figure 2.5.3: PCE spectra for the solar cells detailed in Table V calculated using the scaled average η_{PCE} with Eq. (2.5.3).

Note that separating the η_{PCE} into a wavelength dependent function is of an unphysical basis because it is given by the maximum power point on a solar cell's IV curve. It works because the spectral methods defined here are essentially a normalisation relative to the AM1.5 irradiance spectrum. The integral of the product of power conversion spectra in 2.5.3 and the AM1.5 irradiance spectrum, as a ratio of the integral of the input irradiance, gives the scaled η_{PCE} values in Table V, as required by definition.

The power generated by a solar cell, P_{out}, can now be written as the product of the PV area, A_{har}, and the integral of the product of $\eta_{PCE}(\lambda)$ and $S_{sun}(\lambda)$, as in Eq. (2.5.4);

$$P_{out} = A_{har} \int \eta_{PCE}(\lambda) S_{sun}(\lambda) d\lambda \qquad (2.5.4)$$

It must be highlighted that the light intensity falling on the cell will vary between different LSC designs and any model must be able to take account of this fact in light of Fig. 2.5.1. Because such in depth data is not available for the solar cells studied here an estimation of efficiency versus concentration for the cells is built from literature [72,73,75]. In particular J. F. Randall and J. Jacot (2002)[75] show that the form of the dependence is roughly the same for eight different solar cells, but the peak efficiency varies with respect to concentration. Choosing an optical concentration, C_{opt}, range between 0.01 and 100 suns using the data for GaAs[72,75] and c:Si[73,75] we get a straight curve in log space, similar to Fig. 2.5.1. From this a power correction factor, β, can be defined as the ratio of η_{PCE} as a function of C_{opt} to the η_{PCE} under one sun at AM1.5, thus β is equal to unity when C_{opt} = 1 sun, as shown in Fig. 2.5.4. Then Eq. (2.5.4) becomes;

$$P_{out} = \beta A_{har} \int \eta_{PCE}(\lambda) S_{sun}(\lambda) d\lambda \qquad (2.5.5)$$

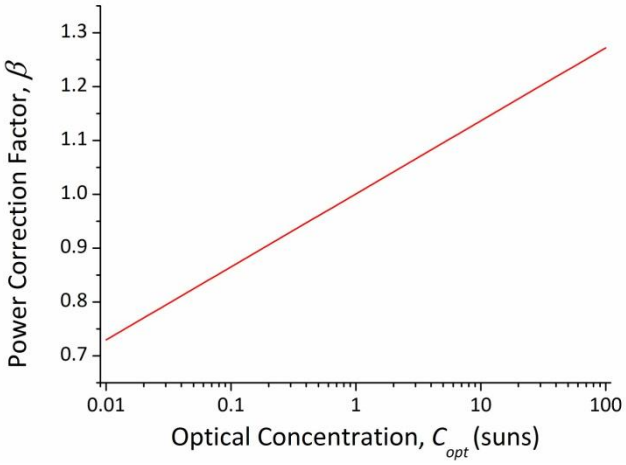

Figure 2.5.4: The power correction factor, β, as a function of optical concentration, C_{opt}. The function is unity at one sun, where the solar cells studied here have available data for.

The power correction factor works well when the solar cell in question follows the curve in Fig. 2.5.4 and there is a high confidence in this for both the c:Si and GaAs solar cells. The other cells in Table V may differ from this with the uncertainty growing with departure from unity, i.e. the original known $\eta_{PCE}(\lambda)$ spectrum under AM1.5, as defined above.

2.6 State of the Art LSC Devices

LSC devices have not developed especially fast since the 1980's, in fact there is a significant reduction in the number of papers on LSC devices in the 1990's with research picking up again in the 2000's. This is largely thanks to the development of new materials, particularly in rare earth materials and quantum dots but also owing to the Lumogen series of organic fluorophores developed by BASF. A review covering the efficiency advancements in LSC devices came out in 2012 [6], which shows growth in power conversion efficiency from 4.5% back in 1984 using CdSe/CdS quantum dots [9] to 7.1% in 2008 using two organic fluorophores [29]. An organic fluorophore based, single layer, square-planar LSC is therefore the current state-of-the-art though this will certainly be improved upon in coming years of research.

In terms of structures explored in working devices the vast majority are square-planar geometries using one or more fluorophores in a single plate. A few square-planar tandem structures have been seen, most notably a 6.7% double layer tandem LSC device using organic fluorophores, which was exhibited in literature in 2009 [19], although this was very small at 2x2x0.3 cm and so had minimised self-absorption. More complex structures, including photonic bandpass filters to increase the trapping efficiency, cylindrical geometries, bi-layer structures and rare-earth materials, have not been reported in complete LSC devices with measured power conversion efficiencies.

A pick of some of the best LSC devices through their short history, with their configurations and components, is exhibited in Table VI. As can be seen in Table VI the best devices from the 1980's were of a larger size compared to those of the 2000's, for which the latter must owe some of their improved efficiency for. Furthermore the two best devices use III-V semiconductor solar cells which, based on the analysis in section 2.5, undoubtedly improve efficiency over c:Si cells. The modern devices really therefore stand as interesting demonstrations, but not as significant advancements. As the authors of M. Debije *et. al.* (2012)[6] state; the key issues to overcome are still inefficiencies in the fluorophore and the lack of intense collaborative effort between the disparate groups working on the technology across the world. This is in contrast to the many photovoltaic technologies which have received far greater attention and concerted effort.

Fluorophore	L x L x W (cm)	G	Solar Cell (# sides)	η_{LSC} (%)	Year	Reference
DCM	120 x 100 x 0.4	68.18	c:Si (4)	1.3	1981	[40]
Coumarin, Rhodamine	140 x 140 x 3	11.67	c:Si (4)	3.2	1984	[12]
CdSe/CdS QDs	140 x 140 x 3	11.67	GaAs (4)	4.5	1984	[12]
CRS040, PR	5 x 5 x 0.5	2.5	GaAs (4)	7.1	2008	[29]
BA241,BA856	2 LSCs at 2 x 2 x 0.3	1.67	GaInP (4)	6.7	2009	[25]
Perylene perinone, PR	2 LSCs at 5 x 5 x 0.5	2.5	c:Si (2)	4.2	2012	[76]

Table VI: A pick of the best LSC devices through the technology's history is shown here. The last two entries are two layer tandem LSC devices and the last entry has two mirrored edges and two edges with c:Si cells connected.

Calculations to determine the cost of LSC devices to explore the economic value of the technology can be found in several places with different approaches [30, 76]. In the most recent work Bende *et. al.* (2008) use a ray-tracing model to optimise the relative cost and relative power density between LSC and standard PV devices. Optimisation is also performed on fluorophore concentration of the organic dye, Yellow CRS040 but PR is used extensively in the models. For cost calculations the model uses the polymer plate cost per unit area as a ratio to the conventional PV cost per unit area as a key parameter. They show that when this quantity is 1/15 the LSC would cost 35% and would generate 21% of the power of conventional PV. By the time this ratio is 1/5 the LSC costs as much as the conventional PV but only generates 22% of the power, at which point you would just use conventional PV.

2.8 References

[1] G. Smestad, H. Ries, R. Winston and E. Yablonovitch, The Thermodynamic Limits of Light Concentrators, *Solar Energy Mater.* **21**, 99 – 111 (1990)

[2] R. Winston, J. C. Minano and P. Benitez, Non-imaging Optics, *Elsevier Academic Press*, Chap. 1, 2 - 6 (2005)

[3] A. Goetzberger and V. Wittwer, Fluorescent Planar Collector-Concentrators: A Review, *Solar Cells* **4**, 3 – 23 (1981)

[4] J. S. Batchelder, A. H. Zewail, and T. Cole, Luminescent Solar Concentrators 1: Theory of Operation and Techniques for Performance Evaluation, *Applied Optics* **18**, 18, 3090 - 3110 (1979)

[5] P. P. C. Verbunt, C. Sánchez-Somolinos, D. J. Broer and M. G. Debije, Anisotropic light emissions in luminescent solar concentrators-isotropic systems, *Opt. Express* **21**, S3, A485-A493 (2013)

[6] M. G. Debije and P. P. C. Verbunt, Thirty Years of Luminescent Solar Concentrator Research: Solar Energy for the Built Environment, *Adv. Energy Mater.* **2**, 12 – 35 (2012)

[7] A. A. Earp, G. B. Smith, P. D. Swift and J. Franklin, Maximising the Light Output of a Luminescent Solar Concentrator, *Solar Energy* **76**, 655 667 (2004)

[8] R. Reisfeld, New Developments in Luminescence for Solar Energy Utilization, *Opt. Mater*. **32** 850-856 (2010)

[9] Freidman, P. S. and Parent, C. R. Luminescent Solar Concentrator Development - Final Subcontract Report, *Solar Energy Research Institute,* U.S. DOE contract No. **DE-AC02-83CH10093** (1987)

[10] M. A. El-Shahawy and A. F. Mansour, Optical Properties of Some Luminescent Solar Concentrators, *J. Mater. Sci. Mater. Elec.*, **7**, 171 – 174 (1996)

[11] J. Mugnier, Y. Dordet, J. Pouget and B. Valeur, A Photometric Approach of Fluorescent Solar Concentrators. Role of Diffuse Reflectors and Spectral Sensitivity of Solar Cells, *Revue Phys. Appl.* **22**, 89-100 (1987)

[12] L. R. Wilson, Thesis on Luminescent Solar Concentrators: A Study of Optical Properties, Re-absorption and Device Optimisation, Bryce Richards' group in Edinburgh (2010)

[13] M. N. Polyanskiy, RefractiveIndex.INFO (2013)
http://refractiveindex.info/legacy/?wavelength=0.55

[14] R. Sóti, É. Farkas, M. Hilbert, Zs. Farkas, I. Ketskeméty, Photon transport in luminescent solar concentrators, *J. Lumin.* **68**, 105 - 114 (1996)

[15] K. R. McIntosh, N. Yamada and B. S. Richards, Theoretical Comparison of Cylindrical and Square-Planar Luminescent Solar Concentrators, *App. Phys. B* **88**, 285-290 (2007)

[16] O. Y. Edelenbosch, M. Fisher, L. Patrignani, W. G. J. H. M. van Sark and A. J. Chatten, Luminescent Solar Concentrators with Fiber Geometry, *Optics Express* **21,** S3, 503 - 514 (2013)

[17] R. Bose, D. J. Farrell, A. J. Chatten, M. Pravettoni, A. Büchtemann and K. W. J. Barnham, Novel Configurations of Luminescent Solar Concentrators, *Proc. 22nd European Photovoltaic Solar Energy Conference*, pp. 210-214, (2007)

[18] Uwe Rau, Florian Einsele and Gerda C. Glaeser, Efficiency Limits of Photovoltaic Fluorescent Concentrators, *Appl. Phys. Lett.* **87**, 171101 (2005)

[19] J. C. Goldschmidt, M. Peters, A. Bösch, H. Helmers, F. Dimroth, S. W. Glunz and G. Willeke, Increasing the Efficiency of Fluorescent Concentrator Systems, *Sol. En. Mater. Sol. Cells* **93**, 176 - 182 (2009)

[20] M. G. Debije, R. H. L. van Der Blom, D. J. Broer and C. W. M. Bastiaansen, Using selectively reflecting organic mirrors to improve light output from a luminescent solar concentrator, in *Proc. World Renewable Energy Congress IX* (2006)

[21] M. G. Debije, M. P. Van, P. P. Verbunt, M. J. Kastelijn, R. H. L. van Der Blom, D. J. Broer and C. W. M. Bastiaansen, Effect on the output of a luminescent solar concentrator on application of organic wavelength-selective mirrors, *Appl. Opt.* **49**, 4, 745-751 (2010)

[22] B. C. Rowan, L. R. Wilson and B. S. Richards, Advanced Material Concepts for Luminescent Solar Concentrators, *IEEE Journal of Selected Topics in Quantum Electronics*. **14**, 5 (2008)

[23] B. A. Swartz, T. Cole and A. H. Zewail, Photon Trapping and Energy Transfer in Multiple-Dye Plastic Matrices: an Efficient Solar-Energy Concentrator, *Opt. Lett.* **1**, 2, 73 - 75 (1977)

[24] S. Chandra, J. Doran, S. McCormack, M. Kennedy and A. Chatten, Enhanced Quantum Dot Emission for Luminescent Solar Concentrators using Plasmonic Interaction, *Sol. Energy Mater. & Sol. Cells* **98**, 385 - 390 (2012)

[25] S. Tsoi, Dirk J. Boer, C. W. M. Bastiaansen and M. G. Debije, Using Lenses to Improve the Output of a Patterned Luminescent Solar Concentrator, *Adv. Energy Mater.* (2012), doi: 10.1002/aenm.201200395

[26] C. L. Mulder, P. D. Reusswig, A. M. Velázquez, H. Kim, C. Rotschild and M. A. Baldo, Dye Alignment in Luminescent Solar Concentrators: I. Vertical Alignment for Improved Waveguide Coupling, *Optics Express* **18**, S1 (2010)

[27] Y. Zhang, K. Aslan, M. Previte and C. Geddes, Metal-enhanced Fluorescence: Surface Plasmons Can Radiate a Fluorophore's Structured Emission, *App. Phys. Lett.* **90**, 053107 (2007)

[28] S. Wang, D.-A. Borca-Tasciuc and D. Kaminski, Spectral Coupling of Fluorescence Solar Concentrators to Plasmonic Solar Cells, *J. App. Phys.* **109**, 7, 074910 (2011)

[29] L. H. Slooff, E. E. Bende, A. R. Burgers, T. Budel, M. Pravettoni, R. P. Kenny, E. D. Dunlop and A. Büchtemann, A Luminescent Solar Concentrator with 7.1% Power Conversion Efficiency, *Phys. Stat. Sol. (RRL)* **2**, 257-259 (2008)

[30] M. J. Currie, J. K. Mapel, T. D. Heidel, S. Goffri and M. A. Baldo, High Efficiency Organic Solar Concentrators for Photovoltaics, *Science* **321**, 226 - 228 (2008)

[31] S. T. Bailey, G. E. Lokey, M. S. Hanes, J. D. M. Shearer, J. B. McLafferty, G. T. Beaumont, T. T. Baseler, J. M. Layhue, D. R. Broussard, Y. Zhang, J. B. Wittmershaus, Optimised excitation energy transfer in a three-dye luminescent solar concentrator, *Sol. En. Mater. Sol. Cells* **91**, 67 -75 (2007)

[32] P. Chiu, C. Huang, C. Yang, T. Meen and Y. Wang, Red polymer light-emitting devices based on dye-dispersed poly(9,9-dioctylfluorene-alt-benzothiadiazole), *Micro. Relia.* **50**, 5, 692-695 (2010)

[33] Y. Hasegawa, Y. Wada and S. Yanagida, Strategies for the design of luminescent lanthanide (III) complexes and their photonic applications, *J. Photochem. Photobiol. C: Photochem. Rev.* **5**, 3, 183-202 (2004)

[34] J. Gordon, J. Ballato, J. Jin and D. W. Smith Jr., Spectroscopic Properties as a Function of Fluorine Content in Eu^{3+}:PMMA, *J. Polym. Sci. B: Polym. Phys.* **44**, 11, 1592 - 1596 (2006)

[35] S. J. Gallagher, P. C. Eames and B. Norton, Quantum dot solar concentrator behaviour, predicted using a ray tracing approach, *Int. J. Ambient Energy*, **25**, 47 (2004)

[36] P. Prentice, Influence of molecular weight on the fracture of poly(methyl methacrylate) (PMMA), *Polymer* **24**, 3, 344 - 350 (1983)

[37] R. Reisfeld, Fluorescent dyes in sol-gel glasses, *J. Fluor.* **12**, 3, 317 - 325 (2002)

[38] J. C. Goldschmidt, M. Peters, L. Prönneke, L. Steidl, R. Zentel, B. Bläsi, A. Gombert, S. Glunz, G. Willeke and U. Rau, Theoretical and Experimental Analysis of Photonic Structures for Fluorescent Concentrators with Increased Efficiencies, *Phys. Stat. Sol. (a)* **205**, 12, 2811 - 2821 (2008)

[39] H. Hernandez-Noyola, D. H. Potterveld, R. J. Holt and S. B. Darling, Optimising Luminescent Solar Concentrator Design, *Energy Environ. Sci.* **5**, 5798 – 5802 (2012)

[40] J. S. Batchelder, A. H. Zewail, and T. Cole, Luminescent Solar Concentrators 2: Experimental and Theoretical Analysis of their Possible Efficiencies, *Applied Optics* **20**, 21, 3733 - 3754 (1981)

[41] L. H. Sloof, T. Budel, A. R. Burgers, N. J. Bakker, R. Danz, T. Meyer and A. Meyer, The Luminescent Concentrator: Stability Issues, in *Proc. 22nd European Photovoltaic Solar Energy Conference* (2007)

[42] L. R. Wilson and B. S. Richards, High-efficiency Dyes for Luminescent Solar Concentrators, in *Proc. 23rd European Photovoltaic Solar Energy Conference* (2008)

[43] K. W. J. Barnham, J. L. Marques, J. Hassard and P. OBrien, Quantum-dot Concentrator and Thermodynamic Model for the Global Redshift, *Appl. Phys. Lett.* **76**, 9, 1197 (2000)

[44] G. V. Shcherbatyuk, R. H. Inman, C. Wang, R. Winston and S. Ghosh, Viability of Using Near Infrared PbS Quantum Dots as Active Materials in Luminescent Solar Concentrators, *Appl. Phys. Lett.* **96**, 19, 191901 (2010)

[45] D. V. Talapin, J. H. Nelson, E. V. Shevchenko, S. Aloni, B. Sadtler and A. P. Alivisatos, Seeded Growth of Highly Luminescent CdSe/CdS Nanoheterostructures with Rod and Tetrapod Morphologies, *Nano Letters* **7**, 10, 2951-2959 (2007)

[46] B. C. Rowan, L. R. Wilson and B. S. Richards, Visible and Near-infrared Emitting Lanthanide Complexes for Luminescent Solar Concentrators, in *Proc. 24th European Photovoltaic Solar Energy Conference* (2009)

[47] L. R. Wilson, B. C. Rowan, N. Robertson, O. Moudam, A. C. Jones and B. S. Richards, Characterisation and Reduction of Reabsorption Losses in Luminescent Solar Concentrators, *Applied Optics* **49**, 1651 (2010)

[48] R. Reisfeld, Industrial Applications of Rare Earths in Fiber Optics, Luminescent Solar Concentrators and Lasers, *Inorganica Chimica Acta* **95**, 69-74 (1984)

[49] http://www.life.illinois.edu/govindjee/biochem494/Abs.html

[50] A. D. Stein and M. D. Fayer, Nanosecond timescale optical inhomogeneous broadening of dye molecules in liquids at and near room temperature, *Chem. Phys. Lett.* **176**, 2, 159 - 166 (1991)

[51] Y. Kawamura, J. Brooks, J. J. Brown, H. Sasabe and C. Adachi, Intermolecular Interaction and a Concentration-Quenching Mechanism of Phosphorescent Ir(III) Complexes in a Solid Film, *Phys. Rev. Lett.* **96**, 017404 (2006)

[52] Rabih O. Al-Kaysi *et. al.*, The Photophysical Properties of Chromophores at High (100mM and above) Concentrations in Polymers and as Neat Solids, *Phys. Chem. Chem. Phys.* **8**, 3453-3459, (2006)

[53] S. A. Bagnich and V. N. Knyukshto, Quenching of Fluorescence of Conjugated Poly(*p*-Pheylene) Polymers by Benzil and Dimethylaminobenzil Molecules, *J. Appl. Spec.* **73**, 6 (2006)

[54] P. L. Burn, S. Lo and I. D. W. Samuel, The Development of Light Emitting Dendrimers for Displays, *Adv. Mater.* **19**, 1675 - 1688 (2007)

[55] M. Shimizu and T. Hiyama, Organic Fluorophores Exhibiting Highly Efficient Photoluminescence in the Solid State, *Chem. Asian J.* **5**, 1516 - 1531 (2010)

[56] J. R. Lakowicz, Principles of Fluorescence Spectroscopy, 3rd ed. (*Springer*, Singapore, 2006), Chap. 6, pp. 205–213.

[57] C. F. Madigan and V. Bulović, Solid State Solvation in Amorphous Organic Thin Films, *Phys. Rev. Lett.* **91**, 247403 (2003)

[58] V. Bulović, R. Deshpande, M. E. Thompson and S. R. Forrest, Tuning the Colour Emission of Thin Film Molecular OLEDs by the Solid State Solvation Effect, *Chem. Phys. Lett.* **308**, 317 - 322 (1999)

[59] A. K. Sheridan, A. R. Buckley, a. M. Fox, A. Bacher, D. D. C. Bradley and I. D. W. Samuel, Efficient energy transfer in organic thin films - implications for organic lasers, J. Appl. Phys. **92**, 6367 (2003)

[60] W. G. J. H. M. van Sark *et. al.*, Luminescent Solar Concentrators - A Review of Recent Results, *Opt. Exp.* **16**, 26, 21773 (2008)

[61] C. M. Ramsdale and N. C. Greenham, The optical constants of emitter and electrode materials in polymer light-emitting diodes, *J. Phys. D: Appl. Phys.* **36**, L29 - L34 (2003)

[62] A. J. Cadby and D. G. Lidzey *et. al.*, Imaging the Fluorescence Decay Lifetime of a Conjugated Polymer Blend By Using a Scanning Near-Field Optical Microscope, *Adv. Mater.* **19**, 107 - 111 (2007)

[63] M. Junghänel, M. Schädel, L. Stolze and S. Peters, Black Multicrystalline Solar Modules Using Novel Multilayer Antireflection Stacks, *Proc. 25th European Photovoltaic Solar Energy Conference*, pp. 2637-2641 (2010)

[64] Solar Glass & Mirrors, *Green Rhino Energy* (2013) http://www.greenrhinoenergy.com/solar/technologies/solar_glass.php

[65] G. Colantuono, A. Buckley and R. Erdélyi, Ray-Optics Modelling of Rectangular and Cylindrical 2-Layer Solar Concentrators, *J. Light. Tech.* **31**, 7, 1033-1044 (2013)

[66] Paradigm Optics Inc., 2000-2012, http://www.paradigmoptics.com/pof/poffaqs.html

[67] V. Fattori, M. Melucci, L. Ferrante, M. Zambianchi, I. Manet, W. Oberhauser, G. Giambastiani, M. Frediani, G. Giachi and N. Camaioni, Poly(lactic acid) as a transparent matrix for luminescent solar concentrators: a renewable material for a renewable energy technology, *Energy Environ. Sci.* **4**, 2849 - 2853 (2011)

[68] Best Research PCE Values, *NREL* (2013), http://www.nrel.gov/ncpv/

[69] M. A. Green, K. Emery, Y. Hishikawa, W. Warta and E. D. Dunlop, Solar Cell Efficiency Tables (Version 38), *Prog. Photovolt: Res. Appl.* **19**, 565-572 (2011)

[70] M. A. Green, K. Emery, Y. Hishikawa, W. Warta and E. D. Dunlop, Solar Cell Efficiency Tables (Version 39), *Prog. Photovolt: Res. Appl.* **20**, 12-20 (2012)

[71] M. A. Green, K. Emery, Y. Hishikawa, W. Warta and E. D. Dunlop, Solar Cell Efficiency Tables (Version 44), *Prog. Photovolt: Res. Appl.* **22**, 701-710 (2014)

[72] C. Algora, E. Ortiz, I. Rey-Stolle, V. Díaz, R. Peña, V. M. Andreev, V. P. Khvostikov and V. D. Rumyantsev, A GaAs Solar Cell with an Efficiency of 26.2% at 1000Suns and 25% at 2000 Suns, *IEEE Transactions on Electron Devices* **48**, 5, 840-844 (2001)

[73] R. McConnell and V. Fthenakis, Third Generation Photovoltaics (*Intech*, 2012), Chap. 7, pp. 167-168

[74] G. Bunea, K. Wilson, Y. Meydbray, M. Campbell and D. D. Ceuster, Low Light Performance of Mono-Crystalline Silicon Solar Cells, in *Proc. 4th World Conference on Photovoltaic Energy Conversion*, pp. 1312-1314 (2006)

[75] J. F. Randall and J. Jacot, The Performance and Modelling of 8 Photovoltaic Materials Under Variable Light Intensity and Spectra, in *Proc. World Renewable Energy Congress* (2002)

[75] L. Desmet, A. J. M. Ras, D. K. G. de Boer and M. G. Debije, Monocrystalline silicon photovoltaic luminescent solar concentrator with 4.2% power conversion efficiency, *Opt. Lett.* **37**, 15, 3087 - 3089 (2012)

[76] E. E. Bende, L. H. Slooff, A. R. Burgers, W. G. J. H. M. van Sark and M. Kennedy, Cost & Efficiency Optimisation of the Fluorescent Solar Concentrator, in *Proc. 23rd European Photovoltaic Solar Energy Conference* (2008)

Chapter 3

Experimental Methods

In this chapter experimental methods and instrumentation are discussed for the experimental chapters of the rest of this thesis. Some methods are not included here, such as the Gauge R&R study design in chapter 4 or the screening design of experiment in chapter 6. Instead they are discussed in the relevant chapter where they aid explanation of the associated work and since such methods are not used in other chapters it made sense to contain them as described. Experimental methods here include absolute measurement of quantum yield in 3.1, determining relative permittivity by impedance spectroscopy in 3.2, absorption and fluorescence spectroscopy in 3.3, spray coating deposition using the Prism Ultra-Coat 300 in 3.4 and measurement of fluorescent lifetime in 3.5.

3.1 Absolute Measurement of Photoluminescence Quantum Yield

Absolute measurement of the photoluminescence quantum yield, η_{QY}, of a luminescent material is typically performed using an integration sphere (a.k.a. Ulbricht sphere) that is optically connected by a fibre-optic to a photospectrometer [1-4]. The measurement methodology applied here has been closely modelled on that of Johnson *et. al.* in 2007 [1]. There are several other approaches outlined by various groups including de Mello *et. al.* [3], whose method is similar to that applied here, and Greenham *et. al.* [4].

An illustration of the measurement process is shown in Fig 3.1.1. The laser excitation source light is guided into the integration sphere for the experiment. The walls of the sphere are made from a Lambertian reflector, in this case barium sulphate, which obey the Lambertian cosine law of reflectance. Employing such materials enables light from the laser or sample to be scattered diffusely around the sphere and thus directional information is lost.

The first measurement, a) in Fig. 3.1.1, is taken with just the excitation light whose intensity in the sphere, $I_{L,0}$, is recorded. Then, in b), small sample of the material, in solution or in the solid state, is loaded into the sphere, excited using the laser and the resultant fluorescence emission and remaining laser light are recorded. The η_{QY} is then given by the total number of counts emitted by the fluorophore, I_S, divided by the total counts absorbed, $I_{abs} = I_{L,0} - I_{L,1}$ as in Eq. (3.1.1).

$$\eta_{QY} = \frac{I_S}{I_{L,0} - I_{L,1}} \qquad (3.1.1)$$

Where $I_{L,0}$ is total number of incident laser counts and $I_{L,1}$ is the number of laser counts after sample absorption.

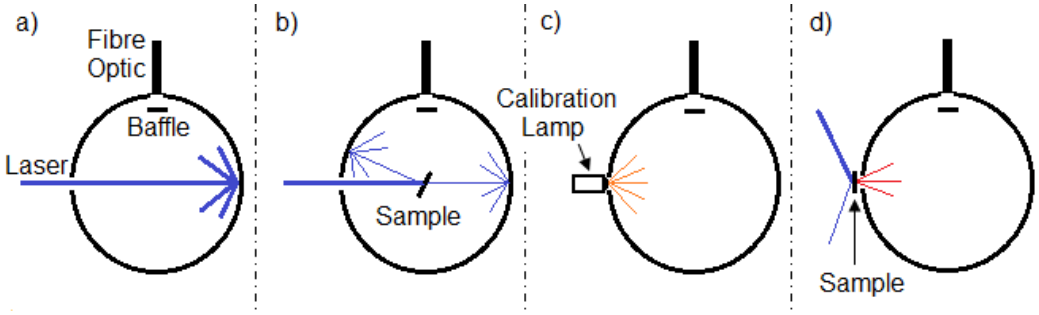

Figure 3.1.1: A schematic of the measurement process. In a) the laser spectrum is measured alone, in b) the combined sample emission and remaining laser light spectrum is measured, in c) a calibration for the measurement run is performed and in d) the sample spectrum is taken again from the excitation aperture for the self-absorption correction.

Due to various sources of uncertainty in the measurement there is a typically large relative random error of ±2% and potentially some systematic uncertainty. These sources of error include; determining the sensitivity of the instruments using a calibration light source, determining and applying a correction for self-absorption, sample-to-sample variance and variance in the laser intensity.

Determining the non-self-absorption corrected η_{QY} requires three measurements; a laser spectrum, $L(\lambda)$ as in Fig. 3.1.1 a), a sample spectrum with remaining laser excitation light, $S(\lambda)$ as in Fig. 3.1.1 b), and a calibration spectrum, $C(\lambda)$ as in Fig. 3.1.1 c). Note that the sample is angled such that reflected excitation light does not escape via the excitation aperture. In this study the calibration source is an Ocean Optics LS-1-CAL, radiometrically characterised, tungsten halogen light source with radiometric spectrum $R(\lambda)$ [$\mu Wcm^{-2}nm^{-1}$]. The sensitivity function, $\phi_{sense}(\lambda)$, which describes the resultant wavelength dependence of the whole measurement system, is found from Eq. (3.1.2);

$$\phi_{sense}(\lambda) = \frac{C(\lambda)}{R(\lambda)} \qquad (3.1.2)$$

The sensitivity function has arbitrary units and for any given apparatus will be different to some degree depending on the integration sphere, fibre optic losses, spectrometer optics and photo-detection system, a CCD in this case. It is important to determine the sensitivity for each measurement run as slight changes in the system, such as the fibre optic position at the detection aperture, will result in changes in the sensitivity function.

Note that the incident laser intensity, $I_{L,0}$, is determined from the laser spectrum, $L(\lambda)$, in isolation from the sample measurement, $S(\lambda)$. This means that the absolute value of $I_{L,0}$ at the time of sample measurement cannot be known. Instead many measurements of $L(\lambda)$ are taken either side of each $S(\lambda)$ measurement and an average $I_{L,0}$ is therefore found from that set of spectra. This introduces uncertainty into Eq. (3.1.1) as discussed in detail during Chapter 4.

Next a self-absorption correction is found for each concentration of each material Fig. 3.1.1 d). This is defined by the ratio of the normalised spectra of the sample outside the sphere at the excitation aperture, $O_{norm}(\lambda)$, and that inside the sphere, $S_{norm}(\lambda)$. The normalisation must be at a wavelength, preferably on a spectral feature, at which little or no self-absorption is possible. This ensures the normalisation is relatively of the same scale in both cases. The self-absorption correction, $\phi_{self}(\lambda)$, is then given by Eq. (3.1.3);

$$\phi_{self}(\lambda) = \frac{O_{norm}(\lambda)}{S_{norm}(\lambda)} \qquad (3.1.3)$$

The result of the integral of Eq. (3.1.3) over all wavelengths will be greater than or equal to unity, with increased divergence from unity resulting from increased self-absorption. Note for measurement of $O_{norm}(\lambda)$, outside the sphere, a higher laser power was necessary to achieve a measureable signal and so a grazing incidence was adopted directing the laser light at an angle of 70° to the aperture normal. This allows a higher laser power of up to 30mW without potentially damaging saturation of the CCD detector. All thusly measured samples were found to be stable at this power with no signs of photo-bleaching effects.

Applying the sensitivity function to both $S(\lambda)$ and $L(\lambda)$ results in corrected functions $S'(\lambda)$ and $L'(\lambda)$ respectively. Then the integrated laser intensity in each of $S'(\lambda)$ and $L'(\lambda)$ is found, giving $I_{L,1}$ and $I_{L,0}$ respectively. The self absorption correction is then applied to $S'(\lambda)$ by first subtracting the excitation, and then multiplying by $\phi_{self}(\lambda)$. The integral of this product gives the total number of counts emitted, I_S, as in Eq. (3.1.4) below:

$$I_S = \int_{\lambda_{min}}^{\lambda_{max}} S'(\lambda) \times \phi_{self}(\lambda) d\lambda \qquad (3.1.4)$$

In practice ϕ_{self} can be integrated separately and then multiplied by η_{QY}, from Eq. (3.1.1), to apply the correction.

3.2 Determining Relative Permittivity with Impedance Spectroscopy

To measure the relative permittivity of composite thin films the method used here is to take an impedance spectrum of the material sandwiched between two electrodes. Samples are prepared by spin-coating the composite thin film onto pre-patterned ITO substrates, as shown in Figure 3.2.1 a), and then depositing 100 nm of silver on top by thermal evaporation. As the diagram shows the substrate design allows for six measurements per sample which is statistically useful. An impedance analyser, in this case the Solartron 1260 Gain Phase Analyser, is then connected to the electrodes for measurement.

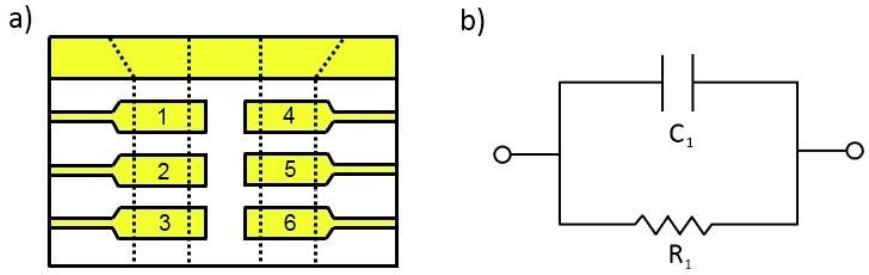

Figure 3.2.1: In a) is a pre-patterned ITO-on-soda lime glass substrate schematic with the ITO shown in yellow. The dashed lines indicate where the shadow mask from the thermal evaporation allows Ag deposition. Connection is made via the edge contact of one of the six device elements, shown by numbers, and the top ITO strip. In b) the equivalent circuit model used is shown consisting of a capacitor, C_1, and a resistor, R_1, in parallel.

Impedance analysis [5] offers a means to probe the internal electrical characteristics of an electrolyte, be that solid or liquid. In this case the solid being tested is a dielectric material and hence conductivity is negligible, which in turn means interfacial interactions will be minimised. Such interactions, amongst others, would introduce interfacial effects into the results and it takes careful interpretation to determine the physicality of the data. The most common approach used is indirect because the frequency response of the electrode-material system under test is modelled by what is known as an Equivalent Circuit (EC). Such ECs vary in complexity and are usually a combination of resistors, capacitors and inductors chosen to accurately represent the system. In the case of the electrode-dielectric material systems of this thesis the most basic parallel RC circuit is chosen for the EC, as depicted in Fig. 3.2.1 b). C_1 is the geometric capacitance and R_1 the bulk resistance, which will be very large for a dielectric material.

For this analysis it is only important to see how the capacitance varies with frequency, as shown in the log-log plot of Fig. 3.2.2. The impedance analyser measures the complex impedance, both real and imaginary components, which are the resistance, $R(\omega)$, and reactance, $X(\omega)$, respectively. From these components of impedance the capacitance as a function of frequency for a parallel RC circuit, $C_P(\omega)$ can be found, as in Eq. (3.2.1);

$$C_P(\omega) = \omega B(\omega) \qquad (3.2.1)$$

$$Where\ susceptance, B(\omega) = \frac{R(\omega)}{R^2(\omega) + X^2(\omega)} \qquad (3.2.2)$$

The capacitance should be constant for all frequencies for a perfect capacitor with no inhomogeneities across the dielectric medium. What is observed is that capacitance varies strongly at low frequency but forms a rough plateau between f = 100 kHz and f = 1 MHz before decreasing at the highest frequencies. At low frequencies any slow oscillating components of capacitance become observable in the frequency response. The nature of these is likely to be inhomogeneous, distributed elements in the plane perpendicular to the electrode surfaces, which are distinct from the bulk capacitance of the device [5]. Such elements cannot be accounted for by the basic EC chosen as the model. At high frequencies, beyond f = 1 MHz, the capacitance drops markedly which is likely due to extrinsic inductance effects from the measurement system and not the test material itself [6].

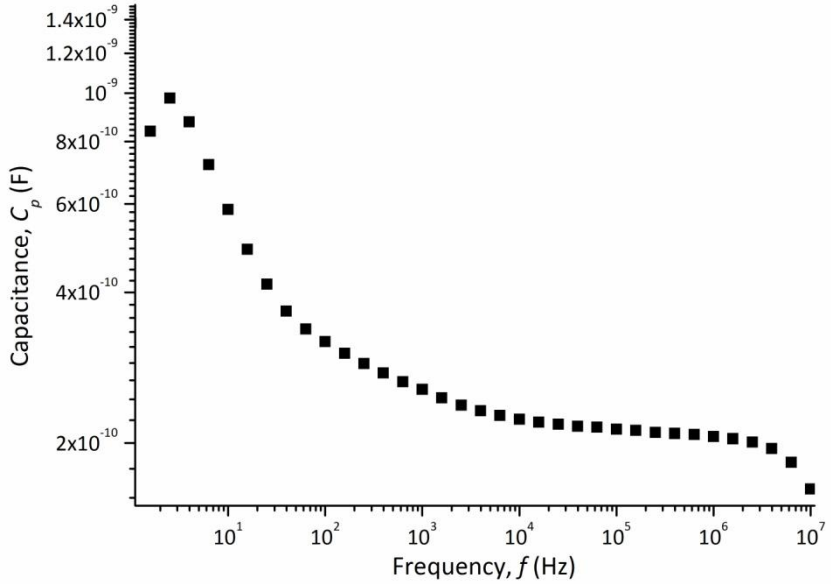

Figure 3.2.2: Log_{10} of capacitance plotted against log_{10} of the AC frequency for PMMA between ITO and Ag electrodes. Geometric capacitance, C_1, is determined from the plateau region between $f = 10^5$ Hz and 10^6 Hz from which the relative permittivity can be calculated.

The relative permittivity is then found using the standard parallel plate capacitor equation given in Eq. 3.2.3:

$$C = \frac{\varepsilon_r \varepsilon_0 A}{d} \qquad (3.2.3)$$

Where $C = C_1$ is found from the plateau region of Fig. 3.2.2, $\varepsilon_0 = 8.854 \times 10^{-12}$ Fm^{-1} is the vacuum permittivity, $A = (4.50 \pm 0.05) \times 10^{-6}$ m^2 is the device area depicted in Fig. 3.2.1 a) and $d = 530 \pm 30$nm is the distance between the electrodes for the sample exhibited here. These values with

C_1 = (2.13 ± 0.06) x 10^{-10} F for 10 kHz < f < 1 MHz gives a relative permittivity of ε_r = 2.83 ± 0.06, which is in line with known values for PMMA [7]. On average across all six device elements for pure PMMA we find ε_r = 2.68 . This methodology is used in Chapter 5 when exploring the effects of solvation on LSC device efficiency.

3.3 Absorption and Fluorescence Spectroscopy

Optical spectroscopy is used extensively throughout this thesis forming a core component of the analysis of the fluorescent materials studied. The vast majority of spectral data were taken using the Fluoromax-4 from Horiba, a schematic of which is shown in Fig. 3.3.1.

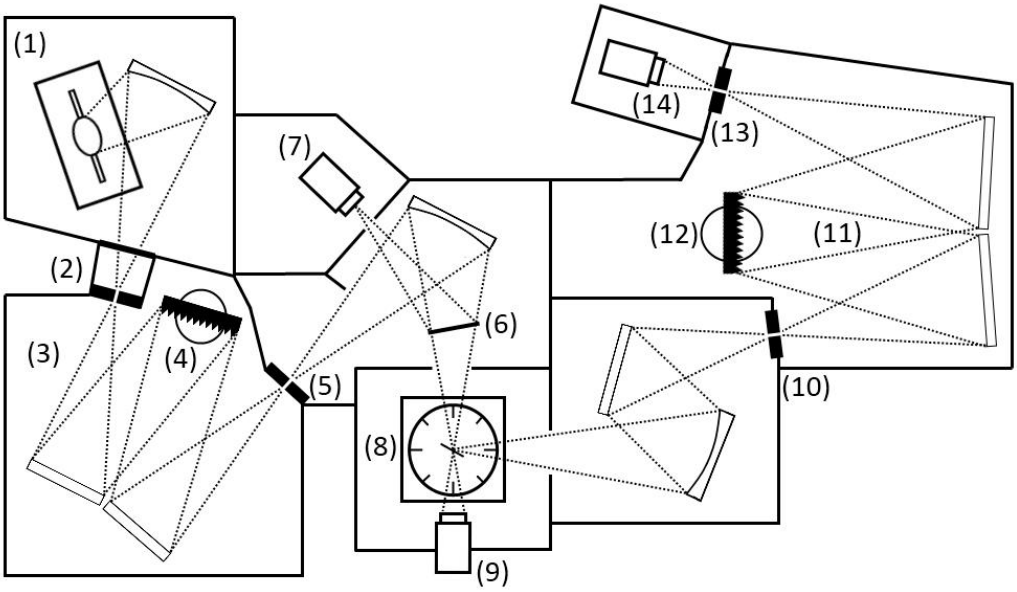

Figure 3.3.1: A schematic representation of the optical layout for the Fluoromax-4 with the following labelled components; (1) is the xenon arc lamp excitation source and housing, (2) is a quartz window for heat dissipation followed by an adjustable slit, (3) is the excitation monochromator assembly, (4) is the excitation monochromator diffraction grating, (5) is an adjustable slit, (6) is a beam splitter, (7) is the reference photodiode detector and current acquisition module, (8) is the adjustable angle sample stage and housing, (9) is the transmission photodiode detector, (10) is an adjustable slit, (11) is the emission monochromator assembly, (12) is the emission monochromator diffraction grating, (13) is an adjustable slit and (14) is the emission photomultiplier tube detector.

Samples are prepared such that the optical density lies between 0.25 and 0.5 with variance depending on the fluorophore being measured. For solutions this is achieved for dye concentrations of around C_{dye} = 0.05 g/l in 1 mm thick cuvettes. For solid samples, prepared by spin coating onto soda-lime glass substrates, this is achieved for film thicknesses of around 500 nm for dyes doped into polymer hosts at C_{dye} = 0.1 wt%. In some cases, such as for the triplet emitter ADS067RE, higher concentrations were necessary due to lower absorption coefficients (for transmission spectra) and/or low quantum yield (for emission spectra). Due to concentration quenching, particularly in the

solid state, increasing concentration may not improve the signal in emission spectra and so either thicker samples or adjustment of the monochromator slit widths (see Fig. 3.3.1) is the best approach. In general alteration of the doping concentration is avoided for the above reason and because self-solvation effects can result in emission spectrum shifts as a function of concentration for fluorophores whose dipole moment changes upon excitation.

Absorption spectroscopy utilises the transmission detector, (9) in Fig. 3.3.1, with the sample positioned normal to the path of the excitation source. Transmission spectra for both the blank substrate, $T_0(\lambda)$, and the sample, $T_1(\lambda)$, are taken so that subtraction of the substrate absorption contribution can be performed. These are first corrected by division by the reference spectrum, (7) in Fig. 4.3.1, to remove the xenon lamp spectrum from the measured transmission. The transmission and reference spectra are measured in μA and therefore division also normalises the units. Slit widths equivalent of a 1 nm bandpass (0.235 mm slit width) are used for the excitation monochromator ((3) in Fig. 3.3.1). The absorption spectrum of the test fluorophore, $S_{abs}(\lambda)$, is then found by Eq. (3.3.1):

$$S_{abs}(\lambda) = 1 - \frac{T_1(\lambda)}{T_0(\lambda)} \quad (3.3.1)$$

The units are intensity relative to the excitation source and $S_{abs}(\lambda)$ is generally normalised by its maximum value to avoid ambiguity. The act of using a blank substrate introduces a systematic error due to differences in reflectivity at the interfaces. Essentially there are two reflections for a blank substrate and one for an optically dense sample. Using the Fresnel equations given by Eqs. (2.2.2) and (2.2.3), with n_2 = 1.52 for a typical crown glass [8] (such as borosilicate glass), this gives an error on the absorption of 4.3% which needs to be corrected. Not doing so can result in negative absorption.

From the transmission data it is also possible to determine the absorption and extinction coefficients for a given fluorophore using the Beer-Lambert law as defined by Eq. (2.2.5). The transmission spectrum as a result purely of the absorption due to the fluorophore is given by the ratio $T_1(\lambda)/ T_0(\lambda)$ which is equivalent to the intensity ratio $I(\lambda)/I_0(\lambda)$ and hence the extinction coefficient can be shown to be;

$$\varepsilon(\lambda) = -\frac{\ln\left(\frac{T_1(\lambda)}{T_0(\lambda)}\right)}{C_{dye} < x >} \quad (3.3.2)$$

Where C_{dye} is the molar dye concentration and $<x>$ is the mean film thickness measured by profilometry.

Lastly the emission spectrum is measured by a PMT, (14) in Fig. 3.3.1, using 1 nm bandpass in most cases and 2 nm (0.471 slit width) for low signal samples. The sample is angled at 30° relative to the normal of the incident excitation light to maximise the signal passing into the emission monochromator, (11) in Fig. 3.3.1, and to minimise self-absorption effects on the spectrum. 45° is not used to avoid specular reflection of excitation light passing into the emission monochromator. Division by the reference spectrum allows any rogue excitation light in the monochromator to be corrected for but it is usually just negligible noise in the reference detector. It is important to note that absolute emission intensity cannot be determined from this measurement system.

3.4 Spray Coating

Spray coating deposition is performed using the Prism Ultra-Coat 300 spray coater made by Ultrasonic Systems, a photograph of which is shown in Fig. 3.4.1.

The Prism 300 is comprised of a sealed chamber filled with air that is cycled through a HPLC filter for solvent extraction. The spray head assembly is mounted on a x-y-z gantry assembly allowing movement in three dimensions. For spraying onto microscope slide substrates the x and z axes are fixed for each spray with motion in the y-axis aligned across the long axis of the substrate. The z position, or height, is varied for different samples as discussed in chapter 6 on spray coater parameter screening. The sample is placed upon a copper plate, which is itself upon a hot plate to allow variable substrate temperature and thus solvent evaporation rate. The copper plate is essential for distributing the heat but also to raise the substrate off the hotplate surface. It is cut to the exact dimensions of length and width as the substrate which has proven important to prevent 'underflow'. Underflow occurs when, because of the quantity of solution sprayed, excess solution is drawn underneath the substrate by capillary action. Apart from making a mess of the underside of the sample this effect also draws solution from the surface and therefore creates undesirable edge effects. The arrangement described does not therefore allow for two sided depositions.

The spray heads are comprised of injection syringes that are connected to a nitrogen gas manifold whose flow rate is controlled via needle valves and reported via dial gauges in units of mbar. Thus the injection pressure behind the deposition solution can be varied according to requirements. The injection system drives the solution through feed lines, into the spray head being used and onto an ultrasonic tip which atomises the jet of solution into a spray. Samples made using this system only required the use of a single spray head.

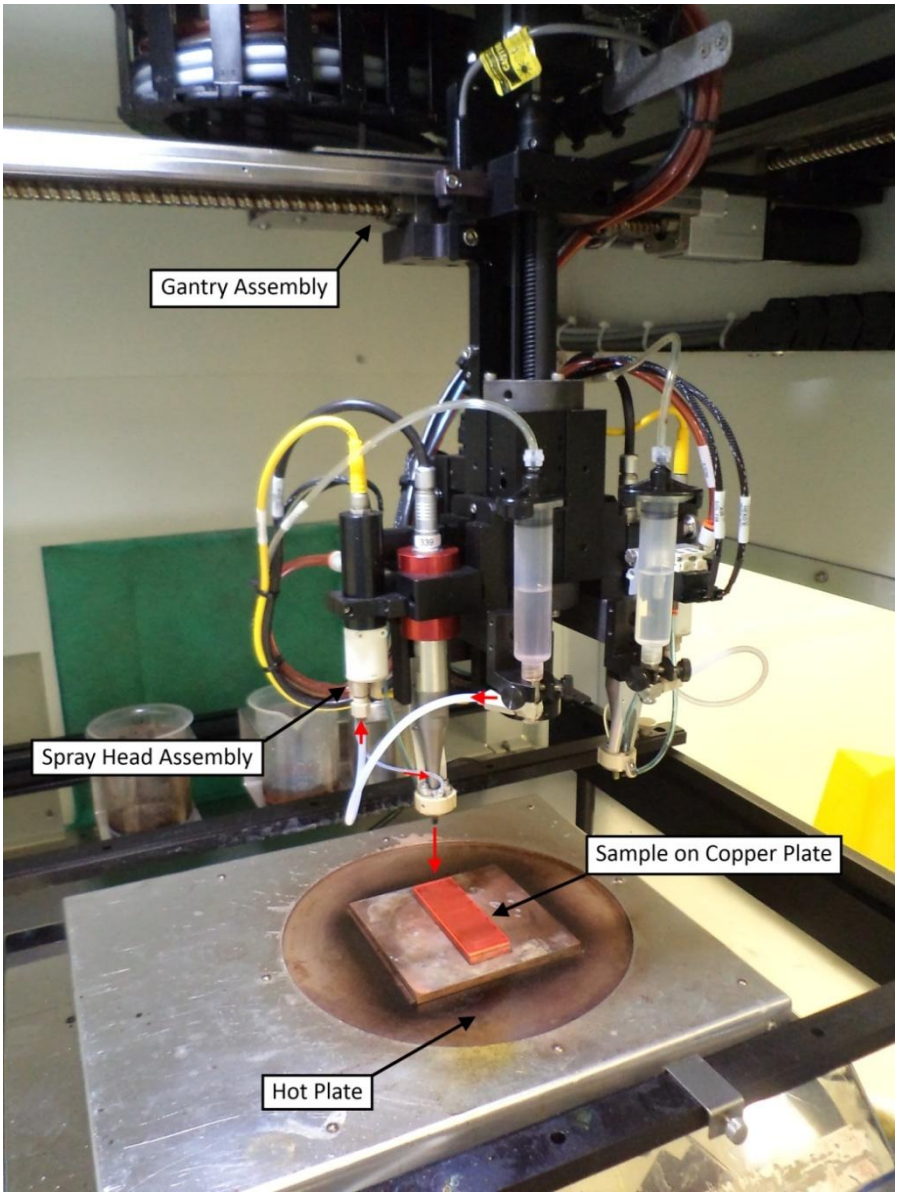

Figure 3.4.1: Annotated photograph of the Prism 300 spray coater showing the x-y-z gantry assembly, spray head assembly, hotplate and a finished sample on a copper plate. The upright syringes at centre contain only isopropanol here as no depositions are being performed. Syringe A, at the image's centre, is used here passing deposition material via the clear white feed line, through an electronically controlled valve and down to the ultrasonic tip of the spray head.

3.5 Time Correlated Single Photon Counting (TCSPC)

A useful optical property to measure for fluorescent materials is the fluorescence lifetime, τ, which is typically measured using Time Correlated Single Photon Counting (TCSPC) [9]. As seen in Eq. (2.4.1) this measured lifetime can be used in conjunction with fluorescence quantum yield measurements, described above in 3.1, to begin to understand the balance between radiative and non-radiative transitions. This lends these complimentary measurements towards appreciation and quantification

of loss mechanisms affecting the fluorescence quantum yield of the fluorophore. The lifetime is determined through the intensity decay law, given by Eq. (3.5.1).

$$I(t) = I_0 e^{-\frac{t}{\tau}} \qquad (3.5.1)$$

Where *I(t)* is intensity as a function of time, *t*, I_0 is the peak intensity and τ is the decay lifetime. By measuring the intensity as a function of time after excitation, using TCSPC, an exponential fit of the form of Eq. (3.5.1) can therefore allow τ to be determined from the exponent.

The TCSPC apparatus for this thesis utilises 400 nm pulsed laser light as an excitation source, a lens based monochromator, a photodiode detector and 40 nm bandpass filters between sample and detector to select the fluorophore emission wavelengths. The 400nm source is a 532nm Nd^{3+}:YVO_4 pumped Ti:Sapphire laser operating at 2mW of ML 800 nm light, which is subsequently frequency doubled to 400nm with an LBO crystal. This is the Verdi -V10/Mira 900 combination from Coherent with a Second Harmonic Generator from APE and provides a repetition rate of 76 MHz with a pulse width of 190 ps.

As with many systems, because of the high repetition rate of the pulsed laser, this set up operates in reverse mode with the emission pulse being used to start the electronic timer (the trigger pulse) and the excitation pulse being used to stop it (the stop pulse). Trigger and stop pulses are recorded by connection of the photodetector and Ti:Sapphire light source to a computer using an SPC card made by Becker & Hickl GmbH (SPC-830), which houses all of the timing and counting electronics. Through the SPC software experimental runs are designed and the resulting intensity decay curves displayed. The BNC wires connecting the photodiode and Mira 900 are matched in length as closely as possible and then the timing offset is tuned in the software to correctly align the arrival of the signals. The experimental apparatus is shown in Fig. 3.5.1.

From the schematic the process TCSPC measurement works as follows; the Verdi-V10 pumps the Mira900 producing 800 nm light, which is mode locked and tuned using real time spectroscopy, provided by the USB4000 from Ocean Optics, and a power meter. A flip mirror alters the beam path into the SHG for frequency doubling, once stable mode-locking is achieved, and then the 400nm light is intensity tuned using a variable reflective ND filter wheel. This excitation light then strikes the sample whose emission is collimated using lenses through a 40 nm bandpass filter and then on into the photodiode detector. Enclosures are used for the excitation/detection and SHG areas of the apparatus to reduce stray light.

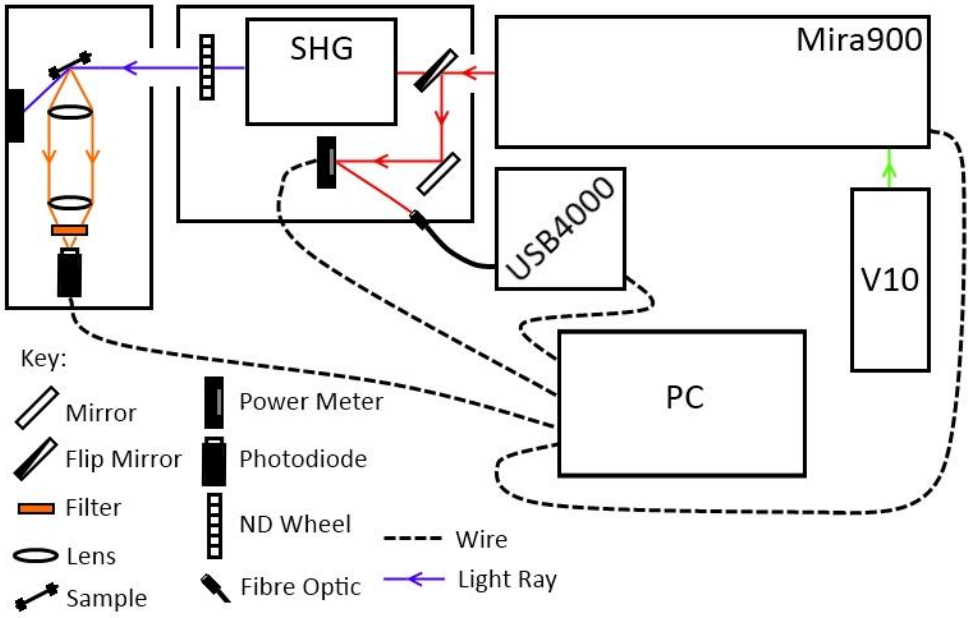

Figure 3.5.1: A schematic diagram of the TCSPC setup with key at bottom left.

The pulse width is important as it defines the minimum lifetime it is possible to measure. This is determined by sampling the laser light at the photodiode by replacing the sample with a diffuse reflector and removing the bandpass filter, giving the instrument response function (IRF). The IRF is shown in the intensity-time plot of Fig. 3.5.2.

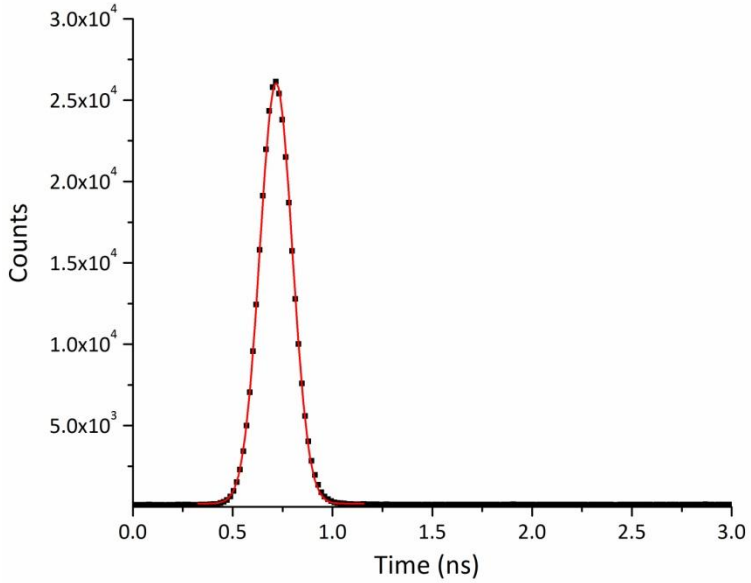

Figure 3.5.2: Instrument response function for this TCSPC set up showing the Gaussian fit (red line), which gives FWHM = 191 ps.

All samples for which lifetime was measured involved single fluorophores in solid host matrices whose emission is dominated by a single transition. This meant no multi-exponential decays were observed. The intensity decay curves are fitted using a LabVIEW based fitting routine which fits a

single exponential decay function to the data across an appropriate interval. The fitted function thus provides the lifetime.

3.6 Spin Coating

The fabrication of thin films for spectroscopic study is typically done by spin coating using a Laurell ws-400bz-6npp/lite spin coater. Such tools are not suited to large area thin film coverage but offer advantage in producing samples quickly and cheaply, relative to more sophisticated techniques such as spray coating. Samples produced by this method are typically used in various optical measurements such as quantum yield, fluorescence lifetime, emission spectra and absorption coefficients. A disadvantage of spin coaters is that the film edges tend to be thicker than the middle as surface tension draws material outwards during fabrication. Total solution concentration strongly affects the resultant thin film thickness, which must be optimised through profilometry (section 3.8) on trial samples to get the desired thickness for a given concentration.

To spin coat a thin film a polymer, which may be a light emitting polymer (chapter 2.4.2) or a optical host (chapter 2.4.3), is first dissolved in a suitable solvent in a sealed vial. If a optical host is used then the host solution is blended with a small molecular fluorophore in the same solvent, or one miscible with the other, to achieve the desired fluorophore concentration. Next a small glass substrate, 1.5 x 1 cm, is placed on the spin coater chuck over a source of vacuum. The substrate is fixed by the vacuum and a rubber o-ring is used to make a seal. Usually the spin coater is set running at the required rpm and then thin films are deposited from solution by a micro-pipette onto the spinning substrate. However, high concentrations of host polymer (>150 g/l) result in high viscosities that require some spreading time prior to starting the spin coater, otherwise full coverage is not achieved.

3.7 Profilometry

Profilometry is performed to measure thin film thickness and roughness throughout this thesis using a Veeco DekTak 150, which is a contact profilometer. The device uses a mechanically controlled stylus, operated by software, which is lowered onto the sample surface until it exerts between 0.03 and 50 mg of force; typically 30 mg is used. The sample is mounted on a xy stage which is tracked when performing a scan so that the sample surface moves under the tip of the stylus. Scan ranges of

up to 10 mm are possible. A camera is used for positioning the start of the scan and to observe the surface features of the sample.

To measure thin film thickness a groove is cut through the thin film using a pair of tweezers, taking care not to scratch the glass underneath, and a scan is made across this groove. Scratching the glass would artificially increase the film thickness so blunter tweezers are preferable for this operation. From the resultant profile a clear step can be seen and the film thickness estimated to an accuracy of ±10 nm through several measurements per sample.

When measuring surface roughness carving a groove in the thin film is not necessary and a long scan is performed over the thin film surface. The profile scan is recorded to a computer for analysis including levelling of the profile and performing a peak detector analysis. This is done exclusively and explained in more detail in chapter 6. Long scan times are generally used to increase the accuracy of the measurement.

3.8 References

[1] A. R. Johnson, S. Lee, J. Klein and J. Kanicki, Absolute photoluminescence quantum efficiency measurement of light-emitting thin films, *Rev. Sci. Instrum.* **78**, 096101 (2007)

[2] T. Ahn, R. O. Al-Kaysi, A. M. Müller, K. M. Wentz and C. J. Bardeen, Self-absorption correction for solid-state photoluminescence quantum yields obtained from integrating sphere measurements, *Rev. Sci. Instrum.* **78**, 086105 (2007)

[3] J. C. de Mello, H. F. Wittmann and R. H. Friend, An improved experimental determination of external photoluminescence quantum efficiency, *Adv. Mater.* **9**, 3 (1997)

[4] N. C. Greenham, I. D. W. Samuel, G. R. Hayes, R. T. Phillips, Y. A. R. R. Kessener, S. C. Moratti, A. B. Holmes and R. H. Friend, Measurement of absolute photoluminescence quantum efficiencies in conjugated polymers, *Chem. Phys. Lett.* **241**, 89 (1995)

[5] E. Barsoukov and J. R. Macdonald, Impedance Spectroscopy Theory, Experiment, and Applications, *Wiley-Interscience*, Chap. 1 + 2, 1 - 42 (2005)

[6] M. Li, D. C. Sinclair and A. R. West, Extrinsic origins of the apparent relaxorlike behavior in $CaCu_3Ti_4O_{12}$ ceramics at high temperatures: A cautionary tale, *J. App. Phys.* **102**, 084106 (2011)

[7] Computer Support Group (CSG) Inc., (1973 - 2013) http://www.csgnetwork.com/dieconstantstable.html

[8] C. R. Nave, Hyper Physics, Georgia State University (2012) http://hyperphysics.phy-astr.gsu.edu/hbase/tables/indrf.html

[9] W. Becker, The bh TCSPC Handbook, 5th Ed., *Becker & Hickl GmbH* (2012)

Chapter 4

Rigorous Measurement of Quantum Yield Using the Gauge R & R Methodology

4.1 Introduction

This chapter explores sources of uncertainty in an integration sphere based measurement of fluorescence quantum yield of solid state systems, η_{QY} [1]. For LSC devices, achieving a high η_{QY} of the luminescent materials is of critical importance to the overall optical efficiency, η_{opt}, as per Eq. 2.2.15. After the absorption of incident solar energy this is the next loss mechanism physically imposed on a LSC device. It is therefore important to be able to make accurate measurements of η_{QY} in order to make useful experimental studies of LSCs.

The assessment methodology employed here discriminates between variance in the sample, day to day variation and the measurement system. Measurement of η_{QY} is complex and involves multiple sources of uncertainty including wavelength sensitivity characterisation using a calibration light source, self-absorption corrections by spectral methods, sample variance and laser intensity variance. These sources of uncertainty pose significant challenges that need addressing to improve the absolute measurement technique using the integration sphere. However, alternative methods of η_{QY} determination, which include the relative method and the thermal lens technique, pose greater challenges. The relative method relies on comparison of the subject fluorophore to a known standard, such as R6G or quinine sulphate, which contains large uncertainty from achieving the correct experimental conditions for the standard and, particularly for solid state systems, in emission anisotropy effects. The thermal lens technique is a purportedly more accurate absolute method but has been seen to be fraught with technical difficulties [2].

Assessment of the integration sphere method is performed using a statistical approach employed in industry for reliable characterisation of measurement gauges in manufacturing. This approach is used to set tolerances on production processes and gives insight into the sources of variance in the manufacturing industry. The method is known as Gauge R&R (GRR). The “Gauge” is the measurement device which may be a ruler, micrometre or, as in this case, a multi-component system with many potential sources of error. The R&R stands for Repeatability and Reproducibility, which relate to the measurement equipment and operative respectively. The GRR method is

demonstrated here to have value in characterising scientific instruments and is described in detail through the section 4.2. In 4.3 experimental methods are discussed providing additional details to those given in chapter 3.1. In section 4.4 the results of the study are explored and discussed in detail. Section 4.5 concludes on the findings of this study.

4.2 The Gauge R & R Methodology

The GRR method presented here is based on D. Wheeler's formulation of the study design [3], which corrects for mathematical inconsistencies in the standard Automotive Industry Action Group (AIAG) formulation. This statistical method allows sources of variance to be ascertained in three groupings; Equipment Variation (*EV*), Appraiser Variation (*AV*) and Manufacturing Variation (*MV*). The three sources of variation reflect the different aspects of the experiment and the production process. The *EV* relates to the measurement system, the *AV* relates to the appraiser, or operative, and the *MV*, also called product variation, relates to sample fabrication. In this study there is only one operative and so the appraiser variation is instead a day-to-day variation. On each day the components of the η_{QY} measurement system are removed and then reconnected and the laser is warmed up and tuned. Suffice to say this variance no longer represents that of an *AV* from a traditional GRR but will instead give indication of a variance associated with setting up and calibrating the experiment. Since this is essentially an equipment variation it is reasonable to expect it to be of roughly the same magnitude as the actual *EV*.

The essential requirement a GRR study is to have a fully crossed data structure, such that a full coverage of the permutations of variables is achieved. The variables here are *n*, *o* and *p* which are the number of repeat measurements per sample, number of days over which the study was performed and the number of samples, respectively. The measured parameter is the quantum yield, but the data structure of the GRR study is based on values the quantum yield takes for the variables *n*, *o* and *p*. Thus by a fully-crossed data structure what is meant is that all permutations of *n*, *o* and *p* have an associated quantum yield measurement, which creates the basis of the GRR statistical analysis.

This experiment is set for three measurements per sample over three days on five different samples, per material, and hence $n = 3$, $o = 3$ and $p = 5$. So there are $k = op = 15$ subgroups, each of size $n = 3$. The first step is to take the average range $\bar{R}_n$ of the *k* subgroups of size *n* = 3, which each have a range, *R*. Then the Upper Range Limit, R_{URL} , is determined using Eq. (4.2.1);

$$R_{URL} = \bar{R}_n \times D_4 \quad (4.2.1)$$

Where D_4 is the statistical anti-biasing constant, equal to 3.267. It is important that none of the ranges, R, are greater than the R_{URL} otherwise this is indicative of very large variance in the range and the statistical analysis is greatly weakened. Next the variance components *EV*, *AV* and *MV* are determined. The *EV* or Repeatability variance, $\hat{\sigma}^2_n$, is given by Eq. (4.2.2);

$$\hat{\sigma}^2_n = \left(\frac{\bar{R}_n}{d_2}\right)^2 \quad (4.2.2)$$

Where d_2 is a bias correction factor which depends on the size of the set, i.e. for n = 3 and o = 3, d_2 = 1.906 whilst for p = 5, d_2 = 2.477 [3]. These bias correction factors, which are actually proportionality factors, are used in statistics to estimate variance. They come from assuming a normal distribution for a quantity whose mean range is proportional to the standard deviation of the quantity. Thus the correction factor is a proportionality constant whose value depends on the size of the sample, as both the standard deviation and mean range do.

Next the *AV* variance, which in this study is a day-to-day variance, $\hat{\sigma}^2_o$, is given by:

$$\hat{\sigma}^2_o = \left(\left(\frac{R_o}{d_2}\right)^2 - \frac{o}{n \times o \times p} \times \hat{\sigma}^2_n\right) \quad (4.2.3)$$

Where R_0 is the range of o averages, which is the range between the daily averages of the η_{QY}. The bias correction factor d_2 is the same as in Eq. (4.2.2), i.e. 1.906. Note the dependence of the day-to-day variance, $\hat{\sigma}^2_o$, on the sample variance, $\hat{\sigma}^2_n$. Using Eqs. (4.2.2) and (4.2.3) the total contribution to the overall variance from the Repeatability (*EV*) and Reproducibility (*AV*) is the sum of these two variances:

$$\hat{\sigma}^2_{GRR} = \hat{\sigma}^2_n + \hat{\sigma}^2_o \quad (4.2.4)$$

The total variance includes the *MV*, $\hat{\sigma}^2_p$, which is determined in a similar manner to $\hat{\sigma}^2_n$ as follows:

$$\hat{\sigma}^2_p = \left(\frac{R_p}{d_2}\right)^2 \quad (4.2.5)$$

Where R_p is the range of p averages, which is the range for each sample between the average η_{QY}, and d_2 for p = 5 is 2.477. Finally the total variance, $\hat{\sigma}^2_t$, is the sum of Eqs. (4.2.4) and (4.2.5):

$$\hat{\sigma}^2_t = \hat{\sigma}^2_{GRR} + \hat{\sigma}^2_p \quad (4.2.6)$$

The ratio of each variance to the total variance, $\hat{\sigma}_t^2$, multiplied by 100 gives a convenient percentage contribution for each to compare.

4.3 Experimental Methods

All integration sphere spectra for this experiment were measured using an ORIEL Multispec with a 50µm slit, a grating blazed at 500nm and a resultant spectral range of 300 nm to 720 nm. This has an ORIEL Instaspec CCD camera set to 0.05s exposures in real time which is cooled to -40°C to reduce thermal noise. In Figure 4.3.1 raw data for the laser spectrum, $L(\lambda)$, sample spectrum for perylene, $S(\lambda)$, and the sensitivity function, $\phi_{sense}(\lambda)$, are shown, scaled appropriately for illustrative purposes. One can see that, compared to Fig. 2.4.6, the perylene spectrum has suffered strong self-absorption in the blue tail due to emission passing through the sample many times in the sphere. This must be corrected for by the methods described in chapter 3.1.

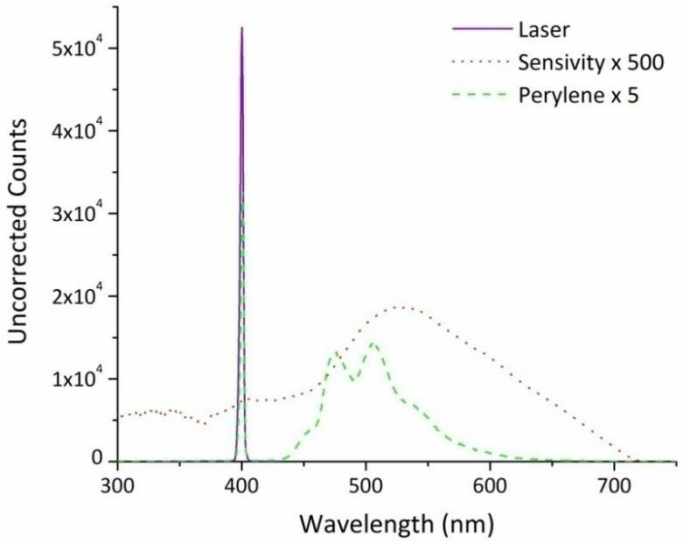

Figure 4.3.1: Raw IS data showing the frequency doubled Ti:Sapphire laser spectrum, $L(\lambda)$, (solid/purple), perylene sample spectrum, $S(\lambda)$, with remaining laser light, scaled by a factor of 5 (dashed/green) and the sensitivity function, $\phi_{sense}(\lambda)$, scaled by a factor of 500 (dots/red).

For excitation of the samples two sources were chosen so as to validate this statistical analysis; using a second gauge allows the difference in variability due to each source to be observed. These sources are a 400nm mode-locked (ML) laser and a 405 nm GaN laser as their wavelengths intersect well with the absorption spectrum of all fluorophores to be studied. The 400 nm source is a 532nm Nd^{3+}:YVO_4 pumped Ti:Sapphire laser operating at 2mW of ML 800 nm light, which is subsequently frequency doubled to 400nm with an LBO crystal. This is the Verdi V10/Mira 900 combination from Coherent with a Second Harmonic Generator from APE. Mode-locking is not essential for the measurement but is useful in order to tune the excitation wavelength and provide a broad laser

spectrum that is more distributed over the CCD detection array. This avoids CCD saturation and provides greater dynamic range between the laser and sample emission integration as discussed subsequently. While mode-locking generates a significantly higher instantaneous power than an equivalent average power continuous wave (CW) laser, the fluorescence lifetime of the materials ranges between 200 ps (F8) to 5 ns (Perylene) and therefore the system behaves in a quasi-continuous way when pulse periods are around 12 ns as in the Ti:Sapphire cavity. We have ensured that all our experimental systems behave linearly by measuring the η_{QY} at different excitation densities. No change in η_{QY} as a function of excitation density was observed but nevertheless excitation power was kept as low as possible. The 405 nm laser is a GaN diode laser which operates in CW mode, provides a steady mW of power and has a larger spot size than the ML laser which lowers energy density.

Five identical samples of each of three materials were fabricated and measured according to the Gauge R & R methodology. Blue-emitting conjugated polymer poly(9,9-dioctylfluorene) (F8) was provided by CDT, blue-green perylene dye was purchased from Sigma Aldrich and red-emitting perylene derivative perylene red (PR) was provided by BASF. F8 was spin coated from a 2.5 g/l solution in toluene at 500rpm in air and then dried on a hotplate at 50°C for 5 minutes to remove all the solvent. The resulting film thickness, measured on a Veeco DekTak, was 28±5 nm. Perylene and PR were first dissolved in toluene at 2 g/l and then blended with a solution of poly(methyl methacrylate) (PMMA) in toluene at 250 g/l in a 1:24 (dye:PMMA w/w) ratio giving a resultant dye concentration of 0.5% by weight. This corresponds to 2.36×10^{-2} M and 6.17×10^{-3} M for perylene and PR respectively. The perylene and PR samples are then prepared by spin coating the blends at 1500rpm in air and then dried on a hotplate at 50°C for 5 minutes. Resultant film thicknesses vary between 4.5 and 5.5 µm.

These choices were made for this study because F8 provides a known standard with well explored properties and because the perylene dyes are a promising material class for molecular dye based LSC devices. In a paper by A. J. Cadby *et. al.* the η_{QY} of F8 was found to be 45 ± 5 %, under different processing conditions to those used here [4]. Previously, for perylene and PR, η_{QY} values have been found ranging between 86 ± 2 % and 63 ± 2 % at concentrations of 0.1 %wt and 1 %wt (4.68×10^{-3} M and 4.73×10^{-2} M) for perylene and η_{QY} between 68 ± 2 % and 46 ± 2 % at concentrations of 0.1 %wt and 1.5 %wt (1.22×10^{-3} M and 1.86×10^{-2} M) for PR. These values for Perylene are in contradiction to that used by S. Lee *et. al.* (2006) [5], which was η_{QY} = 94% at a concentration of 0.1070 M. They do not explain how this value was determined, however. Further, the values found here for PR contradict those measured by Fennel and Lochbrunner (2011) [6] who found η_{QY} = 81 % at a concentration of

$5x10^{-2}$ M. The origin of the contrast between this study and the presented literature is unclear but differing levels of molecular aggregation due to different sample processing could be important.

4.4 Results and Discussion

The results from the GRR study are summarised in Table VII. The R_{URL} values vary significantly between fluorophores and excitation sources with the GaN source exhibiting the lowest values overall, as expected. This is indicative of the greater stability of the GaN laser resulting in a smaller variance in η_{QY} for the n = 3 measurements per sample. Note that due to sample degradation it was not possible to run this study for F8 with the GaN laser. The GRR study quantum yield data for F8 is shown in Fig. 4.4.1.

Material	Source	Mean η_{QY} [%]	R_{URL} [%]	Equipment $\hat{\sigma}_n^2/\hat{\sigma}_t^2$ [%]	Appraiser $\hat{\sigma}_o^2/\hat{\sigma}_t^2$ [%]	Total GRR $\hat{\sigma}_{GRR}^2/\hat{\sigma}_t^2$ [%]	Manufacturing $\hat{\sigma}_p^2/\hat{\sigma}_t^2$ [%]
F8	Ti:Sapph	47 ± 3	15.35	86.1	0.9	87.0	13
Perylene	Ti:Sapph	79 ± 3	13.49	40.5	37.4	77.9	22.1
PR	Ti:Sapph	51 ± 2	4.49	33.2	36.3	69.5	30.5
Perylene	GaN	71 ± 1	1.46	58.3	-2.4	55.9	44.1
PR	GaN	53 ± 2	6.28	28.3	39.5	67.9	32.1

Table VII: Gauge R&R statistics table. For each excitation source-material combination the measured η_{QY} and GRR statistics are summarised here.

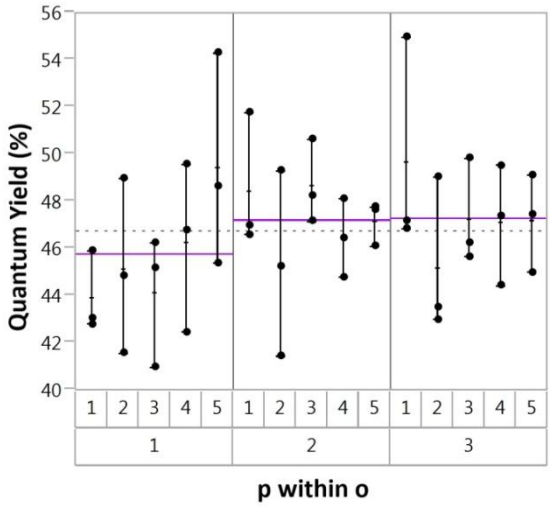

Figure 4.4.1: Variability chart for F8 with the Ti:sapphire laser as the excitation source showing the ranges as data bars. On the x-axis the duplicate samples, *p*, are shown within each day, *o*. The solid green lines in each *o* group are the daily means and the dashed line is the global mean, which is quoted in Table VII.

The mean η_{QY} is given here as a percentage, notice in Table VII that the yield measured for perylene is different for the two excitation sources. The reason for this is unclear as this difference is not reflected in the values for PR and photoluminescence excitation measurements indicate no dark states are present for perylene. None-the-less this discrepancy was observed consistently across the study in perylene's case, which can be seen in the variability charts for perylene in Fig. 4.4.2. The fact that η_{QY} is higher for the Ti:sapphire laser rules out the possibility of quenching due to higher exciton densities. Despite this conundrum the GRR study's validity is not affected with respect to ascertaining sources of variability.

Looking at the GRR statistics in Table VII for the Ti:sapphire laser both perylene and PR show a level of balance between the equipment and appraiser variances as is expected. This trend is not carried for F8 as in this case the variance between the n = 3 measurements per sample dominated over the *AV* component. Looking at Fig. 4.4.1 we can see this in the large fluctuations in individual points relative to *o* group means, in other words large ranges reflected by the R_{URL}. Also note the very low manufacturing variance, which indicates a high production tolerance from part to part for F8. This suggests greater homogeneity across the sample surface relative to the PMMA:dye systems.

The values for *MV* are in all cases below 50% designating this measurement system as a third-class monitor in Gauge R & R terminology. This means that the dominant source of variance lies in the measurement apparatus and not the sample production. We can see from the *MV* values that employing the GaN laser reduces the dominance of the measurement apparatus variance to some extent.

Some sample irregularities are expected and present but they have the smallest influence. Such irregularities will consist of point to point variations in thickness or fluorophore density across the sample films. It would be expected that the small molecules, perylene and PR, doped into PMMA would exhibit this more strongly and indeed the *MV* is lowest for F8, which is the thinnest film and of a single, pure material. Sample inconsistencies translated to a full LSC device are certainly undesirable though probably a relative minor factor compared to other loss mechanisms.

This sample irregularity combined with small oscillations in the intensity of the laser results in the distribution seen in η_{QY}. With this experimental setup it is not possible to know the exact number of laser counts at the time of each measurement. Instead a series of laser spectra are taken, as described in Chapter 3.1, between each sample measurement from which an average laser profile is used for all η_{QY} determinations.

The fact that the *GRR* (*EV* + *AV*) component dominates over *MV*, and thus most error lies in the equipment, does not itself say the measurement system is inaccurate. The GRR statistics only indicate that one source of variance is larger than another, saying nothing therefore of absolute uncertainties. To find the true uncertainties we multiply the *GRR* and *MV* variances as ratios by the uncertainty in η_{QY} for each material and source. Through this the greater stability of the GaN laser is seen by comparing the uncertainties. The results of this are shown in Table VIII.

To further explore the GRR data in Figures 4.4.2 and 4.4.3 are the variability charts for perylene and PR using the two excitation sources. It is immediately obvious that, for particular samples, there is little or no correlation between η_{QY} values over different days, *o*. In other words, few samples have consistent values throughout the study. No pattern of declining yields due to photobleaching or other chemically destructive reactions are observed and these samples were stored in air. PMMA acts a significant barrier to quenching agents such as molecular oxygen or moisture.

Material	**Source**	$\Delta\eta_{QY}$ **[%]**	**Total GRR** $\hat{\sigma}^2_{GRR}/\hat{\sigma}^2_t$	**Manufacturing** $\hat{\sigma}^2_p/\hat{\sigma}^2_t$	***ΔGRR* [%]**	***ΔMV* [%]**
F8	Ti:Sapph	±3	0.87	0.13	±2.61	±0.39
Perylene	Ti:Sapph	±3	0.779	0.221	±2.34	±0.66
PR	Ti:Sapph	±2	0.695	0.305	±1.39	±0.61
Perylene	GaN	±1	0.559	0.441	±0.56	±0.44
PR	GaN	±2	0.679	0.321	±1.36	±0.64

Table VIII: Gauge R&R uncertainties; the contributions from GRR and MV variances to the total uncertainty are summarised here

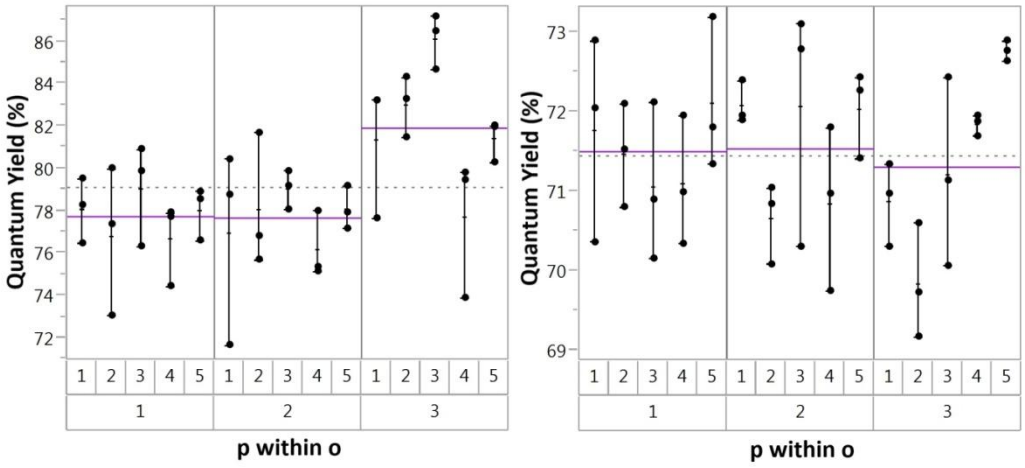

Figure 4.4.2: Variability charts for perylene; on the left using the Ti:Sapphire laser and on the right using the GaN laser.

There does not appear to be any trends in systematic biasing as we compare all the variability charts. In particular one might expect that calibrations performed on a day to day basis may introduce some variable systematic bias, but this is not seen in the results. On day o = 3 perylene and PR show an apparent systematic bias in the group mean, but then this is not seen similarly for F8 in Fig. 4.4.1 and is unclear from the standard deviation. The order of experiment was always conducted by measuring η_{QY} for F8, then perylene and finally PR. The calibration using the standard lamp was performed at the beginning. It is therefore possible that the alignment of certain elements of the system changed after F8 was measured; the fibre optic at the detector aperture of the integration sphere for example.

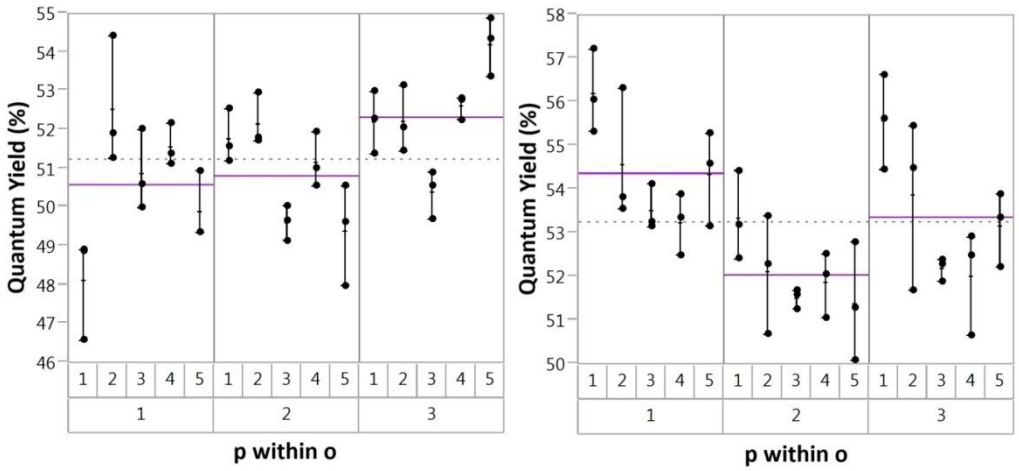

Figure 4.4.3: Variability charts for Lumogen red; on the left using the Ti:Sapphire laser and on the right using the GaN laser.

In all cases the group means for each day were within a standard deviation of the global mean which is a significant testimony to the success of the measurement procedure and the GRR study design. It is important to realise from this that without such a rigorous measurement approach it is difficult to make statements of absolute accuracy for the η_{QY} determination. Thus the GRR study forms an excellent basis for examining a measurement system but it cannot rule out uncertainties from self-absorption corrections and calibration. The total GRR variance will essentially therefore consist of laser intensity variance and systematic uncertainties due to corrections and calibration.

The oscillation in the laser flux, $I_{L,0}$, can be explored further by examining the distribution in laser flux. In particular, the root squared difference from the mean as a percentage of the total laser intensity is used as a metric. By examining the difference from the mean as a percentage of the laser intensity the relative difference is examined and the differing intensity magnitudes between measurement runs is ignored. The square root allows the oscillation magnitude to be isolated giving rise to the distributions shown in Fig. 4.4.4 for the Ti:sapphire and GaN lasers.

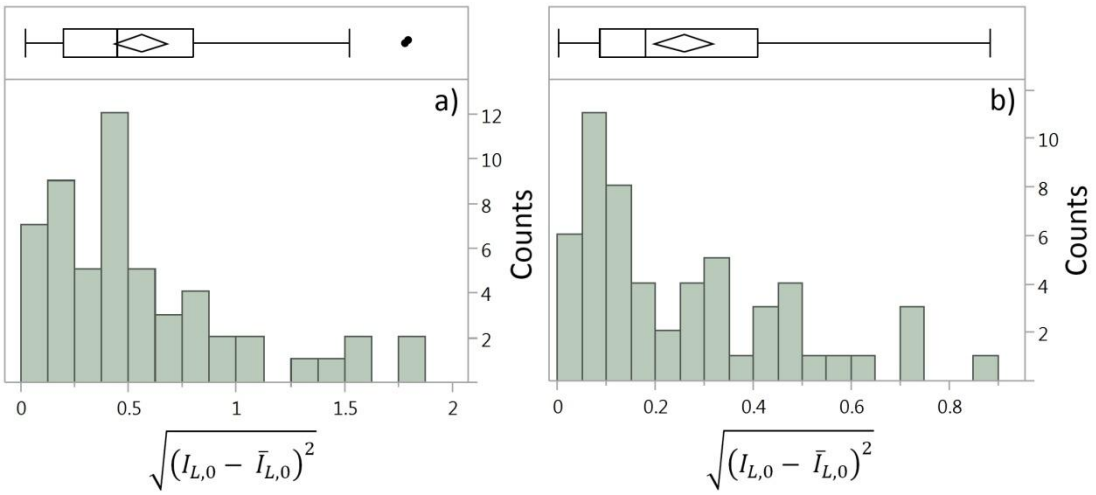

Figure 4.4.4: This histogram shows the laser flux magnitude distributions, as a percentage of total intensity, for a) the Ti:sapphire laser and b) GaN laser. Associated outlier box plots show the median (box's division), quartiles (box edges) and the mean (diamond). The counts axes here are the laser flux not the same as counts collected by the spectrometer.

The distributions in Fig. 4.4.4 are derived from normal distributions of laser flux magnitude with a mean at zero percent. When the root-squared-difference is taken as it has been here the distributions become skewed due to the small number of data points (55 for each laser) and the mean no longer represents the mean of the original normal distribution (which is 0 %). A simple uncertainty analysis follows using the laser flux distribution data to acquire a mean oscillation magnitude for the laser, $\Delta I_{L,0}$, and errors on the integrated intensities of the sample and remaining laser light, ΔI_S and $\Delta I_{L,1}$, respectively. These quantities were defined in chapter 3.1 with the latter two determined by the same means. Uncertainties are propagated as percentage errors to η_{QY} and then compared to those errors found by the GRR study, as shown in Table IX.

Material	Source	$\Delta I_{L,0}$ (±%)	$\Delta I_{L,1}$ (±%)	ΔI_S (±%)	$\Delta \eta_{QY}$ (%)	GRR $\Delta \eta_{QY}$ (%)
F8	Ti:Sapph	0.6	1	2	2	3
Perylene	Ti:Sapph	0.6	3	1	3	3
PR	Ti:Sapph	0.6	1	1	2	2
Perylene	GaN	0.25	0.9	0.9	1	1
PR	GaN	0.25	0.3	1.1	1	2

Table IX: Data table showing results of the error analysis for η_{QY}

Some apparent abnormalities present themselves. First the error on the remaining laser intensity is large for perylene using the Ti:sapphire source, at $\Delta I_{L,1}$ = 3%. This is attributed to the very strong absorption of the 400 nm laser light by perylene and hence the uncertainty has a larger weight. In a similar way the F8 emission intensity error is relatively high due to weaker sample absorption, and hence weaker emission, by the 28 nm thin film. Comparing the two error columns for η_{QY} it can be

see that the GRR study is more conservative in that it generates larger errors. This is likely due to this simple uncertainty analysis specifically looking at uncertainties in the intensities of source and sample, no other factors included. What this shows is that laser flux variance appears to contribute a substantial amount of uncertainty to η_{QY}. This follows from the point raised earlier that one cannot know the exact intensity of the laser at the time of measurement using this setup. The second, somewhat trivial point is that the GaN laser is more stable, as was obvious by observation, and thus provides a more accurate measurement.

4.5 Conclusions

What is clear from this study is that the limit of accuracy possible with this system using the GaN laser is around ± 1%. Such accuracy is not ideal for measurement of η_{QY} for systems with yields close to unity, which is important for LSC devices where high yields are critical. This motivation requires a better performance from the measurement system, though as can be seen at the concentrations used neither perylene nor PR are reaching unity at these concentrations. At lower concentrations they likely will, as has been seen for PR in PMMA [6].

To improve the experiment it is clear the laser flux variance needs a solution. Ideally it would be useful to know the exact intensity of the laser flux at the time of measurement and so a portion of the beam should be sampled using a beam splitter with a second photodiode. Then by correct timing of the electronics an instantaneous measurement of sample and laser flux would be possible. This would also remove extra steps in the analysis and speed up the measurement process into the bargain. This work was not completed for this thesis.

4.6 References

[1] A. P. Green and A.R. Buckley, Application of Gauge R & R to the rigorous measurement of quantum yield in fluorescent organic solid state systems. *Rev. Sci. Instrum.* **83**, 073108 (2012)

[2] L. R. Wilson, Luminescent Solar Concentrators: A Study of Optical Properties, Re-absorption and Device Optimisation, Ph.D, Edinburgh, Scotland (2010)

[3] D. J Wheeler, An Honest Gauge R&R Study, *SPC press*, 2006 ASQ/ASA fall technical conference, manuscript no. 189

[4] A. J. Cadby, R. Dean, C. Elliott, R. A. L. Jones, A. M. Fox and D. G. Lidzey, Imaging the Fluorescence Decay Lifetime of a Conjugated Polymer Blend By Using a Scanning Near-Field Optical Microscope, *Adv. Mater.* **19**, 107-111 (2007)

[5] S. Lee, A. M. Müller, R. Al-Kaysi and C. J. Bardeen, Using Perylene-Doped Polymer Nanotubes as Fluorescence Sensors, *Nano Letters* **6**, 7, 1420 - 1424 (2006)

[6] F. Fennel and S. Lochbrunner, Long distance energy transfer in a polymer matrix doped with a perylene dye, *Phys. Chem. Chem. Phys.* **13**, 3527-3533 (2011)

Chapter 5

Improving Luminescent Solar Concentrator Efficiency by Tuning Fluorophore Emission with Solid State Solvation

5.1 Introduction

In this chapter the results of experiments looking at how the solvation mechanism can be used to reduce self-absorption, and thus improve η_{self}, are discussed [1]. Towards the end of chapter 2.2 self-absorption was discussed as a major loss mechanism and is expressed by Eq. (2.2.13) with the LSC optical efficiency given by Eq. (2.2.15). The self-absorption loss mechanism has a significant impact on performance over short path lengths through an LSC medium, as was shown in a study comparing experiment results and ray-tracing model [2]. In that work square-planar devices are studied showing that η_{self} and matrix losses limit the optical concentration, C_{opt}, to a plateau at a LSC collection area of 1 m^2. In other work, combining experiment and ray-tracing, nanorod fluorophores were shown to have a C_{opt} of nearly a factor of two greater than that for quantum dots [3]. This was attributed to the nanorods (η_{QY} = 0.7) having a smaller overlap in absorption and emission, J, causing the self-absorption efficiency to increase and hence the LSC output irradiance.

Solutions to this problem, apart from geometric considerations, are generally through maximising the Stokes' shift and therefore minimising the overlap in absorption and emission spectra of the fluorophore. The solvation mechanism was described theoretically in chapter 2.4 and can be expressed using the Lippert-Mataga equation given by Eq. (2.4.2). By studying Eq. (2.4.2) it can be seen that the variable physical parameters with which the influence of solvation can be controlled are the host's optical properties, via Δf, and the fluorophore's dipole properties. First in this chapter, in section 5.2, the host properties will be considered and hence ways that they might be influenced to maximise Δf. In section 5.3 the fluorophore properties are discussed with the choices for this study explained. In the results section of 5.4 solvation theory is used with experimental data to make predictions of optical efficiency and of the limits to the gains possible though this phenomenon.

All samples are fabricated by first preparing a stock solutions of host materials in toluene so that total composite host concentration C_{host} = 250 g/l. Blends are made with solutions of DCM, DCM2 or DCJTB in toluene at C_{dye} = 2 g/l so that the blend has 0.1 wt% of dye. Deposition occurs onto glass substrates by spin coating at 1000 rpm giving films of approximate thickness x = 500 ± 30 nm. For

impedance analysis pre-patterned ITO on glass substrates are used with the same film deposition recipe and Ag contacts evaporated on top to create basic parallel plate capacitors.

5.2 Controlling the Orientational Polarisability of the Host Medium

For ease of reference the orientational polarisability (unitless) is given by Eq. (5.2.1);

$$\Delta f = \left(\frac{\varepsilon_r - 1}{2\varepsilon_r + 1} - \frac{n^2 - 1}{2n^2 + 1}\right) \quad (5.2.1)$$

As can be seen from Eq. (5.2.1) Δf has a stronger dependence on refractive index than relative permittivity, which are related through Maxwell's equations via $\varepsilon_r = n^2$ in a vacuum. In a vacuum, by definition, $\Delta f \equiv 0$, since there are no polarisable molecules present. In liquid or solid host environments the relationship between ε_r and n will deviate from the vacuum relation depending on the polarisability of the host, giving non-zero values of Δf. Thus Δf describes the ability of the host medium to polarise.

Typically the refractive index varies very little amongst different host materials whereas the electric permittivity can vary over a greater range, particularly for liquid media. The optical properties and Δf for a range of liquid and solid materials are shown in Table X to highlight this point. It is therefore clear that to maximise the orientational polarisability of the host material it will be necessary to maximise the host's relative permittivity.

Host Medium	**Static ε at 20°C [4, 5]**	**n at 20°C [4, 5] (n)**	**Δf(ε,n)**
Hexane	1.88	1.375	-0.0014
Cyclohexane	2.02	1.427	-0.0019
1,2,4-Trichlorobenzene	2.24	1.572	-0.0212
Toluene	2.38	1.496	0.0135
Mesitylene	2.4	1.498	0.0147
o-Xylene	2.57	1.505	0.0268
Chloroform	4.81	1.443	0.1492
Chlorobenzene	5.62	1.525	0.1429
Ethyl Acetate	6.02	1.372	0.1998
Tetrahydrofuran	7.58	1.408	0.2093
Dichloromethane	8.93	1.424	0.2172
o-Dichlorobenzene	9.93	1.551	0.1861

n-butanol	17.5	1.399	0.2636
Acetone	20.7	1.359	0.2842
Ethanol	24.3	1.361	0.2886
Methanol	32.7	1.329	0.3084
Acetonitrile	37.5	1.344	0.3055
Dimethyl Sulfoxide	46.68	1.478	0.2635
Water	80.1	1.333	0.3201
Poly(methyl methacrylate) (PMMA)	2.68	1.492 [7]	0.0393
Polycarbonate (PC)	2.9 [6]	1.590 [7]	0.0271
Polystyrene (PS)	2.6 [6]	1.596 [7]	0.0042
Poly(lactic acid) (PLA)	3.25 [8]	1.46 [9]	0.0850
Poly(vinylidene fluoride-co-hexafluoropropylene) (PVDF-HFP)	11.38 [10]	1.407 [10]	0.2393

Table X: Various liquid and solid host optical properties and the corresponding orientational polarisability values.

Typical optical quality host materials, introduced in Chapter 2.4.3, exhibit minimal range in ε_r and thus offer little leverage with which to employ solvation. An exception is the highly resistant polymer PVDF-HFP which exhibits an uncommonly high Δf of around 0.24 which is 75% of the value for water. PVDF-HFP, found here to be soluble only in CF or DMSO, has promising properties but was found to produce brittle films when spin coated onto glass.

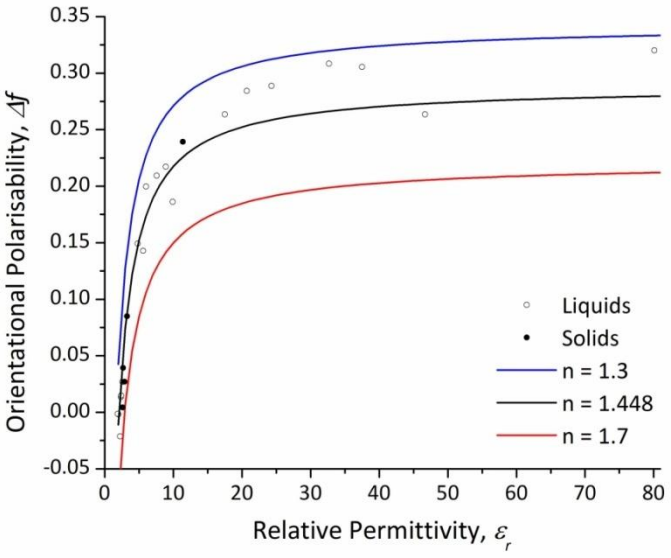

Figure 5.2.1: The orientational polarisability, Δf, is plotted here against the relative permittivity, ε_r for the data in Table X and theoretical line plots for n = 1.3 (blue), n = 1.448 (black) and n = 1.7 (Red). Note n = 1.448 is the average value from Table X.

It is used in this study to exhibit high Δf in the solid state. It is instructive to consider the Δf function graphically, as shown in Figure 5.2.1, by plotting Δf against ε_r for fixed n. In particular n values of 1.3,

1.7 and the average of n values from Table X are used so as to show the influence of small changes in n across the range of real materials. Fig. 5.2.1 shows that the data largely fits the average theoretical line (black) apart from some of the highly polarisable materials which tend to have lower than average refractive indices. The effect of reducing n is to shift the whole curve along the positive y-axis by a factor related to the refractive index term in Eq. (5.2.1). For maximum host polarisability, hence minimised self-absorption and maximised LSC optical efficiency, a lower n is best. This enhancement is in accordance with that of η_{fr} (see Fig. 2.2.2) and converse to that of η_{trap} (see Fig. 2.2.4) and so in employing solvation a further parameter comes into the optimisation process for n. A final point to note is the dependence of Δf on ε_r, which quickly plateaus beyond ε_r = 30 to 40 setting a practical target electric permittivity to reach.

Because the most practical host materials, in terms of processing and film forming properties, exhibit relatively low ε_r values it is necessary to consider another enhancement approach, that of doping. By introducing high permittivity materials to make a composite host the compound polarisability of the host will be greater. This effect can be achieved by increasing the concentration of the fluorophore itself, giving rise to self-solvation by neighbouring fluorophores, which has been shown to be useful for colour tuning of OLEDs [11, 12]. Self-solvation occurs when fluorophores have a greater dipole moment than the surrounding host molecules and thus increase the relative permittivity in the composite medium. A problem with using self-solvation is the effect of concentration quenching, which reduces fluorescence quantum yield and therefore LSC optical efficiency. A better way, in the case of LSC devices, is to introduce high permittivity molecules which blend well with the host matrix and introduce no further parasitic effects on either light transport or fluorescence quantum yield. These molecules may be either organic or inorganic in nature with each class bringing its own advantages and disadvantages.

Organic molecules seem the wisest choice for a practical solution for a variety of reasons. Because of solubility, for solution processing of LSC materials, organic dielectric dopants will offer the easiest application, whether via in-situ polymerisation for bulk-doped LSC structures or one of various coating techniques for surface-doped structures. This ease of processibility is compounded by the lower cost of organic materials which will be a critical factor in calculating the cost efficiency ($/W) of the complete LSC device. Just as with the more expensive RE and QD emitters, employing inorganic materials as dielectric dopants threatens to increase device cost into an uncompetitive regime. This, however, must be balanced against the efficacy of a materials ability to induce appreciable solvation since inorganic materials can easily beat organic ones in terms of the magnitude of ε_r.

With these factors in mind let's consider some materials. As previously mentioned and shown in Table X, molecules in the liquid state exhibit greater values of ε_r, which is due largely to their greater mobility at ambient temperature and pressure [13]. It might therefore be possible to introduce a small weight percentage of a liquid organic molecule into the solid host matrix. Ideally the material would be highly viscous under normal conditions, which suggests materials such as monomers like methyl methacrylate (MMA, ε_r = 7.89 [14]), solvents such as dimethylsulfoxide (DMSO, ε_r = 46.68 [4]) or sugar alcohols such as glycerol (ε_r = 42.5 [15]). Such molecules will be highly mobile and small enough to percolate throughout the host matrix. This is important as an even distribution will reduce local effects and any emission broadening that may result. Key criticisms of this approach are issues of dopant migration over time and of matrix disruption resulting in loss of host matrix integrity and hence device longevity. Such issues may be mitigated with some form of protective coating, one which also acted as an anti-reflection layer would be ideal though it must also be low cost. Experiments conducted to use glycerol or DMSO as dopants have not been encouraging, however, with film forming being heavily disrupted at the concentrations necessary to achieve appreciable solvation. For example, using DMSO, if we wanted to achieve a modest ε_r = 6 using PMMA as the main host (ε_r = 2.68) then we'd need to introduce 8% by weight of DMSO molecules. This is impractical for the strength of thin film matrixes formed by spin coating or drop casting, which fail to solidify entirely and take on a sticky consistency. It may be practical for bulk doped structures with protective coatings, however.

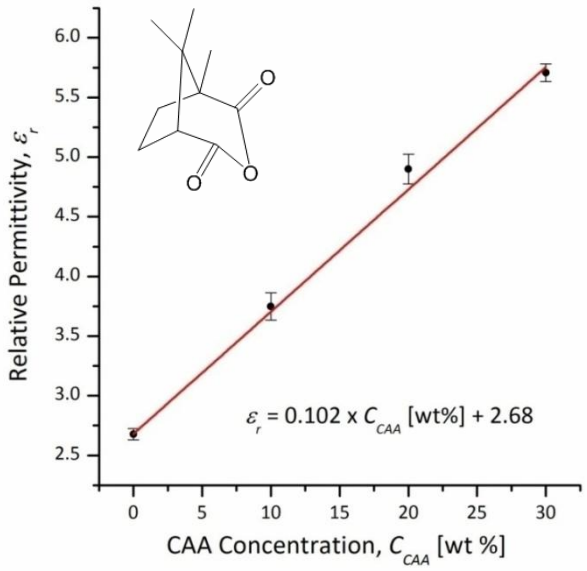

Figure 5.2.2: ε_r against CAA concentration, C_{CAA} [wt %], for PMMA:CAA films of varying composition. The molecular structure of CAA is shown in the inset.

A more obvious approach regarding organic molecular dopants is to employ solid materials that will have less of a structural weakening effect on the host matrix. The only particularly suitable material

found was camphoric acid anhydride (CAA), which was used by C. F. Madigan and V. Bulović (2003) to show that solvation is the mechanism causing the observed red-shifts in emission seen in the solid state previously [11-13, 16]. CAA is a small molecule exhibiting a moderate ε_r = 12.88 according to impedance analysis measurements of $PMMA_x$:CAA_{1-x} films of varying composition, as shown in Figure 5.2.2. The impedance analysis method used to determine ε_r was discussed in chapter 3.3.

The expected linear relationship with increasing CAA concentration is seen with a maximum permittivity of ε_r = 5.74 at C_{CAA} = 30 wt%. This sets a practical upper limit for this composite host system as thin film cohesion breaks down beyond this point. Films including fluorophores at 0.1 wt% were also measured but no noticeable effect from the fluorophore was seen on ε_r, which is unsurprising given their relatively low concentration. Using a composite host of CAA in conjunction with PMMA provides a platform for assessing the potential of the solvation mechanism and will form the basis of this investigation, as will be explored in detail in the next section.

The final option for dielectric dopants are inorganic nanoparticles which offer the most technically challenging but potentially the most promising of solutions. It is necessary to employ very small scale particles to achieve a well distributed dielectric medium since large particulates are likely to result in dominant local effects and hence emission broadening. This is in a similar line to the organic molecular dopants already discussed because of percolation and mobility requirements.

The main reason for the technical challenge this approach faces is the issue of solubility since inorganic materials do not dissolve in the organic solvents used for solution processing of LSC materials. It is possible to create a suspension of nanoparticles in a polar solution, ideally water but also DMSO and alcohols like methanol. However, these solvents are not suitable for processing host polymers like PMMA, nor are they particularly suited for dissolving the fluorophores. DMSO is an exception as it is an excellent solvent for almost every material this thesis discusses, however, it has an extremely high boiling point (189°C) making it almost useless for solution processing at room temperature. It is worth considering that if processing could be done at higher temperatures of around 150°C then it may be possible to use DMSO as the solvent for everything. Such techniques were not available in our laboratories and the extra cost of heat would certainly be detrimental to overall LSC device cost.

Another way to disperse nanoparticles, although certain to add cost to the device, is to make them soluble in the desired solvent by use of dispersants or functionalising the particle surface. Dispersants seem a less hopeful choice for solution processing of solid films as they may add to the disruptive effect on the matrix. Surface modification therefore seems wisest and can be done for

oxide nanoparticles, such as TiO_2 ($\varepsilon_r \approx 80$ - 100 [6]) or $BaSrTiO_3$ ($\varepsilon_r \approx 1250$ [17]) , with phosphonic acids such as octylphosphonic acid [18] and with silane coupling agents, which themselves allow polymer grafting to the nanoparticle surface [19]. This last approach, so called fragmentation chain transfer polymerisation (RAFT), could allow fully functionalised host polymers to be manufactured with high ε_r nanoparticles almost woven into the hosts fabric. Another method is to grow the functional groups in-situ, where surface modification occurs during the nanoparticle synthesis stage via precursor molecules. This offers benefits, particularly when wanting to disperse the nanoparticles in low polarity solvents, as for post synthesis modification it is necessary to use a high polarity solvent to disperse the pure nanoparticles for modification. This is a step that is best avoided due to concerns of residual aggregates and the need to extract the modified particles, basically by boiling off the high polarity solvent. Thermal agitation may then disrupt the cohesion of the bonded functional group, therefore defeating the point. Flushing the high polarity solvent may be successful by fractionating the suspension using a desired solvent, but it must be both lower density and immiscible (another two constraints), and then siphoning this layer off the fractionated mixture.

This is in fact precisely the method attempted using ethanol suspensions of 10 nm diameter TiO_2 anatase nanoparticles. 10nm nanoparticles were used to enhance dispersion in solution and to improve the homogeneity of the resultant thin film. Octylphosphonic acid was introduced as a coupling agent and the suspension was left for over 24hrs to allow the rate of coupling to achieve high cohesion and then hexane was added to fractionate the mixture. Evaporating the hexane is then relatively easy (b.p. 68.7°C) and toluene is added to the dried, weighed powder to blend with PMMA and DCJTB. After a possible false positive increase in Stokes' shift, and problems redispersing into toluene, it was decided that the approach was somehow flawed and thus this line of inquiry ended here due to other work. The potential, however, for employing $BaSrTiO_3$ nanoparticles is obviously impressive, with just 2 wt% of these nanoparticles giving $\varepsilon_r = 28$ which would make using CAA as a dielectric additive a pale comparison.. Nanoparticles of this material were acquired but, with 100 nm diameter, failed to remain in suspension to couple with the phosphonic acid.

5.3 Fluorophore Properties and Choice

Now we'll consider how the properties of the fluorophore itself influences the solvation mechanism. The energy lost to the reaction field due to the change in dipole moment of the fluorophore upon excitation is given by Eq. (5.3.1);

$$\Delta E_R = \frac{2\Delta f(\mu_E - \mu_G)^2}{a^3} \quad (5.3.1)$$

This can be seen by multiplying Eq. (2.4.2) through by *hc* which becomes Eq. (5.3.2) in terms of energy;

$$\Delta E_{stoke} = \Delta E_R + \Delta E_0 \quad (5.3.2)$$

Where ΔE_{stokes} is the energy difference between absorption and emission and ΔE_0 is the unperturbed Stokes' shift. Looking at Eq. (5.3.1) if one desires to maximise ΔE_R then the fluorophore's Onsager radius, a, must be minimised and the change in dipole moment, $\Delta\mu$, must be maximised. To explore the function $E_R(\Delta\mu, a)$ a fixed $\Delta f = 0.16$ was chosen, which is that for the composite host $PMMA_{0.7}$:$CAA_{0.3}$.

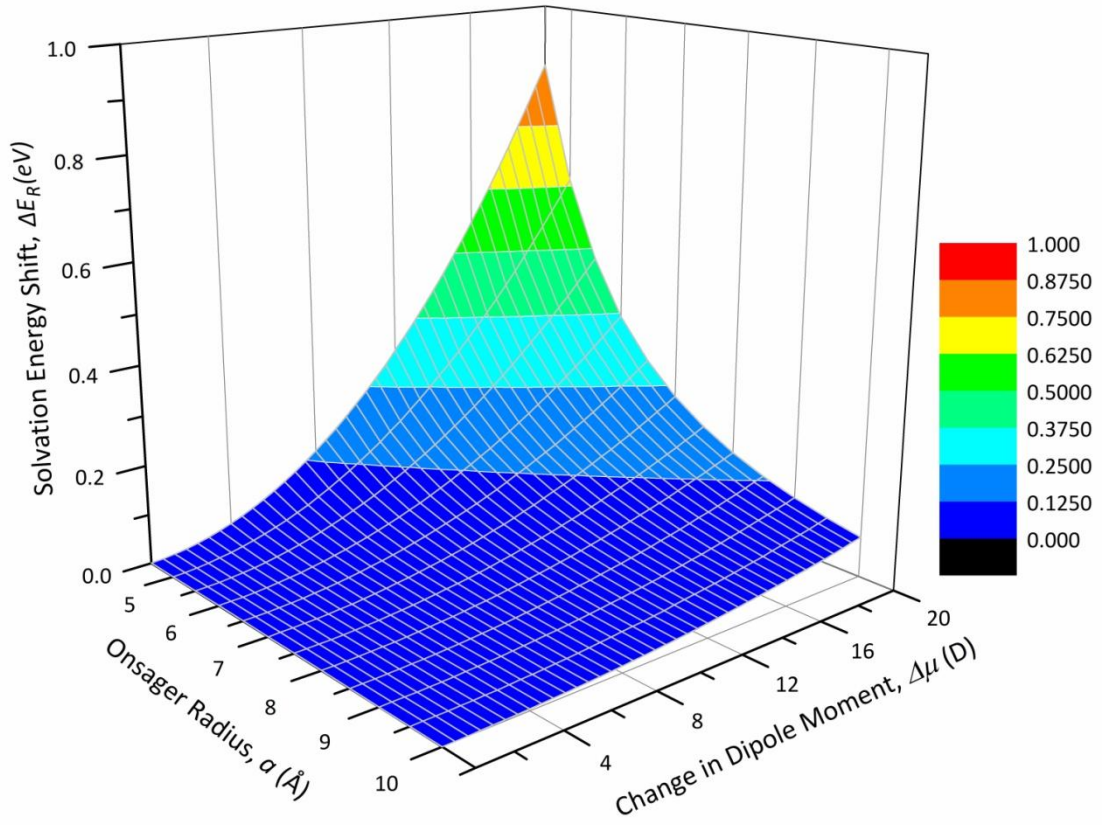

Figure 5.3.1: This 3D colour map shows the energy shift due to solvation as a function of the fluorophore's physical parameter space for a host of $\Delta f = 0.16$.

The 3D colour map exhibited in Fig. 5.3.1 shows a physical parameter space for $\Delta E_R(\Delta\mu, a)$. For large fluorophores, where $a > 10$ Å, very little solvation can be achieved owing to the inverse-cubed proportionality. Additionally the minimum physical size of a fluorescent molecule is limited to several angstroms which means there is only a small range of a to play with. Larger molecules may work so long as the fluorescent centre of the molecule is small such as would be expected on

dendrimer fluorophores. Some charge shielding may occur from the non-active moieties, however. In terms of the change in dipole moment appreciable solvation is achieved for when $\Delta\mu$ > 10 D and fluorophores explored here offer values of up to $\Delta\mu$ = 24.4. Because this plot is for fixed Δf it is also important to remember that increasing ε_r or decreasing n will result in a stretch of the 3D colour map in the positive z-axis (ΔE_R). A positive stretch of this sort represents increased polarisability and would act to relieve some of the constraint on the fluorophore properties, which are harder to control.

With these constrictions on the fluorophore dipole properties come the other requirements such as high quantum yield, broad absorption of incident radiation, long term photochemical stability and deep red emission. All of this seems a tall order and suitable dyes currently do not exist that fulfil all these requirements. Lumogen Red is likely the best fluorophore developed so far but it does not respond to the solvation effect since $\Delta\mu$ = 0. The next best option is DCJTB of the DCM class of fluorophores, a class which lacks in photochemical stability. In literature DCJTB is reported to exhibit $\Delta\mu$ = 13.1 D and a = 6.1 Å [20], equivalent values couldn't be found for DCM and DCM2. Other materials such as DNS and Ph660 (see chapter 2.4) also exhibit large change in dipole moments, that of DNS is reportedly 24.4 D [21], but their low quantum yields make them unsuitable. In this study the DCM class of fluorophores is used to explore the effects of solvation further.

5.4 Optical Efficiency Predictions for the Composite Host $PMMA_x$:CAA_{1-x}

In order to show the potential of solvation to improve optical efficiency, η_{opt}, the composite host $PMMA_x$:CAA_{1-x}, where x is the PMMA fraction, was chosen for reasons of practicality, as discussed in section 5.2. η_{opt} is given by Eq. (2.2.12) which uses the overlap integral, J, as a simple estimator of the self-absorption efficiency, such that η_{self} = (1 - J). In conjunction with this host the DCM class of fluorophores was chosen for their red emission, moderate quantum yield and their large $\Delta\mu$. The particular fluorophores, whose spectra are exhibited in Figs. 2.4.9, 2.4.10 and 2.4.11, are DCM, DCM2 and DCJTB respectively and are to be doped at 0.1 wt%. A constant fluorophore concentration is chosen to negate the influence of self-solvation effects on the results. Critically, the changing host composition should cause little or no change in refractive index of the host environment, which was seen for PS:CAA composite hosts up to C_{CAA} = 24.5 wt% [16] and is therefore also expected in this case.

The Stokes' shift is determined from the absorption and emission spectra of each sample, measured as described in Chapter 3.4. This gives us ΔE_{stokes} in Eq. (5.3.2) and is done for a series of PMMA fractions in the range 0.7 < x < 1 in increments of 0.05. The normalised spectra for DCM, DCM2 and

DCJTB are shown in Figures 5.4.1 a), 5.4.1 b) and 5.4.2 a), respectively. These exhibit the change in emission spectrum as CAA fraction increases. The overlap integral, J, is also measured from the normalised spectra to be used in conjunction with Eq. (2.2.12) to determine η_{opt}. From the spectral plots presented the overlap area is seen to decline as CAA fraction increases.

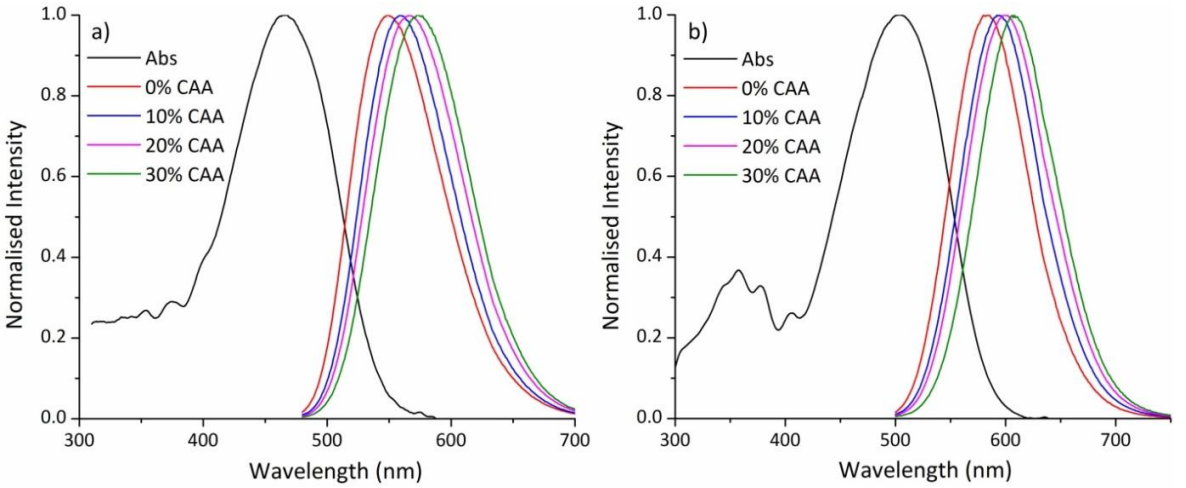

Figure 5.4.1: The absorption (black) and emission (colour) spectra for a) DCM and b) DCM2 in varying compositions of the composite host $PMMA_x:CAA_{1-x}$.

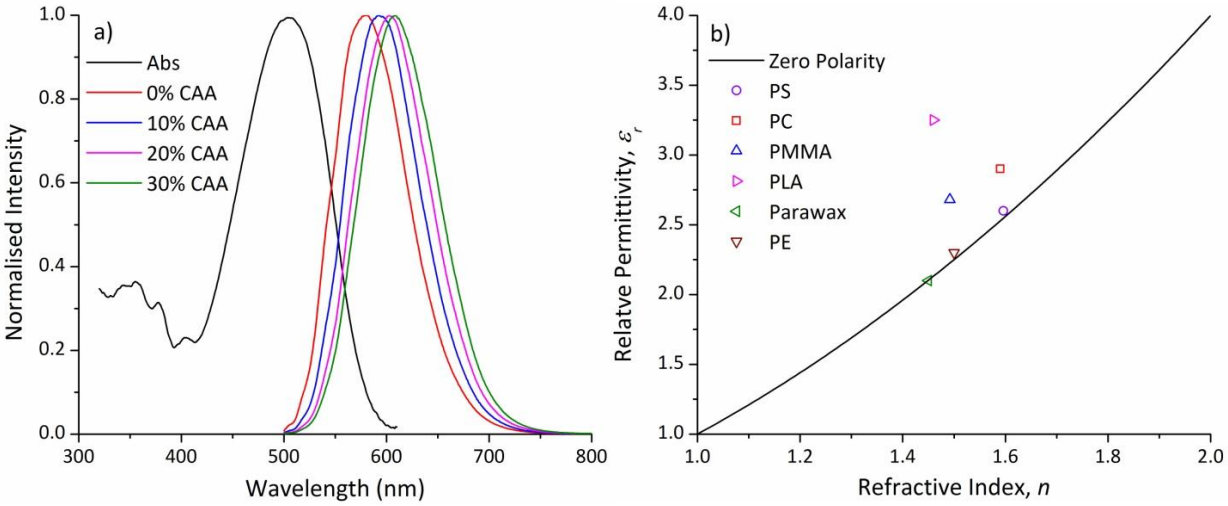

Figure 5.4.2: a) The absorption (black) and emission (colour) spectra for DCJTB in varying compositions of the composite host $PMMA_x:CAA_{1-x}$. b) Various host materials plotted here for ε_r against n with the zero polarity curve for reference.

As discussed in chapter 2.4 the Lippert-Mataga equation, Eq. (2.4.2), allows us to predict the shift in energy due to the solvation effect. To use this predictive power several quantities must first be determined. First is to determine the unperturbed Stokes' shift, ΔE_0. To do this a host of zero polarisability, $\Delta f = 0$, is needed and then the fluorophore emission and absorption spectra are measured in this host. The difference between the peak energies of these gives ΔE_0. By plotting various host material's optical parameters against the zero polarity line given by $\varepsilon_r = n^2$, as shown in Figure 5.4.2 b), it is simple to choose a material for this task. Paraffin wax, or parawax, is an obvious

choice but it is a highly scattering medium and will not work well for spectral measurements. PS is therefore the best material screened for this purpose and although it exhibits a small, non-zero polarisability it will introduce a relatively minor systematic error. The results for DCM, DCM2 and DCJTB give E_0 values of 3076.9 cm^{-1}, 2292.2 cm^{-1} and 2071.5 cm^{-1}, respectively.

To make predictions of η_{opt} the samples must also have their quantum yields measured as per the methodology in Chapter 3.1. It is critical that the quantum yield at least remains constant otherwise CAA is acting as a quenching agent, which is unacceptable. As the results in Figure 5.4.3 and Table XI show there is an apparent η_{QY} enhancement, statistically significant in only the case of DCM. This is not physically understood but it is encouraging.

With J and η_{QY} determined for all samples Eq. (2.2.12) can be applied with some estimations and simplifying assumptions for the other efficiencies. As discussed in depth throughout chapter 2.2 it has been seen for a host of n = 1.492 interfaced with air we have η_{fr} = 0.96, η_{stokes} = 0.75, η_{trap} = 0.75 and hence $\eta_{TIR}\eta_{host}$ = 0.95. η_{abs} depends on the particular fluorophore's absorption coefficients and the device depth through which the incident solar irradiance passes. If we assume a depth sufficient to achieve saturated absorption over the fluorophore's absorption spectrum then crudely this can be estimated as η_{abs} = 0.3 for all DCM fluorophores. A back reflector would help achieve this absorption goal whilst optimising geometric concentration, G. Since DCJTB has a much stronger absorption it requires less depth to achieve this. Now Eq. (2.2.12) can be calculated up to p = 3 giving the results shown in Table XI and Figure 5.4.3.

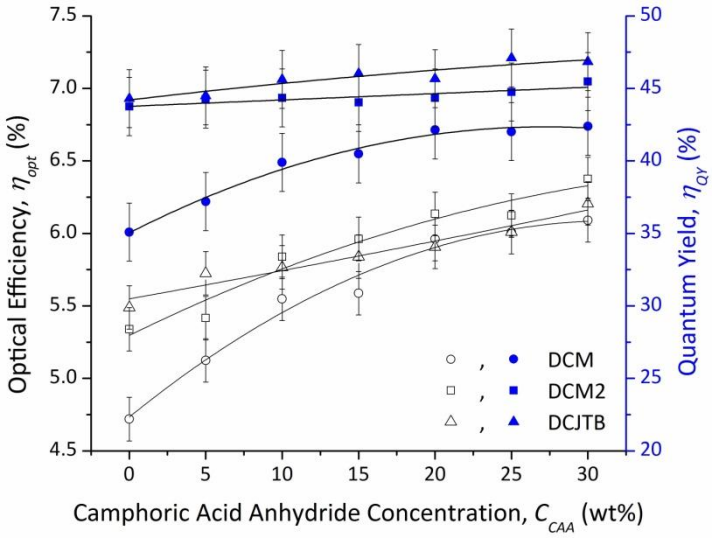

Figure 5.4.3: Fluorophore quantum yield (blue, full shapes) and predicted LSC optical efficiency (black, open shapes) are shown here against C_{CAA} in $PMMA_x$:CAA_{1-x}. Polynomial best fits are included to guide the eye. Error bars on η_{opt} are determined from the 2% error on η_{QY} and the error on J, determined from spectroscopy.

The results indicate a significant relative increase in η_{opt} for DCM, DCM2 and DCJTB of 22.5%, 11.5% and 16.3%, respectively, when ε_r is increased from 2.68 to 5.74. Clearly the larger increase for DCM

is a result of the larger apparent increase in η_{QY} for that fluorophore since the decrease in J is proportionately similar in all cases. The resultant optical efficiency is almost the same across the DCM class exhibited here which is anticipated when looking at the relative sizes of η_{QY} and J. DCM achieves a smaller overlap integral but exhibits lower quantum yield and vice versa is true for both DCM2 and DCJTB. Tentatively DCJTB shows itself to be the best fluorophore in this set.

Using the data from the $PMMA_x$:CAA_{1-x} composite host system it is possible to make predictions of the limits of solvation in the context of improving LSC efficiency. To do this a Lippert plot is produced, which is a plot of $\Delta\nu$ against Δf as shown in Figure 5.4.4, along with a linear best fit interpolated to high Δf. Out of curiosity for exploring higher permittivity parameter space the host PVDF-HFP (see Table X) is used pure with DCM, DCM2 and DCJTB as dopants. PVDF-HFP has ε_r = 11.38 and n = 1.407 (hence Δf = 0.2393), which represents a significant advance on the composite $PMMA_{0.7}$:$CAA_{0.3}$ having ε_r = 5.74 with n = 1.492 (hence Δf = 0.155).

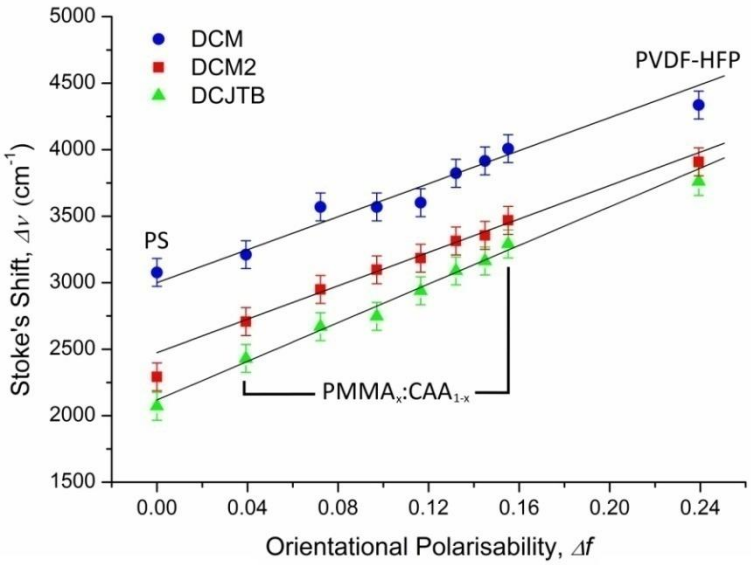

Figure 5.4.4: Lippert plot for DCM, DCM2 and DCJTB with linear best fits interpolated to Δf = 0.2505, which is the equivalent of ε_r = *30* with n = 1.492. For each dye the leftmost data point is for a pure PS host where Δf = 0 and the rightmost data point is for pure PVDF-HFP where Δf = 0.2393.

Figure 5.4.4 shows the linear trend predicted by the Lippert-Mataga equation, Eq. (2.4.2), and serves as an indication that solvation is indeed the mechanism responsible for the observed energy shifts., One notices that, amongst the seven $PMMA_x$:CAA_{1-x} data points for each fluorophore, despite their being evenly spaced in terms of PMMA fraction, the x-axis interval between data points is not constant. This is because of the dependence of Δf on ε_r, as plotted in Fig. 5.2.1, resulting in a diminishing return on $\Delta\nu$ for higher ε_r. From the line equations of the linear best fits in Fig. 5.4.4 we then find $\Delta\nu$ for Δf = 0.2505 (ε_r = *30* with n = 1.492) to be 4624 cm^{-1}, 4156 cm^{-1} and 3904 cm^{-1} for DCM, DCM2 and DCJTB, respectively. This is shown in Table XI, along with calculated values of η_{opt},

which represent an improvement relative to pure PMMA of 24.5%, 18.6% and 23.4% for DCM, DCM2 and DCJTB, respectively. Values for PVDF-HFP are also shown with assumed quantum yields in line with that measured for the fluorophores in PMMA. Looking back to Table IV on page 43 DCM shows a higher quantum yield in PVDF-HFP than PMMA but the yield was not measured for the other fluorophores and so this data was not employed here.

Dye	C_{CAA} [wt%]	ε_r	J [%]	ν_{PL} [cm^{-1}]	ν_{abs} [cm^{-1}]	$\Delta\nu$ [cm^{-1}]	η_{QY} [±0.02]	η_{opt} [%]
DCM	0	2.68	16.2	18248	21459	3211	0.35	4.72
	5	3.19	13.1	17889	21459	3570	0.37	5.12
	10	3.70	13.0	17889	21459	3570	0.40	5.55
	15	4.23	12.1	17857	21459	3602	0.40	5.59
	20	4.73	11.0	17637	21459	3823	0.42	5.96
	25	5.26	10.0	17544	21459	3915	0.42	6.01
	30	5.74	9.3	17452	21459	4007	0.42	6.09
	(PVDF-HFP)	11.38	6.0	17123	21459	4336	0.42	6.19
	Theoretical	30	4.7	16921	21459	4624	0.42	6.25
DCM2	0	2.68	24.7	17253	19960	2707	0.44	5.49
	5	3.19	20.3	17011	19960	2949	0.44	5.73
	10	3.70	19.6	16863	19960	3097	0.44	5.77
	15	4.23	18.2	16776	19960	3184	0.44	5.84
	20	4.73	16.9	16646	19960	3314	0.44	5.91
	25	5.26	14.9	16604	19960	3356	0.44	6.01
	30	5.74	13.3	16491	19960	3469	0.45	6.21
	(PVDF-HFP)	11.38	6.3	16051	19960	3909	0.45	6.55
	Theoretical	30	3.8	15804	19960	4156	0.45	6.74
DCJTB	0	2.68	28.0	17361	19802	2441	0.44	5.34
	5	3.19	26.7	17212	19802	2590	0.44	5.42
	10	3.70	24.0	17065	19802	2737	0.46	5.84
	15	4.23	21.8	16863	19802	2939	0.46	5.96
	20	4.73	18.6	16722	19802	3080	0.46	6.14
	25	5.24	18.8	16639	19802	3163	0.46	6.12
	30	5.74	16.8	16529	19802	3273	0.47	6.38
	(PVDF-HFP)	11.38	7.7	16041	19802	3761	0.47	6.85
	Theoretical	30	5.3	15873	19802	3904	0.47	6.97

Table XI: Solvation study results for the composite host $PMMA_x$:CAA_{1-x} with DCM type fluorophore's doped at 0.1 wt%. Also included are values for pure PVDF-HFP and predicted values for ε_r = 30.

DCJTB is still the favourite achieving an optical efficiency of 7% or 0.07. Combined with an LSC having a reasonable geometric ratio of G = 30 this would give a total optical concentration of C_{opt} = 0.07 x 30 = 2.1. Then solar cells collecting along the edge of such an LSC device would be receiving around twice the irradiant intensity of the incident solar intensity. Higher geometric ratios could be possible but, as discussed in chapter 2.5, current best LSC devices are quite small and exhibit geometric ratios of around G = 2.5 giving, in the case of DCJTB here, C_{opt} = 0.07x2.5 = 0.175. Clearly this is poor and

would be making a waste of solar cells. We thus learn that the geometry of the device is critical and must remind ourselves that there are losses associated with increasing *G* due to the mean path length increasing, such as self-absorption quantified by η_{self}.

Another point of interest is to make a fit of the data to Eq. (2.4.2) as a function of ε_r. Partially to this end the unperturbed Stokes' shift, ΔE_0, was determined using PS as a host for $\Delta f = 0$. Models of Eq. (2.4.2) are to be produced for variable ε_r and $n = 1.492$ and so in addition the fluorophore properties, $\Delta\mu$ and a, must be determined.

First the Onsager Radius, a, is calculated theoretically through quantum chemical calculations, using the GAMESS software [22], of energetically optimised ground state geometries using a combination of B3LYP [23] functional and 6-31G* [24] basis sets. These were found to be 5.20 Å, 5.49 Å and 6.18 Å for DCM, DCM2 and DCJTB, respectively. This work was carried out by Keith T. Butler.

Next the change in dipole moment, $\Delta\mu$, is determined from the gradient of the best fit lines of Figure 5.4.4. Recalling Eq. (2.4.2) and comparing it to a straight line, for y = $\Delta\nu$ and x = Δf, the change in dipole moment can be shown to be given by Eq. (5.4.1);

$$\Delta\mu = \sqrt{\frac{mhca^3}{2}} \qquad (5.4.1)$$

Where m is the gradient and, in cgs units, h is Planck's constant (6.626×10^{-27} erg s) and c is the speed of light (2.9979×10^{10} cm s^{-1}). The Onsager radius was found as described above and so applying Eq. (5.4.1) for DCM, DCM2 and DCJTB the change in dipole was found to be 12.1 ± 0.8 D, 10.2 ± 0.2 D and 13.0 ± 0.4 D, respectively. The errors are determined from the standard error on the gradient of the lines of best fit in Fig. 5.4.4. What has been done here is to use quantum chemical models in conjunction with measured energy shift data to indirectly determine $\Delta\mu$ through the assumption of Eq. (2.4.2)'s validity. The value for DCJTB found here is consistent with the value of 13.1 D found in literature [20].

Using the determined values of $\Delta\mu$ and a with fixed $n = 1.492$, Eq. (2.4.2) can now be employed to model the variation in ΔE as a function of ε_r as shown in Figure 5.4.5. This time ΔE is used in place of $\Delta\nu$ for clarity; the LM equation can be rewritten in terms of energy by multiplying through by hc. Fig. 5.4.5 shows how the data for doped $PMMA_x$:CAA_{1-x} hosts nicely follows the theoretical line of Lippert-Mataga theory. Notice that the PS sample data points drop low relative to the trend, which is owing to the higher refractive index of PS. Similar is true of PVDF-HFP, whose index is lower (refer

back to Fig. 5.2.1 to see how n influences Δf and hence $\Delta \nu$). Thus the models of Figure 5.4.5 only truly apply to the $PMMA_x:CAA_{1-x}$ composite host system.

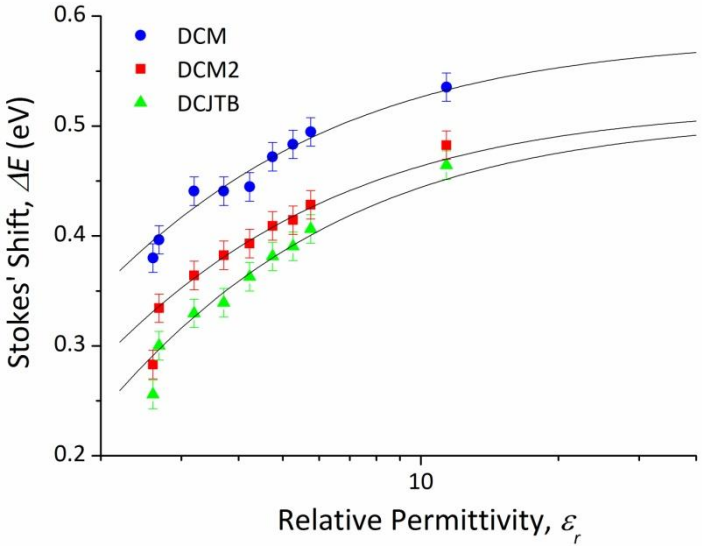

Figure 5.4.5: This plot of ΔE against ε_r shows the data for DCM, DCM2 and DCJTB plotted with models of Eq. (2.4.2) tuned by the value of $\Delta \mu$. As before PS samples are leftmost, the rightmost data points are for pure PVDF-HFP and the rest in the middle are for various compositions of $PMMA_x:CAA_{1-x}$.

Figure 5.4.5 has similarities in form to Figure 5.2.1 as a result of the ε_r dependence, although other influences are present in the former (namely n, $\Delta \mu$ and a). They both give insight into the upper limits achievable through solvation indicating a plateau in $\Delta \nu$ at around $\varepsilon_r = 30$ to 40. This would remain the case whatever values the other key parameters take.

5.5 Conclusions

In this study it has been show that, for the DCM class fluorophores exhibited here, a potential relative increase in optical efficiency of between 18.6% and 24.5% is possible. These theoretical limits are for a relative permittivity of $\varepsilon_r = 30$ and are nearly reached using PVDF-HFP as a host material. The limit at $\varepsilon_r = 30$ is predicted by varying the mass fractions of the composite host $PMMA_x:CAA_{x-1}$ doped with a given fluorophore at 0.1 wt%. The fluorescence quantum yield was seen to remain steady as CAA fraction increases, which indicates CAA does not act as a quenching agent. This is a crucial condition to make gains from the solvation effect for luminescent solar concentrator devices.

A maximum LSC optical efficiency of $\eta_{opt} = 0.07$ was seen for DCJTB with reasonable assumptions for other efficiencies. With developments in fluorophore design to improve properties such as quantum

yield, spectral absorption and photochemical stability, the solvation mechanism could prove a useful enhancement tool to achieve higher optical concentrations in LSC devices, therefore to extract more energy. The technique also requires availability of low cost dielectric dopants to enhance host permittivity, or similarly low cost high permittivity host materials.

5.6 References

[1] A. P. Green, K. T. Butler and A. R. Buckley, Tuning of the emission energy of fluorophores using solid state solvation for efficient luminescent solar concentrators, *App. Phys. Lett.* **102**, 133501 (2013)

[2] R. Bose, D. J. Farrell, A. J. Chatten, M. Pravettoni, A. Büchtemann and K. W. J. Barnham, Novel Configurations of Luminescent Solar Concentrators, *Proc. 22nd European Photovoltaic Solar Energy Conference*, pp. 210-214, (2007)

[3] R. Bose, D. J. Farrell, A. J. Chatten, M. Pravettoni, A. Büchtemann, J. Quilitz, A. Fiore, L. Manna and K. W. J. Barnham, Luminescent Solar Concentrators: Nanorods and Raytrace Modelling, *33rd. IEEE Photovoltaic Specialists Conference*, pp. 1- 5, (2008)

[4] Louisiana State University, http://macro.lsu.edu/HowTo/solvents.htm

[5] Kok Chemware, (1999-2002) http://www.sanderkok.com/techniques/hplc/eluotropic_series_extended.html

[6] The Goodfellow Group, (2008 - 2013) http://www.goodfellow.com/

[7] Mikhail Polyanskiy, Refractive Index Info, (2008 - 2013) http://refractiveindex.info/

[8] K. Shinyama, T. Oi and S. Fujita, Dielectric Relaxation Phenomenon of Polylactic Acid with β-Crystalline Chitin, *Int. J. Polym. Sci.* **2012**, 389491 (2012)

[9] D. Garlotta, A Literature Review of Poly(Lactic Acid), *J. Polym. Environ.* **9**, 2, 63 - 84 (2001)

[10] Sigma Aldrich, Poly(vinylidene fluoride-co-hexafluoropropylene) (PVDF-HFP) http://www.sigmaaldrich.com/catalog/product/aldrich/427187?lang=en&region=GB

[11] V. Bulović, A. Shoustikov, M. A. Baldo, E. Bose, V. G. Kozlov, M. E. Thompson and S. R. Forrest, Bright, saturated, re-to-yellow organic light-emitting devices based on polarization-induced spectral shifts, *Chem. Phys. Lett.* **287**, 455 - 460 (1998)

[12] V. Bulović, R. Deshpande, M. E. Thompson and S. R. Forrest, Tuning the color emission of thin film molecular oraganic light emitting devices by the solid state solvation effect, Chem. Phys. Lett. **308**, 317 - 322 (1999)

[13] R. E. Sau and G. Baur, Influence of the Solvent Matrix on the Overlapping of the Absorption and Emission Bands of Solute Fluorescent Dyes, *Appl. Phys.* **23**, 369 - 372 (1980)

[14] F. Liakath Ali Khan, P. Sivagurunathan, S. Raja Mohamed Kamil and S. C. Mehrotra, Dielectric studies of methyl methacrylate and butyl methacrylate with primary alcohols using time domain reflectometry, *Indian J. Pure Appl. Phys.* **45**, 754 - 758 (2007)

[15] Clipper Controls Inc., http://www.clippercontrols.com/pages/Dielectric-Constant-Values.html#M, (2013)

[16] C. F. Madigan and V. Bulović, Solid State Solvation in Amorphous Organic Thin Films, *Phys. Rev. Lett.* **91**, 24, 247403 (2003)

[17] R. Balachandran, B. H. Ong, H. Y. Wong, K. B. Tan and M. Muhamad Rasat, Dielectric Characteristics of Barium Strontium Titanate Based Metal Insulator Metal Capacitor for Dynamic Random Access Memory Cell, *Int. J. Electrochem. Sci.* **7**, 11895 - 11903 (2012)

[18] A. Colombo, F. Tassone, F. Santolini, N. Contiello, A. Gambirasio and R. Simonutti, Nanoparticle-doped large area PMMA plates with controlled optical diffusion, *J. Mater. Chem. C* **1**, 2927 - 2934 (2013)

[19] M. Iijima and H. Kamiya, Surface Modification for Improving the Stability of Nanoparticles in Liquid Media, *Powd. Part. J.* **27**, 119 - 129 (2009)

[20] Y. Yao, Q. Zhou, X. Wang, Y. Wang and B. Zhang, A DCM-Type Red-Fluorescent Dopant for High-Performance Organic Electroluminescent Devices, *Adv. Funct. Mater.* **17**, 93 - 100 (2007)

[21] J. M. Warman, M. P. De Haas and A. Hummel, Dipole Moment Changes in the Singlet and Triplet Excited States of 4-Dimethylamino-4'-nitrostilbene Detected by Nanosecond Time-Resolved Microwave Conductivity, *Chem. Phys. Lett.* **87**, 1 (1982)

[22] M. W. Schmidt, K. K. Baldridge, J. A. Boatz, S. T. Elbert, M. S. Gordon, J. H. Hansen, S. Koseki, N. Matsunuga, K. A. Nguyen, S. Su, T. L. Windus, M. Dupuis and J. A. Montgomery Jr., General atomic and molecular electronic structure system, *J. Comput. Chem.* **14**, 1347 - 1363 (1993)

[23] A. D. Becke, Density-functional thermochemistry. III. The role of exact exchange, *J. Chem. Phys.* **98**, 5648 - 5652 (1993)

[24] M. M. Francl, W. J. Pietro, W. J. Hehre, J. S. Binkley, M. S. Gordon, D. J. Defrees and J. A. Pople, Self-consistent molecular orbital methods. XXIII. A polarisation-type basis set for second-row elements, J. Chem. Phys. **77**, 3654 - 3665 (1982)

Chapter 6

Parameter Screening for Spray Coating Deposition of Surface Coated Luminescent Solar Concentrators

6.1 Introduction

This chapter is an examination of the results of a screening study to explore the influence of different operational parameters of a spray coating deposition system. Spray coating offers a fast, low cost and large area deposition methodology for surface coating LSC devices with a fluorophore containing layer. To better understand the spray coating method a parameter screening study has been used. Screening approaches offer a fast and statistically powerful method to assess how the operational parameters affect the film qualities that are of interest.

Spray coating is relatively complex when compared to other deposition methods because of the large number of operational parameters, or *factors*, involved. In the terminology of screening experiments factors are independent variables which may affect the outcome of the experiment. For example all deposition methods rely in some manner on the solvent and on the solute concentrations, and so also the viscosity of the solution. Similarly they can also all utilise film forming control techniques, such as control of vapour pressure and fume extraction rate, and substrate conditioning such as plasma ashing or surface modification. These all affect the resultant film deposited but apart from these universal factors each deposition method carries personalised factors.

Spin coater operation relies on spin speed and is ill suited to large area deposition. Spin coating finds use in small area research applications and not in production scale methods. Also ill suited to large area deposition is dip coating which depends on withdrawal speed from the coating trough. Dip coating could be suitable for small LSC devices on the scale of 10 cm or so but would lack high production speeds offered by spray coating. Bar coating, which could be a potential method for high speed, large area depositions, depends on the number of winds of wire per unit length, the wire thickness and the carrying speed (the speed the bar travels at). Doctor blading is similar in many respects to bar coating and is well suited to large area deposition. It depends on the distance between the blade and substrate and the carrying speed. For spray coating deposition the

dependences include injection pressure, spray head speed and height, substrate temperature and the number of coatings. It is because of this number of factors that a screening study was preferred.

The film quality in this study is assessed by 7 measured dependent variables, or *responses*, which are the roughness ratio, $\langle R_R \rangle$, the standard deviation of this, σ_R, the height range, R_h, the average film thickness, $\langle t \rangle$, the relative absorption intensity, I_{abs}, the change in Stokes' shift, $\Delta\lambda_{PL}$ and a de-broadening parameter. The screening experiment is designed and built using JMP statistical software developed by SAS Institute Inc. JMP uses a random seed to build an experiment consisting of a number of samples with associated factor values for their fabrication. The program ensures by the arrangement of factor values that the parameter space is explored thoroughly in as few samples as possible.

As discussed through Chapter 2.3 an ideal geometry to apply such coatings to would be that of a multi-cylindrical structure [1], though here only square planar type structures are explored. Multi-cylindrical PC substrates were produced for this study by injection moulding but were found to be unsuitable due to the solvents being used for the coating. Instead standard microscope slides of 75 mm x 25 mm x 1 mm (hence $G = 9.375$) are employed and are made of soda-lime glass having refractive index $n_3 = 1.52$. It is important for the undoped core of the surface doped LSC to have a higher refractive index than the doped coating, which is in this case PMMA with $n_2 = 1.492$ and this is interfaced with air having $n_1 = 1$. This is a requirement due to the laws of refraction as fluoresced light in the active coating will not be waveguided through the core if $n_2 > n_3$ [2]. Instead in such a device light would be trapped in the active coating which is by design a highly absorbing medium and hence strong attenuation is expected. Optimisation by reduction of mean path length travelled through the LSC is achieved for minimisation of the ratio n_2/n_3. This must be optimised in tandem with n_1/n_2 due to Fresnel reflection (Eqs. (2.2.2) and (2.2.3)) and trapping efficiency (Eq. (2.2.4)) and, as seen in the last chapter, if solvation is employed the orientational polarisability must also be optimised through n_2, as described by Eq. (5.2.1).

6.2 Spray Coating Parameter Space

What follows now is a detailed look at the spray-coating deposition method, starting with specific consideration of the functional parameters, or factors. This discussion will follow on to develop the output metrics, or *responses*, which shall be used to ascertain the effectiveness of a given set of input factors at depositing active coatings onto soda-lime glass microscope slides. Chapter 3.4 provides a diagram and technical details of the Prism Ultra-Coat 300 spray-coating system and its

operation. Fig. 6.2.1 shows a schematic of a spray deposition to help illustrate the parameters in the process.

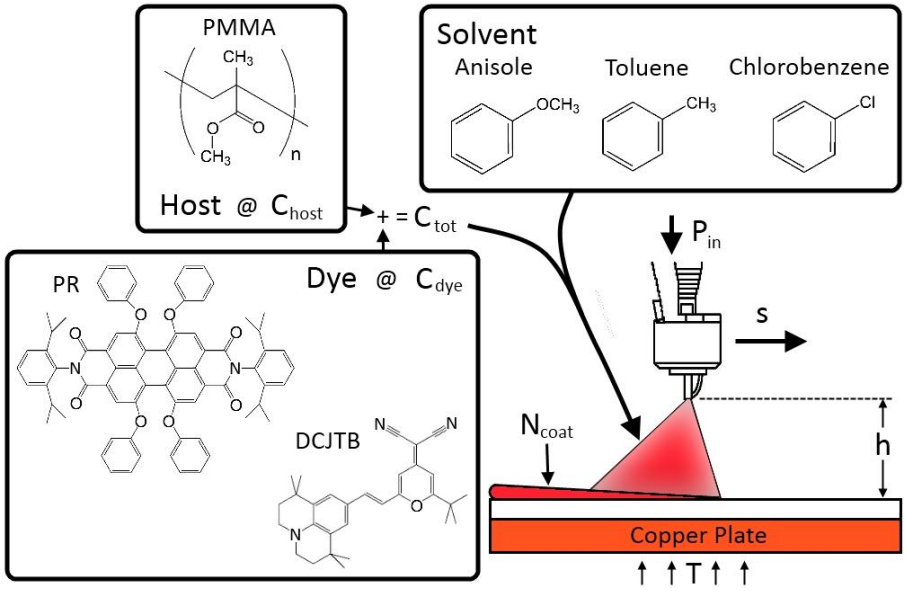

Figure 6.2.1: Schematic infographic of a spray deposition showing the factors chosen for optimisation and the materials employed. The spray head moves with speed *s*, at height *h* with injection pressure, P_{in}. The LSC concentration formulation consists of a host:dye blend with total concentration, C_{tot}, and dye concentration, C_{dye}, in some solvent and is deposited onto a glass microscope slide at temperature, *T*. The number of coats, N_{coat}, is also considered.

In spray coating there are many variables that need mutual optimisation, from those of the material blend to be sprayed to those of the spray system itself. These include the dye and host materials, their concentrations, choice of solvent, spray head height, speed and injection pressure, to name just a few. Clearly taking either a trial and error or a full factorial approach over such a range of parameters, many of which are continuous in nature and thus occupy a very large space, is nonsensical. Trial and error approaches look at detailed cross sections through the parameter space by picking one factor and varying it continuously to find the optimum, and then moving on to the next factor. This never captures the full response surface, unlike the full factorial study which explores the whole parameter space but is very costly in materials and time. By contrast the screening study design saves time and materials by exploring the entire response surface with as few samples as necessary. Screening experiments employ the idea of the sparsity principle (sparsity-of-effects principle), which advises a screening approach to the problem of having many known factors of which most will be essentially inactive and/or trivial in the responses that are of interest. The sparsity-of-effects principle assumes that the process under consideration is dominated by only a few key effects of statistical significance [3,4].

Here the sparsity principle is applied to the spray coating technique in the form of an effect screening experiment. Nine key factors were chosen for mutual optimisation, discussed in the next

paragraphs, and these are either continuous or discrete in nature. The factors are illustrated in Fig. 6.2.1 and the parameter settings are tabulated in Table XII by sample. Those parameters that are continuous are designated physically reasonable maximum and minimum values for which the deposition system can operate. Discrete factors are designated 2 or 3 discrete values.

First is the total concentration of the polymer:dye blend, C_{tot}, which is the sum of the host polymer (PMMA) and dye concentrations in units of g/l. Some experimentation was necessary to appreciate the tolerances of the spray coating system in this regard; if C_{tot} is set too high then we find higher pressures are required and eventually the material loading is too great and one observes polymer threads forming mid-air in streamers like candyfloss. A maximum workable concentration for PMMA loading was found to be roughly at C_{tot} = 120 g/l and a minimum was set at C_{tot} = 50 g/l.

The dye concentration, C_{dye}, in wt% units was also chosen to see if this affects the film forming properties and because it is expected to have strong importance on absorption processes. Minimum and maximum were taken to be 0.3% and 1% respectively. This range is chosen by appreciation of dye extinction and concentration quenching of quantum yield; a certain concentration is required to absorb incoming light but too high a concentration will result in lower rates of radiative recombination. The arguments for these values are explored in more detail shortly when considering goal setting for the thickness response, <*t*>.

The dye type is chosen to understand the influence of particular dye properties. This is set to be a two-level categorical factor with the non-polar dye PR and the polar dye DCJTB favoured for this study. DCJTB exhibits stronger intrinsic absorption than PR but has lower quantum yield at any given concentration.

Next the solvent used is designated a 3-level categorical with polar solvents chlorobenzene (CB), anisole (AS) and non-polar toluene (T) chosen for study. Toluene has a lower boiling point (110.6°C) than CB (131.7°C) or AS (155.5°C) and so films from this solvent will dry faster, which may have strong influence on the resultant film particularly with regards to surface roughness.

Injection pressure, P_{in}, is an important continuous factor characterising the rate of flow of material onto the ultrasonic tip of the spray head. Higher pressures should result in greater thicknesses but there is a need to explore what other effects pressure may have, particularly regarding film surface effects. Some experimentation was needed to properly ascertain workable pressure ranges with the concentrations of solution used. If the pressure is too low at a given concentration then little material is injected and a proper spray is not formed. Too high a pressure and the spray becomes a

gush, material is wasted and the substrate becomes drenched. Pressures between 50 and 200 mbar were found to be suitable for the concentration ranges used here.

Substrate temperature, *T*, controlled by hot plate is a continuous factor whose value range was chosen though experimentation. It was found that at temperatures over 70°C the films would appear very rough and wetting issues began to appear making the film coverage patchy. The cleanroom is maintained at a temperature of around 21°C so 30°C was chosen as a controllable lower boundary and 50°C as an upper boundary.

Spray head height, *h*, was chosen as a continuous factor with minimum and maximum chosen as 40 and 70 mm respectively. If spraying is commenced from lower than 40 mm the spray is unable to cover the whole substrate area in its pass. At heights above 70 mm the spray density becomes quite low making for patchy coverage under some conditions of solution properties and pressure.

Spray nozzle speed, *s*, is another important property of the spray coater mechanics to include and is designated minimum and maximum at 40 and 70 mm s^{-1}. Similar arguments to those above apply; too fast and poor coverage is achieved and too slow and the substrate can become drenched.

Finally the number of coats, N_{coat}, is chosen as a 3-level categorical factor with values 1, 2 and 3. These were chosen arbitrarily for ease of sample fabrication and will have important effects on the thickness of the sample produced, and therefore how much light it can absorb. Adding extra coats may disrupt surface properties such as roughness, however, which would have a negative impact on reflection loss mechanisms. Visually it can be seen that spraying multiple layers can negatively affect the homogeneity of the PMMA:dye coating. Figure 6.2.2 shows two photographs of samples in this study to highlight this point (see Table XII).

Figure 6.2.2: Photographs of samples S09 (N_{coat} = 3), on left, and S10 (N_{coat} = 1), on right, showing how extra coats can affect thin film homogeneity. See Table XII for more details on these samples.

The JMP DoE has no physical understanding and will happily combine highly incompatible parameters, such as low boiling point solvents with high substrate temperatures. Avoiding this problem requires careful thought of the chosen variables, their minima and maxima and, in some cases, manual retuning of the DoE configuration. In such manual retuning care must be taken to avoid repeated arrangements of the factors so as to maintain the purpose of the screening study; that being to explore the whole parameter space with as few samples as possible.

The resultant screening DoE is summarised in Table XII. A total of 24 samples are required including centre-point values, which are samples S10 through to S15. These centre-point values serve the purpose of a check for any statistical model applied to the results and to detect any higher order effects in that assumed model.

	Pattern	C_{tot} (g/l)	C_{dye} (wt%)	P_{in} (mbar)	T (°C)	h (mm)	S (mm s^{-1})	Dye	N_{coat}	Solvent
S01	-------+0	50	0.3	50	30	40	40	DCJTB	3	AS
S02	-------++	50	0.3	50	30	40	40	DCJTB	3	T
S03	---++++--	50	0.3	50	50	40	70	PR	1	CB
S04	--+-++-00	50	0.3	200	30	70	70	DCJTB	2	AS
S05	--++--+0-	50	0.3	200	50	40	40	PR	2	CB
S06	-+--+-+-+	50	1	50	30	70	40	PR	1	T
S07	-+-+-+-0+	50	1	50	50	40	70	DCJTB	2	T
S08	-++--++-0	50	1	200	30	40	70	PR	1	AS
S09	-++++--+-	50	1	200	50	70	40	DCJTB	3	CB
S10	000000112	85	0.65	120	40	55	55	DCJTB	1	AS
S11	000000111	85	0.65	120	40	55	55	DCJTB	1	CB
S12	000000113	85	0.65	120	40	55	55	DCJTB	1	T
S13	000000212	85	0.65	120	40	55	55	PR	1	AS
S14	000000211	85	0.65	120	40	55	55	PR	1	CB
S15	000000213	85	0.65	120	40	55	55	PR	1	T
S16	+----+++-	120	0.3	50	30	40	70	PR	3	CB
S17	+--++---0	120	0.3	50	50	70	40	DCJTB	1	AS
S18	+-+-+-+0+	120	0.3	200	30	70	40	PR	2	T
S19	+-++-+--+	120	0.3	200	50	40	70	DCJTB	1	T
S20	++--++-0-	120	1	50	30	70	70	DCJTB	2	CB
S21	++-+--+00	120	1	50	50	40	40	PR	2	AS
S22	+++------	120	1	200	30	40	40	DCJTB	1	CB
S23	++++++++0	120	1	200	50	70	70	PR	3	AS
S24	+++++++++	120	1	200	50	70	70	PR	3	T

Table XII: Parameter screening design of experiment showing the factor values for the full set of 24 samples. The pattern column shows the left to right minima/maxima ordering where '-' is the minimum value, '+' is the maximum value and '0' represents centre-point values. '1', '2' and '3' are centre-point values for categorical factors.

6.3 Definitions of Response Metrics

From the factors laid out in Table XII we next turn to the responses which characterise the quality and performance of the resultant spray-deposited films. These responses naturally tie in closely as metrics of LSC performance with respect to the components of optical efficiency defined through Chapter 2.2. Seven such response metrics have been defined as shall now be detailed.

A high quality LSC thin film coating will necessarily be highly smooth across the whole of its surface as higher roughness will impact on reflection efficiencies, both Fresnel (η_{fr}) and TIR (η_{TIR}). Nanoscale imperfections in the surface are out of the measurement range of profilometry so as to quantify η_{TIR} in some manner but the microscopic scale roughness referred to here will also have a strong impact on overall efficiency. To characterise this critical property three metrics were chosen; the mean roughness ratio, $\langle R_R \rangle$, the standard deviation of this, σ_R, for roughness variation across the sample, and lastly the height range, R_h. A Veeco DekTak profilometer is used to measure these quantities and is done in a standardised way across all samples. Figure 6.3.1 shows a photograph of sample S01 (see Table XII) with dashed lines roughly marking the scan positions, labelled a), b) and c), which are of 10 mm in length.

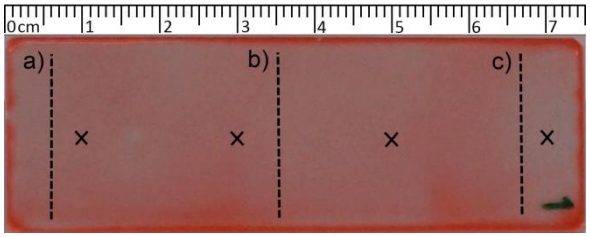

Figure 6.3.1: Annotated photograph of sample S01 showing, in dashed lines, the three 10 mm profile scans performed on each sample. The crosses indicate the positions of the self-absorption measurements as a function of excitation point distance from the emission edge, described shortly. The acquisition edge is taken as the right-hand edge of this image. The edges of these microscope slides are polished to a fine optical quality by the manufacturer.

The mean roughness ratio is then defined by the mean for each of the three profile scans on each sample. For each profile the roughness is determined by the ratio of the mean height between peaks, $\langle \Delta h \rangle$, and the mean distance between peaks, $\langle \Delta x \rangle$, as per Eq. (6.3.1);

$$R_R = \frac{\langle \Delta h \rangle}{\langle \Delta x \rangle} \qquad (6.3.1)$$

These quantities are determined from a peak detector analysis of each profile producing a graphical output as shown in Fig. 6.3.2. Note that the profiles necessarily have to be smoothed for this analysis otherwise multiple false peaks will be detected.

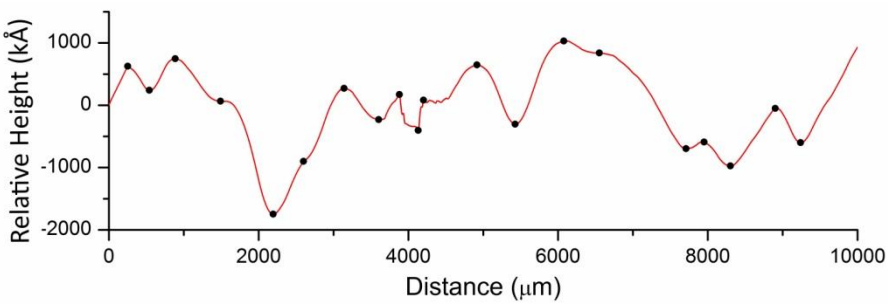

Figure 6.3.2: Smoothed 10 mm profile scan (red line) for S01 at position a), as indicated in Fig. 6.3.1, showing the peaks detected and used in the analysis (black points).

The lower value $<R_R>$ takes the better and should ideally be well below 1%. The standard deviation of this, σ_R, is indicative of the sample global and also would desirably be low thus characterising a more even coating across the entire surface of the substrate. Lastly for this characterisation the height range, R_h, is used as to further characterise the variability across the sample.

The next two metrics have been chosen as indicators for absorption efficiency, η_{abs}, though they do not characterise the radiometric absorption itself. Instead the mean film thickness, $<t>$, and the relative integrated absorption intensity, I_{abs}, are measures of how much material is deposited and what the relative absorption strengths from sample to sample are, respectively. To achieve strong absorption in the spectral region of the dye a thickness on the order of tens to hundreds of microns is required for dye concentrations ranging from 1 wt% to 0.1 wt%. The absolute values of $<t>$ required can be explored more thoroughly via the Beer-Lambert law given in Eq. (2.2.5). For the purposes of this screening study these metrics will be considered in relative terms. $<t>$ is determined from profilometry of samples by scratching through the film and scanning a profile across the gap. This is done after all other measurements are complete as the samples are damaged in the process. I_{abs} is determined from absorption spectra in three positions per sample, judged by eye to exhibit roughly the mean optical density of the sample, which are averaged and then integrated, as described in Eq. (6.3.2). The absorption spectrum, $S_{abs}(\lambda)$, is determined via the transmission spectrum and Eq. (3.3.1).

$$I_{abs} = \int_{\lambda_{min}}^{\lambda_{max}} \frac{S_{abs,1}(\lambda) + S_{abs,2}(\lambda) + S_{abs,3}(\lambda)}{3} d\lambda \qquad (6.3.2)$$

Figures 6.3.3 and 6.3.4 show the absorption spectra in relative intensity units thus recorded for DCJTB and PR respectively. A clear progression in absorption intensity can be seen from these spectra with the trivial causal link to both film thickness and dye concentration.

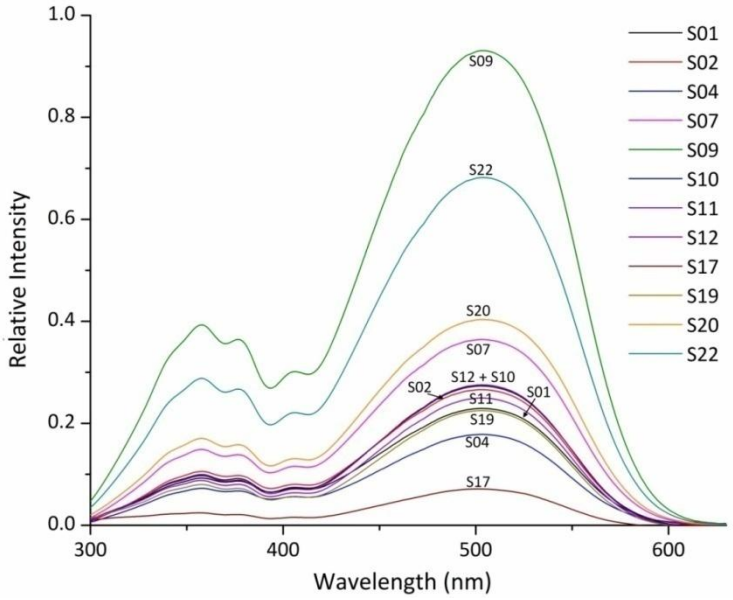

Figure 6.3.3: Averaged relative intensity absorption spectra for DCJTB samples.

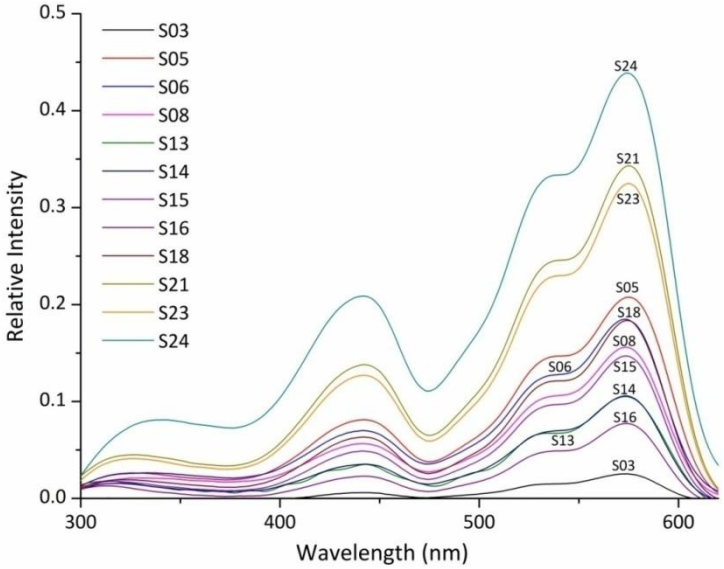

Figure 6.3.4: Averaged relative intensity absorption spectra for PR samples.

The final two metrics are the change in Stokes' shift, $\Delta\lambda_{PL}$, and the de-broadening parameter, Δw, relate directly to the self-absorption loss mechanism, quantified by the efficiency η_{self}, and use a spectroscopy method specific to this chapter. This method shown in Fig. 6.3.5. The excitation source is a 405 nm GaN diode laser with a 1 mW output which is intensity modulated using a continuously variable reflective ND filter. This is directed perpendicular to the sample's coated surface. The sample is positioned so that the laser can be scanned across the film surface and any unabsorbed excitation light passes through and can be ignored. One of the short concentration edges of the sample faces towards a lens based collimator which collimates light into a fibre optic. Trapped fluorescence is concentrated along the edges and the lens collimator captures part of this at the *acquisition edge* for measurement. The collimator lenses have focal lengths of 10 cm with a diameter

of 23.5 mm giving a numerical aperture of *NA* = 0.117. This low *NA* means that some of the wide angle acquisition edge emission is lost. Additionally the acquisition edge is 2 mm in width, which is wider than the lens itself and hence focusing the image of this onto a circular fibre optic aperture is going to include losses. The fibre optic is then connected to an ORIEL Multispec spectrometer (cooled to 40°C) via a Shamrock reflective optics monochromator with the adjustable slit set to 0.1 mm and with a diffraction grating with 300 grooves mm^{-1}, blazed at 500nm and having a range of 280 nm.

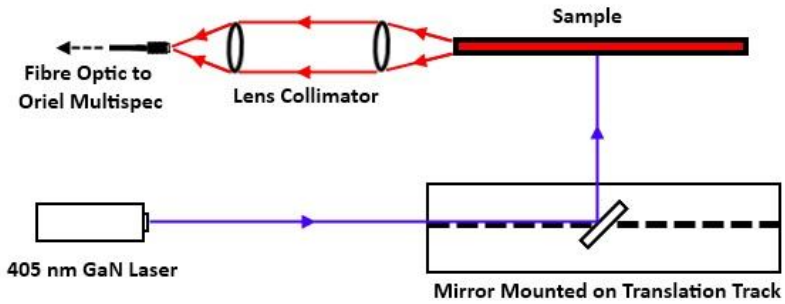

Figure 6.3.5: Schematic of the measurement setup used to determine the response metrics of Stokes' shift, $\Delta\lambda_{PL}$, and the de-broadening parameter, Δw. the 405 nm GaN source is directed onto a mirror mounted on a translation track allowing the point of excitation across the sample to be adjusted. Light exiting the acquisition edge is collimated onto a fibre optic for delivery to the spectrometer.

From this set up four measurements per sample are taken as depicted by the crosses in Fig. 6.3.1. These are 2cm apart starting with the first excitation point being 0.5 cm from the acquisition edge. Note that absolute edge emission is not measured but by adjusting the laser intensity a strong signal can be collected and comparison between the normalised edge emission spectra can be drawn. It is a comparison between the spectral shape and peak energy that is of interest here for characterising the self-absorption.

The first self absorption metric from this measurement is the change in Stokes' shift, $\Delta\lambda_{PL}$, due to self-absorption over a 6 cm change in excitation position relative to the acquisition edge. This is distinct from the Stokes' shift, $\Delta\lambda$, as it is the change in $\Delta\lambda$. The increased path length through the device as a function of distance from the acquisition edge results in truncation of the blue tail of the emission spectrum giving rise to an apparent redshift. Thicker films and higher concentrations will be expected to magnify this effect. Because absolute edge intensity is not known the spectra are normalised by the maximum, before $\Delta\lambda_{PL}$ is determined.

The final metric, the de-broadening parameter, Δw, is complimentary to that above and uses the fact that the full width at half maximum, w, (FWHM) of a spectrum is reduced by self-absorption. This is because the red-shift is not a result of an actual shift in the emission energy, unlike the case of solvation, but a consequence of preferential attenuation of bluer emission. By fitting a Gaussian

profile to a given spectrum the FWHM can be estimated and then a change, Δw, can be measured in the FWHM as a function of excitation distance from the acquisition edge. Δw is thus a de-broadening parameter due to self-absorption. At first glance choosing a Gaussian fit, rather than using the FWHM of the emission spectrum, appears incorrect since DCJTB and especially PR do not have Gaussian emission line shapes. However, for DCJTB it is a reasonable approximation with very little difference either way and for PR using the FWHM of the emission spectrum is very problematic. This is because as self-absorption reduces the primary peak of the PR emission spectrum the FWHM can actually increase. This problem is created by the fact there are two peaks in the PR spectrum and so approximating to a Gaussian provides a solution. This issue highlights than measuring de-broadening using the FWHM is not ideal for spectra with more than one transition.

An example set of spectral data is shown in Fig. 6.3.6 a) for S02 in which the de-broadening can be seen. Fig. 6.3.6 b) shows the FWHM of the Gaussian fits to each of the spectra in Fig. 6.3.6 a), with a quadratic fit to the data. From Fig. 6.3.6 b) the change in FWHM, Δw, is not exactly linear but to a first order approximation it is taken to be so. The response parameter takes the total de-broadening between excitation distances of 0.5 and 6.5 cm to characterise the spray-coated samples.

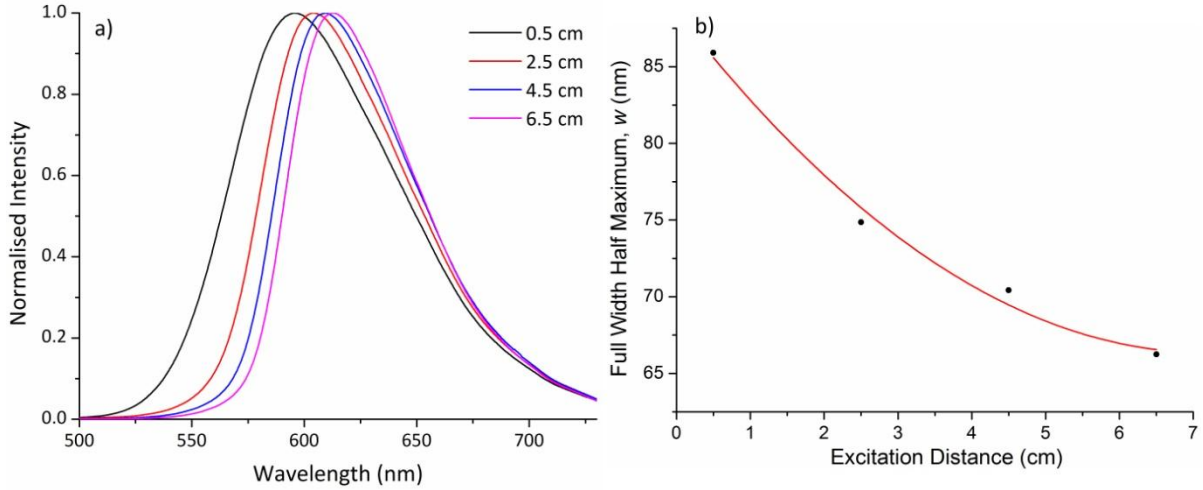

Figure 6.3.6: In a) the normalised acquisition edge emission spectra for sample S02 (DCJTB) are shown to exhibit the redshift in peak emission and de-broadening due to self-absorption. In b) the full width half maximum of Gaussian fits to the spectra in part a) are shown with a quadratic best fit.

6.4 Setting Response Goals

The seven metrics defined above, $\langle R_R \rangle$, σ_R, R_h, $\langle t \rangle$, I_{abs}, $\Delta\lambda_{PL}$ and Δw, are determined for each sample from Table XII. The analysis of these data then follows a multivariate approach, which involves plotting each factor and response against each other and looking at the correlation so as to discover which factors and responses influence one another. This is conveniently shown through leverage

analysis and prediction profiling, based on a least squares fitting model, and further characterised using the Derringer-Suich desirability function, given in Equation (6.4.1).

$$D = (d_1 \times d_2 \times \ \ldots \times d_n)^{\frac{1}{n}} = \left(\prod_{i=1}^{n} d_i\right)^{\frac{1}{n}} \qquad (6.4.1)$$

Where D is the desirability, d_i is the individual desirability function for the ith response and n is the total number of responses, which is $n = 7$ in this case. For each response d_i must be determined and will range from 1 to 0 depending on how well the individual goals for each response were met. The goals and limits for each response are outlined in Table XIII.

In this study goals are set for minimising or maximising a given response toward the lower or upper limit respectively. The specific limit to which the goal is set towards is chosen to reflect the best film quality and performance. It should however be recognised that some of these goals may be mutually exclusive. For example; maximised absorption, I_{abs}, and minimised self-absorption losses must be carefully optimised together since higher absorption of incident light will also mean increased self-absorption. Similar concerns apply between $\langle t \rangle$ and the self-absorption parameters, $\Delta\lambda_{PL}$ and Δw. This is because increasing the film thickness or the absorption of incident light will result in greater attenuation of waveguided light travelling to the acquisition edge of the LSC. Desirability analysis will therefore be used to try and determine the optimum conditions and deposition recipe for these conflicting parameters.

d_i	Response	Goal	Lower Limit	Upper Limit
d_1	$\langle R_R \rangle$	Minimise	0.01 µm	8 µm
d_2	σ_R	Minimise	0 %	100 %
d_3	R_h	Minimise	0.01 µm	20 µm
d_4	$\langle t \rangle$	Maximise	0.1 µm	50 µm
d_5	I_{abs}	Maximise	0.1	150
d_6	$\Delta\lambda_{PL}$	Minimise	1 nm	50 nm
d_7	Δw	Minimise	1 nm	50 nm

Table XIII: Response goals with the associated upper and lower limits built into the effect screening model. Desirability for a particular response is calculated by the goal and the limits.

Each response's desirability can be defined clearly in light of the goal and the targeted limit. For a minimisation goal the response desirability, d_i, will be 1 at or below the lower limit and 0 at or above the upper limit, and a linearly varying fraction of 1 for points in between. The opposite is true for a maximisation goal. For example; in the case of the roughness ratio, $\langle R_R \rangle$, the goal is the lower limit,

set at 0.01 µm. If the measured value of $<R_R>$ for a given sample equals the lower limit or below then $d_1 = 1$. If it was somewhere between the lower and upper limits then a linear equation between the limits provides the desirability, for example if $<R_R> = 3$ µm then $d_1 = 0.6257$. It may be the case that the goals set are too ambitious for the deposition technique, which will be revealed by the results of the leverage and desirability analysis. Of course what limits are chosen will inevitably have an impact on the desirability so care must be taken to choose goals applicable to a near ideal deposited film and plausible limits.

For the mean roughness ratio, $<R_R>$, the limit chosen is an order of magnitude higher than the DekTak profiler's precision edge and represents a surface which appears uniform to the eye. In fact visual acuity is not so nearly so sharp, tens of microns is the best precision for features on a 2D plane, but surface roughness is more easily observable under illumination through reflection and shadowing effects. It would be a difficult matter to numerically model LSC optical efficiency, η_{opt}, as a function of the surface roughness, as quantified by $< R_R>$, and so a precision limited value is preferred. The upper limit at 8µm is representative of a highly rough surface that would be appear dull in hue due to high levels of scattering.

For the standard deviation of the roughness ratio, σ_R, which is as a percentage of $< R_R>$, a minimisation goal of 0% is chosen as an absolute target. This parameter looks at the global variance in roughness and so characterises a globally consistent film, which is essential for a finished coating product.

For height range, R_h, minimum limit of 0.01µm is chosen, again the precision limited value is preferred. The upper limit at 20µm is greater than the upper limit for $< R_R>$ because of global variance in film thickness and roughness. This variance means that R_h tends to be greater than $< R_R>$.

For film thickness, $<t>$, the goal is at the upper limit of 50µm. This has been determined as a rough target by use of models generated using the Beer-Lambert law given in Eq. (2.2.5). Having measured the absorption coefficients (see Chapter 2.4.1) Eq. (2.2.5) can be used to model how absorption of sunlight depends on film thickness and dye concentration. Figures 6.4.1 and 6.4.2 show how the global irradiance spectrum at AM 1.5 [5] is absorbed by various thicknesses of PMMA containing DCJTB at a concentration of 0.3 wt% (7.844×10^{-3} M) and PR at 0.5 wt% (6.167×10^{-3} M), respectively.

From Figures 6.4.1 and 6.4.2 it can be inferred that a film thickness of around 50 µm is necessary at a fairly high concentration of 6.167×10^{-3} M for PR. DCJTB is more intrinsically absorbing than PR, as can be seen by comparing Figures 2.4.7 and 2.4.11, and it has a lower molecular weight hence it absorbs more at both the same molar concentration and the same weight percentage concentration. This is

why different concentrations were used for the plots; so as to capture the proper range of depths for each dye.

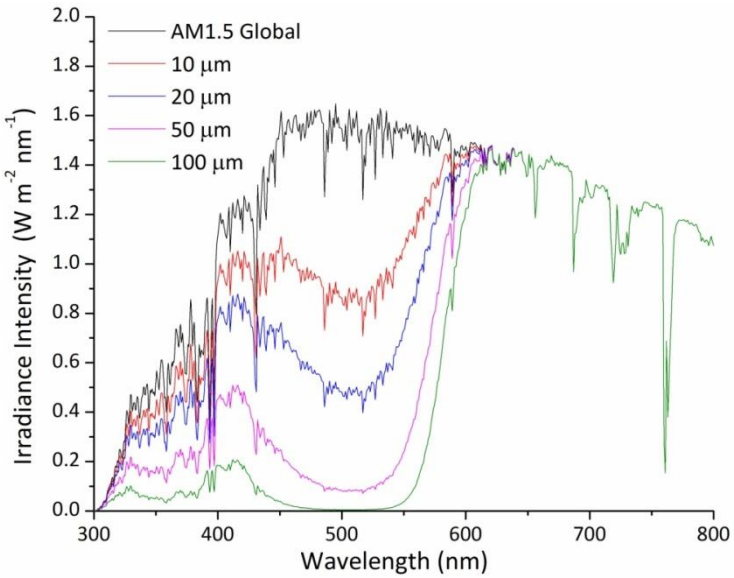

Figure 6.4.1: Absorption of the AM1.5 global irradiance spectrum as a function of depth through a PMMA film doped with DCJTB at 0.3 wt% (7.844×10^{-3} M). Saturation occurs at around 50 µm but with a back reflector under the LSC then around 30 µm film thickness is required.

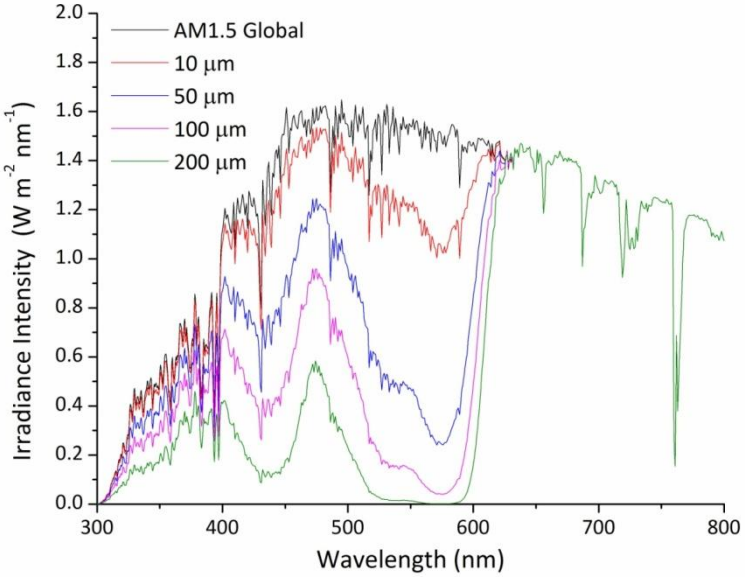

Figure 6.4.2: Absorption of the AM1.5 global irradiance spectrum as a function of depth through a PMMA film doped with PR at 0.5 wt% (6.167×10^{-3} M). Saturation occurs at around 100 µm but with a back reflector under the LSC then around 50 µm film thickness is required.

An important point to note here is that increasing concentration to reduce the required film thickness is going to be negatively impacted by concentration quenching effects. One can take this side exploration of thickness optimisation a step further by considering, in absence of other effects, that an LSC has an optical efficiency proportional to the product $\eta_{abs}\eta_{QY}$. The absorption efficiency,

η_{abs}, for a given film thickness is the integral of the AM1.5 global spectrum minus the same spectrum after absorption by a given dye and film thickness. By expressing this absorption integral as a fraction of the total and multiplying by the associated quantum yield, η_{QY}, one gets an efficiency estimation for the fluorophores. This enables the optimisation of their properties for thin film LSCs and as is shown in Fig. 6.4.3 for DCJTB and PR at several concentrations as a function of film thickness.

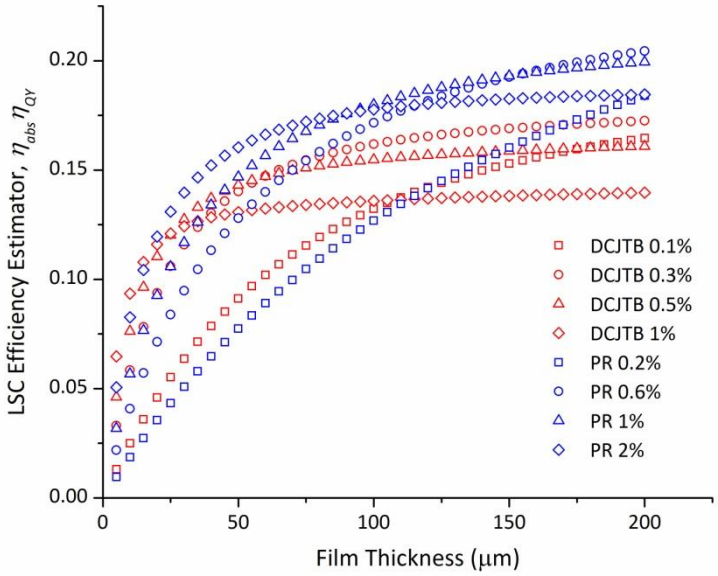

Figure 6.4.3: The LSC efficiency estimator, $\eta_{abs}\eta_{QY}$, is plotted here against film thickness for various concentrations of DCJTB and PR in PMMA. Weight percentage concentrations are chosen so as to have comparable molar concentrations; so 0.1 wt% DCJTB is similar to 0.2 wt% PR, 0.3 wt% DCJTB is similar to 0.6 wt% PR and so on.

Fig. 6.4.3 shows PR to be the best dye due to its higher η_{QY} at a given concentration, though DCJTB plateaus at lower film thickness due to its higher intrinsic absorption. The figure also reveals, with careful evaluation, the optimum thicknesses and concentrations to use. The fluorophore concentration need to be minimised due to reduction of quantum yield by concentration quenching (see chapter 7). Additionally the film thickness needs to be minimised for the practicalities of fabrication. For DCJTB a concentration between 0.3 wt% and 0.5 wt% will be ideal with a thickness at around 30 to 40 µm. As can be seen at this point the absorption has not saturated to a plateau but with a back reflector it will get close; one can consider a back reflector to essentially double the effective film thickness. For PR the concentration will be best at around 0.6 wt% at a thickness of 100 µm. Notice how in both cases for DCJTB and PR the circles (0.3 wt% and 0.6 wt% respectively) end up the highest in collection efficiency as characterised here. This comes about due to the higher quantum yields, and hence lower concentration quenching, allowing more energy to be harvested for thicker films. One can see that for film thicknesses well above 200 µm the lowest concentrations (squares) are likely to reach even higher values of $\eta_{abs}\eta_{QY}$ but such film thicknesses become

impractical to achieve. The curves in Fig. 6.4.3 are only part of the story as this efficiency evaluation lacks representation of self-absorption effects, which are highly dependent on film thickness.

The next response goal to discuss is that of the relative absorption intensity, I_{abs}, whose desirability is a maximum and given the value 300. Considering Figs. 6.3.3 and 6.3.4, this is defined by considering the number of total possible absorption counts across a 300 nm range with 1nm bin sizes. The lower limit here is taken as 0.1, which is representative of almost negligible absorption.

Lastly for both $\Delta\lambda_{PL}$ and Δw the goal set is a minimisation to represent a small self-absorption. These goals were again somewhat arbitrary; it is expected that at least a few nanometres difference will be observed in both the Stokes' shift and Gaussian FWHM and so 1 nm is an appropriate minimum. The maximum at 50 nm is informed by looking at spectra such as in Fig. 6.3.5; a 50 nm peak shift solely due to self-absorption would necessarily require most of the blue tail and peak energy, around 50% of the total, to be removed. In fact because of the red-tail of absorption cutting off somewhere over 600 nm there is a limit to amount of self-absorption possible. It is difficult to exactly measure this cut off point because of limitations in the precision of spectroscopy measurements. Based on these considerations a 50 nm shift is taken to roughly represent total self-absorption.

This chapter has thus far examined the screening study design with focus on the input factors and measured responses. Responses have been rigorously defined in terms of their measurement and the goals associated with them. The aim of this study is to reach conclusions on the strength of a given factor's influence on a given response and thus form a statistically informed spray coating methodology. To do this the measured responses are analysed using JMP which looks at the correlations between factors and responses and builds a model around these interactions. It is important to understand that correlation does not imply causation so we have to be careful when drawing conclusions to avoid non-physical interpretations. Also note that, while the work presented here does not include higher order interactions between factors and response outcomes, such interactions were analysed but found not to be statistically significant.

6.5 Results and Discussion

With the responses measured as defined above JMP is used to perform a standard least squares fit, assuming a normal distribution in the response data, between all factors and responses. The results can then be displayed via various statistical methods, one of the most useful of which is effect leverage analysis.

6.5.1 Effect Leverage Analysis

Effect leverage analysis is performed response by response and looks at the influence of each factor by plotting the response residuals without the given factor against the response residuals with that factor included. Thus there are nine leverage plots for each response, too many to display here, which are usefully combined into a whole model leverage plot where the measured response is plotted against the predicted response from the least squares model. Figure 6.5.1 shows whole model leverage plots for the roughness parameters $\langle R_R \rangle$, σ_R and R_h.

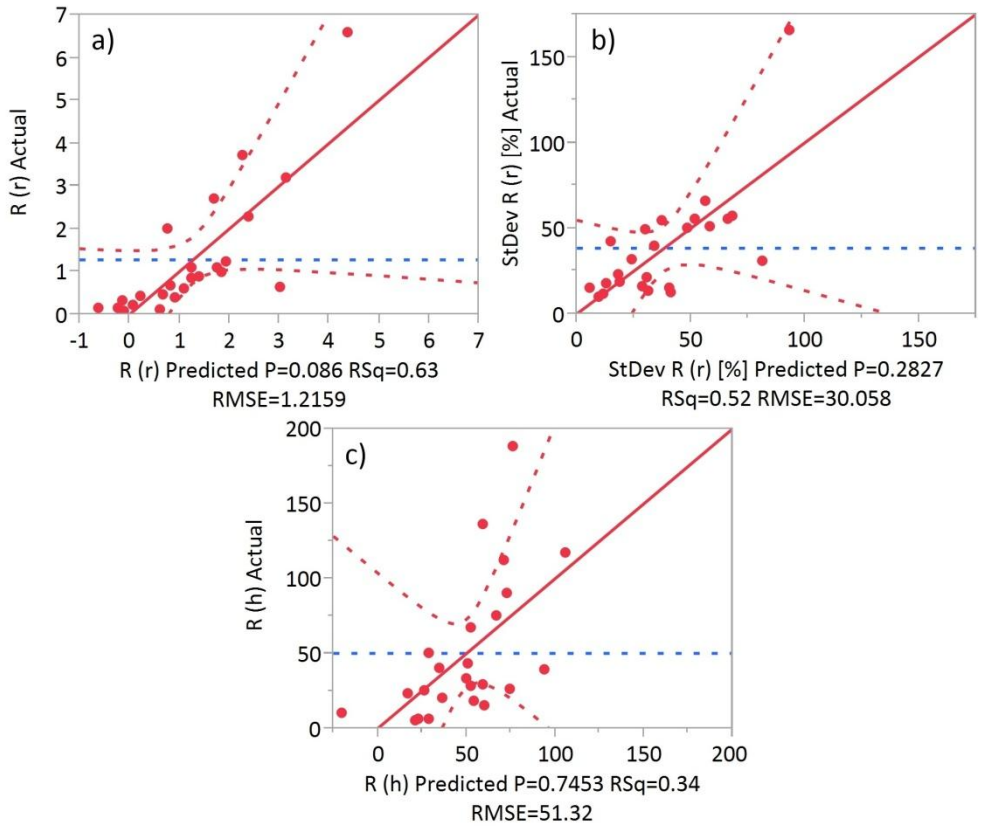

Figure 6.5.1: Leverage plots of the whole fitted least squares model including each of the nine factors for each of a) $\langle R_R \rangle$, b) σ_R and c) R_h. Data points refer to the measured and predicted response values for each sample, the dashed-blue line is the y-axis mean for the measured response values, the solid-red line is the least squares fit and the dashed-red lines are the 5% significance levels. The P value, R^2 and RMSE goodness of fit statistics are also included.

What is immediately clear from Fig. 6.5.1 is that these responses are not significantly influenced by the chosen factors. The mean roughness ratio $\langle R_R \rangle$ is the best of these with P = 0.086, or over 90% confidence which is not regarded significant. This is seen by the dashed-red confidence intervals enclosing the dashed-blue measured response mean. The other goodness of fit statistics further corroborate this impression from the leverage plots, as shown in Table XIV. One also notices, particularly for R_h, that the gradients are unstable which is seen by the angle with which the red-

dashed lines depart from least squares fit line. Such instabilities are anathema to a model's predicting power and come from large sources of unexplained variance.

Why is this the case? It was expected that the roughness of the deposited film would vary more substantially with the chosen factors, particularly with solvent, T, C_{tot}, P_{in} and N_{coat}. Despite there being obvious difference in roughness between samples these results show that it is not possible to strongly attribute these differences to the chosen factors. It could be concluded from this that controlling surface roughness, to the limits set in Table XIII, by spray-coating deposition will be very challenging though there may be other factors that weren't considered here. This does not bode well for fine tuning the deposition so as to reduce reflection losses at the interface.

Figure 6.5.2 shows leverage plots for the thickness and relative absorption intensity parameters, <t> and I_{abs}, respectively. <t> is seen to have a strong dependence on the fitted model which indicates that there is significant influence on this response from many of the factors. Only the height, h, of the spray head had a no confidence result and N_{coat}, P_{in} and s are factors with a high significance on <t>. All other factors had a borderline significance. This is a somewhat trivial result since when more material is deposited one would expect greater film thickness. More coats, higher pressure and slower spray head speeds would all be expected to increase film thickness. These relationships do show the leveraging process is working, which acts as a test of the statistical method; if there was no significance on <t> then problems with the model would need consideration.

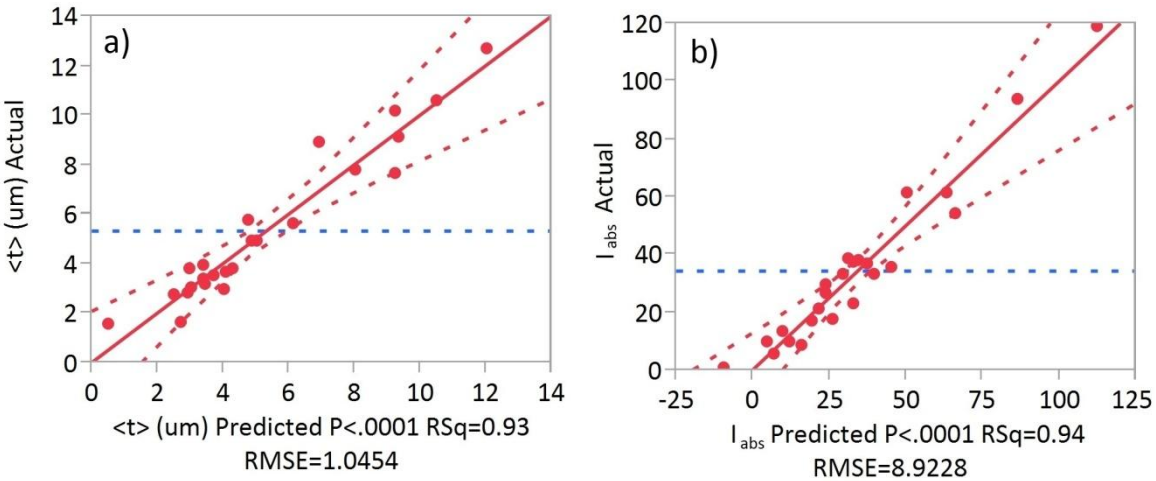

Figure 6.5.2: Leverage plots of the whole fitted least squares model including each of the nine factors for a) <t> and b) I_{abs}.

The integrated absorption, I_{abs}, effect leverage shows significance above the 99.9% confidence borderline in the model. This comes due to strong confidence in nearly all factors except C_{tot} and h. The leverage plots for I_{abs} by the factors head height, h, and dye concentration, C_{dye}, are shown in Fig.

6.5.3 to illustrate factors of negligible and strong influence. These factors have the lowest and highest significance for I_{abs}, respectively.

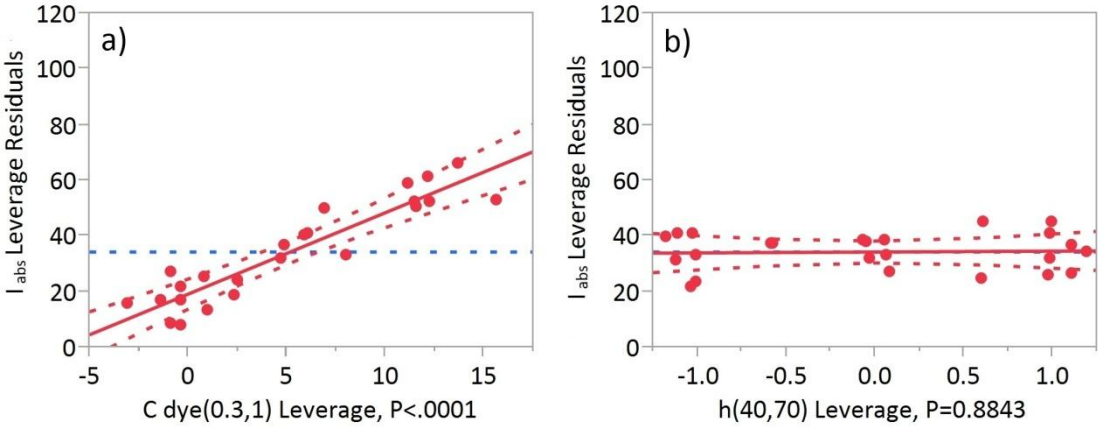

Figure 6.5.3: Leverage plots for I_{abs} against the factors a) C_{dye} and b) h.

Clearly increased dye concentration has a massive positive effect on the total absorption of incident radiation from the xenon arc lamp used in the spectrometer. This is to be expected and is a trivial relationship better described by the Beer-Lambert law. Similarly a strong relationship to the dye type, because of intrinsic absorption strength, is seen and to be expected. Strong ties with the thickness parameter also show in the mutually high confidence relations with N_{coat}, P_{in} and s.

Figure 6.5.4 shows leverage plots for the self-absorption parameters, $\Delta\lambda_{PL}$ and Δw.

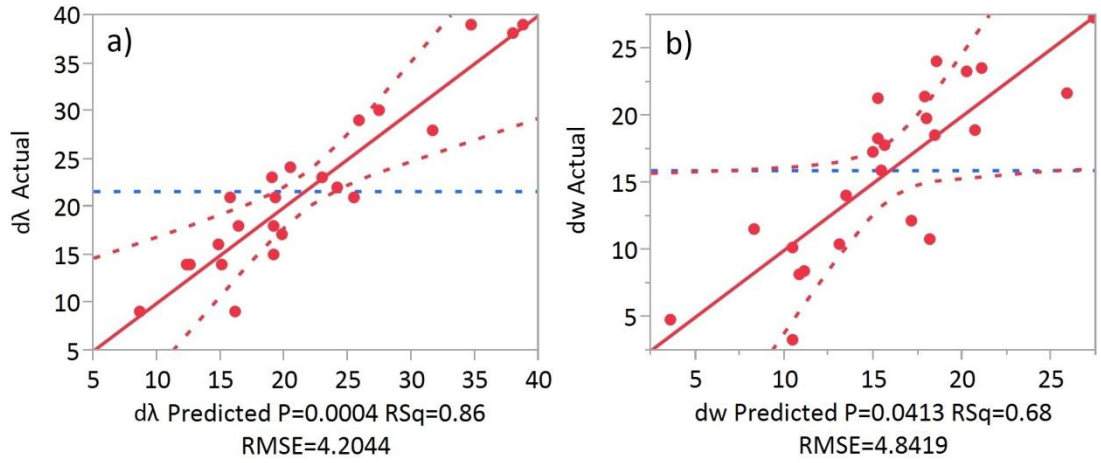

Figure 6.5.4: Leverage plots of the whole fitted least squares model including each of the nine factors for a) $\Delta\lambda_{PL}$ and b) Δw.

The change in Stokes' shift self-absorption parameter, $\Delta\lambda_{PL}$, shows high confidence of above 99% in the model whereas the de-broadening parameter, Δw, shows a confidence of about 96%. Some similarities between these two, $\langle t \rangle$ and I_{abs} are to be expected in the factors of influence. For $\Delta\lambda_{PL}$ the factors of significance are N_{coat}, dye type, C_{tot} and C_{dye} whereas for Δw the factors of significance are C_{dye} and s. There is a cross over here between $\Delta\lambda_{PL}$, Δw, $\langle t \rangle$ and I_{abs} with common factors of

significance because of the relationship between film thickness, the path length of light and self-absorption. Clearly the dye concentration is critically important on the self-absorption metrics but much less so on the film thickness.

These interrelations are somewhat trivial but informative; to maximise <t> as required it is necessary to increase N_{coat} and P_{in} but decrease spray head speed, s. However to minimise self-absorption as required it is necessary to decrease N_{coat} and increase s because the converse would result in greater film thicknesses. Hence absorbing incident radiation efficiently and reduction of self-absorption are goals at cross-purposes. Intuitively this was known all along but is corroborated here in the statistics.

Table XIV summarises the results from the effect-leveraging analysis.

Response	P-Value	R^2	Significant Factors (p<0.05)
<R_R>	0.086	0.63	None
σ_R	0.2827	0.52	None
R_h	0.7453	0.34	None
<t>	<0.0001	0.93	N_{coat}, C_{dye}, P_{in} and s
I_{abs}	<0.0001	0.63	N_{coat}, Dye, C_{dye}, P_{in} and s
$\Delta\lambda_{PL}$	0.0004	0.86	N_{coat}, Dye, C_{tot} and C_{dye}
Δw	0.0413	0.68	C_{dye} and s

Table XIV: Whole model best fit statistics for the response and their associated factors for which p<0.05

6.5.2 Desirability Analysis

The effect-leveraging analysis gives a general overview of which factors influence which responses. A preliminary conclusion at this point is that rather trivial relationships have been observed but there appears to be a lack of control over the resultant deposited film, particularly with regards to film roughness. Further effect profiling is done through a desirability analysis which looks particularly at the ability of the deposition method to reach the goals set in Table XIV. The maximum, minimum, median and range values are shown for each desirability factor to illustrate their distribution in Table XV. This summarises the calculated desirabilities, d_n, and total desirability, D, given by Eq. (6.4.1). The median is chosen since this represents the peak of the distribution in desirability values across all samples.

	Maximum	Minimum	Median	Range
$\mathbf{d_1}$ **(<R_R>)**	0.99	0.18	0.91	0.81
$\mathbf{d_2}$ **(σ_R)**	0.90	0	0.69	0.90
$\mathbf{d_3}$ **(R_h)**	0.99	0.15	0.92	0.85
$\mathbf{d_4}$ **(<t>)**	0.25	0.03	0.08	0.22
$\mathbf{d_5}$ **(I_{abs})**	0.392	0.003	0.103	0.389
$\mathbf{d_6}$ **($\Delta\lambda_{PL}$)**	0.84	0.22	0.59	0.61
$\mathbf{d_7}$ **(Δw)**	0.95	0.47	0.66	0.49
D	0.56	0.30	0.42	0.26

Table XV: Desirability table showing, over all samples, the maximum, minimum, median and range for each individual desirability, d_n, and the total desirability, D, which take values between 1 and 0 depending on goal limit and the response value for a given sample. Individual desirabilities are labelled for each associated response in brackets.

Table XV is interesting because it shows which responses are achieving the required goals. Notice in particular that d_4 and d_5 have relatively low desirability values as seen by their median values. These desirabilities are for <t> and I_{abs}, respectively, and indicate that spray coating deposition will struggle to achieve these goals. In fact the greatest film thickness was 12.67µm for sample S09 which had 3 coats at high pressure so 50 µm, or indeed 100 µm, is out of the question with this system. S09 incidentally also has the highest desirability of these devices with D_{max} = 0.482, owing largely to it having the greatest thickness and absorption of incident light. This comes as a bit of a deal breaker indicating that even at high concentrations of PMMA, and thus more viscous solutions, and with multiple coatings this spray coater fails to reach the minimum required thickness for maximum absorption for both dyes, even with a back reflector. It is not clear how this could be remedied except through increasing the number of coatings and it appears to achieve 50 µm would require somewhere in the region of N_{coat} = 20, which is certainly impractical for a number of reasons. First is because a large scale process requiring multiple coats would slow production and increase costs significantly. Additionally it was noticed during sample preparation that increasing N_{coat} resulted in a reduction in the homogeneity of fluorophore distribution. This is attributed to the partial re-dissolving of previous layers. Increasing fluorophore concentration so as to reduce the required N_{coat} is not a good option since this will reduce quantum yield and increase attenuation for rays of light travelling through the fluorescent coating.

Another point of interest is that of the self-absorption parameters, $\Delta\lambda_{PL}$ and Δw, whose individual desirabilities, d_6 and d_7 respectively, show large variation and median values in the middle of the

desirability range. This was understood through the interactions found earlier in the effect leverage analysis and exhibited in Table XIV; clearly for the ranges of thicknesses produced and dye concentrations used there is to be significant self-absorption for waveguided light in such an LSC device. The median average of d_6 is 0.59 which corresponds to $\Delta\lambda_{PL} \approx 22$ nm for light emitted 6cm from the acquisition edge and this is substantial.

To examine this effect further consider the acquisition edge emission spectrum for S18 and S22 as shown in Fig. 6.5.5, which have $d_6 = 0.408$ and $d_6 = 0.572$, respectively. In this plot the spectra are normalised with respect to the spectrum nearest the acquisition edge at 0.5 cm. For DCJTB the normalisation is done to the intensity of the 0.5 cm spectrum at the peak wavelength of the more distant spectra. For PR all normalisations for the more distant spectra are on the shoulder at 650 nm. These normalisations provide an estimation of the relative spectral areas based solely on the red-shift in emission energy due to self-absorption. This operation is not ideal as the red tails should overlap, but as an estimator it suffices.

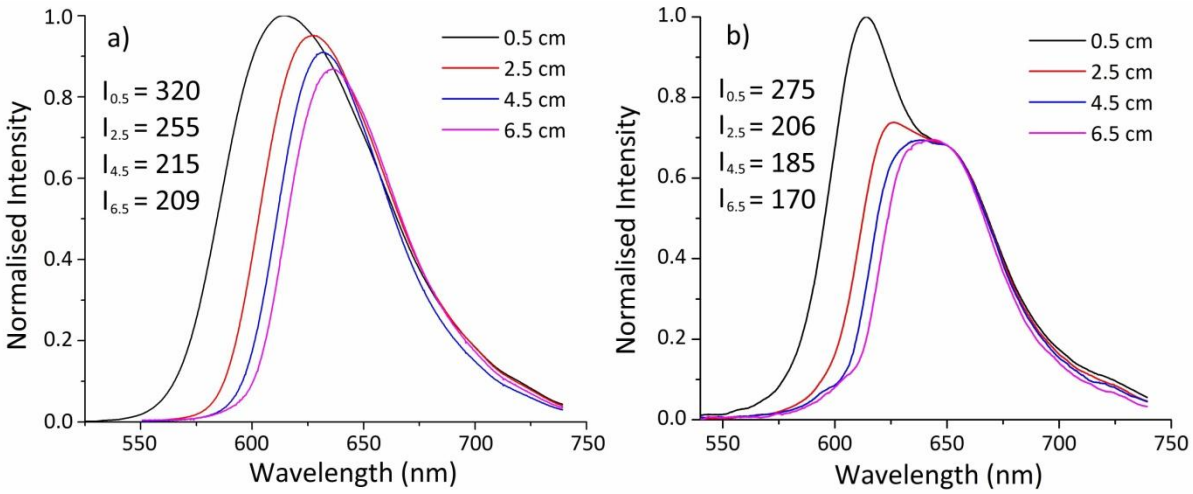

Figure 6.5.5: Sample acquisition edge emission spectra for a) S22 (DCJTB) and b) S18 (PR). For a) normalisation is done to the intensity of the near edge spectrum at the peak wavelength of the others. For b) normalisation is done on the shoulder at 650 nm. Intensity integrals are included showing an estimated 35% (DCJTB) to 38% (PR) total drop in collected energy.

So on average, over a 6cm distance to the acquisition edge, 35-38% of the collected energy is expected to be lost to self-absorption, the true figure is slightly more. PR suffers this effect more over shorter distances, which can seen by considering the differences between S18 and S22 via Table XII and Figs. 6.3.3 and 6.3.4. S22 is actually thinner but has a significantly higher concentration of DCJTB molecules than PR in S18. Hence S22 actually absorbs more incident light but this analysis shows that S18 suffers slightly higher self-absorption than S22, and therefore PR suffers more over shorter distances than DCJTB. Of course some self-absorbed light is re-emitted and trapped again by TIR, as was explored more thoroughly in the last chapter, but it still represents a severe loss mode

that cannot be reduced through control of deposition methodology. This must to considered in light also of the solar cell EQE because some cells absorb red light preferentially which would reduce the impact of this loss.

The final step in the desirability analysis is to consider the minimum desirability, D_{min}, and maximum desirability, D_{max}, projected by the model based on the factors and responses here. JMP allows the prediction profiler generated through the model to be automatically set to the maximum D. This essentially provides a recipe of input factors to achieve the most desirable response values in the produced film and an understanding of the range of the desirability space encompassed by the model. This range is important to consider because it acts as an indicator of how much control over the process is evident. The maximum desirability was given as D_{max} = 0.496 and the minimum is found to be D_{min} = 0.240 and hence gives a desirability range of ΔD = 0.256. This range is small and low in value owing to the lack of control over several of the variables, as discussed through the leverage analysis, and the low desirabilities achieved for $<t>$ and I_{abs}. Table XVI shows the input factor conditions predicted for the maximum and minimum desirabilities.

D	C_{tot} (g/l)	C_{dye} (g/l)	P_{in} (mbar)	T (°C)	h (mm)	S (mm s^{-1})	Dye	N_{coat}	Solvent
0.240	120	0.3	50	30	40	70	PR	1	AS
0.496	50	1	200	30	70	70	DCJTB	3	CB

Table XVI: Factor values for the maximum and minimum desirability predicted by the model.

Table XVI gives an indication of what values the input factors should take to maximise desirability, though caution is needed in light of lack of control and predictability in the model for the roughness parameters. Due to the low significance of these parameters they introduce unexplained variance into the model used by the prediction profiler. This is however a small effect since most of the variance in the model, and the desirability, comes from the other factors where strong effects are observed. The prediction profiler is shown in Fig. 6.5.6 set at the maximum desirability.

For D_{max} low concentration solutions at high pressure are preferred, converse to the case of D_{min}. Because the roughness measures are included in calculating these scenarios, despite weakness of confidence, they will certainly have bearing on this arrangement since for $<R_R>$ the total concentration, C_{tot}, was found to be borderline significance. High C_{tot} values are seen to most strongly affect self- absorption and less the film thickness, particularly through $\Delta\lambda_{PL}$. In contrast high P_{in} values more strongly affect the film thickness and less the self-absorption, though this position is in tenuous balance as Fig. 6.5.6 shows. Such counter-balancing factors are to be expected when trying to optimise for goals at odds with each other, as with maximising incident absorption and minimising self-absorption. N_{coat} needs to be maximised as expected to maximise $<t>$ and I_{abs}.

Note in Table XVI that for D_{max} and D_{min} the substrate temperature, *T*, and head speed, *s*, are the same in both cases, being low for *T* and high for *s*. *T* is found to have low confidence of effect on all responses which tells us there is no way to predict what those responses will be at any given substrate temperature. Therefore the value of 30°C has no meaning; 50°C would work just as well as far as the confidence of the model is concerned. That being said one recognises through experience that as the substrate temperature approaches a solvent's boiling point other dynamics start to come into play. Spraying onto a very hot substrate results in highly rough and messy films though the threshold was not investigated.

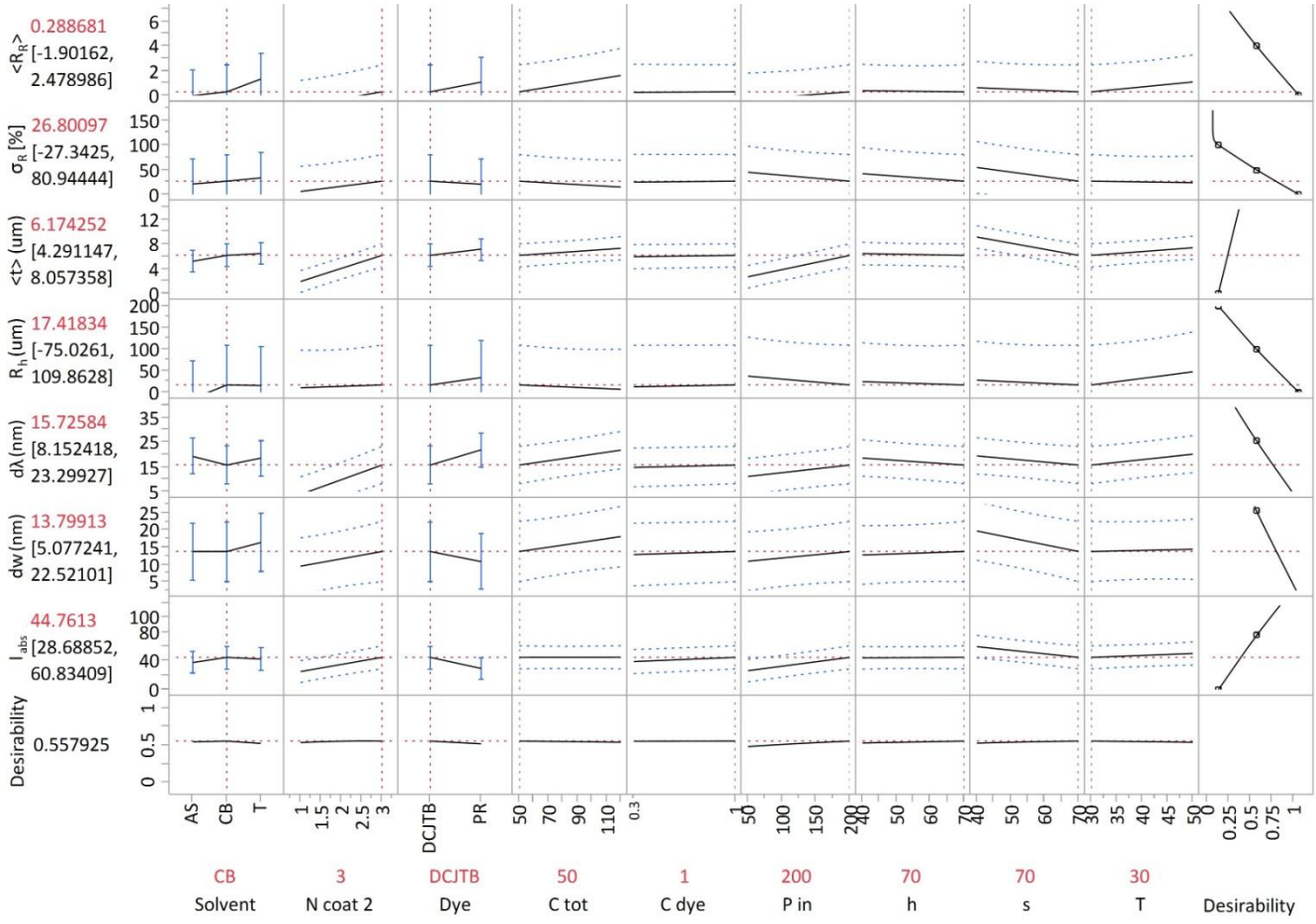

Figure 6.5.6: Prediction profiler for the model generated by screening study, set at maximum desirability, D_{max} = 0.482. Factors lie on the y-axis whilst responses lie along the x. Desirability plots lie along the bottom and right hand edge of the main plot of profiles, which themselves are miniature versions of leverage plots seen in section 6.5.

As for speed it seems erroneous that the minimum desirability could have the same as the maximum since all leverage profiles have the same gradient, as seen in Fig. 6.5.6. However, the desirability profiles for the responses, seen at right of the image, do not have the same gradient. It just so happens in this case that the arrangement of factors and responses at minimum and maximum result in the same speed in each case. In this study speed is seen to have great influence only on thickness and absorption of incident light.

The choice of solvent was expected to show more interesting influence and so it is surprising to see that it has only near borderline significance of effect in any response leverage plots. The greatest effect on a response was for <*t*> with near borderline significance at 91.8% confidence and saw toluene as providing greatest thickness. *s* also shows confidence of 89.3% with the roughness ratio but in this time with anisole being more desirable with lowest $<R_R>$ values. Such a predictions hold too much uncertainty for definitive statement however, and so does statement that chlorobenzene proves better than anisole as Table XVI suggests.

For choice of dye and C_{dye} the model indicates that DCJTB and higher concentration provide the optimum desirability, but it is absent considerations of concentration quenching of quantum yield, self-absorption effects and photochemical molecular stability. The model considers DCJTB to be the best because of its higher intrinsic absorption which has great impact on the relative absorption intensities, as seen by comparing Figures 6.3.3 and 6.3.4. Dye type also is seen to have a significant influence, at 99.4% confidence, on the peak shift due to self-absorption, $\Delta\lambda_{PL}$. The leverage analysis indicates that the least squares mean for DCJTB is at $\Delta\lambda_{PL}$ = 18.5 ± 1.3 nm and for PR it is $\Delta\lambda_{PL}$ = 24.7 ± 1.3 nm. So based on this model, at high confidence, DCJTB is expected to have significantly lower self-absorption than PR. This makes sense considering DCJTB has a broader spectrum with a larger Stokes' shift, as seen comparing Fig. 2.4.7 and 2.4.11. Also consider that the spectrum of PR is composed of two main transitions where the first of which is largest and lies in the red tail of the absorption spectrum. Much of this larger component can be consumed by self-absorption over relatively short distances, as has been seen for DCJTB in Fig.6.5.5. PR does however exhibit higher quantum yield than DCJTB at all concentrations which, as Fig. 6.4.3 has shown, can improve the collection efficiency of light. Furthermore PR has much greater photochemical stability with over 80% of the original efficiency remaining after a year long exposure [6], whereas DCM class fluorophores are known to have low stability.

6.6 Conclusions

The screening design has found success in its ability to assess to value of the spray coating deposition of LSC bi-layer devices using the Prism Ultra-Coat 300. The clear conclusion based on the defined response parameters, and their goals set in the desirability analysis, is that this spray coating system cannot achieve the thicknesses of film required and that the surface roughness cannot be controlled at all in the range of parameter space explored. Furthermore optimal absorption of incident light, which cannot be achieved due to the thickness problem, necessitates strong self-

absorption effects over the range of several cm, even with a back reflector considered to reduce necessary thickness.

The model predicts PR to suffer more from the self-absorption phenomenon than DCJTB which is supported by considering the spectra of these dyes. The self-absorbed energy in a DCJTB sample with average change in peak wavelength over 6 cm excitation difference is crudely estimated to be around 35% based on measured spectra. This shows that self-absorption is strong in these bi-layer devices which may be exacerbated by longer path lengths due unfavourable scattering from a rough reflection interface.

6.7 References

[1] K. R. McIntosh, N. Yamada and B. S. Richards, Theoretical Comparison of Cylindrical and Square-Planar Luminescent Solar Concentrators, *App. Phys. B* **88**, 285-290 (2007)

[2] G. Colantuono, A. Buckley and R. Erdélyi, Ray-Optics Modelling of Rectangular and Cylindrical 2-Layer Solar Concentrators, *J. Light. Tech.* **31**, 7, 1033 – 1044 (2013)

[3] A. von Eye, P. Mair and E. Y. Mun, Advances in Configural Frequency Analysis, 3rd ed. (*Guilford Press*, USA, 2010), Chap. 12, pp. 223–226.

[4] JMP® 8 Design of Experiments Guide, 2nd ed. (*SAS Institute Inc.*, Cary, NC, USA, 2009), Chap. 2

[5] American Society for Testing and Materials (ASTM), ASTM G173-03 Tables, AM 1.5 Solar Irradiance Reference Spectrum, http://rredc.nrel.gov/solar/spectra/am1.5/

[6] W. G. J. H. M. van Sark *et. al.*, Luminescent Solar Concentrators - A Review of Recent Results, *Opt. Exp.* **16**, 26, 21773 (2008)

Chapter 7

Solid State Concentration Quenching Effects for Organic Fluorophores and Implications for LSC Devices

7.1 Introduction

This chapter reviews a series of results exploring concentration quenching effects in organic fluorophores in the solid state so as to consider the impacts this loss mechanism will have on LSC optical efficiency. Concentration quenching is a phenomenon observed with all small molecular fluorescent materials where increased concentration results in diminished fluorescence efficiency, as briefly discussed in chapter 2.4. When the term concentration quenching of fluorescence is used what is really being discussed is a change in the balance of radiative and non-radiative transition decay rates, and from this an inverse relationship between fluorescence quantum yield and fluorophore concentration. From Eq. (2.4.1) the quantum yield is understood in terms of the ratio of radiative decay rate to the sum of all transition rates. Therefore through both quantum yield measurements (chapter 3.1) and fluorescence lifetime measurements (Chapter 3.5), as a function of fluorophore concentration, $\eta_{QY}(C_{dye})$ and $\tau(C_{dye})$, the influence of concentration quenching can be explored and quantified.

Explored in this chapter are measurements on samples consisting of single fluorophores doped into solid polymer hosts. The effect of host type, fluorophore concentration and fluorophore type are all explored in some detail throughout section 7.2. Quantum yield combined with fluorescence lifetime data using Eq. (2.4.1) allows the concentration quenching effect to be quantified in two fluorophores, DCM and C102, in sections 7.3 and 7.4, respectively. These data were not available for PR or the other fluorophores as it was taken early in my research when thought was not given in preference of particular fluorophores.

The exact mechanism of concentration quenching depends on the system being studied. Dipole-dipole deactivation interactions between neighbouring fluorophores have been demonstrated in the solid state for Iridium based phosphor complexes [1]. In this case an r^{-6} dependence on fluorophore separation is observed as predicted by Förster in the case of two interacting point-like dipoles. In reality the approximation of point-like dipoles may not hold, for example in solid state polymer blends where point-surface or surface-surface interactions may occur. In such cases the dependence

on fluorophore separation could be of r^{-3} or r^{-2} [2, 3], respectively. Exciplex formation [4] and the presence of quenching agents [5] have also been identified as forms of quenching in particular cases. Concentration quenching of fluorescence is therefore the result of a number of mechanisms that act to reduce the fluorescent emission efficiency of a particular transition of interest. What mechanisms are actually present will depend on the local environment of the fluorophore, so host properties will be important, and also on the chemical and photophysical properties of the fluorophore itself. It therefore may or may not be possible to discern the nature of the quenching in the case of DCM and C102.

All samples are fabricated by first preparing a stock solutions of host materials in chlorobenzene, or chloroform for polycarbonate (PC), at C_{host} = 250 g/l. Blends are made with stock solutions of fluorophores in chlorobenzene or chloroform at C_{dye} = 2 g/l or 0.05 g/l. Fluorophore stock solutions of different C_{dye} values are needed to achieve dye concentrations in the resultant thin film in the range $1x10^{-4}$ M < C_{dye} < 0.1 M. Deposition occurs onto glass substrates by spin coating at 1000 rpm giving films of thickness in the range (350 < x < 600) ± 30 nm.

7.2 The Impact of Host Material on Fluorescence

This first results section qualitatively explores a selection of results looking at how different host and fluorescent materials interact and how the fluorescence is affected. Fig. 7.2.1 shows η_{QY} for a number fluorophores doped in PMMA plotted as a function fluorophore concentration, C_{dye}.

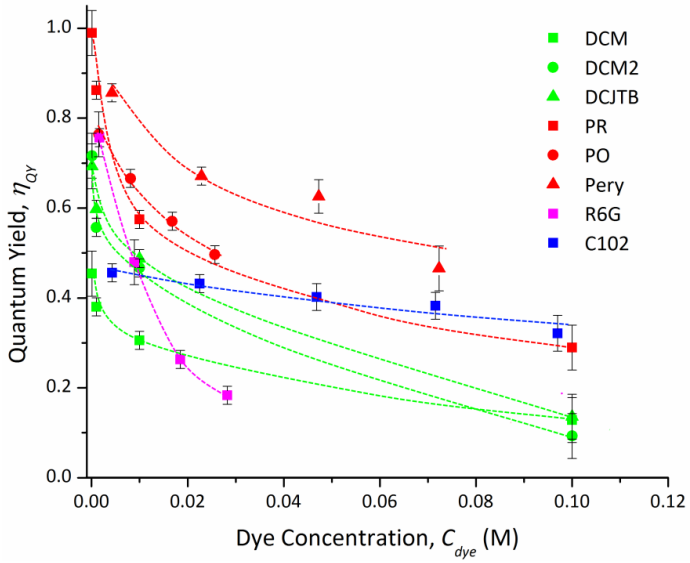

Figure 7.2.1: Plot of quantum yield against dye concentration for PMMA doped with various fluorophores including three DCM class dyes (green), three perylene based dyes (red), R6G (magenta) and C102 (blue). These fluorophores have spectra and chemical structures exhibited in chapter 2.4.1. Lines are a guide to the eye.

As can be seen in Fig. 7.2.1 the perylene based dyes exhibit much higher η_{QY} values than the DCM class. PR is seen to achieve near unity quantum yield at C_{dye} = 1 x 10^{-4} M, in line with corresponding values in literature [6]. Note that samples having very high or very low C_{dye} have larger associated uncertainty due to low signal in those regions. C102 shows a much slower rate of quantum yield decline than the other dyes indicating a weaker or shorter ranged quenching mechanism is dominant in this case. Conversely R6G shows a much stronger decline. DCM2 and DCJTB are more or less the same in terms of their quantum yields as shown here whereas DCM remains least favourable of this class of fluorophores.

Many interactions may occur between the guest fluorophore and host material such as chemical, photochemical and photophysical interactions. Some of these may be beneficial, such as solvation discussed in chapter 5, but many will not and may act to cause fluorescence states to de-excite non-radiatively, or to react with and destroy the fluorophore's chemical structure. Non-radiative de-excitation pathways act as loss mechanisms for excitation energy and therefore need to be minimised. To this end the choice of host must be inert for fluorophore chemical stability and be resistant to the migration of quenching agents such as oxygen and moisture.

It is evident from Fig. 7.2.1 that different fluorophores exhibit quite different dependences on C_{dye}, but what happens if we change the host material? In Fig 7.2.2 the quantum yield of DCM2 is explored as a function of concentration and mean molecular separation for different molecular weights, M_w, of PMMA.

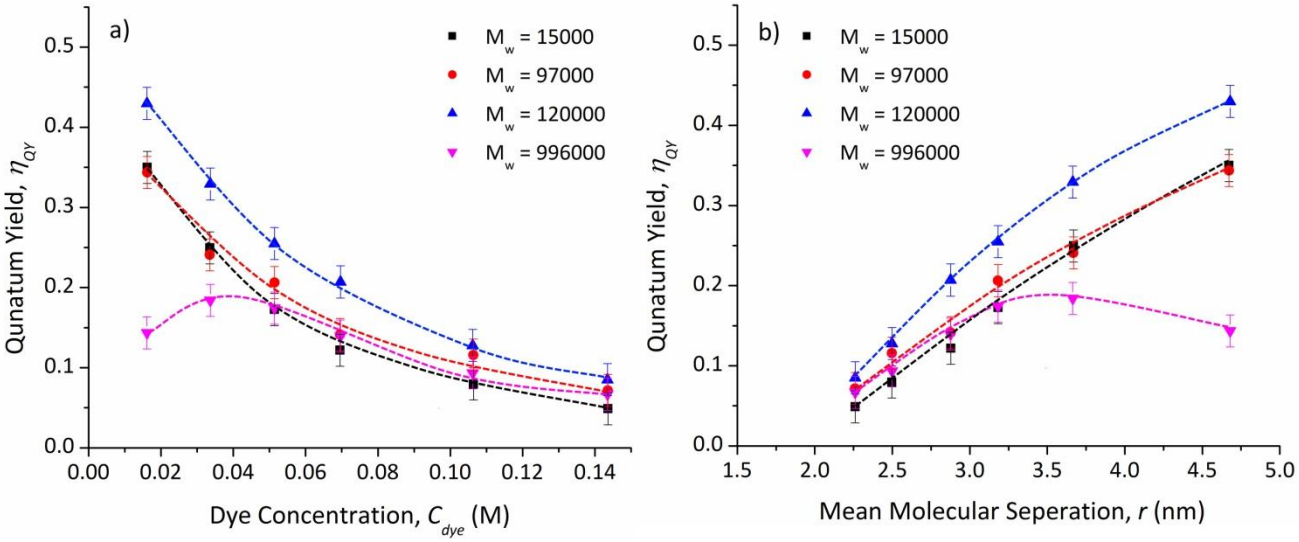

Figure 7.2.2: Plots of η_{QY} for DCM2 in several different M_w PMMA grades as a function of a) concentration and b) mean molecular separation. Lines are a guide to the eye.

In Fig. 7.2.2 the PMMA grade of M_w = 120000 shows higher quantum yield than the other low M_w grades by as much as $\Delta\eta_{QY}$ = 0.1, which is a very large difference. As such all samples in preceding

chapters using PMMA have been done with this M_w. The highest molecular weight, some 8 times greater than the closest counterpart, shows very odd behaviour with a dip in η_{QY} at low concentration, contrary to all other observations of concentration quenching I've performed myself or seen in literature. Lacking further investigation this effect has not been accredited to a particular mechanism but it is hard to imagine what that might be. The dip here could just be an artefact of measurement or, more likely, the sample itself. Consideration of potential contamination or PMMA grade purity may explain the difference. In part b) of Fig. 7.2.2 C_{dye} has been translated to mean molecular separation, r, to show roughly at what separation the η_{QY} becomes negligible. This is at around r = 1.75 nm, which corresponds to C_{dye} = 0.31 M and in turn this is roughly 8 wt% of DCM2 in PMMA.

The M_w appears to have some significance at first glance but what about different solid host materials? Fig. 7.2.3 shows the η_{QY} of DCM in a variety of host materials as a function of concentration and mean molecular separation.

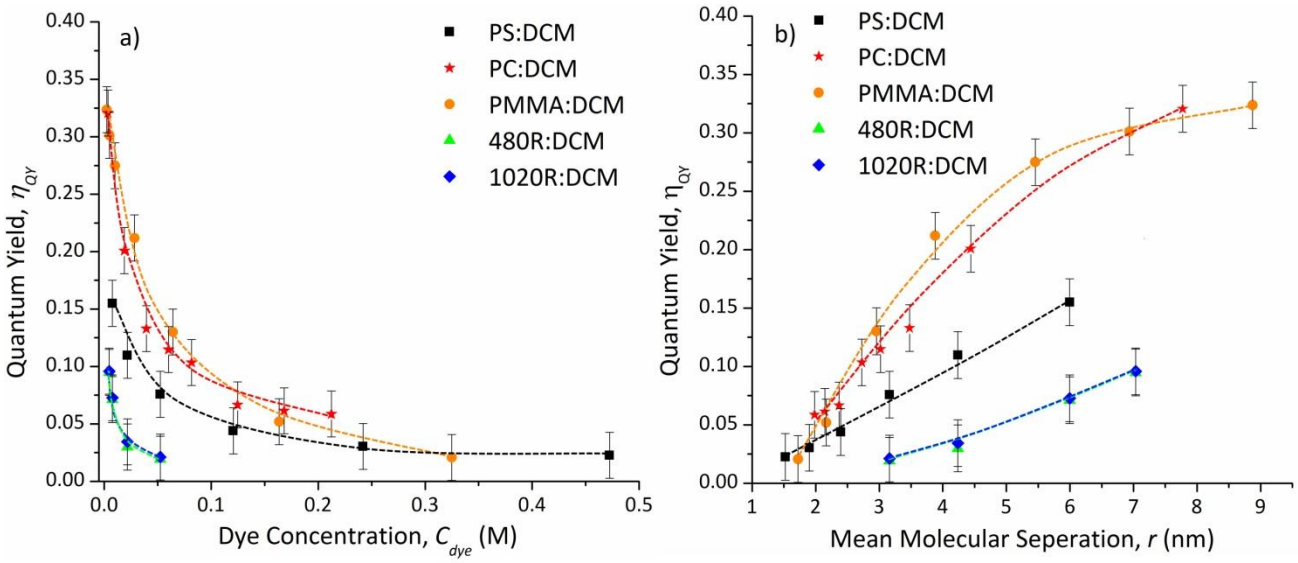

Figure 7.2.3: Plots of η_{QY} for DCM in a variety of solid host materials as a function of a) concentration and b) mean molecular separation. Lines are a guide to the eye.

From Fig. 7.2.3 it can be seen that PMMA and PC are approximately the same in terms of maximising η_{QY} with PMMA achieving η_{QY} = 0.32 at r = 8.9 nm and PC achieving η_{QY} = 0.32 at r = 7.8 nm. The PS host exhibits significantly lower quantum yield than PMMA and PC, achieving η_{QY} = 0.16 at r = 6 nm. The Zeonex polymers, 480R and 1020R, both exhibit strong quenching achieving η_{QY} = 0.09 and 0.10 at r = 7 nm, respectively. R grade Zeonex polymers are cyclo olefins designed for use in optical applications including the manufacture of plastic lenses and prisms. It is not clear why these polymers suppress the quantum yield so much since they have low water absorption, a high purity and do not have reactive chemical moieties. They also have lower dielectric constants than the other polymers here.

From plot b) in Fig. 7.2.3 the mean *r* for negligible η_{QY} is roughly the same as in the case of DCM2 in Fig. 7.2.2. It is hard to be clearer because only one set of data for PMMA is present and the other polymers appear to also differ in this respect.

PMMA stands out as the best material in light of processibility but has a lower refractive index than PC. Going back to the LSC optical efficiency considerations of chapter 2.2, pages 13 - 17, higher refractive indices reduce transmission efficiency, η_{fr}, but increase trapping efficiency, η_{trap}. We also learnt in chapter 5, page 76, that increasing refractive index would reduce the influence of solvation for a fixed value of relative permittivity. It is through this balance of efficiencies that the choice between PMMA and PC must be made, which is summarised for the product $\eta_{fr}\eta_{trap}$ in Fig. 2.2.4. A further consideration is the host absorption coefficients across the visible spectrum; Table IV shows PMMA to be considerably better than PC in this property.

Finally in this exploration of different solid host materials two other forms of acrylic polymer, poly(butyl methacrylate) (PBMA) and poly(cyclohexyl methacrylate) (PCHMA), are compared to PMMA. These polymers were chosen due to their similarities to PMMA and availability from Sigma Aldrich. In Fig 7.2.4 the fluorescence lifetime of DCM is plotted against $\log_{10}$ of concentration for these three acrylic polymers.

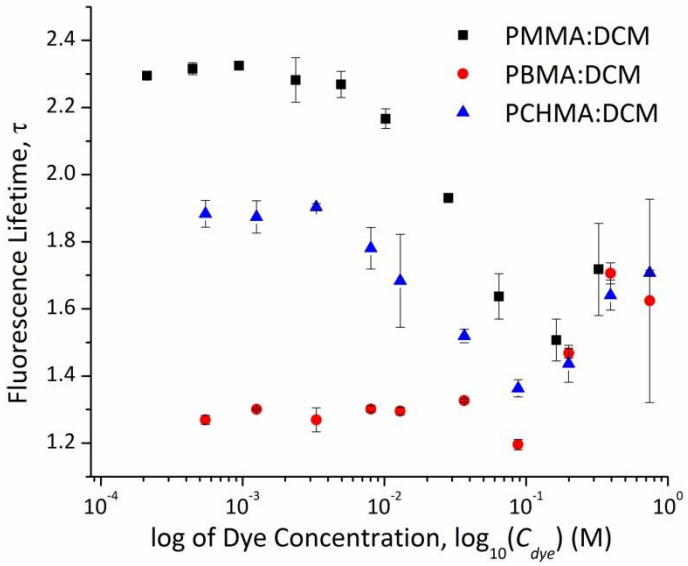

Figure 7.2.4: Fluorescence lifetime is plotted here against $\log_{10}$ of DCM concentration for three solid acrylic hosts; PMMA, PBMA and PCHMA.

Fig. 7.2.4 shows a significant difference in the lifetime of the fluorescence state at low concentrations. This does not necessarily translate to PMMA having a greater quantum yield since the measured lifetime, τ, is the inverse of the sum of all excited state decay rates. Hence if either the radiative rate or non-radiative rate decrease then the lifetime with increase. PBMA shows no

dependence on C_{dye} at lower concentrations ranging from 10^{-1} to 10^{-3} M. For PMMA and PCHMA the lifetime plateaus at around C_{dye} = 3x10^{-3} M, or 0.085 wt%. Note that the DCM excited state lifetime for all acrylic hosts seem to converge just below 10^{-1} M.

A larger range of concentrations is explored in Fig. 7.2.4 than previously which shows some interesting high C_{dye} lifetime behaviour. For C_{dye} > 0.1 M, which corresponds to C_{dye} > 0.253 wt%, an increase in the measured lifetime is observed. Such behaviour is unexpected but seen in all three cases of host material tested here, which indicates that it is either a systematic artefact of the measurement process or an actual high concentration effect that switches on at a concentration of about 10^{-1} M. The data for PMMA here was measured from the same samples as that of PMMA:DCM in Fig. 7.2.3 and this set of associated τ and η_{QY} values is plotted together in Fig. 7.2.5.

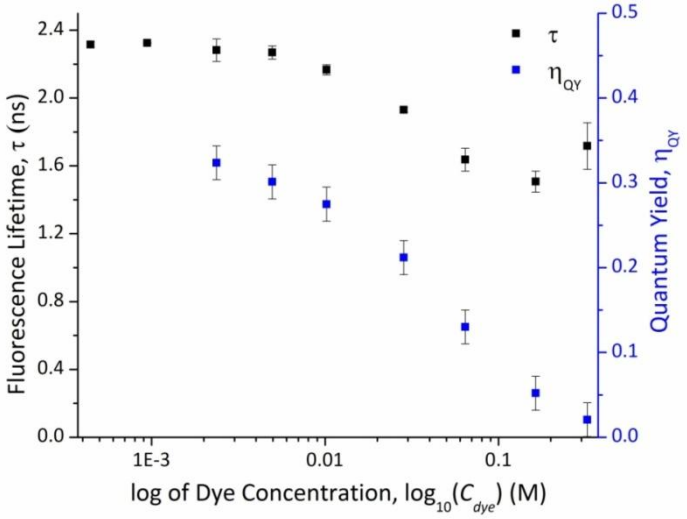

Figure 7.2.5: Fluorescence lifetime and quantum yield are plotted here for PMMA:DCM samples at various concentrations. The two lowest concentration samples provided too faint a signal for the measurement of η_{QY}.

Figure 7.2.5 shows that at least part of the high C_{dye} turning point and rise in τ is not seen also in the quantum yield, which continues to decrease with C_{dye}. This leaves the question as to the increase in fluorescence lifetime which may merely be due to the weak signal from these samples affecting the measurement. Fig 7.2.5 also shows for the lower concentrations that the quantum yield and lifetime have similar dependence on C_{dye} and plateaus at roughly the same concentrations. These data are analysed further in the next section to gain deeper understanding of the quenching process.

7.3 Concentration Quenching in PMMA:DCM Systems

It has been shown that the host material can have a strong impact on the fluorescence quantum yield but so far this has only been done in a generalised, qualitative way. In this section PMMA:DCM

samples are analysed further to attempt to quantify the concentration quenching mechanism and determine its dependence on mean molecular separation, *r*. This dependence will give insight into the quenching mechanism as it defines the strength or range of its effect. A pertinent example is Förster Resonant Energy Transfer (FRET) based point-like dipole-dipole interactions which have a rate, k_{FRET}, with a r^{-6} dependence as given by Eq. (7.3.1).

$$k_{FRET} = \frac{1}{\tau_0}\left(\frac{r_0}{r}\right)^6 \qquad (7.3.1)$$

Where τ_0 the intrinsic decay lifetime of the fluorescent state and r_0 is the Förster radius for interacting point-like dipoles at which FRET efficiency is 50%. For point-surface interactions, as developed in J. Cabanillas-Gonzalez *et. al.* 2004[2], this rate equation becomes that of Eq. (7.3.2) for k_{ET};

$$k_{ET} = \frac{1}{\tau_0}\left(\frac{\underline{r}_0}{r}\right)^3 \qquad (7.3.2)$$

$$With\ \underline{r}_0{}^3 = \frac{\pi\rho {r_0}^6}{6} \qquad (7.3.3)$$

Where $\underline{r}_0$ is the Förster radius for point-surface interaction related to r_0 by Eq. (7.3.3) in which ρ is the donor fluorophore density; in this case this is the same as the fluorophore density as the interaction is between same species fluorophores. To determine the dependence of the concentration quenching rate, k_Q, on *r* we turn back to the data exhibited in Fig. 7.2.5, but now only consider the values for C_{dye} < 0.1 M. This is shown with exponential best fit curves in Fig. 7.3.1.

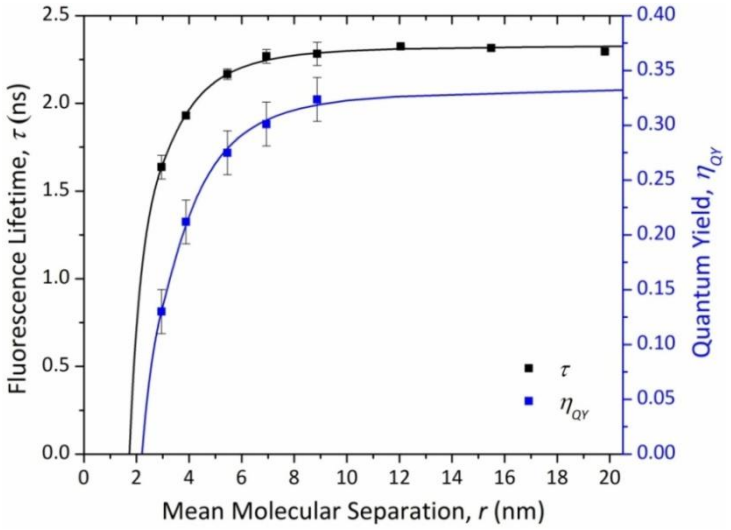

Figure 7.3.1: Double-y plot showing fluorescence lifetime and quantum yield as a function of mean molecular separation for PMMA:DCM films. Best fit curves are exponential decay fits extrapolated to the intercept.

The x axis intercept of both curves in Fig. 7.3.1 is approximately equal within the error margins of the data, which is expected since as quantum yield tends to zero so must the lifetime. η_{QY} in particular exhibits larger errors and it would be preferable to have data points at lower separation. However, as seen in Fig.7.2.5, this was not possible since there is some presently unexplainable high concentration behaviour for τ, which is assumed to be in error for this analysis. The predicted η_{QY} intercept is at r = 2.21 nm or C_{dye} = 0.154 M (3.9 wt%).

From Fig. 7.3.1 both $\tau(C_{dye})$ and $\eta_{QY}(C_{dye})$ are known (or $\tau(r)$ and $\eta_{QY}(r)$) and so rewriting Eq. (2.4.1) the fluorescence decay rate, k_{fl}, can be determined by Eq. (7.3.4).

$$k_{fl}(r) = \frac{\eta_{QY}(r)}{\tau(r)} \quad (7.3.4)$$

If k_{fl} is constant as a function of concentration then it is an easy matter to rearrange Eq. (2.4.1) in terms of the concentration quenching rate, $k_Q(r)$, but this is not the case as Fig. 7.3.2 shows.

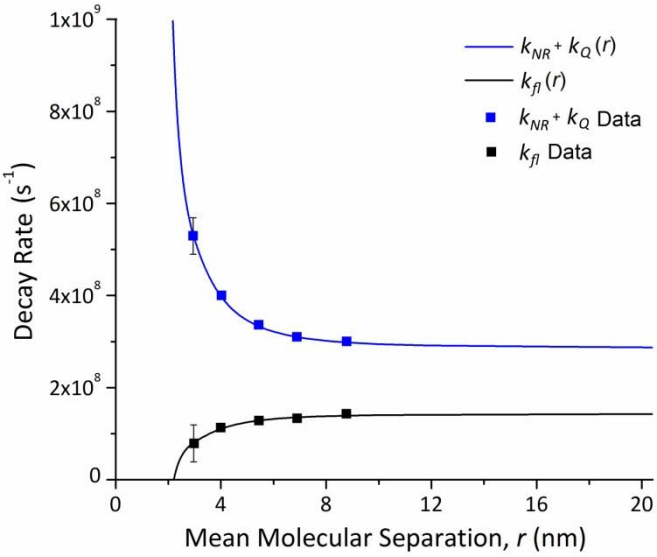

Figure 7.3.2: Double-y plot of the fluorescence decay rate and the sum of non-radiative and quenching rates as a function of mean molecular separation. Both best fits and data points are shown.

The dependence seen for k_{fl} on r means that the denominator of Eq. (2.4.1) has at least two functions of r and so a simple substitution for when k_Q = 0 is not possible. Nor can we assume that the non-radiative decay rate, $k_{NR,}$ is constant with r. Instead, with $k_{fl}(r)$ known, Eq. (2.4.1) is rearranged to find the sum of $k_{NR}(r)$ and $k_Q(r)$ as given by Eq. (7.3.5) and plotted in Fig. 7.3.2.

$$k_{NR}(r) + k_Q(r) = k_{fl}(r)\left(\frac{1}{\eta_{QY}(r)} - 1\right) \quad (7.3.5)$$

Fig. 7.3.2 shows for low concentrations that both functions reach a steady value, roughly beyond a molecular separation of 10 nm. In this regime k_Q = 0 and k_{NR} takes a steady value of 2.84x10^8 s^{-1},

whilst k_{fl} reaches a peak value of 1.44×10^8 s^{-1}. This corresponds to a peak quantum yield given by the ratio of k_{fl} to (k_{fl} + k_{NR}), which is η_{QY} = 0.336 or 33.6%, as can be seen in Fig. 7.3.1.

Given the steady state regime seen for (k_{NR} + k_Q)(r), it may be reasonable to suggest that k_{NR} is constant with respect to dye concentration. This would assume therefore that all concentration dependent quenching is characterised by $k_Q(r)$. Taking this to be the case a simple subtraction of k_{NR} from (k_{NR} + k_Q)(r) gives $k_Q(r)$. We're now in a position to test the hypothesis that the quenching is a result of point-like dipole-dipole interactions between neighbouring DCM fluorophores, as characterised by Eq. (7.3.1). This equation has a monomial form of $y = ax^b$ and so a log-log plot of $k_Q(r)$ should produce a straight line if the quenching process is dominated solely by the FRET mechanism. The log-log plot of $k_Q(r)$ for the PMMA:DCM system is shown in Fig. 7.3.3.

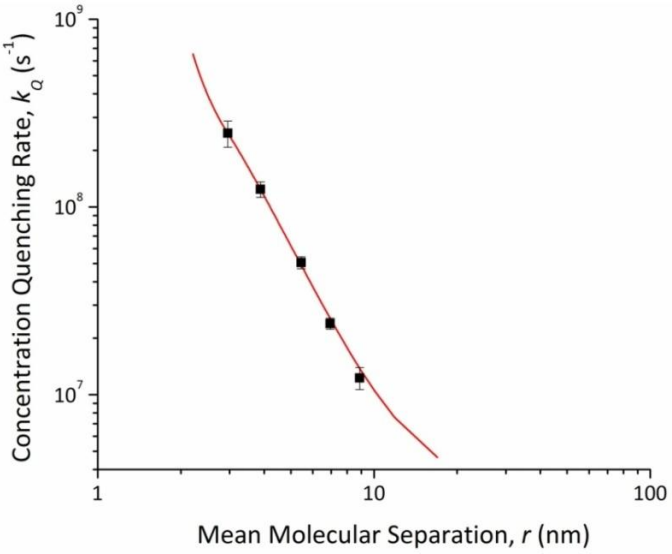

Figure 7.3.3: A log-log plot of concentration quenching rate against mean molecular separation is plotted for the best fit function of $k_Q(r)$ (red line) and data points calculated from the five paired η_{QY} and τ data points in Fig. 7.3.1.

From Fig. 7.3.3 a linear regime is seen within the bounds of the data which confirms the first hypothesis that some form of monomial decay function fits the data. The curvature at the ends of the best fit function of $k_Q(r)$ show that the best fit loses accuracy quickly beyond the bounds of the data, which might be expected for extrapolated best fit curves. The curvature at the low r end of $k_Q(r)$ is due to a forming asymptote where η_{QY} tends to zero. The curve is truncated at this point as further extrapolation leads into an unphysical regime.

Fitting a line to the data in Fig. 7.3.3 yields Eq. (7.3.6) whose power in r indicates that concentration quenching from point-like dipole-dipole interactions is not dominant in this system. One can see this looking at the gradient of Fig. 7.3.3 which has a value of -2.9 ± 0.2. The error on the power of r is determined from the best fit standard error.

$$k_Q[s^{-1}] = \frac{(6 \pm 1) \times 10^9}{r^{2.9 \pm 0.2}} \qquad (7.3.6)$$

This equation suggests that what is controlling the quenching has a longer range influence than a point-like FRET interaction though it is likely that at least a small amount FRET is occurring. In other work the Dexter energy transfer (DET) mechanism has been considered, which should cause k_Q to decline exponentially with r [1]. In that work, and this one, the DET mechanism is clearly seen not to be dominant by the log-log plot of k_Q against r. The power of r here lies between that of Eq. (7.3.2) for point-surface interactions and that of a surface-surface interaction, as suggested in J. Hill *et. al.* 2003 [3].

Why concentration quenching for DCM differs from the point-like model is unclear. The fluorophore was found to have an Onsager radius of a = 5.2 Å in chapter 5, which can be thought of as an effective dipole radius. If the host, PMMA in this case, was completely inert then only interactions between neighbouring small molecular dipoles of radius 0.52 nm would be possible. The results of the previous section did however show that not all hosts offer the same stability for the guest fluorophore, which may imply that all host materials are to some extent electronically active. This would explain why some hosts exhibit quantum yield suppression of fluorophores relative to other hosts, though other factors such as impurities and aggregation may also be present.

As the molecular separation approaches 1 nm the quenching rate tends towards the numerator of Eq. (7.3.6). The power of r is an irrational number whose error range also defines it as a non-integer. The point here is that laws of nature that depend on distance do not tend to doing so to an irrational power, because of the mathematics behind them, therefore it is probable that the quenching behaviour here is a response from more than one mechanism. This could also explain the concentration dependence of k_{fl} which, elsewhere in a study by C. Adachi *et. al.* 2006 [1] on Iridium complexes, was found to be independent of r. DCM obviously has stronger concentration quenching, and probably greater intrinsic non-radiative loss, than those Iridium phosphors which achieve much higher quantum yield at smaller molecular distances, and much longer lifetimes (being phosphors). In that paper the decline in η_{QY} occurs at around 3 nm as opposed to 10 nm shown here in Fig.7.3.1. By knowing this point of decline for η_{QY} in relation to r one can therefore get a qualitative feel for the strength and range of the interaction behind k_Q.

7.4 Concentration Quenching in PMMA:C102 Systems

Now follows an identical analysis to that above in section 7.3 for DCM but for C102, which was seen in Fig. 7.2.1 to show a significantly slower decline in η_{QY} with C_{dye}. The fluorescent lifetime and quantum yield for PMMA:C102 samples, with exponential best fits, are shown in Fig. 7.4.1 as a function of mean molecular separation. This time, to avoid τ being non-zero when $\eta_{QY} = 0$, the fit for τ is constrained to the x-axis intercept for $\eta_{QY}(r)$.

Comparing Fig. 7.3.1 and 7.4.1 the point at which η_{QY} begins to decline also differs; for C102 it is around 5 nm whereas for DCM it is around 10 nm. From the study by C. Adachi *et. al.* 2006 [1] we saw iridium phosphors had a plateau value at around 3 nm. Already then one can guess that the C102 concentration quenching rate, k_Q, will not be dominated by a FRET based quenching mechanism as with the phosphors. It must be a shorter range effect than DCM but longer than the phosphors, obeying a power law in r whose exponent lies in between -6 and -2.61.

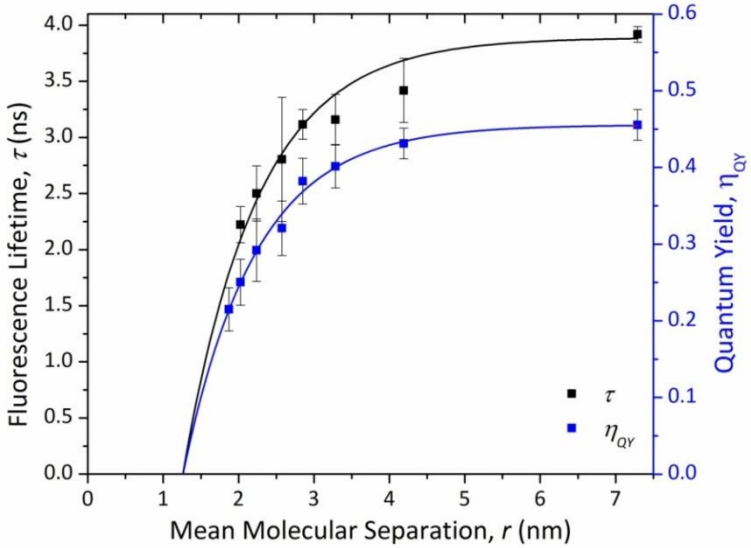

Figure 7.4.1: Double-y plot showing fluorescence lifetime and quantum yield as a function of mean molecular separation for PMMA:C102 films. Best fit curves are exponential decay fits.

From Fig. 7.4.1 the lifetime and quantum yield are known as a function of molecular separation and so as before Eq. (7.3.4) allows the fluorescence decay rate, $k_{fl}(r)$, to be determined. For C102 this is seen to be constant with r, as shown in Fig. 7.4.2. Also plotted is $k_Q(r)$ calculated from Eq. (7.3.5).

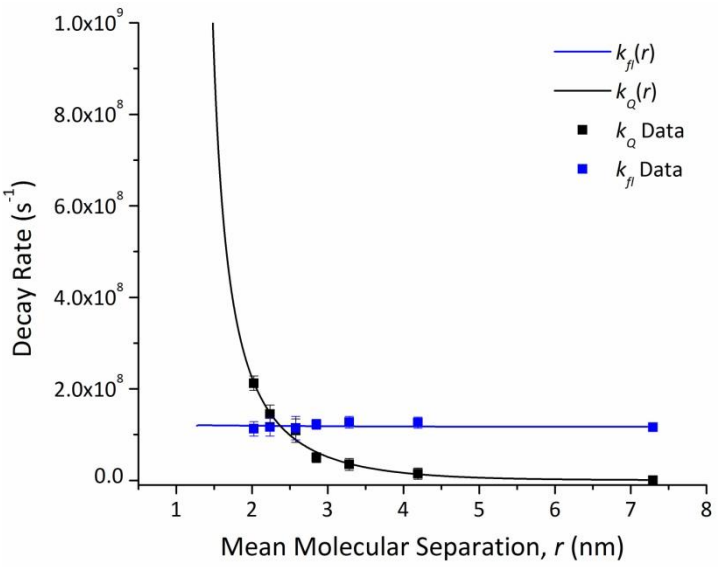

Figure 7.4.2: Decay rate against mean molecular separation for the concentration quenching rate, k_Q, and the fluorescence decay rate, k_{fl}. Both data and best fits are plotted.

The fluorescence decay rate takes a steady average value of $k_{fl} = 1.18 \times 10^8$ s^{-1} and the non-radiative rate is assumed constant and found to be $k_{NR} = 1.41 \times 10^8$ s^{-1}. This implies a maximum quantum yield of η_{QY} =0.457 for PMMA:C102, somewhat higher than DCM which has maximum at η_{QY} =0.336.

Now the k_Q data is plotted on a log-log scale to test the hypothesis of a monomial power law and from that assess the nature of the quenching mechanism. This is shown in Fig. 7.4.3 plotted with the data points. Very large curvature is seen beyond the bounds of the data at low r which shows that constraining the fluorescence lifetime to the zero point of η_{QY} creates large uncertainty beyond the bounds of the data. Ideally more samples at smaller r would be preferable.

Within the bounds of the data a straight line is seen in Fig. 7.4.3 and thus the monomial power law hypothesis holds for concentration quenching in PMMA:C102 films. The gradient of the plot shows, as does a fit to the data given by Eq. (7.4.1), that k_Q depends on $r^{-3.2\pm0.2}$, which suggests that FRET is not the only mechanism operating to quench the fluorescence of C102. Again in this case it is conjectured that point-surface interactions are present. C102 has been shown to have an Onsager radius of a = 3.98 Å [7], making is somewhat smaller than DCM (a = 5.2 Å). Hence C102 would appear more point-like to nearby fluorophores , which could explain why C102 is exhibiting quenching closer to the FRET model in Eq. (7.3.1).

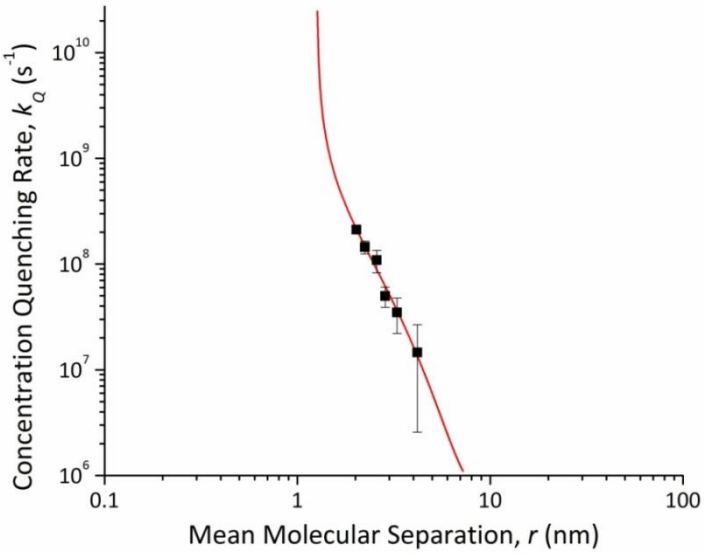

Figure 7.4.3: A log-log plot of concentration quenching rate against mean molecular separation is plotted here for C102. Both the best fit function of $k_Q(r)$ (red line) and data points are shown.

$$k_Q[s^{-1}] = \frac{(1.9 \pm 0.3) \times 10^9}{r^{3.2 \pm 0.2}} \qquad (7.4.1)$$

Comparing Eqs. (7.3.5) and (7.4.1) the numerator takes a similar value. For these equations to balance dimensionally the numerators must have rather odd units; in the case of Eq. (7.4.1) this is $nm^{4.18}s^{-1}$. This is attributed to this monomial expression being the empirical equivalent of more than one quenching mechanism. The powers of r in these equations represent the gradients of the linear fits to the data in Figs. 7.3.3 and 7.4.3 and the numerators are the values k_Q would have at r = 1 nm, though as has been seen the quantum yield falls to zero before this point anyway.

C102 shows a stronger dependence on r than DCM but this also means that the range of the quenching process is longer for DCM. The non-radiative rate for DCM is considerably higher at 2.84×10^8 s^{-1} compared to 1.41×10^8 s^{-1} for C102 whereas DCM has a faster fluorescence rate at 1.44×10^8 s^{-1} compared to 1.18×10^8 s^{-1}. These values give maximum quantum yields of 0.336 and 0.457 for DCM and C102 respectively. This seems to be correct but quantum yield measurements of very low concentrations for DCM, shown in Fig. 7.2.1, indicate this is not quite accurate since DCM was measured to have η_{QY} = 0.45 ± 0.05 at C_{dye} = 1×10^{-4} M (r = 25.44) in PMMA. For a truer analysis samples over a greater range of fluorophore concentrations should have been measured with correspondent pairs of quantum yield and fluorescence lifetime data.

7.5 Conclusion

The results of this chapter have shown that concentration quenching is a significant effect for all fluorophores and the host material itself has an important role to play in providing a stable, inert environment. DCM class fluorophores are found to be much less efficient than perylene based ones and it is apparent that different fluorophores exhibit differing quantum yield dependence on concentration. This suggests a range of quenching processes are being observed in many of the organic fluorophores studied.

The quenching process was seen to likely be the result of a combination of quenching mechanisms for two of the fluorophores studied, DCM and C102, based on the dependence on mean molecular separation, *r*, observed. The form of the dependence was seen to be of a monomial power law in terms of *r* to the power of -2.9±0.2 and -3.2±0.2 for DCM and C102, respectively. These values tell us the combined effect of all quenching processes is of longer range than point-like dipole-dipole interactions, proportional to r^{-6}. Point-surface and surface-surface interactions may be responsible for this deviation. If aggregates of fluorophores form between host polymer fibres then the proximity may lead to surface-like dipole distributions. electronic interaction with the host polymer may also be responsible. The result of a longer range effect is for the quantum yield to fall into decline at longer *r*, which is undesirable in LSC devices as lower concentrations and thicker devices will be necessary.

7.6 References

[1] Y. Kawamura, J. Brooks, J. J. Brown, H. Sasabe and C. Adachi, Intermolecular Interaction and a Concentration-Quenching Mechanism of Phosphorescent Ir(III) Complexes in a Solid Film, *Phys. Rev. Lett.* **96**, 017404 (2006)

[2] J. Cabanillas-Gonzalez, A. M. Fox, J. Hill and D. D. C. Bradley, Model for Energy Transfer in Polymer/Dye Blends Based on Point-Surface Dipole Interaction, *Chem. Mater.* **16**, 4705-4710 (2004)

[3] J. Hill, S. Y. Heriot, O. Worsfold, T. H. Richardson, A. M. Fox and D. D. C. Bradley, Dynamics of Förster transfer in polyfluorene-based polymer blends and Langmuir-Blodgett nanostructures, *Synth. Met.* **139**, 787-790 (2003)

[4] Rabih O. Al-Kaysi *et. al.*, The Photophysical Properties of Chromophores at High (100mM and above) Concentrations in Polymers and as Neat Solids, *Phys. Chem. Chem. Phys.* **8**, 3453-3459 (2006)

[5] S. A. Bagnich and V. N. Knyukshto, Quenching of Fluorescence of Conjugated Poly(*p*-Pheylene) Polymers by Benzil and Dimethylaminobenzil Molecules, *J. Appl. Spec.* **73**, 6 (2006)

[6] F. Fennel and S. Lochbrunner, Long distance energy transfer in a polymer matrix doped with a perylene dye, *Phys. Chem. Chem. Phys.* **13**, 3527-3533 (2011)

[7] J. Y. Choi, E. J. Park, S. H. Chang and T. J. Kang, Solvent Effects on the Solvatochromism of 7-Aminocoumarin Derivatives in Neat and Binary Solvent Mixtures: Correlation of the Electronic Transition Energies with the Solvent Polarity Parameters, *Bull. Korean Chem. Soc.* **30**, 7, 1452-1458 (2009)

Chapter 8

Spectral Based Models and Implications for LSC Devices

8.1 Introduction

In this final results chapter many of the preceding results are brought together to build a model in order to try and answer some fundamental questions about LSC technology and the performances that can be achieved. What kind of optical concentrations and performances can one expect from an LSC with the materials studied in this thesis? What are the optimal LSC properties to maximise output power? What kind of cost efficiencies can be achieved? How will solvation improve LSC performance?

To answer these kinds of questions on performance we turn back to the definition of optical concentration and the various associated efficiencies, which were laid out in chapter 2.2 and 2.3. The optical concentration, C_{opt}, is given in Eq. (2.3.2) as the product of the optical efficiency, η_{opt}, and the geometric concentration, G, which are given by Eqs. (2.2.15) and (2.3.1) respectively. By assuming suitable physical ranges for the different efficiency parameters, and the geometry of the LSC, various scenarios can be formed in a spectral based modelling approach. In section 8.2 a hypothetical ideal LSC is realised to calculate an upper limit of optical concentration.

The choice of model chosen for this work is different from those employed in literature [1] due to time constraints on this thesis and hence a requirement for ease of design. Typically either thermodynamic [2-4] or ray-tracing approaches [5-8] are used which are more accurate and therefore deserve discussion in some detail. Both of these modelling techniques require considerably more computational power than the spectral based model developed here, which stands as a clear advantage of the current work. However the accuracy and hence applicability to experiment is more limited in this case, for reasons to be discussed.

Thermodynamic modelling uses detailed balance arguments to relate the absorption and emission in terms of flux in 3D, allowing the photon chemical potential as a function of position to be determined. Detailed analytical expressions can be derived from this approach allowing accurate predictions of LSC device irradiance and power output. Such models can also be expanded using boundary conditions from experiment, for example when modelling how cholesteric coatings can be used as wavelength selective mirrors [4]. These models still make idealised assumptions about device

properties but are very instructive in optimising LSC performance. Compared to ray-tracing the thermodynamic approach requires less input data and is computationally less expensive.

3D ray-tracing models work by tracking individual photon paths through the device, the standard approach being to use a statistically averaged absorption process to reduce computation time [5, 6]. An extension to this in more recent ray-tracing models is to introduce the absorption and emission of the fluorophore [7, 8]. Ray-tracing provides more flexibility than other modelling approaches as it can be adapted to include multiple dyes, different LSC geometries and the modelling of thin film device structures. It has been shown to have a similar accuracy in prediction to the thermodynamic approach [1] and is fast becoming the dominant method.

The main advantages of the spectral modelling approach used here is in its analytical simplicity and low computational requirements. It still requires a significant amount of input data, discussed next, which include all sorts of properties about the different components in the concentration and conversion process, from sun to LSC to solar cell. The model exhibited here has not been developed to treat for more complex geometries and device architectures but could in principle do so with the right inputs and boundary conditions. Therefore it has the potential to be as flexible as ray-tracing approaches. Considering that it provides poorer accuracy with respect to experiment it is clear as to why the spectral modelling method not really used, particularly considering the wide availability of computational power.

Section 8.3 discusses the methods for predicting LSC performance by a detailed spectral analysis and methods for optimisation. Performance is characterised by the LSC output irradiance, $S_{LSC}(\lambda)$, the resultant power generated by an attached solar cell, P_{out}, and hence the LSC power conversion efficiency, η_{LSC}. These quantities are determined by knowing key inputs for the model which are; the solar irradiance spectrum, $S_{sun}(\lambda)$, host refractive index, n_2, fluorophore extinction spectrum, $\varepsilon(\lambda)$, fluorophore quantum yield as a function of concentration, $\eta_{QY}(C_{dye})$, normalised fluorophore emission spectrum, $S_N(\lambda)$, and the solar cell power conversion efficiency spectrum, $\eta_{PCE}(\lambda)$. Other efficiencies on which the optical efficiency of Eq. (2.2.15) depends are calculated through the spectral model or otherwise given reasonable assumed values from literature. LSC models are constrained to the square-planar geometry with a range of dimensions and geometric concentrations, G, explored.

Performance of the modelled LSC structures is also characterised by the £/W cost efficiency, which is calculated on the basis of the LSC volume and area of solar cells using reasoned cost values discussed in section 8.4.

The bulk of results is then discussed through section 8.5, looking in detail at single fluorophore LSC devices using two different models for attenuation of waveguided fluorescence. Comparison with the best devices in literature is made to assess the accuracy of the model with detailed analysis of all measures of performance.

8.2 The Ideal Case

Idealised values for the LSC efficiency parameters are summarised in Table XVII. This is for normally incident radiation on a LSC having a host of n = 2 which maximises reflection and trapping efficiencies. The Stokes' loss, η_{stokes}, is assumed negligible here under the argument that this loss of energy would occur at the solar cell under direct illumination anyway. The product of matrix transport efficiency and TIR efficiency, $\eta_{TIR}\eta_{host}$, is set at 0.95; the maximum predicted by Goetzberger and Vittwer 1981 [9]. Fluorophore quantum yield is set as unity and no overlap in absorption and emission spectra is present. The absorption efficiency, η_{abs}, is determined for a LSC with the thickness optimised such that absorption is maximised and the fluorophore, or system of fluorophores, has hypothetical absorption covering the solar spectrum up to 750 nm and delta function like emission at the peak of the EQE spectrum of a GaAs solar cell, around 800 nm. The geometric concentration is set at 250 which corresponds to a square-planar LSC of 1m^2 collection area and a thickness of 1 mm.

η_{fr}	η_{trap}	η_{stokes}	$\eta_{TIR}\eta_{host}$	η_{QY}	η_{abs}	η_{self}	G	C_{opt}
0.889	0.866	1	0.95	1	0.54	1	250	98.3

Table XVII: Ideal values for LSC optical concentration parameters.

The purpose of this first idealised exercise is to gauge the upper most limit of LSC optical concentration. As current materials and technology stand it can be seen the scenario of Table XVII is purely hypothetical; suitable hosts of n =2 do not exist for example and the nature of the hypothetical fluorophore system considered here is a mile away from current fluorophore technology. To maximise η_{abs} a FRET based LSC utilising multiple dyes might be considered but such a system would still struggle to achieve unity quantum yield, no self-absorption and such minimised matrix related losses for such a high G value. It is expected for large G that losses from transport, self-absorption and TIR imperfections will magnify with increased device size and it is not currently clear just how big G could be in a real, optimised device [10]. Such a thin device would be easily damaged and concentration quenching may become an issue due to a requirement for higher fluorophore concentrations to optimise η_{abs}.

8.3 Predicting LSC Power Output Using a Spectral Based Approach

Some more realistic scenarios shall now be considered in greater detail using methods developed in chapter 2.2 and 2.5 to make estimates of the relevant parameters. The relevant parameters are as in Table XVII on the previous page; C_{opt}, G, η_{opt}, η_{fr}, η_{trap}, η_{stokes}, η_{TIR}, η_{host}, η_{QY}, η_{abs} and η_{self}. The total internal reflection efficiency will take the best value predicted, η_{TIR} = 0.99, and η_{stokes} = 0.75 [9] as discussed in chapter 2, page. For these models square-planar concentrators are considered for various G and mean path length, $\langle r \rangle$, which impacts on self-absorption. Cylindrical LSC devices are only worth considering for bi-layer structures due to the way trapping efficiency increases with distance from the centre of the cylinder [5, 11]. Because of this, and the complexity of the mathematics, bi-layer cylindrical devices cannot be considered here but have elsewhere in ray-tracing models [5, 8] and for PR doped fibre LSC devices [12].

The aim is to find C_{opt} but also, using Eqs. (2.2.10), (2.2.13) and (2.2.15), to determine the irradiant intensity of light arriving at the solar cell. Then using external quantum efficiency spectra , $\eta_{EQE}(\lambda)$, for various solar cells digitised from graphical data with known power conversion efficiencies [13-15], the power conversion efficiency spectra were determined as discussed in chapter 2.5 using Eq. (2.5.3). Also note that now, because of Eq. (2.2.13), the optical efficiency, and therefore C_{opt}, is a function of wavelength due to the self-absorption process. Matrix related losses would also depend on wavelength but are quantified more simply in this exercise by the host attenuation at 550 nm. Since only PMMA is considered an attenuation of 3.5×10^{-4} cm^{-1} is adopted for calculating η_{host} throughout the models presented here.

First is to think about the fluorophore to be used; several basic single dye designs will be considered using DCJTB, PR and Perylene. Other fluorophores were considered but PR shows the best absorption properties and DCJTB offers the chance to exhibit the solvation enhancement, explored previously in chapter 5. Perylene is a very high quantum yield blue-green emitter and is therefore a good choice for the upper plate of a tandem LSC. These fluorophores have properties summarised in Table II on page 42, chapter 2.4, including extinction coefficients.

With these fluorophores in mind it is important to choose the optimum solar cell for absorbing the emission wavelengths. Fig. 8.3.1 shows a selection of solar cell $\eta_{PCE}(\lambda)$ spectra with the peak wavelengths of each dye shown. Clearly the GaAs solar cell will the best choice for each fluorophore followed by CIGS cells for DCJTB and PR and c:Si cells for Perylene.

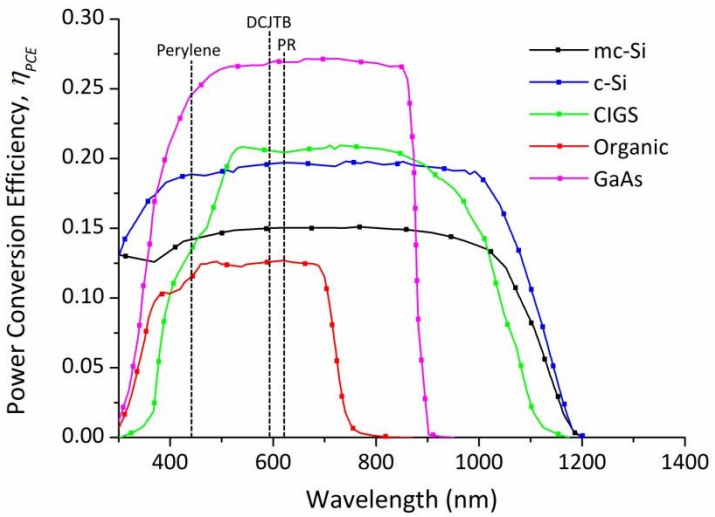

Figure 8.3.1: $\eta_{PCE}(\lambda)$ spectra for a range of solar cells with the emission peaks of the selected fluorophores shown by the dotted lines. These were defined in chapter 2.5 and expressed via Eq. (2.5.3).

To assess which solar cell is best Eq. (2.5.4) is used with the harvesting area set to unity; the PCE spectrum, $\eta_{PCE}(\lambda)$, for each cell is multiplied by the normalised spectra, $S_N(\lambda)$, of each dye, and the result is integrated to give a unitless relative output power, P_N.

$$P_N = \int \eta_{PCE}(\lambda) * S_N(\lambda)\, d\lambda \qquad (8.3.1)$$

The results of this process are shown in Table XVIII, normalised to the maximum value of P_N, showing the cell η_{PCE} values used and the values of P_N for each fluorophore/cell combination in a data matrix. Note that the η_{PCE} values, from NREL lab device efficiencies, are scaled by 0.6 for modular configurations, which is based on typical c:Si panel efficiencies of $\eta_{PCE} \approx 15\%$ and best lab devices of $\eta_{PCE} \approx 25\%$.

	mc-Si	**c-Si**	**CIGS**	**Organic**	**GaAs**
0.6η_{PCE}	0.117	0.154	0.14	0.06	0.17
DCJTB30	0.557	0.728	0.763	0.452	1
DCJTB	0.556	0.727	0.763	0.463	0.996
PR	0.439	0.574	0.601	0.363	0.788
Pery	0.360	0.471	0.402	0.304	0.638

Table XVIII: Data matrix for P_N values calculated by Eq. (8.3.1) and normalised to the maximum value, which is DCJTB-30 with GaAs. DCJTB-30 is for DJCTB in a host of $\varepsilon_r = 30$. The η_{PCE} values used are also shown in the first row, which are peak lab values from NREL scaled by 0.6.

Table XVIII shows DCJTB-30 (DCJTB with a solvation induced emission redshift) to be the best by this analysis but this does not take quantum yield and other factors into account since a normalised spectrum was used. GaAs cells prove to be the most effective of all the cells exhibited here with c:Si cells close behind. Since c:Si cells are of lower cost and it will be easier to find cost information for

them their power conversion spectrum will be used here for the most part. Some models with GaAs cells are explored since the best devices in literature have used them. It seems reasonable to assume the very best technology for an LSC since the point is to reduce the area of the solar cells required and PCE gains are to be had by removing the need for large area modular devices where losses are greater.

The next step in the recipe is to determine the reflection efficiency, η_{fr}, and the trapping efficiency, η_{trap}. These depend on the host refractive index, n, and, for η_{fr}, on the angle of incidence of solar irradiance. The irradiance entering the device is given by the product of the solar irradiance spectrum, $S_{sun}(\lambda)$, and η_{fr}, to give the transmitted irradiance, $T(\lambda)$. The chosen solar spectrum is the AM1.5 global irradiance spectrum from NREL [16].

The average absorption path length for light, l, is then given by Eq. (8.3.2) through Snell's law.

$$l = \frac{2W}{\left(1 - \frac{\sin^2\theta_i}{n_2^2}\right)^{1/2}} \qquad (8.3.2)$$

Where W is the LSC thickness and the factor of 2 comes from the back reflector giving rise to two passes through the device. A device designed to absorb diffuse light may therefore benefit from being thinner because the absorption length is on average greater, since diffuse light comes from many angles, and one could increase G to improve the diffuse yield in this way. At θ_i = 42.75° for PMMA we find l = 1.123W, which is a significant increase in absorption length compared to l = W for normal incidence.

Using the absorption length and the extinction coefficients of the fluorophores allows the absorbed intensity, $S_0(\lambda)$, to be determined using Eq. (2.2.5) in a similar way to that done in chapter 6.4, but with the irradiance input $T(\lambda) = \eta_{fr}S_{sun}(\lambda)$. Then the absorption efficiency, η_{abs}, is easily found by comparing the absorbed intensity to the total incident intensity. From $S_0(\lambda)$, measured η_{QY} values and using Eq. (2.2.10) the quantum yield corrected equivalent intensity spectrum, $S_1(\lambda)$, is determined. This is the irradiance spectrum of the first order emission to be propagated through the device.

For propagation of light through waveguide modes we must consider the self-absorption, host attenuation and TIR processes. As discussed in chapter 2, page 18, the TIR efficiency is expected to have a near unity value and is set at η_{TIR} = 0.99. The host attenuation is modelled using the absorption coefficient for pure PMMA measured at 550 nm, which is around $\alpha_h \approx 3.5\text{x}10^{-4}$ cm^{-1}. The Eq. 2.2.6 in chapter 2 then gives the host efficiency as $\eta_{host} = e^{-\alpha_h(\lambda)<r>}$. Lastly then η_{self} is

described by Eq. (2.2.13) and the mean path length of waveguide modes in square planar concentrators is described by Eq. (2.2.14). In Eq. (2.2.13) the self-absorbed irradiance spectrum is seen as $S_1(\lambda)(1 - e^{-\alpha_d(\lambda)<r>})$, which is set as the new $S_0(\lambda)$ in Eq. (2.2.10) in an iterative process that generates an irradiance spectrum for each order of emission. The actual emission from a given order that reaches the solar cell is thus taken to be $\eta_{TIR}\eta_{stokes}S_p(\lambda)e^{-\alpha_h<r>}e^{-\alpha_d(\lambda)<r>}$ for the pth order where $\eta_{TIR}\eta_{stokes}$ = 0.7425. Additionally the final LSC irradiance output, $S_{LSC}(\lambda)$, must be corrected for the geometric ratio, G, to take account of the concentration effect. Hence the combined LSC irradiance output for all p orders is given by the sum in Eq. (8.3.3).

$$S_{LSC}(\lambda) = G\eta_{TIR}\eta_{stokes}\sum_{p} S_p(\lambda)\left(e^{-\alpha_h<r>}e^{-\varepsilon(\lambda)C_{dye}<r>}\right) \quad for\ p = 1, 2, 3 \ldots \qquad (8.3.3)$$

Eq. (8.3.3) generates a spectrum which has been corrected for all losses through the LSC as faithfully as the available data allows. Strong confidence should be reasonable on both η_{QY} and η_{self} given available spectral and quantum yield information, though local variance in concentration will affect these values. The lack of information for η_{host}, which is likely to have some wavelength dependence, will result in some deviation in spectral shape and power density distribution from reality. An example set of LSC spectra calculated using these equations is shown in Fig. 8.3.2 for PR with G = 31.25 and $<r>$ = 26.7 cm.

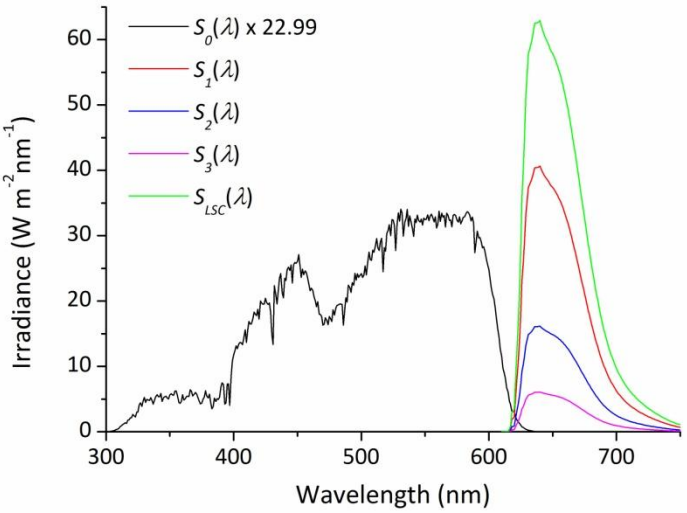

Figure 8.3.2: Plotted here for the fluorophore PR is; the absorbed irradiance spectrum, $S_0(\lambda)$, the emission irradiance spectrum for each order of emission after losses, $S_1(\lambda)$, $S_2(\lambda)$, and $S_3(\lambda)$, and their sum, $S_{LSC}(\lambda)$. LSC dimensions are W = 4 mm, L = 50 m, hence G = 31.25 and $<r>$ = 26.7 cm. The correction $G\eta_{TIR}\eta_{host}\eta_{stokes}$ = 22.99 is applied to emission and LSC output spectra, which gives a physical result for the concentrated irradiance, whereas the absorbed irradiance is scaled by the same factor for illustration.

As Figure 8.3.2 shows that the absorbed intensity is much smaller than the concentrated irradiance the LSC is outputting to the solar cells. This is due to the geometric concentration, quantified

through *G*. The total irradiance output for the case in Fig. 8.3.2 is equivalent to an optical efficiency of $\eta_{opt} \approx 6\%$ and an optical concentration of $C_{opt} = 1.87$ suns. Self-absorption is evident but after the average path length of 26.7 cm there is still some overlap and self-absorption is not exhausted.

With the result in Eq. (8.3.3) an equation similar to Eq. (8.3.1) can now be written to calculate the output power of the LSC. Replacing $S_{sun}(\lambda)$ in Eq. (2.5.4) with $S_{LSC}(\lambda)$ and then multiplying through by the area of solar cell, A_{har}, gives the power collected, as in Eq. (8.3.4). Note also the power correction factor, β, which corrects for change in solar cell efficiency with light intensity, as explained in chapter 2, page 48.

$$P_{out} = \beta A_{har} \int \eta_{PCE}(\lambda) S_{LSC}(\lambda) d\lambda \qquad (8.3.4)$$

As was done in chapter 5 on the solvation enhancement of η_{self}, the optical efficiency, η_{opt}, can be calculated up to the third generation using Eq. (2.2.15), at which point further orders of self-absorption and emission are considered negligible.

A back reflector, with reflectivity = 0.97, will generally be used to maximise absorption which introduces a factor of two in absorption path length equations. It also introduces a small contribution to the LSC output from cone light from all escape cones facing the back reflector, leading to a modified Eq. (8.3.3) for the output irradiance spectrum. ECL transfer gains of this sort can be quite large, up to several percent of the total output irradiance with a strong dependence on dye concentration. The LSC plate emits total $S_1(\lambda)/\eta_{trap}$ for each emission order, determined as discussed above, and of this a fraction $(1 - \eta_{trap})$ escapes via ECL, so the irradiance spectrum leaving via the escape cones, $S_{ECL}(\lambda)$, is given by Eq. (8.3.5).

$$S_{ECL}(\lambda) = \sum_{p} \frac{S_p(\lambda)}{\eta_{trap}} (1 - \eta_{trap}) \qquad for\ p = 1, 2, 3 \ldots \quad (8.3.5)$$

Note that the ECL irradiance doesn't suffer from a η_{TIR}; this is because TIR is irrelevant since escape cone light does not internally reflect. Also note the irradiance for the *p*th order is divided by η_{trap} due to the definition of $S_p(\lambda)$ from Eq. (2.2.10). Only one of the two escape cones is directed onto the back reflector and so the ECL irradiance that is reflected is given by half of Eq. (8.3.5). The angle at which this occurs is again done on average. For PMMA with n = 1.492 gives critical angle $\theta_c = 42.09°$ and hence $\theta_{ECL} = 21.05°$. By replacing θ_i with θ_{ECL} in Eq. (8.3.2) the mean absorption path length for this contribution is determined and hence the self-absorbed irradiance spectrum can be found. Note that on average light is emitted at height *W*/2 in the z plane, so the total z distance is 3*W*/2 for back

reflected irradiance. As before the self-absorbed irradiance is translated to an emission irradiance via Eq. (2.2.10) and this contribution propagated to the LSC edge.

We also need to consider is what values of geometric ratio, *G*, to use and there are two ways to do this. First is to optimise *G* for each dye by the absorption path length of the incident irradiance (hence the thickness of the LSC plate) in light of the extinction coefficients. DCJTB has greater extinction than perylene or PR and hence will benefit by reduced thickness and enhanced *G*. The other way is to use the same values of *G* but tune the fluorophore concentration, hence quantum yield and normalised emission spectrum, of the fluorophores to achieve optimised absorption efficiency. Here the second approach is preferred as comparing LSC devices of different *G* values is unnecessarily complicated.

This is done with the fluorophores detailed above whose optimised concentrations are dictated by both the need to maximise absorption of incident light and reduce loss across the LSC. The size of the LSC is critical in this because of self-absorption and host attenuation. Thicker plates achieve peak output at lower concentrations because they require less dye to maximise absorption of sunlight. The energy density coming out of the LSC is lower for thicker plates, due to having a lower *G*, but the amount of power generated also depends on the area of solar cells, so thicker plates may still generate more power.

The peak of irradiance output occurs for C_{dye} between 10^{-4} M and 10^{-3} M, depending on which fluorophore we look at and the LSC plate dimensions. Optimised quantum yield/fluorophore concentration, self-absorption and absorption of incident radiation are contained within this characterisation. For the fluorophore concentrations both PR and DCJTB use $C_{dye} = 10^{-4}$ M and perylene uses $C_{dye} = 5\text{x}10^{-4}$ M.

Everything that has been developed above leads to determining the optical concentration, C_{opt}, the LSC output spectrum, $S_{LSC}(\lambda)$, and from this the power generated by the cell, $P_{out.}$. The ratio of the integral of $S_{LSC}(\lambda)$ to that of the solar irradiance spectrum, $S_{sun}(\lambda)$, should be equal to C_{opt} calculated by Eqs. (2.2.15) and (2.3.2), since they are determined with the same inputs. One can now also calculate the LSC power conversion efficiency, η_{LSC}, which is given by the ratio of power in to power out as in Eq. (8.3.6).

$$\eta_{LSC} = \frac{P_{out}}{P_{in}} = \frac{A_{har} \int \eta_{PCE}(\lambda) S_{LSC}(\lambda) d\lambda}{A_{col} \int S_{sun}(\lambda) d\lambda} \qquad (8.3.6)$$

Where P_{in} is the integral of solar irradiance spectrum times by collection area, A_{col}, and P_{out} is given by Eq. (8.3.4). As discussed in chapter 2.6 the two best state of the art LSC devices give $\eta_{LSC} = 7.1\%$ [17]

and η_{LSC} = 6.7% [18] for devices of dimensions 5 x 5 x 0.5 cm (G = 2.5) and a two stack of 2 x 2 x 0.3 cm (G = 5/3), respectively. Both of these used two dye systems and will make interesting comparison for some of the models produced here. These LSC devices and others in literature are seen in Table VI, chapter 2.6, page 50.

8.4 Estimating the Cost Efficiency of a LSC Device

The last thing that can be estimated is the cost per unit power delivered by the modelled device structures. This has been done in detail alongside LSC device optimisation through ray-tracing simulations [19]. In that work the performance is characterised through three measures; the cost per unit area, power output per unit area and their ratio The LSC structure will have a cost per unit volume for the host and dye materials. The solar cell will have a cost per unit area; production costs are included by considering the cost of typical c:Si panels available online. These costs are determined for the given LSC structure of volume, V_{LSC}, dye concentration, C_{dye} (in mol m^{-3}), and solar cell area, A_{har}. By summing the costs and dividing the result by the power estimated by the model we arrive at an estimate of the cost per unit power delivered, (£/W)$_{conc}$, with the target to achieve < 0.61 £/W (or < 1 $/W). This is given by Eq. (8.4.1).

$$\left(\pounds/W\right)_{conc} = \frac{V_{LSC}\left(\left(\pounds_{host}/m^3\right) + C_{dye}\left(\pounds_{dye}/mol\right)\right) + A_{har}\left(\pounds_{PV}/m^2\right)}{P_{out}} \qquad (8.4.1)$$

By canvassing c:Si solar panels online that are available to end users, typically with cost efficiency around 1$/W, one arrives at a panel cost per unit area of (£$_{c:Si}$/m^2) ≈ £ 120 m^{-2}. This number includes balance of system (BOS) costs in production and transport which will suffice for approximating the BOS for our hypothetical LSC devices.

The fluorophores PR, DCJTB and perylene can be found available at various laser accessory retailers but the profit mark-up and poor economies of scale at such vendors make the prices uneconomic. For example Photonic Solutions Ltd. sells PR under Exciton trade name Exalite 613 at £140 per g. Not a great deal; compare this to Rhodamine 6G, a fluorophore often used in LSC research and in other scientific pursuits, which comes at £15 per g from the same source. Clearly economies of scale allow for reduction of price by an order of magnitude and will be taken as 2% [20] of the prices found from sources such as Photonics Solutions Ltd. These are taken to be £1.8 g^{-1}, £2.8 g^{-1} and £1 g^{-1} for DCJTB, PR and perylene respectively. With the cost per gram known the (£$_{dye}$/mol) cost can be found from

the molecular weights, which are 453.63 g mol^{-1}, 963.956 g mol^{-1} and 252.32 g mol^{-1} for DCJTB, PR and perylene, respectively. Now (£$_{dye}$/mol) ≈ £ 820 mol^{-1}, £2700 mol^{-1} and £250 mol^{-1} for DCJTB, PR and perylene respectively. PR is significantly more expensive by this analysis which will offset gains in power due to its better performance.

The final cost to approximate is the cost of the host material. PMMA is produced on larges scales by various techniques. Companies such as Shenzhen Xintao Acrylic Co. Ltd. use extrusion to create highly uniform sheets of such thermoplastics, which may be a viable large scale production method for LSC devices. Typical costs are at around £2 per kg of material extruded and 50% should be added to account for complexities in the process introduced by the requirements of a LSC. So at £3 per kg with the density of PMMA at ρ_{PMMA} = 1180 kg m^{-3} we find a cost of (£$_{host}$/m^3) ≈ £3500 m^{-3}.

For DCJTB with the solvation enhancement some extra cost must be factored in for some high permittivity material to induce the effect. TiO_2 nanoparticles can be bought, silane coated for dissolving in solution, at around £360 per kg from companies like SkySpring Nanomaterials, Inc. TiO_2 has a relative permittivity around 100 and hence around 28 wt% of TiO_2 nanoparticles in PMMA is required to achieve ε_r = 30, which is an impractically high concentration. If it were $SrBaTiO_3$, a more expensive titanate, only 2 wt% would be required as it has a permittivity of 1250. Assuming ten times the cost for $SrBaTiO_3$, £3600 per kg, then for every m^3 of host 23.6 kg of nanoparticles are needed, hence (£$_{SrBaTiO3}$/m^3) ≈ £85000 m^{-3}. This cost is added in with host costs and greatly increases the cost of the concentrator.

All of the cost considerations here are based on reasonable approximations but are still quite arguable. They are meant to give a ballpark cost efficiency to consider, approached with the caution of appreciation of the large uncertainties involved.

8.5 Spectral Analysis for a Single Fluorophore LSC Devices

In this first results section single fluorophore plates are considered for perylene, PR, DCJTB and DCJTB-30, which is for DCJTB influenced by the solvation effect with host permittivity at ε_r = 30. For each fluorophore the model requires the quantum yield, $\eta_{QY}(C_{dye})$, extinction coefficients, $\varepsilon(\lambda)$, and the normalised emission spectrum, $S_N(\lambda)$. The latter two are seen in chapter 2.4 and the fluorophore quantum yields are determined for a given concentration from fits to the data in Fig. 7.2.1.

Other inputs to model are; the AM1.5 global solar irradiance spectrum, $S_{sun}(\lambda)$, which is incident at normal incidence, θ_i = 0°, on a host of n = 1.492, that of PMMA. This sets the reflection and trapping

efficiencies at η_{fr} = 0.961 and η_{trap} = 0.742. With these inputs fixed the analysis described in the preceding two sections is run for various side lengths, *L*, and thicknesses, *W*, of a square-planar geometry and hence various geometric concentrations, *G*. Thickness and dye concentration, C_{dye}, will determine the absorption efficiency, η_{abs}, of the LSC plate. In Fig. 8.5.1 irradiance is plotted against wavelength to show absorption of solar irradiance by DCJTB and the resultant trapped emission irradiance, $S_1(\lambda)$, prior to self-absorption and concentration.

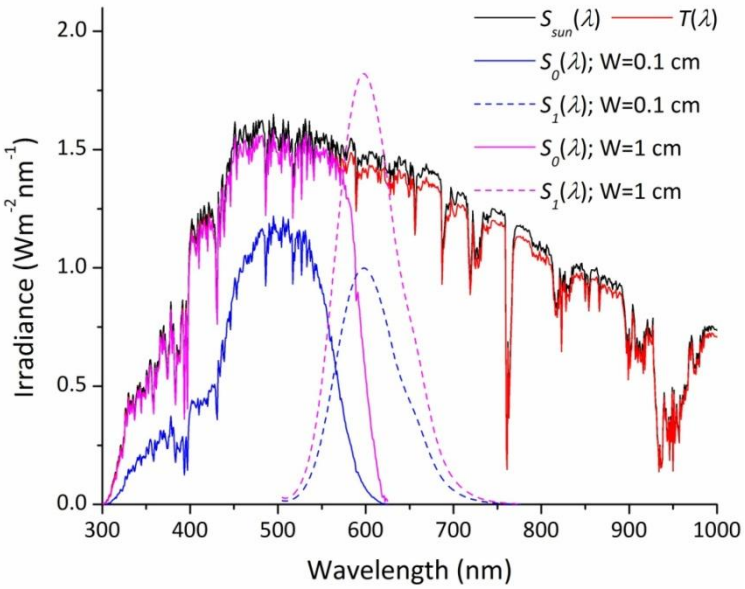

Figure 8.5.1: The solar irradiance spectrum, $S_{sun}(\lambda)$, is partially reflected before being transmitted into the LSC as transmitted irradiance, $T(\lambda)$. Absorption takes place, here for DCJTB at C_{dye} = 10^{-4} M, generating the absorbed irradiance, $S_0(\lambda)$, which is subsequently emitted and corrected for η_{trap} = 0.742 and η_{QY} = 0.69 to give the emitted irradiance, $S_1(\lambda)$. Because of geometric concentration the irradiance falling on the solar cell can peak at many times the irradiant intensities in this plot.

Every time the thickness is changed, or if fluorophore properties are changed, the curves in Fig. 8.5.1 will also change. By varying dye concentration and LSC thickness the optimal absorption of irradiance can be achieved. At this stage of the spectral analysis the outputs can be considered quite accurate in terms of the quantum yield and absorption coefficient measurements.

8.5.1 Absorption and Self-absorption Efficiencies

The absorption efficiency is determined from the irradiance spectra, such as that presented in Fig. 8.5.1. η_{abs} is shown in Fig. 8.5.2 as a function of LSC thickness for the three fluorophores here at C_{dye} = 10^{-4} M. Back reflectors are not included so that the true absorption as a function of depth is considered. DCJTB-30 has the same absorption as DCJTB because influence of solvation over the absorption spectrum was measured to be negligible in chapter 5 and hence the same absorption

spectrum is used. Solvation does not affect the absorption transition since it occurs too fast for the surrounding medium to respond.

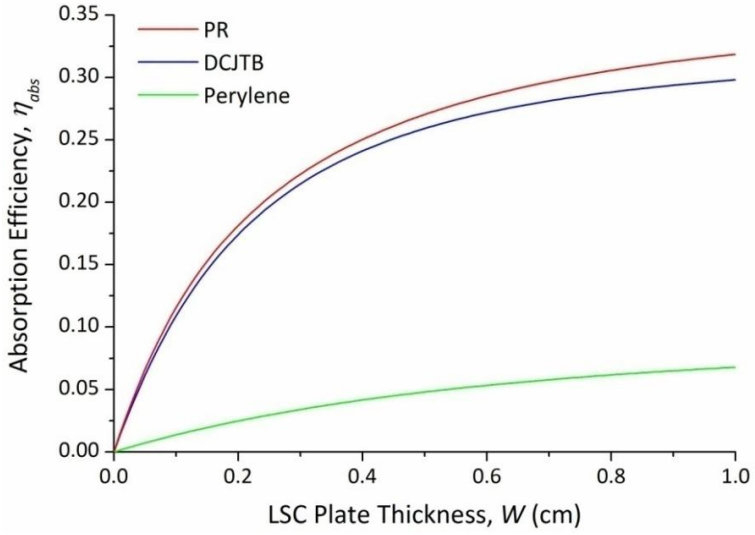

Figure 8.5.2: The efficiency of absorption of incident solar irradiance is plotted against LSC plate thickness here for DCJTB (blue), PR (red) and perylene (green).

It is somewhat of a surprise that PR shows greater absorption efficiency than DCJTB since DCJTB has greater extinction. The stronger extinction in the red tail of PR must be responsible for this. Perylene only absorbs in a small portion in the blue tail of the solar spectrum making it a poor solar irradiance collecting material on its own. The maximum that either PR or DCJTB can absorb is below 35% of incident solar energy and hence this stands as one of the major limiting factors in LSC performance.

The next step of the model begins to introduce greater uncertainty as we consider the self-absorption process and propagate the irradiance to the LSC edge. The side length, and hence mean path $\langle r \rangle$, and C_{dye} will determine the self-absorption efficiency, η_{self}. By taking a mean path rather than calculating the self-absorption for each path, as in ray-tracing calculations, some uncertainty is expected in the shape of the output. Measuring absorption coefficients accurately beyond the red tail of extinction is difficult with the fluorospectrometer used for these measurements, as described in chapter 3.3. To account for this issue a Gaussian tail is added to the red-tail of the fluorophore extinction spectra.

With these sources of uncertainty in mind the self-absorption efficiency, η_{self}, has been calculated using Eq. (2.2.13), as shown in Fig. 8.5.3. This shows η_{self} as a function of the LSC side length, L, for each dye for a LSC thickness of W = 1 cm and concentration for all dyes at $C_{dye} = 10^{-4}$ M.

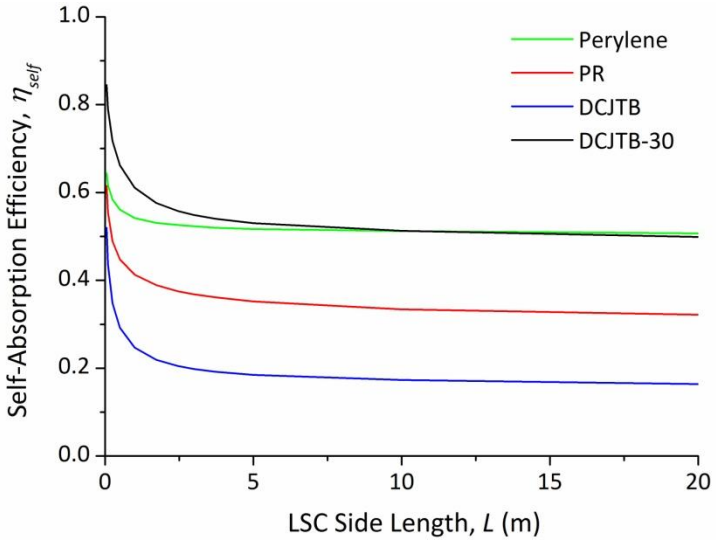

Figure 8.5.3: Self-absorption efficiency against LSC side length for LSC devices of W = 1cm. Each of DCJTB-30 (black), DCJTB (blue), PR (red) and perylene (green) are shown.

Fig. 8.5.3 gives insight into the workings of the model. DCJTB-30 shows much higher η_{self} values than the other fluorophores thanks to solvation induced redshift of emission. The models show that the self-absorption efficiency reaches a steady value after a certain side length of LSC, which is due to total absorption of the all irradiance in the extinction region. To ensure optimal absorption of solar irradiance a perylene based LSC plate must be thicker to achieve lower fluorophore concentrations and therefore longer lengths. This is an important point if a tandem LSC were considered; it is desirable to match the side lengths of the stack layers but some layers may find optimum η_{LSC} for different thicknesses.

The model shows a sharp dependence on side length below 2.5m, particularly for lower LSC lengths which indicate that as the LSC side length tends to 0 the self-absorption efficiency will tend to unity. However, such sizes are not particularly practical in terms of power generation due to low geometric ratios and sub-solar irradiant output, which means the c:Si solar cell will not be operating at optimum efficiency.

8.5.2 Optical Concentration

With the absorption and self-absorption efficiencies determined it is now possible to determine both the optical concentration, C_{opt}, and the LSC output irradiance, $S_{LSC}(\lambda)$, as outlined in section 8.2. As stated in that section the ratio of the integral of $S_{LSC}(\lambda)$ to that of the input solar irradiance, $S_{sun}(\lambda)$, should be equal to C_{opt}. This will not be true when using Eq. (2.2.15) for the optical efficiency, η_{opt}, because this does not account for addition of escape cone gains due to back reflection. Since back

reflectors have been used in these models this must be added into the equations for optical efficiency. The easiest way to do this is to consider the gain from escape cone back reflection as to effectively increase the trapping efficiency, η_{trap}. The trapping efficiency can be written in terms of the integrals of the absorbed irradiance, $S_0(\lambda)$, and the trapped emitted irradiance without quantum yield correction, $S_{trap}(\lambda)$. The EC gain irradiance, $S_{ECL,1}(\lambda)$, is added to the trapped emitted irradiance to find the new effective trapping efficiency, η'_{trap}, as in Eq. (8.5.1);

$$\eta'_{trap} = 1 - \frac{\int S_0(\lambda)d\lambda - \int \left(S_{trap}(\lambda) + S_{ECL,1}(\lambda)\right) d\lambda}{\int S_0(\lambda)d\lambda} \qquad (8.5.1)$$

Using Eq. (8.5.1) in Eq. (2.2.15) gives the correct optical efficiency and thus for a given geometry the optical concentration can be found via Eq. (2.3.2). This is plotted as a function of both LSC side length and geometric concentration in Fig. 8.5.4 for the fluorophore case used in Figure 8.5.3 with the concentration for both PR and DCJTB as C_{dye} = 10^{-4} M and perylene has C_{dye} = 5x10^{-4} M and LSC thickness W = 1 cm.

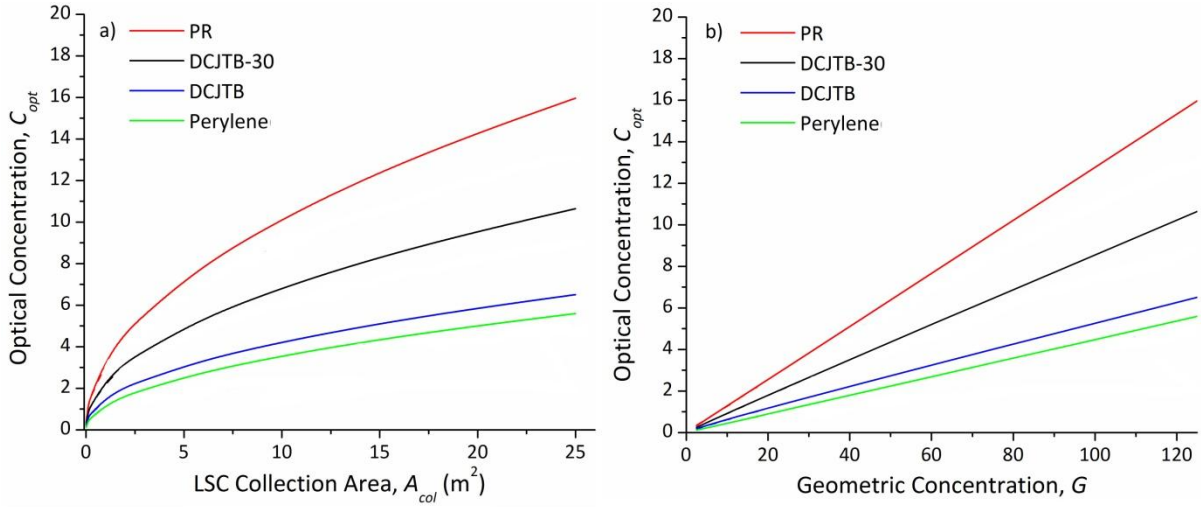

Figure 8.5.4: Plot of optical concentration against a) LSC collection area and b) geometric concentration for LSC devices of W = 1 cm. Each of DCJTB-30 (black), DCJTB (blue), PR (red) and perylene (green) are shown.

For a LSC thickness of 1 cm the collection area required to achieve high optical concentrations is very large. According to the model for PR at A_{col} = 1 m^2 the optical concentration is C_{opt} ≈ 3. However, if the LSC thickness is decreased by a factor the geometric concentration will increase by the same factor which means for W = 0.1 cm the optical concentration will be approximately ten times higher. This is approximate because decreasing thickness decreases absorption efficiency, η_{abs}, and thus the optical efficiency tends to be lower for thinner structures.

Note that Figure 8.5.4 is not in line with other models and experiments since the optical concentration is expected to plateau for LSC side lengths of around 1m [21]. This is because the self-

absorption and host attenuation are poorly matched to reality. To improve this a complete host attenuation spectrum and a more accurate fluorophore extinction spectrum across the whole emission spectrum would be needed. The fact that the Gaussian tails added to the extinction coefficient spectra indicates that there is likely to be a significant extinction by the fluorophore beyond that characterised here.

Optical concentration tells us the intensity of the irradiance coming out of the LSC edge relative to the solar irradiance intensity. The best way to enhance this is by increasing the geometric concentration which is done by reducing the thickness or increasing the side lengths. As Figs. 8.5.2 and 8.5.3 have shown us doing either of these adjustments leads to decreased absorption or increased self-absorption. As a result optical concentration does not translate to increased power conversion efficiency, in fact quite the opposite as we shall see.

8.5.3 Power Conversion Estimates

Power conversion is first considered for the c:Si solar cell's $\eta_{PCE}(\lambda)$ spectrum and later with that of GaAs. The sun's energy falls on an area A_{col} and hence a known power is delivered to a given size of LSC. By plotting the estimated power out, P_{out}, from the LSC device against A_{col} one can see how the modelled concentrator deviates from the input power. This is shown in Fig. 8.5.5 for LSC devices of W = 1 cm and again for both PR and DCJTB $C_{dye} = 10^{-4}$ M and for perylene $C_{dye} = 5\text{x}10^{-4}$ M.

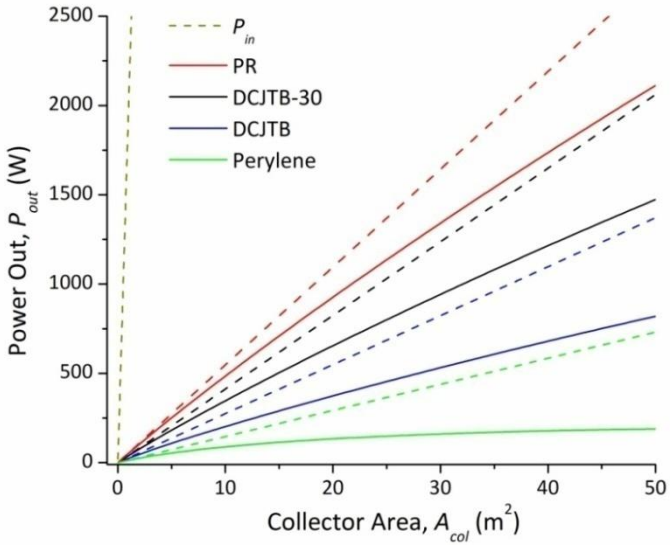

Figure 8.5.5: Power against LSC collector area for single dye plates of thickness W = 1 cm doped with the fluorophores PR (red), DCJTB (blue), DCJTB-30 (black) or perylene (green). Included is a back reflector, escape cone back reflection gain and fluorophore concentration set at 10^{-4} M. Dashed lines show the low area gradient linearly fixed to large collector areas to show the curvature. The power arriving from the sun (dashed gold line) is also shown for comparison.

From Fig. 8.5.5 there is a huge difference seen between the irradiant power coming from the sun and the electrical power out of the LSC-solar cell combination. One can see that overall LSC power conversion efficiencies, which shall be exhibited shortly, are of the order of a percent or so. The gradient of the power curves is closely related to η_{LSC} and is seen to decrease with collector area due to the increased self-absorption losses. Importantly there are extra losses due to the attenuation added into the fluorophore extinction spectra in the red tail.

The dashed lines in Fig. 8.5.5 show that an array of LSC devices will perform much better than one large one. This must be balanced against extra cost because as we decrease the collection area of each LSC array element so as to increase the power conversion the number of array elements for a given total collection area increases. This means more solar cell area per unit volume of concentrator, which will increase the cost. Such matters will be considered in detail shortly.

With the power out and power in known it is a trivial matter to determine the LSC power conversion efficiency, as in Eq. (8.3.6). This is shown in Fig. 8.5.6 as a function of the log of collector area for LSC devices of W = 1cm. The best LSC devices in literature are also added as single data points and for the configuration of the 7.1% device the model is run for PR as a comparison.

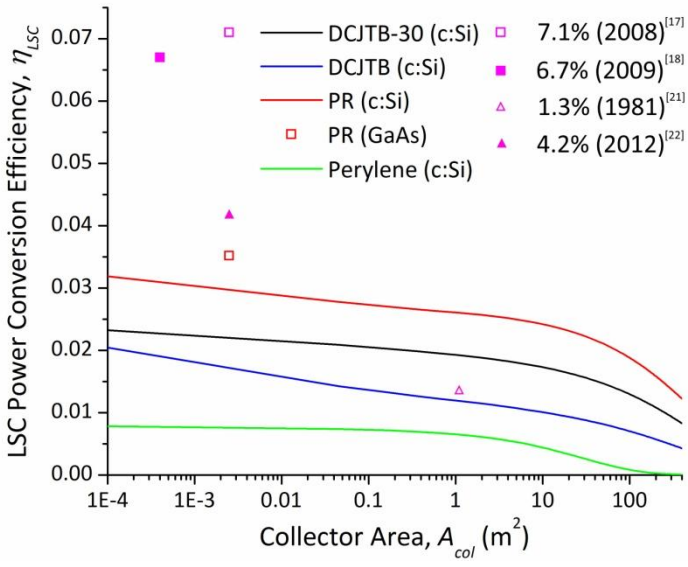

Figure 8.5.6: LSC power conversion efficiency against collector area on a logarithmic scale for single dye plates of thickness W = 1 cm doped with the fluorophores PR (red), DCJTB (blue), DCJTB-30 (black) or perylene (green). The extended extinction model is used with a back reflector, escape cone back reflection gain is added and fluorophore concentration optimised. Some LSC devices from literature, see Table VI on page 48, are shown for comparison (magenta shapes) and the model is run for PR under the same device configuration as the 7.1% device (red open square).

For all the modelled plates here severe attenuation of waveguided light begins between 1 m^2 and 10 m^2. As has been seen by the power curves of Fig. 8.5.5 the best arrangement for a LSC installation will be some form of array balancing efficiency against device cost. Array elements will certainly

need to be less than $1m^2$ to avoid the severe losses from the extended path lengths for such large areas.

Comparing Figs. 8.5.4 and 8.5.6 it can be seen that increasing optical concentration necessarily results in decreased power conversion efficiency. It is not possible to determine the optical concentration of the devices from literature shown in Fig. 8.5.6 because η_{abs} and η_{self} cannot be calculated from the information presented in those papers. However, the PR (GaAs) device has $C_{opt} \approx 0.3$ for $\eta_{LSC} = 0.035$, which means the irradiance intensity coming from the LSC edge is less than a third of that of the incident irradiance. By comparison the devices from literature cannot have a $C_{opt} > 1$.

The best LSC devices in literature are of very small collection area, which enhances the output but makes them unlikely to find application as a marketable device. The 7.1% device [17] is a PMMA plate doped with PR and a yellow coumarin fluorophore, CRS040, with area $A_{col} = 25\ cm^2$ and thickness $W = 0.5$ cm. GaAs cells were used on all four sides, which will perform better than the c:Si cells used for the modelled curves of Fig. 8.5.6. The 6.7% device [18] is a two layer tandem LSC using fluorophores BA241 and BA856 with $A_{col} = 4\ cm^2$, $W = 0.3$ cm and GaInP solar cells on all four sides.

The 1.3% device made back in 1981 [22] has DCM as the fluorophore at $C_{dye} = 2.2 \times 10^{-4}$ M, which makes interesting comparison with DCJTB since they are of the same chemical family. DCJTB has a higher quantum yield than DCM and was modelled here at 10^{-4} M so one might expect the blue curve in Fig. 8.5.6 to sit a little above the open magenta triangle. Additionally the DCM device was 0.4 cm thick whilst the DCJTB model here is run for a 1 cm plate, which means the 1.3% device will be absorbing less solar irradiance. This tells us that there is a significant difference between the model and reality, despite the apparently pleasing visual comparison in Fig. 8.5.6. Another point is that of self-absorption, which may be less for DCM and we must also consider that self-absorption and attenuation in the model is based on an estimate, not reality.

Another reasonable comparison can be made with the 7.1% device to compare against the single fluorophore PR LSC of the model. The c:Si $\eta_{PCE}(\lambda)$ spectrum is exchanged with that of GaAs and the fluorophore concentration is set to 1.2×10^{-4}M. The result of this is also in Fig. 8.5.6 and the model predicts this will device will have roughly half of that of the 7.1% device of literature. Again there is a lot of uncertainty in the model that will account for this discrepancy and the presence of a second dye will also increase the power conversion to some extent. The 0.6 scaling of the GaAs $\eta_{PCE}(\lambda)$ spectrum will play an important role as will other assumed parameters in the model such as η_{stokes}. Additional differences lie in the electrical characteristics in the real device; for example series and

parallel cell circuit configurations are built and also the back reflector they use has 0.97 reflection efficiency, not unity. Despite these differences and the uncertainties in the model the results presented here seem to lie in general agreement with that of real devices with perhaps too much lost by the model to cell efficiency scaling and extended extinction.

The gains from solvation for DCJTB increase as collector area increases because of the steeper increase in self-absorption seen for pure DCJTB. At about A_{col} = 1 m^2 the enhancement of LSC power conversion efficiency of DCJTB-30 relative to pure DCJTB is roughly 61.3%, which is significantly greater than the 23.4% predicted in chapter 5 for DCJTB using the overlap integral, *J*, to parameterise the self-absorption. Chapter 5 actually made predictions of the optical efficiency, η_{opt}, but the comparison still holds since we're comparing devices of the same geometric concentration, *G*. Therefore the only difference between DCJTB-30 and DCJTB is in the irradiant intensity falling on the solar cells which is governed by η_{opt}.

There is an issue with this comparison; in chapter 5 the fluorophore concentration was fixed at C_{dye} = 0.1 wt% or 2.6x10^{-3} M, which means faster extinction. The result of increasing fluorophore concentration at fixed A_{col} is to increase the gains from the solvation effect because transport losses increase faster for pure DCJTB. For A_{col} = 10^{-4} m^2 the solvation enhancement is reduced to just 13.6% relative, which is less than that predicted using *J*. It can be concluded that *J* is a poor estimator of the true effect of self-absorption and is a value only appropriate for very small path lengths of around 1 cm. Self-absorption is a stronger effect than characterised in chapter 5 and as a result solvation gives rise to greater efficiency enhancements than expected from that earlier analysis.

Another effect that can be considered is that of a change in host material and hence refractive index. Fig 8.5.7 shows LSC efficiency as a function of collector area for the fluorophore PR with several values of *n* with *W* = 1 cm.

Fig. 8.5.7 shows, in a more detailed manner, a similar result to Fig. 2.2.4. Increasing host *n* results in various changes; the amount of reflected incident irradiance increases but the escape cone shrinks increasing the amount of trapped light. Additionally the mean path length increases with increased *n* due to the introduction of extra emission rays by the reduced escape cone, which have smaller angles relative to the LSC surface normal. Because of this the self-absorption efficiency, η_{self}, decreases slightly but not significantly enough to stop higher refractive indices delivering higher power conversion efficiencies. Changing a host material does not just change *n*, however, but also host attenuation, film forming and mechanical properties must also be considered.

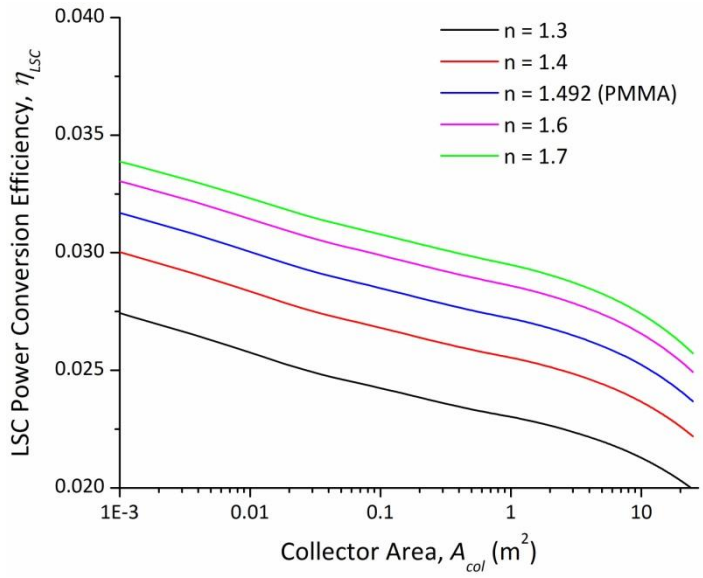

Figure 8.5.7: LSC power conversion efficiency against collector area on a logarithmic scale for the fluorophore PR in different host refractive indices. These modelled LSC plates have W = 1 cm and use attenuation model X. These n values can be compared those of the host materials in Table IV.

8.5.4 Cost Efficiency Estimates

Using the method and cost estimates from section 8.4 the power delivered by the modelled LSC devices can be used to determine the device cost per watt of electrical power out. This is done again for W = 1 cm and the again both PR and DCJTB use $C_{dye} = 10^{-4}$ M and perylene uses $C_{dye} = 5\text{x}10^{-4}$ M for comparison with the LSC power conversion efficiency. Fig. 8.5.8 shows a double-y plot for both η_{LSC} and $(£/W)_{conc}$ against the length of LSC sides.

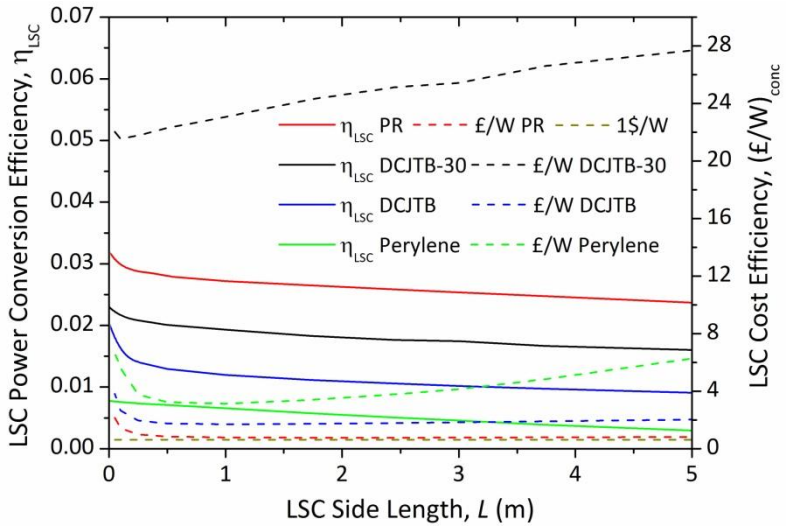

Figure 8.5.8: η_{LSC} (solid lines) and $(£/W)_{conc}$ (dashed lines) against the LSC side length for DCJTB-30 (black), DCJTB (blue), PR (red) and perylene (green). The target of 1 $/W is also shown as a line with no gradient (short-dashed, grey). All models here have W = 1 cm.

For small scale devices, such as the best in literature discussed earlier, the LSC efficiency is at a peak due to minimised self-absorption losses. This declines quickly to the regime where self-absorption saturates except in the extended red tail of extinction, which causes a slower decline in η_{LSC} with increased L. At around L = 0.3 m the cost efficiency reaches a minimum which holds for PR, DCJTB and perylene up to 1 or 2 metres. PR has a minimum of $(£/W)_{conc}$ = 0.76 £/W at around L = 1.7 m; this length will not give the best power conversion efficiency for the LSC but will deliver the best economics. According to these models a single dye LSC based on PR should perform at double the cost per watt as a c:Si solar module. An array of LSC devices using PR based on the results here would be made of square LSC devices with a side length of 1.7 m. At this size each plate, with c:Si cells attached, is generating around 160 W and the collector area is A_{col} = 3 m^2. That gives approximately 53 W/m^2 for a total device cost of £120. By contrast a modular c:Si solar panel generating 160 W/m^2 and costs around 0.61 £/W; therefore for an area of A_{col} = 3 m^2 such a panel would generate 480 W and would cost about £293. It is less costly to cover a larger area with LSC devices based on PR but the result is less power and poorer economics of wattage.

The cost per watt of power out is seen to be higher at very small L due to the way in which the different costs vary with LSC geometry. Consider Eq. (8.4.1); the cost of solar cells depends on edge area, $A_{har} = 4LW$, whilst the host and dye materials depend on LSC volume, $V_{LSC} = L^2W$. Therefore, since volume grows faster than harvesting area, the costs from host and fluorophore materials will dominate very quickly. At small lengths L^2 is very small and the cost of the cells will dominate, except in the case of DCJTB-30 using nanoparticles. This is seen in Fig. 8.5.9.

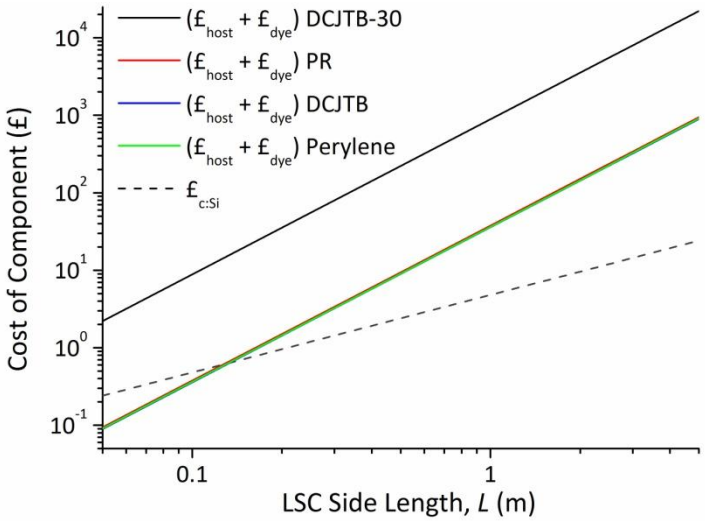

Figure 8.5.9: Log-log plot of costs in pounds (£) for the concentrator (solid lines) and solar cell (dashed line) components of a W = 1 cm LSC device as a function of LSC side length. DCJTB-30 (black), DCJTB (blue), PR (red) and perylene (green) dyes are shown.

Figs. 8.5.9 shows that the cost of solar cells dominates until around 15 cm for DCJTB, PR and Perylene with not much difference between these fluorophores. This is because the cost of the host material dominates the cost of the concentrator component. The solvation enhancements modelled for DCJTB-30 come at tremendous extra cost when using nanoparticles and the analysis gives immediate indication that this is not going to be an economic option. The only way for solvation to be useful is to employ a low cost organic material of high relative permittivity, which is a problem in itself, or a low cost high permittivity host. Using camphoric acid anhydride (CAA), used in chapter 5 to exhibit the solvation effect, as a dopant would be expensive as 30 wt% would needed to double the relative permittivity to 5.75 in PMMA. It costs £35 for 50 g via Sigma Aldrich and is not sold by the tonnage like PMMA. Even at 10% of the Sigma price CAA will significantly increase the cost of the device; £3.5 per 50 g so £70 per kg. For every cubic metre 354 kg of CAA will be needed so ($£_{CAA}/m^3$) ≈ £25000 m^{-3}, and for less gains than with the nanoparticles.

It would seem that without a low cost high permittivity optical host, or similarly low cost dielectric additives, solvation gains are going to be too expensive to deploy. PVDF-HFP was introduced in chapter 5 as a high permittivity host polymer with ε_r = 11.38 and exhibited high quantum yields for DCM, as shown in Table IV. Unfortunately films made from this were found to be very brittle and of rather poor quality from spin coating. Perhaps with polymerisation techniques a bulk-doped LSC device could be made with this material.

8.6 Conclusions

Presented in this chapter is a detailed spectral model which offers insight into the interplay between different processes and parameters in square-planar LSC device structures. The model requires the solar irradiance spectrum, host and fluorophore optical properties and the LSC dimensions to compute the output irradiance spectrum. External quantum efficiency spectra and average power conversion efficiency values for a given solar cell allow the power conversion efficiency spectrum to be determined. A power correction factor is then applied to correct for efficiency variation due to change in light intensity. With this and the output irradiance spectrum the power generated by the LSC can be calculated. Finally the cost have be determined based on reasonable arguments for the materials and solar cells used.

Optimisation of device structures is done by determining the LSC output irradiance for different fluorophore concentrations and device dimensions. Because of self-absorption effects concentrations of the order of 10^{-4} M are optimal for thicknesses of 1 cm. Optimal output irradiance

depends on device thickness, because absorption of solar irradiance must be maximised, but also on side length and hence mean path length because of self-absorption effects. The application of back reflectors also plays a role, because this doubles the effective absorption length. This means thinner devices and higher *G* values for the same absorption efficiency.

Although GaAs PV cells were seen to be most appropriate in terms of collecting LSC output irradiance, the bulk of modelling was done with the c:Si power conversion efficiency spectrum. This is because c:Si cells are widely available and likely to provide lower cost estimates. Compared to devices in literature the model provides slightly lower estimates than might be expected. Devices in literature only provide single data points so available empirical evidence is currently small.

Cost efficiency estimates show that the best modelled structure was using PR with a LSC side length of L = 1.3 m and thickness W = 1 cm. This gave a cost efficiency of $(£/W)_{conc}$ = 0.76 £/W, double the target of 1 $/W (0.61 £/W). Such LSC plates in an array would cover a larger area for lower cost than a c:Si module solar field but would deliver about a third of the power and poorer economics.

8.7 References

[1] W. G. J. H. M. van Sark *et. al.*, Luminescent Solar Concentrators - A Review of Recent Results, *Opt. Exp.* **16**, 26, 21773 (2008)

[2] A. J. Chatten, K. W. J. Barnham, B. F. Buxton, N. J. Ekins-Daukes and M. A. Malik, Quantum Dot Solar Concentrators, *Semiconductors* **38**, 8, 909 - 917 (2004)

[3] A. J. Chatten, D. J. Farrell, C. M. Jermyn, P. A. THomas, B. F. Buxton, A. Büchtemann, R. Danz, and K. W. J. Barnham, Thermodynamic Modelling of the Luminescent Solar Concentrator, *Proc. 31st IEEE Photovoltaic Specialists Conference*, pp. 82-85 (2005)

[4] A. J. Chatten, D. J. Farrell, R. Bose, M. G. Debije, A. Büchtemann, and K. W. J. Barnham, Thermodynamic Modelling of Luminescent Solar Concentrators With Reduced Top Surface Losses, in *Proc. 22nd European Photovoltaic Solar Energy Conference*, pp. 349-353 (2007)

[5] G. Colantuono, A. Buckley and R. Erdélyi, Ray-Optics Modelling of Rectangular and Cylindrical 2-Layer Solar Concentrators, *J. Light. Tech.* **31**, 7, 1033-1044 (2013)

[6] S. J. Gallagher, P. C. Eames and B. Norton, Quantum Dot Solar Concentrator Behaviour, Predicted Using a Ray Trace Approach, *J. Ambient Energy* **25**, 47-56 (2004)

[7] R. Bose, D. J. Farrell, A. J. Chatten, M. Pravettoni, A. Büchtemann, J. Quilitz, A. Fiore, L. Manna and K. W. J. Barnham, Luminescent Solar Concentrators: Nanorods and Raytrace Modelling, *33rd. IEEE Photovoltaic Specialists Conference*, pp. 1- 5, (2008)

[8] R. Bose, D. J. Farrell, A. J. Chatten, M. Pravettoni, A. Büchtemann and K. W. J. Barnham, Luminescent Solar Concentrators: Cylindrical Design, *Proc. 24nd European Photovoltaic Solar Energy Conference*, pp. 359-362, (2009)

[9] A. Goetzberger and V. Wittwer, Fluorescent Planar Collector-Concentrators: A Review, *Solar Cells* **4**, 3 – 23 (1981)

[10] W. R. L. Thomas, J. M. Drake and M. L. Lesiecki, Light transport in planar luminescent solar concentrators: the role of matrix losses, *Appl. Opt.* **22**, 12, 3440-3450 (1983)

[11] K. R. McIntosh, N. Yamada and B. S. Richards, Theoretical Comparison of Cylindrical and Square-Planar Luminescent Solar Concentrators, *App. Phys. B* **88**, 285-290 (2007)

[12] O. Y. Edelenbosch, M. Fisher, L. Patrignani, W. G. J. H. M. van Sark and A. J. Chatten, Luminescent solar concentrators with fiber geometry, *Optics Express* **21**, S3 (2013)

[13] M. A. Green, K. Emery, Y. Hishikawa, W. Warta and E. D. Dunlop, Solar Cell Efficiency Tables (Version 38), *Prog. Photovolt: Res. Appl.* **19**, 565-572 (2011)

[14] M. A. Green, K. Emery, Y. Hishikawa, W. Warta and E. D. Dunlop, Solar Cell Efficiency Tables (Version 39), *Prog. Photovolt: Res. Appl.* **20**, 12-20 (2012)

[15] M. A. Green, K. Emery, Y. Hishikawa, W. Warta and E. D. Dunlop, Solar Cell Efficiency Tables (Version 44), *Prog. Photovolt: Res. Appl.* **22**, 701-710 (2014)

[16] NREL, AM1.5 Direct Irradiance Spectrum, Excel Data, http://rredc.nrel.gov/solar/spectra/am1.5/

[17] L. H. Slooff, E. E. Bende, A. R. Burgers, T. Budel, M. Pravettoni, R. P. Kenny, E. D. Dunlop and A. Büchtemann, A Luminescent Solar Concentrator with 7.1% Power Conversion Efficiency, *Phys. Stat. Sol. (RRL)* **2**, 257-259 (2008)

[18] J. C. Goldschmidt, M. Peters, A. Bösch, H. Helmers, F. Dimroth, S. W. Gunz and G. Willeke, Increasing the efficiency of fluorescent concentrator systems, *Sol. En. Mater. Sol. Cells* **93**, 176 - 182 (2009)

[19] E. E. Bende, L. H. Slooff, A. R. Burgers, W. G. J. H. M. van Sark and M. Kennedy, Cost & Efficiency Optimisation of the Fluorescent Solar Concentrator, in *Proc. 23rd European Photovoltaic Solar Energy Conference* (2008)

[20] Personal communication, in light of [19], with A. J. Cadby, *University of Sheffield* (2014)

[21] R. Bose, D. J. Farrell, A. J. Chatten, M. Pravettoni, A. Büchtemann, J. Quilitz, A. Fiore, L. Manna, J. Nelson, A. P. Alivisatos and K. W. J. Barnham, The Effect of Size and Dopant Concentration on the Performance of Nanorod Lumienscent Soalr Concentrators, *Proc. 23nd European Photovoltaic Solar Energy Conference*, (2008)

[22] J. S. Batchelder, A. H. Zewail, and T. Cole, Luminescent Solar Concentrators 2: Experimental and Theoretical Analysis of their Possible Efficiencies, *Applied Optics* **20**, 21, 3733 - 3754 (1981)

[23] L. Desmet, A. J. M. Ras, D. K. G. de Boer and M. G. Debije, Monocrystalline silicon photovoltaic luminescent solar concentrator with 4.2% power conversion efficiency, *Opt. Lett.* **37**, 15, 3087 - 3089 (2012)

Chapter 9

Conclusion

9.1 Summary

Over the preceding five chapters the major experimental work of this research project has been discussed in detail. The findings are summarised here first before framing the results in the context of luminescent solar concentrator devices and their place in the wider energy market.

In chapter 4 a Gauge R & R (GRR) study design is used on the absolute measurement of fluorescence quantum yield using an integration sphere so as to assess different sources of variance in the process. The GRR study shows that most of the variance lies within the measurement system rather than in sample fabrication. Fluctuations in laser intensity were found to be the largest source of variance to the total uncertainty in the measurement, although some systematic uncertainty due to calibration and self-absorption corrections could not be ruled out, even when using the light emitting polymer F8 as a fluorescence standard. The more stable GaN laser excitation source was found to achieve a minimum uncertainty on the η_{QY} of ±0.01. Simultaneous measurement of the excitation intensity and sample emission, using a beam splitter and second photodetector, would allow the laser uncertainty to be made negligible. Improving the accuracy of this measurement is an important goal for optical characterisation, particularly for fluorophores with near unity η_{QY}.

In chapter 5 improvements in the self-absorption efficiency, η_{self}, are shown to be possible using the solvation mechanism in the solid state. This phenomenon occurs for particular fluorophores where the molecular dipole moment increases upon absorption of a photon. This in turn causes the surrounding medium to readjust physically and electronically around the new dipole state and in turn this sets up a reaction field which takes energy from the excited state, shifting the emission spectrum towards lower energies. By introducing high permittivity small organic molecules into PMMA along with DCM class fluorophores an improvement in optical efficiency of up to 25% is shown to be possible when using the overlap integral, *J*, as a metric for self-absorption. Later on, in the spectral analytical models of chapter 8, this metric is seen to be far too conservative and much greater improvement in optical efficiency is predicted in that work. However, the cost efficiency analysis in chapter 8 indicates that finding suitable dielectric dopants of low enough cost is likely to be one of the biggest obstacles to employing this method.

In chapter 6 a Prism Ultra-Coat 300 spray-coating deposition tool is assessed for its efficacy in producing thin films for bi-layer LSC devices. A screening study design of experiment is employed to assess the influence of different input factors on the deposited film quality. Quality is characterised by seven response metrics which describe roughness, absorption of incident light and self-absorption of waveguided light. The deposition system offers low control of roughness but typical values of the relevant response metrics are in the range of acceptable levels of surface roughness. Low control is also seen for the self-absorption metrics, which is to be expected since this phenomenon depends primarily on path length through the waveguide and fluorophore properties, not on the deposition method itself. In terms of film thickness, and hence absorption of incident light, the spray coater offers good control in a limited range, which is significantly less than that required to achieve optimal absorption efficiency, even considering use of back reflectors. Ultimately, because of constraints on the possible film thickness and on the fluorophore concentration, this spray-coating deposition system is found to be unsuitable for delivering the requirements of a bi-layer LSC device. It is thus unclear whether spray deposition would work for bi-layer LSC devices.

In chapter 7 an exploration of concentration quenching is exhibited showing results of fluorescence quantum yield and lifetime studies. Different fluorophores are seen to exhibit different forms of quenching response in terms of range (*r* dependence) and strength. Explorations of a variety of organic polymer host materials gives strong indication that the host environment also plays a big part in stabilising fluorophore excited states. By exploring the quenching rate as a function of molecular separation for DCM and C102 in the PMMA host the form of the quenching response is conjectured to be the empirical result of different interactions. The magnitude of the monomial power law determined for the quenching rate indicates that point-like dipole-dipole deactivation interactions, as in FRET, are not the sole responsible mechanism of concentration quenching. Other forms of photophysical interaction are considered to explain this discrepancy including surface-surface and point-surface electronic interactions.

Finally in chapter 8 a spectral based analytical model for estimating LSC performances is described and discussed. The AM1.5 solar irradiance spectrum is used under normal incidence to the LSC collection face of a square-planar LSC geometry. Transmission and absorption of this solar irradiance are considered through host optical properties, LSC thickness and fluorophore extinction coefficients. With the quantum yield and normalised emission spectrum of the fluorophore a corrected equivalent intensity irradiant output is generated from the absorbed irradiance. Trapping efficiency and transport losses, due to both the matrix and self-absorption by the fluorophore, are

then factored into the model so that an LSC output irradiance spectrum is generated for three orders of emission. This output irradiance is coupled with c:Si or GaAs solar cell power conversion efficiency (PCE) spectra to determine the power generated by the modelled LSC device. The LSC PCE can then be calculated and the cost efficiency determined using reasoned values for the costs of each LSC component; the host, dye and solar cells.

The spectral models of chapter 8 show that current fluorophore technology can at best achieve roughly double the 1 $/W cost competitiveness of c:Si modules already on the market. Advancements in fluorophore technology have not translated to much better LSC devices in literature. A comparison of the model with LSC devices from literature finds some level of agreement in the power conversion efficiencies but also that real devices do not occupy a large parameter space, making it harder to justify the model. Almost all literature devices are square-planar LSC devices with one or two fluorophores in single plate LSC designs. Many are small in size, particularly the newest devices, which drives up efficiencies because of reduced light transport losses. Furthermore the newest devices use solar cells that are better suited to the LSC output spectrum and so in real terms the improvement in empirical LSC devices is smaller than a first glance would suggest.

9.2 Implications for LSC Devices

As stated in chapter 1.3 LSC devices are unlikely to see a main role in the global solar energy market. This is borne out by the models of chapter 8 which show low power conversion efficiencies (PCE) and poorer economics than competing solar energy technologies. The main costs of LSC devices are shown to be dominated by the host and dye materials for devices larger than five centimetres in side length. Therefore to reduce LSC costs most significantly the host and dye materials need to be synthesised and processed at as low a cost as possible. Including any new components such as extra dye materials, multiple stacks, more expensive solar cells or photonic band stops will ultimately result in increasing the device cost.

Current fluorophore technology does not offer the high photostability, high quantum yield, low self-absorption and strong absorption of the solar spectrum that LSC devices require. The best fluorophores offer near unity quantum yield for low concentrations, ideal for bulk-doped LSC structures, but still exhibit strong overlap of absorption and emission spectra. The solvation mechanism was considered to alleviate this problem but has been shown to introduce too much

extra expense due to the cost of high permittivity dopants. Development in low cost, high permittivity host materials and suitable fluorophores could solve this and make the technique viable.

The absorption of solar irradiance remains one of the biggest challenges facing fluorophore technology with single dye systems typically able to absorb up to 30 to 35% of solar energy. If all the solar energy up to 750 nm could be absorbed then that would give an absorption efficiency of 54% for AM1.5 irradiance. A concerted, exhaustive effort to explore novel fluorophore compounds is needed to push absorption efficiency up and ultimately test whether all the requirements on LSC fluorophores are feasible. Quantum chemical modelling seems an appropriate way to search for suitable fluorophores without having to synthesise them and test their individual properties.

Current host materials do not offer high enough refractive indices, *n*, which could increase power conversion efficiency by up to 10% relative to PMMA, for $n = 1.7$ or more. Also transport losses due to host matrix related attenuation must be minimised. Considering the concentration quenching results of chapter 7 the properties and interactions of the host with the fluorophore also need to be understood better with a view to improving fluorophore stability and emission efficiency. A more detailed investigation of quenching processes for different hosts with various fluorophores would be a step towards this.

In final conclusion LSC devices do not yet offer the power conversion and cost efficiencies required for marketable devices. The models of chapter 8 suggest that arrays of LSC plates may already find place in niche market roles such as energy windows, paving slabs and awnings. Such systems, if the models are correct, could currently generate around 50 W per m^2 of LSC plate doped with PR, under normal incidence AM1.5 irradiance and using c:Si cells. These would cover any given area for less cost than c:Si modules and could easily be integrated into structures. The power delivered would be a third of that for PV collection under direct solar irradiance. The hypothetical installations proposed would probably need the concentrator plate replacing every two years or so, though the c:Si cells will last much longer. How long the solar cells will last for under LSC output irradiance is another question. Further research and development is really needed to mature the technology before even the above niche markets are considered.